Alma Mater Studiorum – Università di Bologna

DOTTORATO DI RICERCA IN

CHIMICA

Ciclo XXXII

Settore Concorsuale: 03/C2 - CHIMICA INDUSTRIALE

Settore Scientifico Disciplinare: CHIM/04 – CHIMICA INDUSTRIALE

Hydrogen production by enhanced methane reforming with membrane reactors or with CO_2 capture materials

Presentata da: Andrea Fasolini

Coordinatore Dottorato **Supervisore**

Prof. Domenica Tonelli **Prof. Francesco Basile**

Esame finale anno 2020

ABSTRACT

Pure hydrogen production from methane is a multi-step process run on a large scale for economic reasons. However, hydrogen can be produced in a one-pot continuous process for small scale applications, namely Low Temperature Steam Reforming. Here, Steam Reforming is carried out in a reactor whose walls are composed by a membrane selective toward hydrogen. Pd is the most used membrane material due to its high permeability and selectivity. However, Pd deteriorates at temperatures higher than 500°C, thus the operative temperature of the reaction has to be lowered. However, the employment of a membrane reactor may allow to give high yields thanks to hydrogen removal, which shifts the reaction toward the products. Moreover, pure hydrogen is produced. This work is concentrated on the synthesis of a catalytic system and the investigation of its performances in different processes, namely oxy-reforming, steam reforming and water gas shift, to find appropriate conditions for hydrogen production in a catalytic membrane reactor. The catalyst supports were CeZr and Zr oxides synthesized by microemulsion, impregnated with different noble metals. Pt, Rh and PtRh based catalysts were tested in the oxy reforming process at 500°C, where Rh on CeZr gave the most interesting results. On the opposite, the best performances in low temperature steam reforming were obtained with Rh impregnated on Zr oxide. This catalyst was selected to perform low temperature steam reforming in a Pd membrane reactor. The hydrogen removal given by the membrane allowed to increase the methane conversion over the equilibrium of a classical fixed bed reactor thanks to an equilibrium shift effect. High hydrogen production and recoveries were also obtained, and no other compound permeated through the membrane which proved to be hydrogen selective.

SUMMARY

1. CHAPTER 1 – INTRODUCTION

1.1. Hydrogen: uses and new trends

The continuous exploitation of fossil fuels and concurrent production of greenhouse gasses have required the investigation of alternative renewable and greener fuels. In fact, this answers to crucial problems such as the increasing price of conventional fuels, their shortage and the need of reducing the alarming climate change consequences [1,2]. This choice, however, involves not only a change of feedstock, but also a shift in the way energy is produced. In fact, in spite of a centralised energy production carried out close to the petrol extraction site, a novel, delocalized production that takes in account the qualities and resources of the examined area shall be considered. In this way, each area may select and develop the strategy which best fits itself on an environmental, social and economic basis, making energy production more a resource than a need. For instance, if an area produces high quantities of biomasses, it may transform this feedstock, linking energy production with waste elimination and reducing its dependence from petrol import. However, renewable energy depends on the availability of their primary sources, which supply is usually intrinsically intermittent and cannot be stored for a long time. For this reason, the exploitation of renewable energy cannot be independent from energy storage [3,4].In

particular, the storing system must be able to store energy for a long time, to readily provide it when needed and must be economically feasible and transportable. Hydrogen has been addressed for this pursue [5]. In fact, although it is not found in nature as H2 molecule, it can be produced from an energy source, stored and reconverted into energy via combustion of through fuel cells, giving water as the only product. This implies that an improved air quality is obtained where a large amount of hydrogen vehicles are used, a theme which is of high concern in lot of cities nowadays. Moreover, hydrogen presents major high and low heating values (HHV and LHV) than conventional fuels (Table 1).

Table 1: Higher and lower heating values of different fuels at 25°C and 1 atm.

Fuel	HHV (kJ/g)	LHV (kJ/g)
Hydrogen	141.9	119.9
Methane	55.5	50.0
Gasoline	47.5	44.5
Diesel	20.0	18.1

Although the substitution of fossil fuels with hydrogen is far to be completed, many organizations have stressed the importance of such a shift. First of all, the "Hydrogen Council" was launched at the World Economic Forum 2017 in Davos by 13 leading transport, energy and industry companies, with the aim of accelerating the investments for the development and commercialization of hydrogen and fuel cells and encouraging key stakeholders to include hydrogen in their future energy mix[5]. In particular their vision for 2050 comprises the use of hydrogen to answer to 18% of the total energy demand, which would lead to abatement of 6 Gt/year of carbon dioxide, a 2.5 trillion $ market and 30 million new working places. By September 2018, the hydrogen council has increased the number of partners to 53, including among them companies such as Air Liquide, Alstom, Audi, BMW GROUP, China Energy, General Motors, Great Wall Motor, Honda, Hyundai Motor, Johnson Matthey, JXTG Nippon Oil & Energy Corporation, Kawasaki, The Bosch Group, The Linde Group, Total, Toyota and Weichai, just to cite few. After meeting with 11 members of the Hydrogen Council at an event organized by Hyunday, the Korean government announced the creation of 310 hydrogen refilling stations by 2022 [6]. In 2018, the first hydrogen-powered train started to operate in Germany [7] while Mercedes

delivered hydrogen-electricity hybrid cars to different companies [8]._Finally, hydrogen buses have been tested worldwide, hydrogen cars are available in the US and hydrogen trucks operates in Switzerland, Netherlands and Norway [9].

However, only a small amount of hydrogen is nowadays produced and used for energy, as shown in Figure 1 (included among Others). In fact, most of hydrogen is produced to obtain ammonia and in oil refineries for hydrotreating, which comprises 61% and 23% of hydrogen consumption respectively. Finally, methanol production shares a quite consistent portion of 9%.

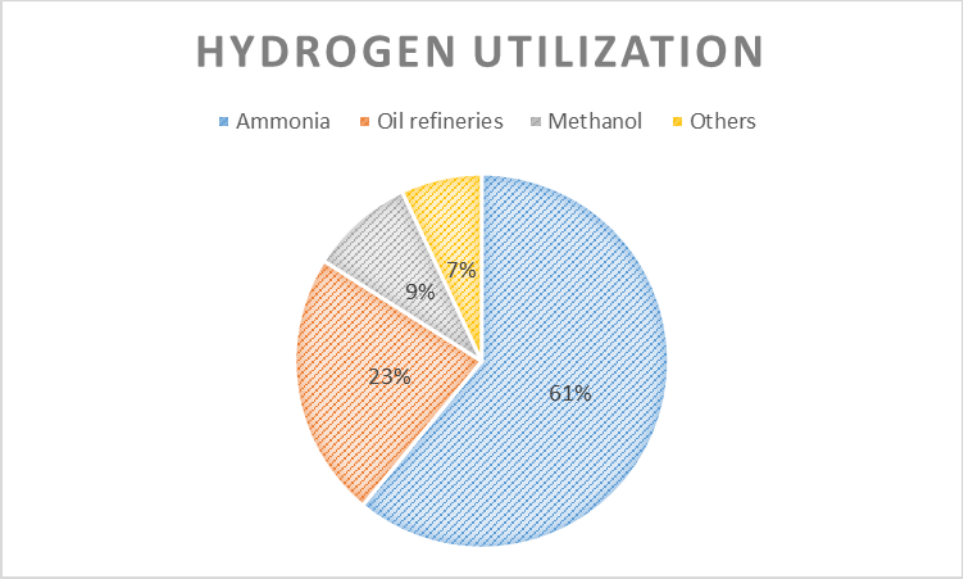

Figure 1: hydrogen utilization, adapted from [10].

Moreover, it is mostly produced from methane in large-scale steam reforming plants (46%), or by oil reforming (30%). A smaller fraction is obtained form coal, while the green electrolysis route accounts for only 4% due to low efficiencies and yields (Figure 2).

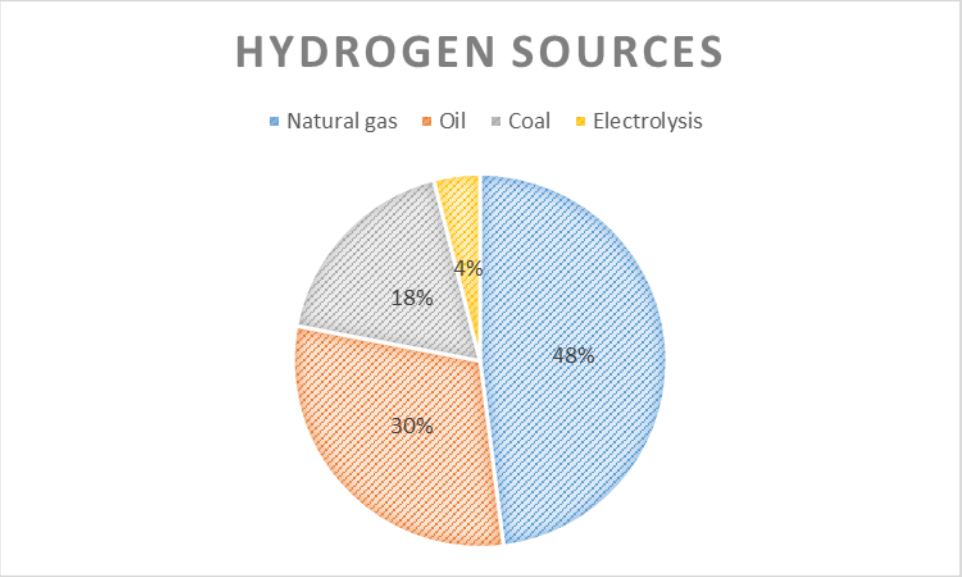

Figure 2: Hydrogen sources

Hydrogen plants are usually very large due to economies of scale and thus highly energy and heat intensive [11].

However, this large scale production will not be able to fulfil the requirement of an economy in which hydrogen in used as main energy source. In fact, such a market would require a production of around 600 tons/year of hydrogen, which means that the actual production must be largely increased [12]. Building smaller plants is less cost effective especially because of feedstock cost [11]. However, hydrogen must be delivered in vast diverse areas in an hydrogen economy scenario, but fulfilling this objective with large-scale plants would not be economically viable because cost of delivery counts for a wide share of hydrogen total cost. Rather, a possible solution consists in thousands of delocalized small-scale hydrogen production sites that are able to provide low pressure hydrogen to feed their surroundings, cutting the delivery cost, especially for regions where low cost natural gas is available [11,13].

Thus, in order to shift toward a hydrogen economy, natural gas conversion can be seen as a near-term alternative which, thanks to the well-developed steam reforming technology, may provide an early market which helps to develop the novel infrastructures. However, greenhouse gases reduction for these processes is a key factor for this option. Moreover, the flexible nature of a delocalised production may provide social and economic advantages by adapting to the local resources. However, additional work on the steam

reforming technology are needed such as: (i) make it economical on a small-scale, especially reducing the energy cost and environmental impact of the process; (ii) couple the methane feedstock with bio-methane one; (iii) implement direct hydrogen purification, which allows to reduce the cost of separation and to more easily capture the CO_2-rich sub-product, to store it or further react it. The following chapters give an outlook on the main processes used for industrial hydrogen production, followed by the presentation of some processes focused on the limitation of energy consumption in the former. In particular, this study focus on hydrogen production from methane through thermochemical processes, which are, at the moment, the most employed for its production. However, it must be noted that new processes which uses greener feedstocks and routes may become more economically convenient and environmentally friendly and thus might be applied to an industrial scale. Poullikkas et al provided an interesting review on this topic [14].

1.2. **Commercial hydrogen production from methane**

Nowadays, methane in the main source of hydrogen on an industrial scale. In particular, the main industrial routes comprise natural gas steam reforming (SR), catalytic partial oxidation (CPO) and autothermal reforming (ATR). To a lower extent, heavier hydrocarbons catalytic partial oxidation, coal gasification and green routes can be accounted. Many factors concur in the relative competitiveness of each process, for instance catalyst efficiency, scale, required purity of hydrogen, cost of the raw materials and energy. Although most of these processes rely on fossil fuels, they are still projected to be more economical than renewable routes for the next year and will play an important role in the near term, as soon as a green hydrogen production is available at low cost [15].

1.2.1. Steam reforming of methane

Steam reforming of methane is the main industrial process for hydrogen production. It exploits the catalytic reaction of steam and methane to give hydrogen and carbon monoxide (syngas) (Eq.1).

$$CH_4 + H_2O \leftrightarrows 3H_2 + CO \qquad \Delta H^0_{298} = +206\ kJ / mol \qquad (Eq.1)$$

To obtain acceptable conversions, the process needs to operate at high temperatures (700-1000°C) due to the endothermic nature of this reaction and the fact that it increases entropy and thus needs external heating, usually provided by burning part of the methane in an external furnace. In particular, a multi-tubular reactor is employed where the reaction stream passes over the catalyst, which is filled inside the tubes, while methane is burned in the external part. Moreover, although the reaction is favored at low pressures, the process is run at 20-30 bars on an industrial scale in order to reduce the reactor volume, obtain a more economical process and fulfill the market requirement for high pressure hydrogen. The inlet methane is firstly pre-heated and desulfurized. A Co-Mo catalyst is used to convert thiols in hydrogen sulfide, then a ZnO bed removes the H_2S. This is done because the Ni-based catalyst usually employed in the steam reforming is sensitive to sulfur impurities which lead to deactivation by formation of Ni-S species. Then over-heated vapor is added. In particular, a steam to carbon (S/C) ratio of 3-4 is usually employed at large scales, even though the stoichiometry of the reaction would suggest to use a S/C of 1. This is done to increase the hydrogen yield and to avoid unwanted reactions such as carbon formation, which would lead to deactivation of the catalyst. In order to decrease the heat needed in the reformer, an adiabatic pre-reformer can be employed, which converts the small fraction of higher hydrocarbons that can be found in natural gas at temperature between 350 and 550°C [16]. Moreover, a heating zone can be placed between the pre-reformer and the reforming reactor, which raises the feed temperature to 650°C, so that the size of the reforming reactor can be reduced. This helps to reduce the capital cost of the plant as costly alloys containing Ni and Cr must be employed to produce the tubular reactor because of the high temperature required for the SR. In particular, a critical feature of this process is the creation of temperature differences between the catalytic bed and the outer walls of the tubes as high as 200°C. Nevertheless, the average lifetime of reactor is estimated to be around 100000 h before creep rupture [17].

Steam reformers are built in different arrangements. Usually four different setups are found: bottom-fired, terrace-wall fired, top-fired and side-wall fired. The first one is characterized by a constant heat profile along the bed, thanks to a counter-current heating that results in high temperatures at the reforming end; the terrace-wall fired reformer consists in a modification of the former one, but provides lower tube wall temperatures. the third is

characterized by temperature peaks in the upper part of the reactor; the last one is more flexible and permits a better control of temperature. The catalysts are mainly nickel-based. Co and noble metals are also very active, but more expensive than Ni, thus less used. Appropriate supports are required to well-disperse Ni particles and avoid sintering, which is favored over 600°C, as the catalytic activity is related to Ni surface area [18,19]. Alfa-Alumina and MgO are usually employed for this purpose as they are stable at high temperatures. However, they possess surface areas between 5 and 50 m^2/g due to their high employment temperature. Nevertheless, they are suitable to disperse Ni for industrial catalysts. Another issue in industrial reformers is mass transport, mainly inside the pores of the catalyst. Moreover, the high gas velocities employed in industrial reformer require large catalyst size. A proper catalyst shape is designed in order to provide the highest activity with minimum pressure drops, improving heat and mass transfer. Generally, these catalysts can carry out the reforming reaction for more than 5 years of continuous operation

1.2.2. Catalytic Partial Oxidation

Partial oxidation, is an exothermic reaction that consumes oxygen and methane (or another hydrocarbon) to produce syngas (Eq.2).

$$CH_4 + 0.5O_2 \leftrightarrows 2H_2 + CO \qquad (\Delta H^0_{298} = -36 \text{ kJ mol}^{-1}) \quad \text{(Eq.2)}$$

Homogeneous gas-phase partial oxidation occurs over 1200 °C, though a catalyst is usually employed to lower it to 800-900 °C (Catalytic Partial Oxidation – CPO), providing a more energy efficient process. Giving the widespread application of Ni-based catalyst to SR, these catalysts have been applied to CPO too. However, even in this case, deactivation by carbon formation was found to be troublesome. The main feature of partial oxidation is the complete consumption of oxygen and almost total conversion of methane over the catalytic bed. In particular, two mechanism have been mainly proposed for CPO: direct and indirect [20,21].

In the former, methane is decomposed to elemental carbon and hydrogen over the catalytic surface, then carbon reacts with oxygen to give CO and finally CO and H_2 are desorbed. The indirect mechanism supposes that oxygen reacts in the first part of the catalytic bed through exothermic combustion, as this area was found to be much hotter

than the second part of the catalytic bed [22]. There, endothermic reactions such as steam reforming and dry reforming, lower the temperature and consume the produced water and CO_2 to provide hydrogen and CO. However, this mechanism is still under debate. In general, it is complex to determine the reaction mechanism because: (i) more than one mechanism may be involved [21]; (ii) and the nature of the active phase may change with time, affecting which mechanism dominates the process; (iii) the support can play a role in the mechanism dominance and (iv) different operating conditions may favor different mechanisms.

The partial oxidation mainly gives three advantages over classical steam reforming: first, it is more suitable for downstream processes such as methanol and Fischer-Tropsch syntheses, as it provides a H_2:CO ratio of 2. Second, the cost of heating and the amount of released CO_2 in this operation are cut thanks to the exothermicity of the process. However, pure oxygen is needed, and expensive oxygen separation plant are required. In fact, air should not be employed, as it would create sub-products and dilute the syngas, requiring to separate it from nitrogen. Finally, hot spots may form, especially in the first part of the catalytic bed, favoring deactivation phenomena such as sintering of the active phase. Third, it can be run at short contact times and thus in a more compact setup. In fact, this characteristic linked to the possibility of avoiding to feed steam, allows to reduce the amount of catalyst and reactor volume to produce the same amount of hydrogen via steam reforming. In particular, it has been calculated that a volume of around 11000 m^3 and 21 tons of catalyst were required to produce 55000 Nm^3/h of pure hydrogen via SR, while CPO needed 70 m^3 and 0.85 tons of catalyst [23]. Thus, CPO is more suitable for a delocalized small-scale production for hydrogen distribution or on-site production for direct use.

1.2.3. Autothermal reforming

The autothermal reforming is a process in which non-catalytic partial oxidation and catalytic steam and CO_2 reforming are carried out in a single reactor. It was developed by Haldor Topsøe in 1950s and is mainly used to produce syngas for methanol and Fischer-Tropsch synthesis thanks to the ideal H_2/CO ratio of 2 obtained [24,25]. The first part of the reactor comprises a combustion chamber in which the mixture of natural gas, oxygen and steam is ignited to combustion, consuming methane and oxygen. Then steam and dry reforming take place over the catalytic bed placed after the furnace. By adjusting O/C and S/C it is

possible to provide the heat needed to conduct steam and dry reforming, through the oxidations that occur in the combustion chamber [26]. In the 1990s more progresses were reached which made possible to run ATR with low S/C ratio (as low as 0.6). Among the important parameters of this process, good mixing of reagent in the combustion chamber is important to avoid soot formation and well-shaped catalyst are required to provide high activity and avoid pressure drops [24]. Catalyst with high mechanical properties and stable at high temperatures (1000-1200°C) are needed to withstand the harsh conditions of the ATR. For instance, Ni supported over Mg-Al spinel can be employed. Also in ATR an appropriate catalyst shape is needed to avoid pressure drops. Finally, different reactor configurations have been studies to avoid this problem [13]. ATR runs nowadays on an industrial scale to produce syngas for ammonia, methanol and for methanol and Fischer-Tropsch or as a second reformer after a steam reforming reactor to completely convert methane to syngas.

1.2.4. Water gas shift

The syngas produced by the processes cited above can be further processed to get, for example, methanol or diesel, via Fisher-Tropsch synthesis. However, if pure hydrogen is desired the syngas production is followed by water gas shift (WGS) to reduce the CO amount in the syngas and increase the hydrogen yield. In fact, WGS consumes carbon monoxide and water to give carbon dioxide and hydrogen (Eq.3).

$$CO + H_2O \leftrightarrows H_2 + CO_2 \qquad \text{(Eq.3)}$$

The reaction is slightly exothermic, thus favored at low temperatures and not influenced by pressure. Thus, high pressures are industrially employed to obtain a compact design. However, temperatures as high as 400°C are used industrially to favor kinetics especially when cheap catalyst, such as iron-based are used. However, to improve the hydrogen yield the process is carried out in two stages, namely high temperature shift (HTS) followed by a low temperature shift (LTS) [27]. In particular, the HTS reactor operates at 400-450°C and carries our most of the CO conversion. Then the stream temperature is decreased with a thermal exchanger around 300°C where the CO amount is reduced to less than 1% thanks to the increased equilibrium conversion given by the lower temperature.

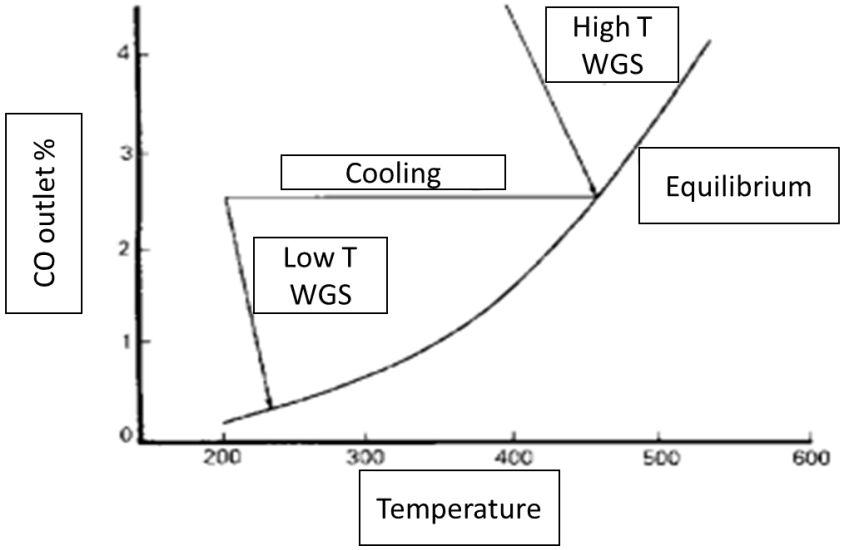

Figure 3: Stages of water gas shift reaction on industrial scale, adapted from [27]

WGS catalyst must be selective toward water gas shift and unselective toward methanation reaction which can occur in presence of CO and H_2 at low temperature (Eq.4).

$$CO + 3H_2 \leftrightarrows CH_4 + H_2O \qquad \text{(Eq.4)}$$

The HTS is catalyzed by a FeCr-based catalyst which needs higher temperatures to provide high activities. while the LTS employs a more expensive copper based one which is active even at lower temperatures. Although a high conversion could be obtained with only the LTS, the use of the HTS reactor is justified by the cheaper price of the Fe-Cr catalyst and to the fact that the syngas inlet that comes from a reformer is already at high temperature. However, this must be lowered and heat recovered because the HTS catalyst suffers from sintering deactivation at temperatures higher than 450°C and because the equilibrium conversion lowers at higher temperatures.

1.2.5. Economic considerations for hydrogen production from methane

The choice between the processes described above, depends on the scale economy. For instance, steam reforming requires burners and is economically convenient if heat recovery units are considered. In general, SR is usually used for production that ranges between 200 and 250000 Nm^3/h of H_2 because of its high investment cost and low utility cost[1]. However, the feedstock account for a great share of the cost. In particular, 60% of the cost is due to natural gas for plants with capacities between 50000 and 250000 Nm^3/h, while 30%

is capital cost related and 10% is accounted to operation and maintenance. On the opposite, partial oxidation and ATR reduce the cost of heating but require expensive oxygen purification facilities, that counts for 40% of the total cost. This consistent investment makes these two technologies convenient only at large scale. If air were used as oxidant, bigger plants, heat exchangers and compressors would be needed because of the dilution by nitrogen. So, ATR integrates or substitutes SR at capacities superior to 100000 Nm^3/ h [13].

At lower scales SR is the preferred technologies. However, it is less economical because of the absence of efficient heat recovery systems. Heat recovery and energy demand are crucial problems for small scale SR and new types of reactor are being produced to provide more efficient processes. It is the case of Haldor Topsoe convective reformer, fabricated for applications between 50 and 300 Nm^3/ h of hydrogen [13]. Low temperature steam reforming (LTSR) is an option to reduce the capital cost and operating cost of small scale steam reformers. This process is analogue to the classical SR, but works at temperatures around 500°C compared to 700-900°C usually found in SR. This allows to reduce the energy demanded to heat the reaction and to use cheaper materials to build the reactor reducing capital cost, operation cost and maintenance. Moreover, WGS reactors are not needed as this reaction also occurs at the temperatures employed in the LTSR. Finally, even methane consumption and cost is reduced as LTSR needs around 0.38 m^3 of CH_4 per m^3 of produced hydrogen, while SR consumes 0.45 m^3 CH_4 per m^3 of H_2 produced.

Figure 4 compares the production cost of small scale LTSR and SR, namely 100 and 200 Nm3/ h. LTSR is more convenient at smaller scale, while the production cost is comparable for the two processes at 200 Nm3/ h.

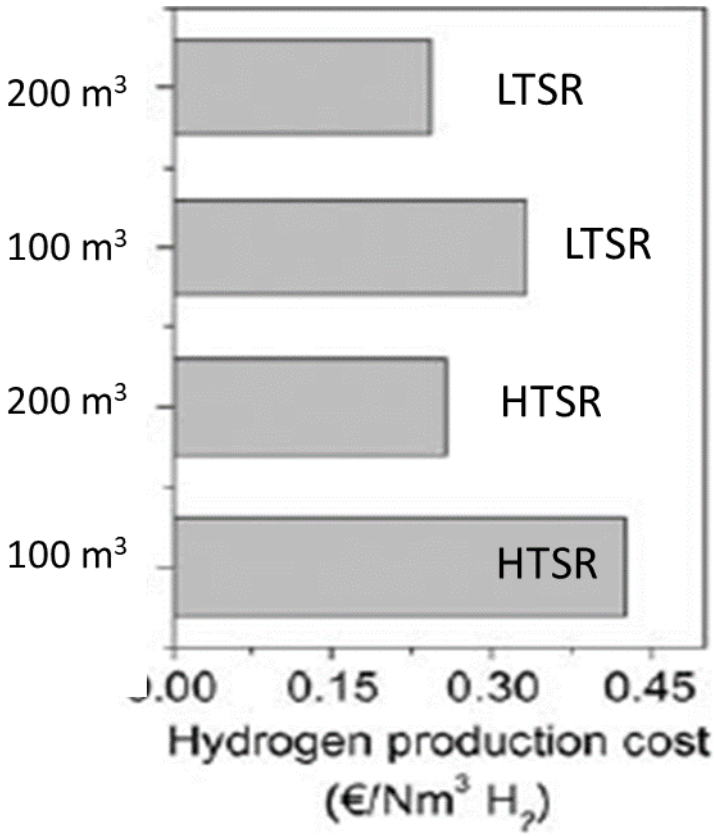

Figure 4: Hydrogen production cost on different scales, adapted from [13]

Deeper economic analysis are found in different reviews [28,29].

1.3. **Hydrogen purification**

1.3.1. Commercial hydrogen purification: Pressure Swing Adsorption (PSA)

Water gas shift provides a stream enriched in hydrogen with a low CO content. However, CO_2 is produced as a subproduct and must be separated to get pure hydrogen. Pressure swing adsorption is the main industrial option for purifying hydrogen and several hundreds of PSA units have been installed all over the world thanks to the high hydrogen purity provided [30]. In PSA the gas stream passes over a microporous-macroporous solid (adsorbent) at a relatively high pressure, which selectively adsorbs carbon dioxide. So, a stream enriched in hydrogen in obtained. Subsequently, CO_2 is desorbed from the adsorbent by lowering its partial pressure in the adsorption column, so that the solid is regenerated. PSA provides hydrogen with a 98–99.999 mol% purity and a hydrogen recovery of 70-90%.

1.3.2. Novel hydrogen purifications: hydrogen-selective membranes

The new trend of pure hydrogen production, shifted toward a small-scale delocalized production, requires a separation method different from PSA that is economically suitable on a large scale. Membrane separation is a suitable technique that can be employed in such cases. A hydrogen selective membrane is a material which is able to let hydrogen permeate through itself, but is not permeable to other gas, allowing hydrogen purification. Membranes can be produced in tubular or planar fashion and exist in different types, that separates hydrogen through different processes. The next chapter presents the different types of membrane and their permeation mechanism.

1.3.2.1. Types of membranes for hydrogen purification

Part of this chapter was published in the book:
Basile, F., Fasolini, A. & Lombardi, E. CHAPTER 7 Membrane Processes for Pure Hydrogen Production from Biomass. in Membrane Engineering for the Treatment of Gases: Volume 2: Gas-separation Issues Combined with Membrane Reactors (2) 2, 212–246 (The Royal Society of Chemistry, 2018)
Reproduced from Ref. [31] *with the permission of Royal Society Chemistry.*

Membranes for hydrogen separation are multiple, made of different materials which come with different separation mechanisms. Dense membranes are by far the most used ones in hydrogen separation due to their high selectivity.
In dense membranes, a solution-diffusion mechanism takes place. At first, the molecule undergoes a dissociative chemisorption over the surface of the membrane. This is followed by the dissolution of the chemisorbed atoms and their diffusion toward the opposite side. There, recombination of the starting molecule and desorption occurs. Each one of these consecutive steps may become rate limiting, depending on temperature, pressure, and gas mixture composition [32]. This mechanism is characteristic for dense metallic membranes, e.g. palladium ones.
A similar mechanism is involved for dense ceramic membrane, e.g. perovskite ones. However, instead of solubilizing hydrogen in the atomic form, they provide separation by

transferring protons and electrons separately. After being adsorbed over the membrane surface, molecular hydrogen is dissociated into protons and electrons, both of which then diffuse to the other side of the membrane surface, where they recombine to form the molecule again. The separation thus relies on the ability of the ceramic substrate to conduct both protons and electrons. To achieve this property, high temperatures have to be employed and this make ceramic membrane suitable for high temperature applications. Figure 5 shows the separation mechanism involved.

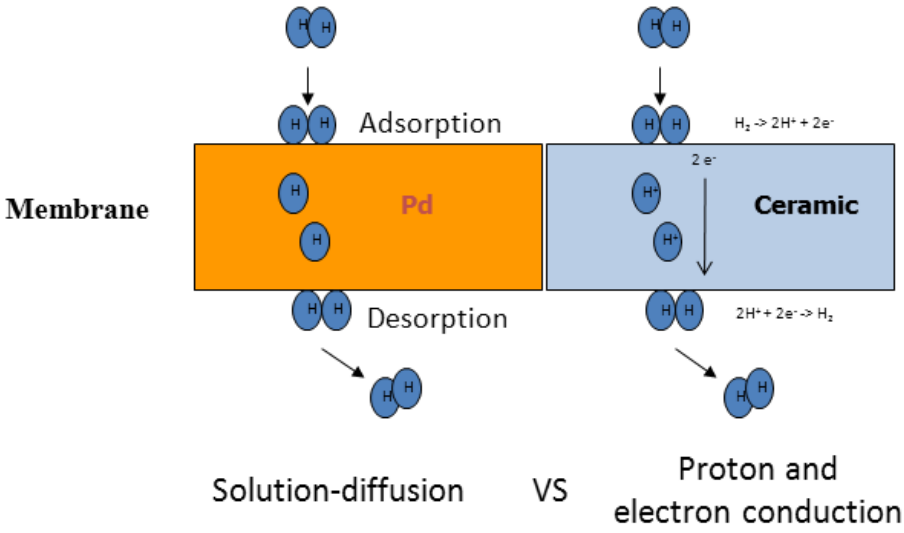

Figure 5: Permeation mechanism in dense metal membranes and dense ceramic membranes

Another kind of classification is made according to the materials the membrane is made of. In particular, metal, polymeric (organic), and ceramic membranes are used to separate hydrogen. The advantages and disadvantages of each one are treated below.

1.3.2.1.1. Dense metal membranes for hydrogen separation

The study of metallic membranes for hydrogen separation has been focusing on palladium ones. Among all membranes, palladium ones offer a complete hydrogen perm-selectivity [33]. They are dense membranes which involve a solution-diffusion mechanism. In particular, permeation can be expressed by the Sievert-Fick's law:

$$JH2 = \frac{Pe_{H2}(p^n{}_{H2},\text{ret} - p^n{}_{H2},\text{perm})}{\delta} \quad \text{(Eq. 5)}$$

J_{H2} is the hydrogen flux through the membrane, Pe_{H2} is the permeability of hydrogen, $p^n{}_{H2,ret}$ and $p^n{}_{H2,perm}$ are the partial pressures of hydrogen at the retentate and permeate side respectively and δ is the thickness of the palladium layer. Finally, n is a constant that depends on the type of membrane. It is usually comprised between 0.5 and 1.0 and is determined experimentally. In particular, n can be experimentally calculated by performing hydrogen permeation tests at constant temperature and different pressures, then graphically plotting the dependence of hydrogen flux over hydrogen partial pressure and fitting with a linear regression the equation with different n values. The n value that provides the highest R^2, which indicates highest fitting, is the one that characterizes the investigated membrane.

The permeability (Pe_{H2}) is dependent on temperature according to the Arrhenius equation (Eq. 6).

$$Pe_{H2} = Pe^0{}_{H2}\exp^{(-\frac{Ea}{RT})} \quad \text{(Eq. 6)}$$

Where $Pe^0{}_{H2}$ is the pre-exponential factor, Ea the activation energy, T is the temperature expressed in Kelvin and R is the gas constant.

Thus, the difference in the hydrogen partial pressure between the retentate and permeate can be increased in order to raise J_{H2}. This is usually done by working at high pressures and using a sweep gas on the permeate side in order to lower hydrogen concentration. However, it may not be enough to provide adequate fluxes and the cost of compression, of sweep gas production and of the downstream separation set a limit for this technique. Another strategy used to enhance hydrogen flux is the reduction of the membrane thickness. However, this may be limited by the need of complex and expensive synthesis. Moreover, the permeability can be enhanced by increasing the temperature. However, it must be remembered that too high temperatures may promote carbon formation and membrane degradation. Finally, a way to increase the hydrogen flux through the membrane is using bigger ones that thus possess a higher separation area although this is not advisable as these membranes would be too expensive.

Pd membrane employment is limited by the high cost of palladium. In order to lower it, thin palladium films deposited over membrane supports have been widely studied [34–38]. Moreover, the support provides the membrane with improved mechanical strength and resistance. However, the ceramic support poses problems related to connections when the membrane is applied in plants. In fact, it is challenging to provide sealing when the ceramic support is sealed to metal tubes, due to different expansion coefficient of metal and ceramic materials. This disfavor high temperature applications. In addition, elevated temperatures may cause problems to the stability of the membrane. The expansion problem of the ceramic support could be eliminated by using a metal ones. However, interdiffusion of metals of the support occurs in the palladium layer, obstructing the permeance of hydrogen.

In order to avoid interdiffusion of the metallic support, a coating layer may be deposited between the Pd layer and the support itself (figure 6). This would provide a membrane that can be easily connected to plant pipes thanks to the metallic support, while not suffering from interdiffusion thanks to the coating layer. Talking about this, the catalyst may be layered over Pd as well, in a membrane reactor configuration. This would provide a more intimate contact between hydrogen and palladium, leading to a more efficient production and

separation.

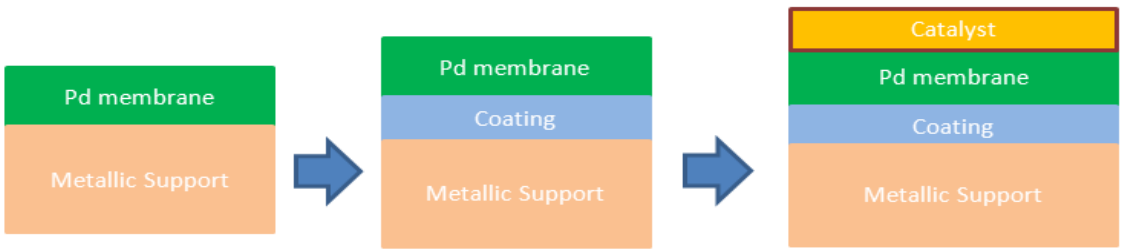

Figure 6: Layered membrane module hypothesis

Finally, carbon deposits over the palladium are found at temperatures higher than 450 °C. On the other hand, low temperature applications are limited by several phenomena. The first one is called embrittlement. It occurs at temperatures lower than 300 °C when some of the elemental hydrogen that permeates the membrane combines inside the palladium layer to give molecular hydrogen. In this way some pressure is created inside the metal and results in diminished ductility [39,40]. Moreover, carbon monoxide, which is found in syngas or WGS outlet, adsorbs over palladium surface and blocks hydrogen dissociation sites. This results in a lower hydrogen permeability. To avoid CO adsorption, temperatures higher than 300°C must be applied [41]. In addition, high temperatures are needed to avoid poisoning by H_2S, which can be found as an impurity in some feedstocks. These issues can be lowered by alloying palladium with Ag, Cu, Fe, Ni, Pt and Y [42–47]. Finally, water, which is present in WGS outlet. can also adsorb on palladium sites, reducing their availability.

Though, palladium and palladium-alloyed supported membranes seem to be one of the best options for hydrogen separation, but their application is limited to a certain temperature range (350-500°C) due to embrittlement, phase modification, CO and water adsorption, carbon deposition, stability and thermal expansion coefficient.

1.3.2.1.2. Polymeric membranes for hydrogen separation

Polymeric membranes are dense membranes, commercially available and at a good stage of development. Despite many polymeric membranes can permeate hydrogen, their employment is limited by their operating temperature which is around 100 °C. This make them not suitable for high temperature application, which are required in industrial processes. In fact, cooling down and reheating the gaseous feed results in a high cost of process.

1.3.2.1.3. Ceramic membranes for hydrogen separation

Recently, dense ceramic membranes are gaining more and more importance in hydrogen separation. Dense ceramic membranes are usually made of polycrystalline ceramic materials, mostly perovskites, which allow specific gas species to permeate or adsorb in the

dense material. An advantage of dense ceramic membranes is the possibility to operate at high temperature, flanked with chemical resistance to CO, CO_2 and H_2S and good hydrogen selectivity.

1.3.2.1.4. Membranes for high temperature applications

As many processes for hydrogen production employs high temperatures, membranes that can operate in this range would avoid cooling of the feed and provide a reliable tool for membrane reactors, where reaction and separation are carried out together inside the membrane.

According to their optimal operating temperature membranes can be divided as follows:

- For temperatures up to 100 °C only dense polymer membranes can be used.
- For temperatures between 200 °C and 600 °C dense metallic membranes are employed.
- For temperatures over 600 °C dense ceramic membranes are suitable.

Thus, it is difficult to carry out a thermal process in a polymeric membrane, while metallic ones seem to be optimal for the water gas shift reaction only, which usually operates between 300 and 400 °C.

On the other hand, in processes such as steam reforming, oxy-reforming and gasification temperatures higher than 700°C are needed. In this regard, dense ceramic membranes are gaining more and more interest.

The separation for dense ceramic membranes is based on their ability to dissociate hydrogen into protons and electrons, to conduct both of them through the membrane and to associate them again to form molecular hydrogen on the opposite side. As this property is activated only at high temperatures, these membranes seem suitable as membrane reactors for the cited processes.

The membranes are usually made of perovskite, even though a metal is sometimes present as a composite in order to provide electron conductivity, while the ceramic plays the role of proton conductor. However, a lot of research have focused on single phase ceramic membranes able to conduct both protons and electrons, i.e. doped $SrCeO_3$ and $BaCeO_3$ perovskite membranes. Unfortunately, these two are poisoned by water and carbon dioxide, which disfavor their employment. Thus, other membranes have been developed,

but had to be integrated with an auxiliary external electronic circuit, as the ceramic material could not conduct electrons well. Finally, another kind of membranes called mixed proton and electron conduction channels (MPECs) are able to transport both protons and electron at the same time, without the aim of an electric circuit. MPECs offer fast and selective H_2 transport, and provide a simple, low-cost, efficient way to separate hydrogen from gas streams at high temperatures.

On the other hand, the following are open challenges that hinder dense ceramic membrane commercialization at the moment: (i) stability to acidic atmospheres at high temperatures must be increased [48,49], (ii) proton and electron conductivities and hydrogen dissociation and association rates have to be enhanced [50,51], (iii) mechanical strength and thermal stability for long term operation have to be studied [50].

An example of a dense ceramic membrane that is able to separate hydrogen at high temperatures was reported by Sullivan et al. [48], who tested the permeation of a planar $BaCe_{0.8}Y_{0.2}O_3$ and $Ce_{0.8}Y_{0.2}O_2$ perovskite membrane. $BaCe_{0.8}Y_{0.2}O_3$ serves as the proton conductor, while $Ce_{0.8}Y_{0.2}O_2$ as an electron one. The enhancement of the protonic and electronic conductivity of the membrane at higher temperatures were confirmed by experimental results. Separation was raised by increasing the difference in hydrogen partial pressure between the sides of the membrane as well. A maximum hydrogen flux of 0.0744 ml cm^{-2} min^{-1} was observed at 900°C and 0.5 hydrogen pressure gradient. However, due to stability concerns, a difference in partial pressure of 0.1 atm is preferable, which results in a hydrogen flux of 0.03 ml cm^{-2} min^{-1} at 900°C.

1.3.2.2. Commercially available hydrogen selective membranes

Although the cost of Pd does not favor a widespread application of these membranes on an industrial scale, Jonhson-Mattey already used a Pd membrane to purify hydrogen to a less than 0.1 ppm impurities in 1964. Moreover, they later developed a membrane reactor to carry out methanol steam reforming for hydrogen production. Tokyo Gas Company Ltd. developed a steam reforming membrane reactor to convert city gas (with a methane content of 88% methane, 4.6% ethane, 5.4% propane and 1.5% of propane): This plant was able to provide 40Nm^3/h of 99.999% pure hydrogen. Hydrogen selective membranes for

pilot scale are nowadays produced by Air Products, Grasys, IGS, Air Liquide, Hysep and DivexGlobal and commercially available.

In conclusion, palladium membranes are the most studied and developed membranes for hydrogen separation and their implementation in an industrial process may be possible if the cost of the membrane itself can be lowered. On the other hand, other kind of membranes are promising alternatives and their study and development is an ongoing challenge. In particular, dense ceramic membranes are emerging as a valuable alternative for high temperature applications.

1.4. **Novel processes for hydrogen production**

Large scale steam reforming is a well-developed and well-established process for industrial hydrogen production. However, the evolving economic, social and environmental scenario is pushing for the development of new processes for hydrogen production. Among those, this work was focused on oxy-reforming and low temperature steam reforming associated with membrane reactors, in the optic of providing efficient small-scale options for pure hydrogen production.

1.4.1. Oxy-reforming

The oxy reforming is a process in which steam reforming and catalytic partial oxidation are carried out on the same catalyst to produce syngas. In fact, large differences in temperature between the catalyst and the reactor walls are produced during steam reforming operation due to the endothermic nature of the reaction, requiring to heat the reactor walls at temperatures higher than 900°C with a consequent high energy demand and the need for specific material for the reactor. On the opposite, the CPO process produces hot spots that can increase the catalyst temperature by as much as 200°C [22]. This can result in catalyst deactivation and breakage. However, by performing SR and CPO together, the oxy-reforming process allows to drastically reduce the temperature gap between the heating system and the catalyst to 20-50°C, employing temperatures around 750°C, sub-stoichiometric oxygen and a low steam to carbon ratio [49,50].

Lower operative temperatures also help to reduce catalyst deactivation by sintering. Moreover, the oxy-reforming characteristics make it an optimal process to be coupled with a membrane separation unit. In fact, low amount of steam is employed which not only requires less heat to overheat excess steam, but also avoid to dilute the hydrogen content of the outlet stream, giving high hydrogen partial pressures, which are the driving force of separation is case of dense palladium membranes. Nevertheless, high total pressure are advisable to further increase hydrogen partial pressure and favour permeation.

Due to the presence of water, steam and oxygen, many reactions can occur and are kinetically and thermodynamically favoured depending on the catalyst and operative conditions employed. In particular, the desired reactions are steam reforming and partial oxidation of methane as they produce syngas. However, carbon formation becomes a consistent problem in the oxy-reforming conditions. This phenomenon, has been widely studied as it is important for both steam reforming and CPO reactions and will be deeply analysed in a following chapter [51–55].

1.4.2. Low Temperature Steam Reforming (LTSR) and LTSR in a membrane reactor.

Steam reforming is industrially conducted at temperatures around 900°C. In fact, methane conversion and hydrogen production are favoured in these conditions due to the nature of the reaction which is endothermic and increases entropy. However, this requires large amount of heat to be fed to the reactor and in some conditions lower operative temperature may be advisable as previously highlighted. This entails advantages in terms of energy consumptions as operative temperatures can be lowered to 400 to 600°C, even though it decreases the equilibrium conversion. The water gas shift reaction, which is usually carried out in reactor downstream the high temperature steam reforming, is in fact favoured in the low temperature range employed in LTSR. Due to the presence of steam in the process feed, the two reaction occur consequently in the same reactor. This allows to drastically decrease the CO content compared to the classical steam reforming, providing an outlet gas with a high H_2/CO ratio. Finally, the temperatures employed are compatible with the employment of a Pd membrane for hydrogen separation.

This opens the possibility of carrying out the process in a membrane reactor setup in which the steam reforming occurs inside a tubular membrane from whose walls hydrogen is separated. However, the employment of a membrane requires high operative pressures that reduces equilibrium methane conversion. Higher pressures and lower temperatures, however, disfavour the methane conversion and favour carbon formation. However, the hydrogen removal from the membrane reactor allows to increase hydrogen yield and methane conversion over the equilibrium limit thanks to the Le Chatelier's principle allowing to provide a more efficient process.

For these reasons, very active, selective and stable catalysts are required to perform LTSR in an efficiently. In fact, these must be able to activate methane at low temperatures compared to classical steam reforming catalysts and need to drive methane conversion to the equilibrium value even at low contact times. Furthermore, they must be resistant to carbon formation, which is particularly favoured in the temperature range involved in LTSR (as it will be discussed in section 1.4.2.2.1). Moreover, challenges for membrane reactors involve the cost of Pd, sulphur tolerance and mechanical resistant of the membrane reactor.

1.4.2.1. Thermodynamic analysis of steam reforming, partial oxidation and oxy-reforming

1.4.2.1.1. Thermodynamic analysis of steam reforming

Methane steam reforming is an endothermic reaction. However, it usually occurs together with the subsequent water gas shift reaction, which is slightly endothermic. Moreover, the presence of CO_2 in the reaction product may favour the occurrence of dry reforming (Eq. 7).

$CH_4 + CO_2 \leftrightarrows 2H_2 + 2CO$ (Eq. 7)

Steam reforming and water gas shift thermodynamic is well known and studied in literature [60]. In this work the equilibrium molar fractions, conversions and yield were examined using the CEA NASA software. The software provides the molar gaseous outlet composition (non-converted CH_4, non-converted H_2O, CO, CO_2, H_2 and deposited carbon if present), based on the feed composition in terms of molar percentage, the reaction temperature and pressure. Figure 7 shows equilibrium methane conversion and hydrogen partial pressure as function of temperature at different steam to carbon ratio.

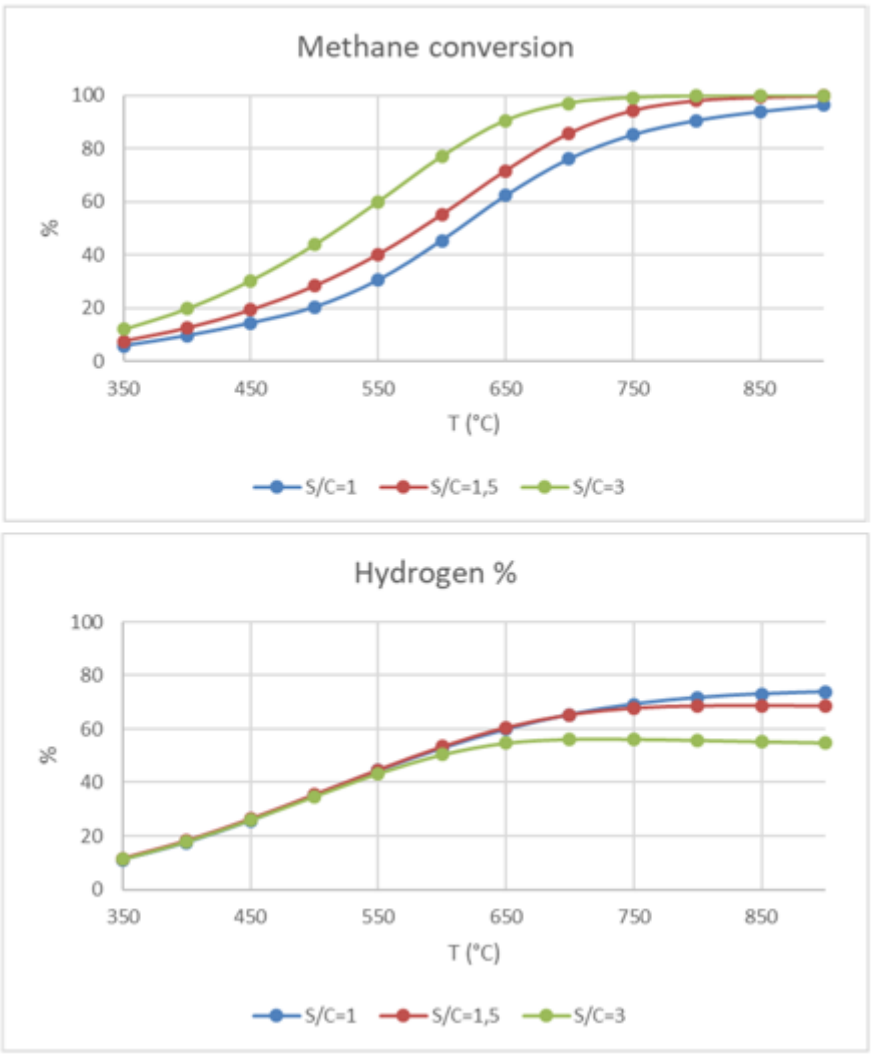

Figure 7: Equilibrium methane conversion and hydrogen partial pressure as function of temperature at different steam to carbon ratio.

Due to its high endothermicity, steam reforming is favoured at high temperatures. Instead, water gas shift is favoured at lower temperatures because it is slightly exothermic. Increasing temperature in fact enhances methane conversion and hydrogen content, although the latter shows a slower raise due to the decreased occurrence of the water gas shift reaction at higher temperatures. The steam to carbon (S/C) ratio also influences the process performances as higher methane conversion are obtained at higher S/C ratio. In fact, methane conversion is almost complete at 700°C for S/C ratios of 3, and is then stable at higher temperatures, while the plateaux is reached at 800 in the case of S/C=1,5. This is due to the increased amount of reagent present at higher S/C. It is interesting to note however, that hydrogen content decreases by increasing the S/C ratio. This effect is not due

to a decreased hydrogen yield but is related to the dilution effect given by the higher amount of unreacted steam found in the products.

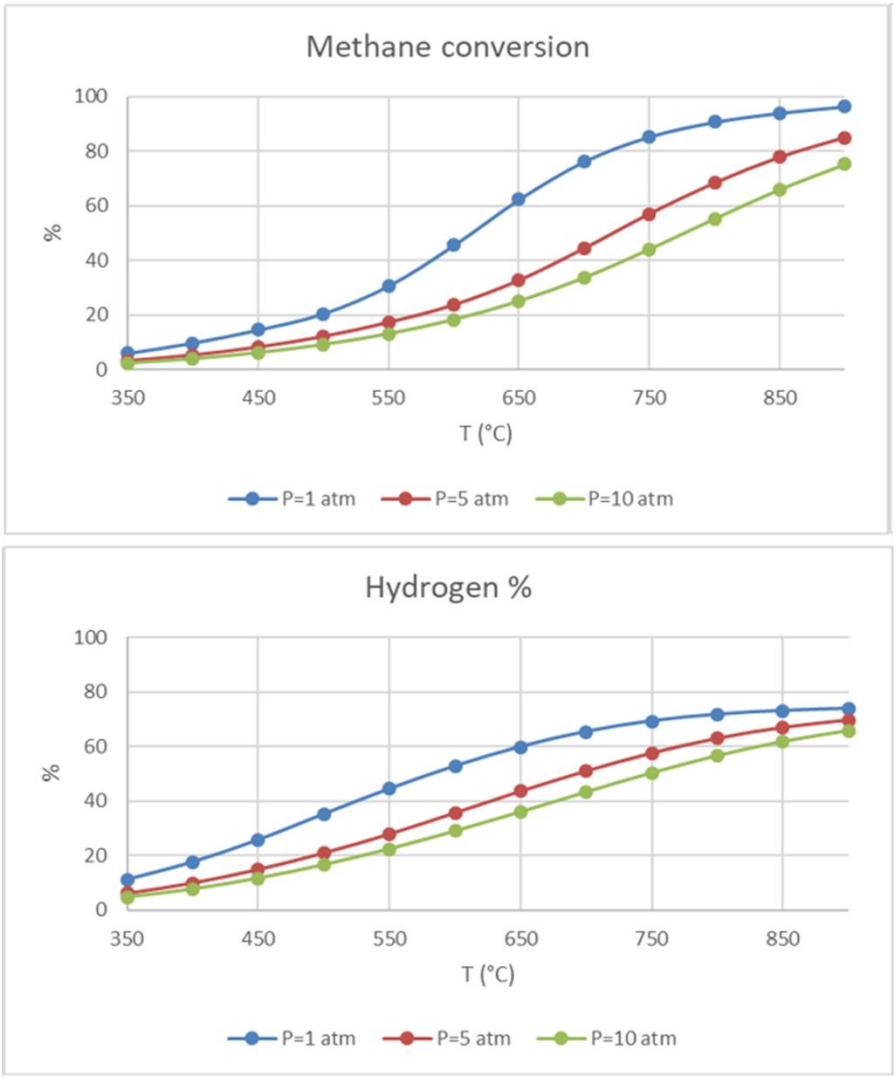

Figure 8: Equilibrium methane conversion and hydrogen partial pressure as function of temperature at different total pressures.

Steam reforming it is badly affected by pressure increase due to the fact that it produces an increase in the number of moles, giving three moles of hydrogen and one of carbon monoxide from one of methane and one of steam (Figure 8). Water gas shift is unaffected by pressure as no increase or decrease in the number of moles is obtained by this reaction. In fact, equilibrium methane conversion sharply decreases when pressure is raised from 1 to 5 atm and further lowers at 10 atm, where it is not able to reach 100% even at 900°C. Hydrogen content follows an analogous trend. However, it is important to note that hydrogen partial pressure would be higher at 10 atm even though the hydrogen content is

lower, as this value is proportional to the total pressure. Figure 9 reports the molar fractions of the steam reforming products and unconverted reagents at the equilibrium (expressed as molar percentages) at different pressures and S/C, from which the conversion values reported above were calculated.

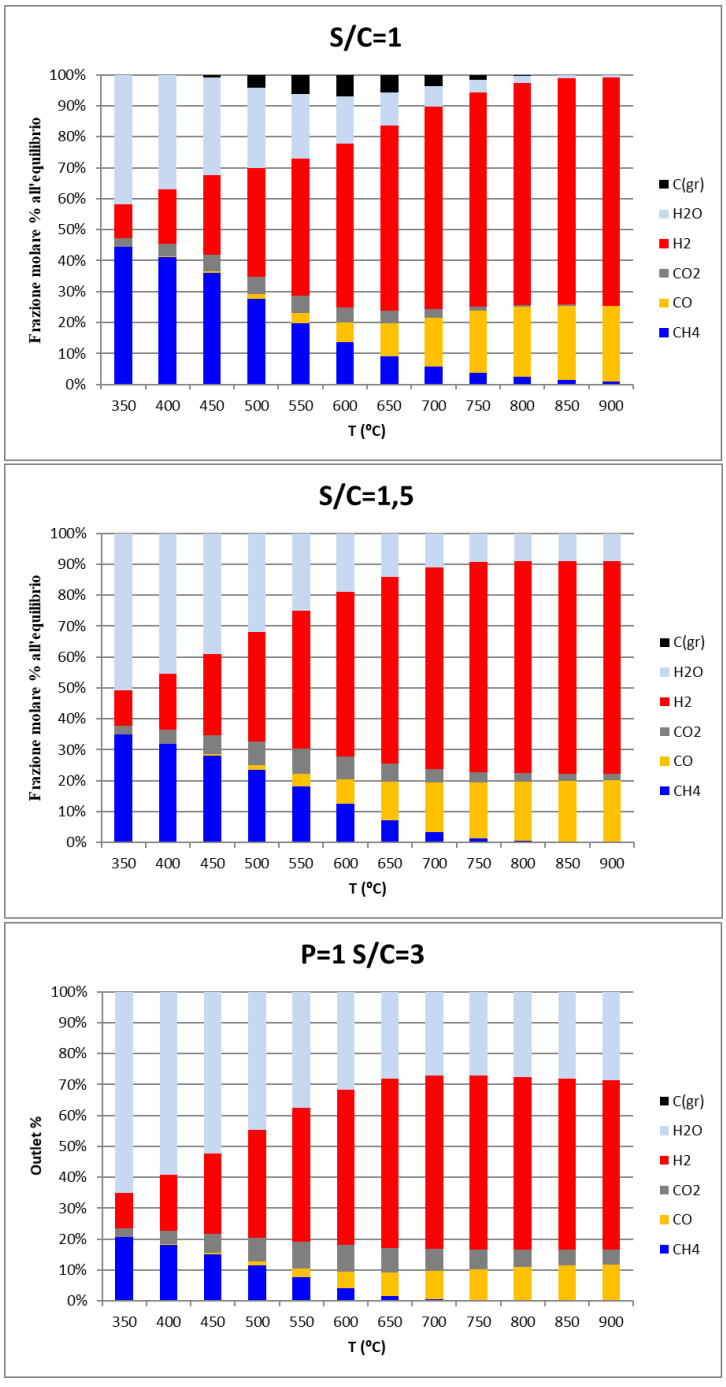

Figure 9: molar fractions of the steam reforming products and unconverted reagents at the equilibrium at different S/C and 1 atm.

Other thermodynamic consideration can be taken by looking at these graphs. In fact, it is interesting to observe the CO and CO_2 production. CO is produced by steam reforming and found at higher temperatures where CO_2 is negligible. At lower temperatures instead CO content decreases in favour of carbon dioxide which is produced form it by water gas shift reaction. The latter can be pushed by increasing the steam to carbon ratio as CO_2 is found even at higher temperatures in the case of S/C=3. Moreover, it is clear that high S/C favour methane conversion but result in unconverted steam that dilutes the content of the mixture. Finally, carbon formation, which is an unwanted reaction found in steam reforming, occurs at low steam to carbon and intermediate pressures. Carbon can be formed by different reactions, which will be treated in detail in a following chapter. These are Boudouard reaction, methane decomposition and CO hydrogenation. Steam favours the inverse CO hydrogenation reaction, also known as carbon gasification, thus disfavouring the carbon formation

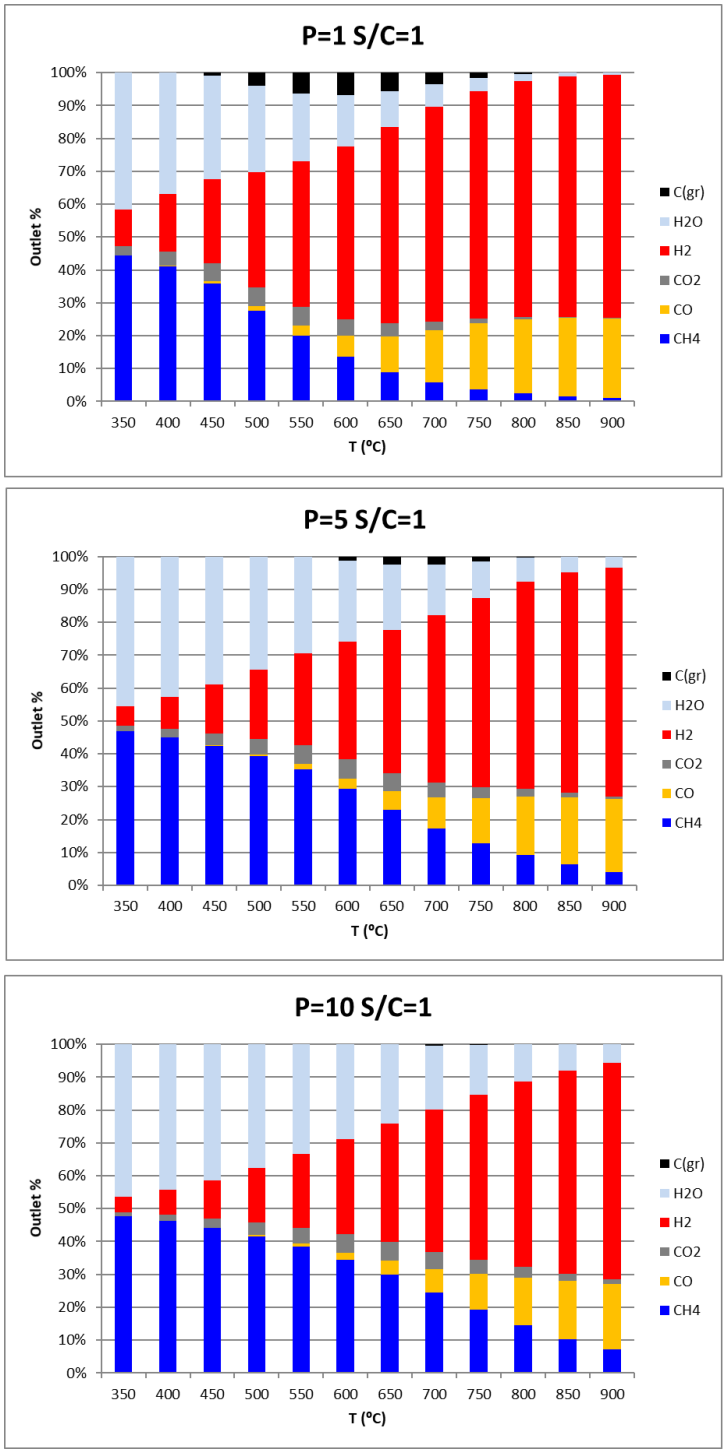

Figure 10: molar fractions of the steam reforming products and unconverted reagents at the equilibrium at S/C 1 and different pressure.

Carbon monoxide and carbon dioxide ratio is unaffected by pressure as the water gas shift equilibrium does not change modifying this parameter. Carbon formation is disfavoured at high pressures as methane decomposition, CO hydrogenation and Boudouard reaction produce a decrease in gaseous moles from reagents to products. The higher amount of

steam and methane found at higher pressure and same S/C is due to the lower conversion of methane and steam due to unfavourable thermodynamic conditions.

1.4.2.1.2. Thermodynamic analysis of catalytic partial oxidation

Catalytic partial oxidation is an exothermic reaction that occurs between methane and substoichiometric oxygen. However, methane combustion also contributes to the process due to the presence of oxygen. This reaction, which is highly exothermic produces sharp increase of temperature and is favoured at all temperatures. Moreover, also CO oxidation to carbon dioxide may occur. The presence of steam and carbon dioxide in the reaction products may finally favour steam reforming and dry reforming reaction. Although the large number of reactions involved make the exact mechanism difficult to understand, the influence of operative conditions on the equilibrium can be analysed by CEA NASA. In this case a constant oxygen to carbon ratio of 0.5 was taken in account (figure 11).

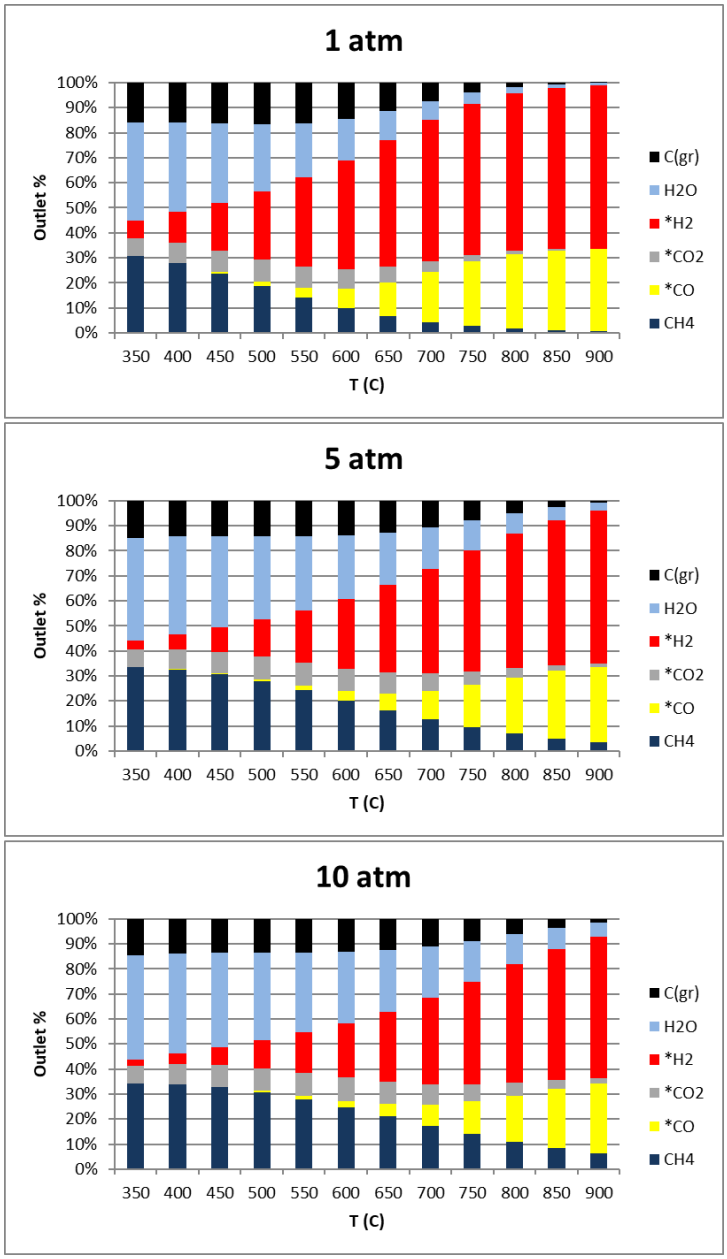

Figure 11: molar fractions of the CPO products and unconverted reagents at the equilibrium at different pressure and O_2/CH_4=0,5 (mol/mol).

Similarly to SR, the reaction is favoured at high temperature, where methane concentration in the products is low and hydrogen is present in high amount. An increase in pressure disfavour the CPO reaction and some methane is found unreacted even a high temperatures. Moreover, at low temperatures combustion is favoured over CPO and steam is produced. Finally, the absence of steam in the reagents make carbon formation more favoured than in the case of SR.

The oxy reforming process is a combination of these two reactions, so its thermodynamic behaviour is related to the considerations stated above. In particular, O/C and S/C ratio will affect the process making it more similar to CPO or steam reforming respectively. High temperatures are preferred as steam reforming is consistent and combustion is disfavoured in those conditions. In general, it is important to note that the coupling of the two reactions provides a more energy efficient process that need less energy and develops narrower endothermic peaks. This allows the catalyst to work at higher temperatures compared to classical steam reforming in the same conditions and thus helps to obtain higher equilibrium conversions at lower furnace temperatures.

1.4.2.1.3. Thermodynamic analysis of methane steam reforming in a membrane rector.

The employment of a membrane reactor can affect the equilibrium values of steam reforming thanks to the Le Chatelier principle. In fact, hydrogen removal through the reactor walls provide an increase in the steam reforming and water gas shift occurrence, thus in methane and steam conversion and hydrogen production. In this way methane conversions and hydrogen yields higher than those obtained at the equilibrium in a fixed bed reactor can be reached.

A thermodynamic analysis of methane steam reforming in a membrane reactor was carried out by Bottino et al. [61]. They analysed a non adiabatic steam methane reforming membrane reactor working in equilibrium conditions looking at the influence of different variables such as temperature profile and separation efficiency. From their study it was clear how the employment of a membrane reactor can lead to higher methane conversion and hydrogen fluxes, especially if more than one stages employed (figure 12)

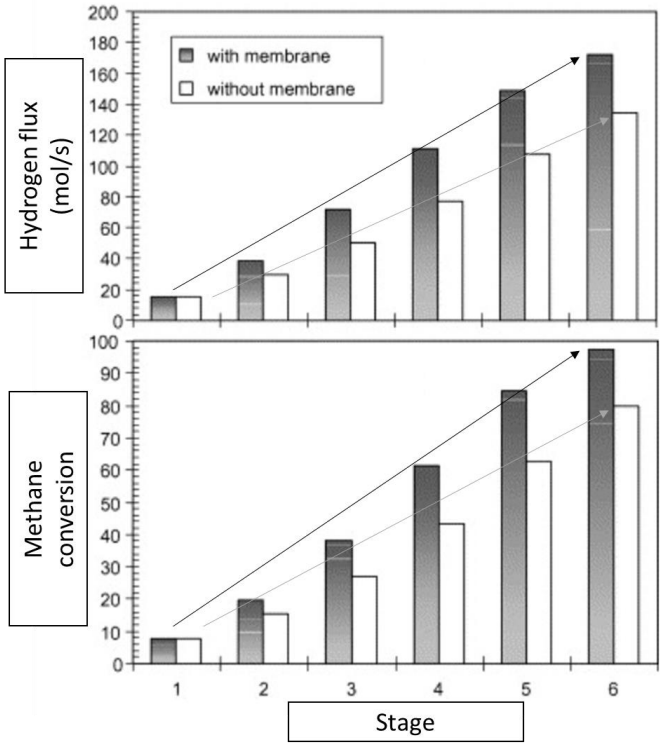

Figure 12: Methane conversion and hydrogen flux for a membrane reactor and a fixed bed reactor carried out in different stages (1-6), The following conditions were assumed: Temperature: 500°C, Pressure: 20 bar, m_{CH4}: 3000 kg/h, S/C 2, pressure at permeate side: 2 bar, Pd thickness: 30 mm, hydrogen permeability at each stage: 80%. It was assumed a temperature profile increasing Along the sequence of stages a temperature increase of ΔT/Δstage of 80°C was also assumed by the authors. Adapted from [61]

In general, it is important to remember that the driving force of permeation is the difference in hydrogen partial pressure between the inner and outer sides of the membrane. Thus, hydrogen partial pressure produced by the catalyst placed in the membrane reactor must be higher than 1 atm, if only hydrogen fluxes from the permeate side. However, this might not be fairly easy to obtain as the operating condition that can be employed in the membrane disfavour the reforming reaction. In fact, the system cannot be operated over 500°C as higher temperature would drastically decrease membrane life due to creation of pinholes. However, steam reforming is not favoured at low temperature as explained above and thus only low hydrogen concentrations can be obtained. To increase the latter, a lower S/C ratio can be employed avoiding hydrogen dilution by unconverted steam or higher total pressures. However, these options further disfavours methane conversions. In order to understand which operative conditions are suitable for membrane operation, the equilibrium hydrogen concentrations and partial pressures were calculated

with CEA NASA software varying pressure, S/C and temperature. 10 atm were chosen as higher pressures due to operative limitation of the membrane setup.

Figure 13 shows the hydrogen partial pressure as function of temperature at different S/C ratios.

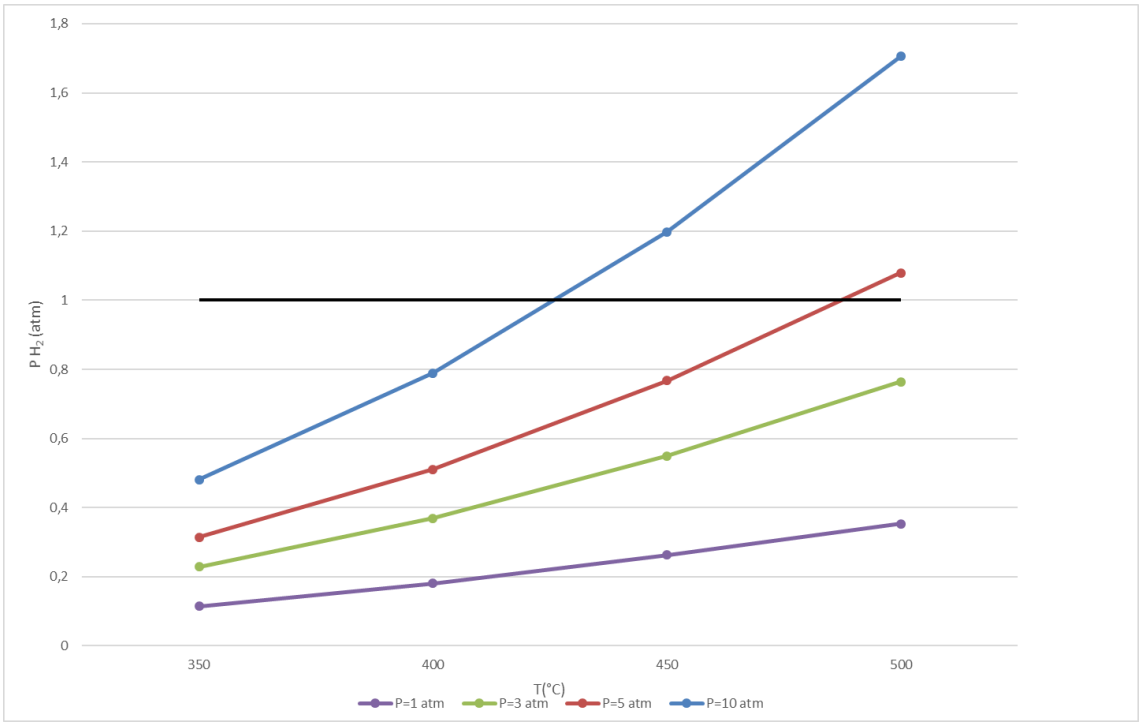

Figure 13: The equilibrium hydrogen partial pressure as function of temperature at different pressures.

From this analysis it was found that it is not possible to obtain sufficient hydrogen partial pressures below 450°C, and that 10 atm must be employed at this temperature. Moreover, in such conditions only a slight driving force is obtained as the pressure difference obtained would be lower than 0.2 atm. This can be increase by raising the temperature to 500°C and using a pressure of 10 atm thanks to the enhanced methane conversion at higher temperatures and higher hydrogen partial pressure at higher total pressures. Even the S/C ratio has an influence of hydrogen partial pressure as high amount of steam favours the steam reforming but also dilutes the products. Figure 14 shows the dependence of hydrogen partial pressure by S/C ratio calculated at 500°C and 10 atm.

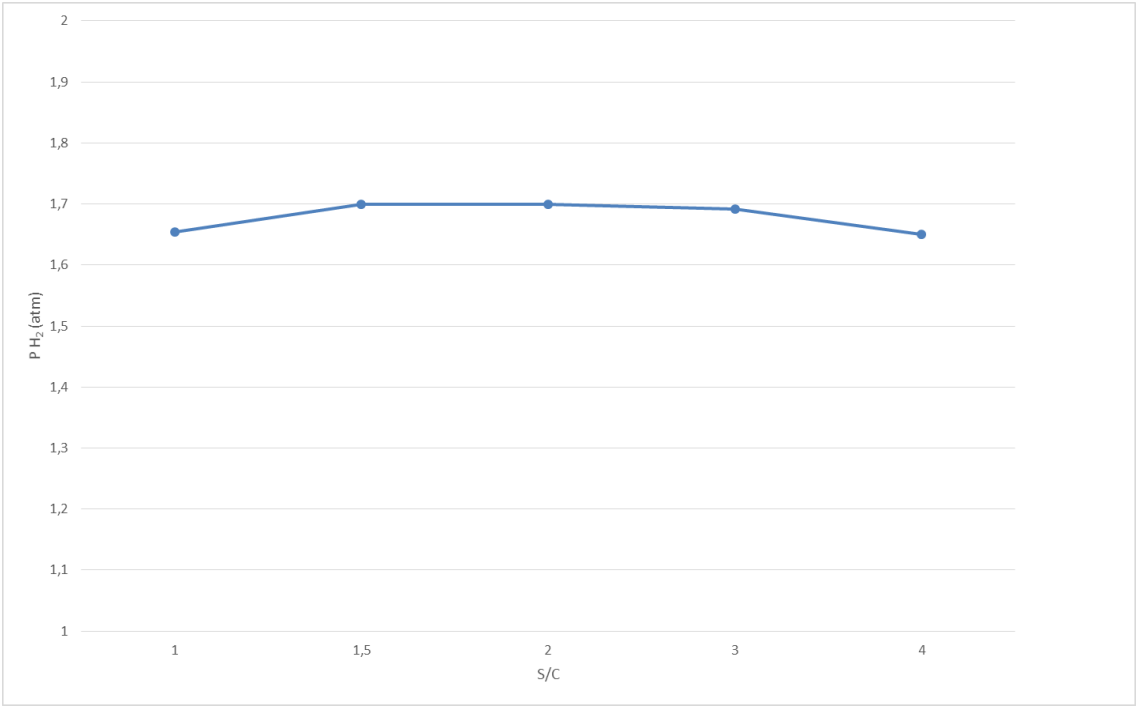

Figure 14: dependence of hydrogen partial pressure by S/C ratio calculated at 500°C and 10 atm.

This sets a clear limit to the conditions that can be used and requires the employment of a catalyst with a high activity and stability in these cases.

However, the membrane driving force can be also increased by decreasing the partial pressure of the permeate hydrogen. This can be done employing a sweep gas, i.e. a flux that transports and dilutes the permeate hydrogen. An ideal sweep gas is steam as it is then easily separated by condensation, providing a pure hydrogen stream. However, inert gases such as nitrogen or helium are usually employed in lab scale test because they are easier to handle.

Barbieri et al. [62] studied the effect of the amount of sweep gas on equilibrium methane conversion of a Pd membrane reactor. In particular they calculated that increasing the sweep factor (l), higher conversion can be obtained (Figure 15)

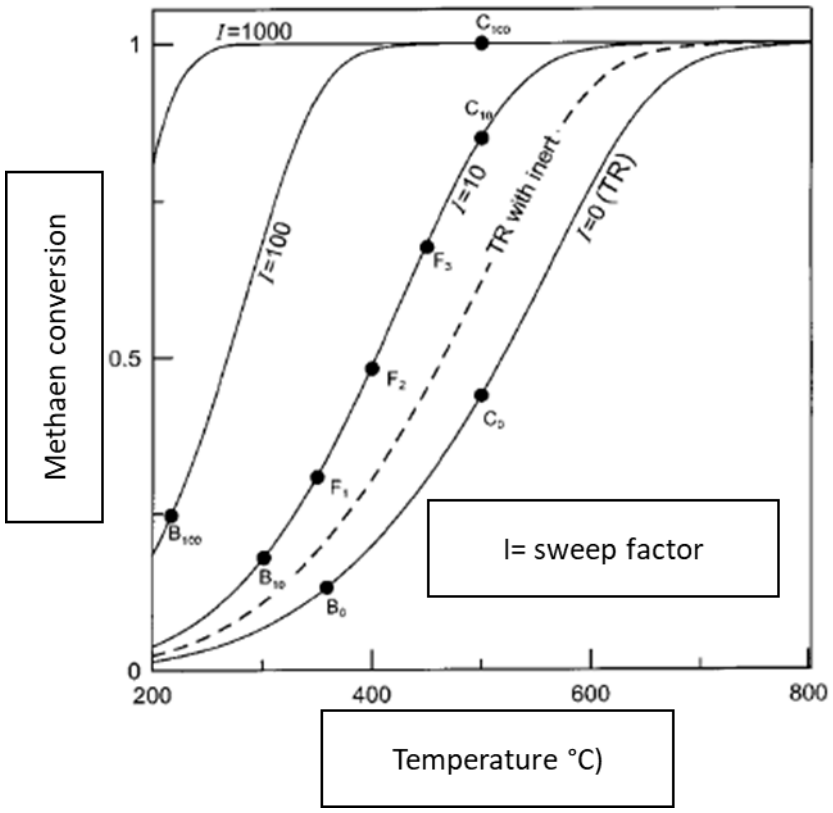

Figure 15: Effect of sweep factor (l) on methane conversion in a membrane reactor, adapted form [62]

1.4.2.2. Membrane reactors for hydrogen production from methane

Part of this chapter was published in the book:

Basile, F., Fasolini, A. & Lombardi, E. CHAPTER 7 Membrane Processes for Pure Hydrogen Production from Biomass. in Membrane Engineering for the Treatment of Gases: Volume 2: Gas-separation Issues Combined with Membrane Reactors (2) 2, 212–246 (The Royal Society of Chemistry, 2018)

Reproduced from Ref. [31] *with the permission of Royal Society Chemistry.*

Membranes for hydrogen separation can be employed to upgrade the reforming process leading to a cheaper and more efficient operation. For example, a membrane can be set after the reformer outlet to purify the obtained stream. In addition, more complex configuration have been tested in order to further increase the hydrogen yield and recovery. Among them, it is worth mentioning those employing two membranes: in Figure 16A it is shown a setup where a membrane separates hydrogen after a reforming reactor.

The reformate, which still contains some methane and is depleted in hydrogen, undergoes another reforming followed by another separation. In this way, higher conversions and yields can be obtained. In Figure 16B, a CO_2 selective membrane is employed together with a hydrogen selective one in an analogous setup. This is advisable if syngas is the desired product, as the undesired carbon dioxide is eliminated.

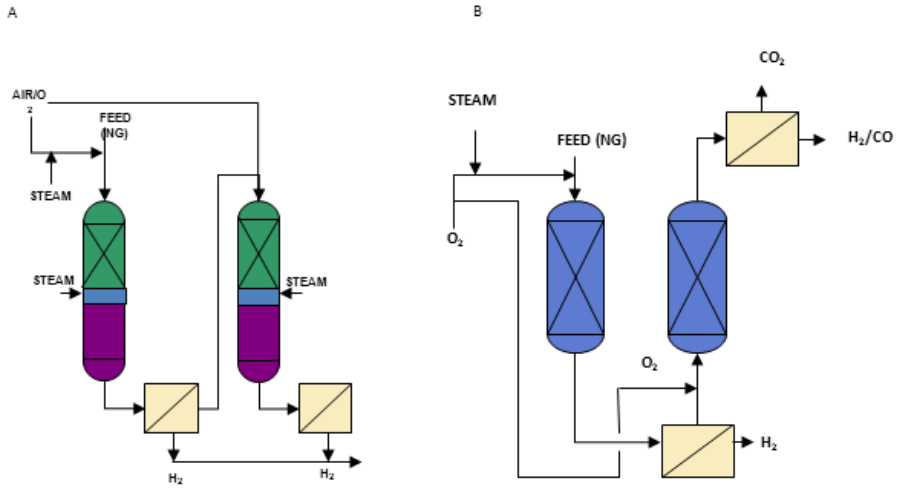

Figure 16: Possible setups of membrane operations.

Talking about the kind of membrane employed, palladium-based ones are those which have been studied most in recent times due to their high hydrogen selectivity. However, their employment on an industrial scale is still limited by drawbacks such as high cost and mechanical resistance. On the other hand, a compact and efficient configuration has been studied. In fact, instead of carrying out the reaction in a reactor followed by hydrogen separation in a membrane, these two units have been fused together in what is known as membrane reactor (Figure 17). In this way, the efficiency of the process is further enhanced as the hydrogen product is removed during the reaction. The reaction is shifted toward the formation of more products and the result is a higher yield.

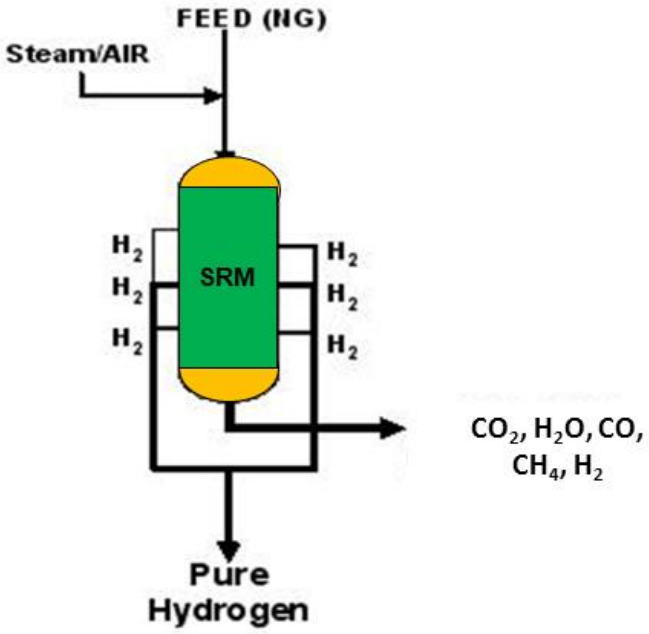

Figure 17: Scheme of a membrane reactor.

However, some issues are related to operative temperature and pressure, which can influence the hydrogen separation efficiency and the durability of the membrane. For instance, steam reforming of methane is an endothermic reaction that produces an increase in the number of moles.

Due to its endothermic nature, steam reforming is favored at high temperatures and low pressure and it is carried out at high temperatures on industrial scale using high pressure to favor downstream process. On the other hand, palladium-based membranes should work at milder conditions as temperatures over 450-500°C would decrease the membrane life. In terms of pressure, membrane reactor and separation, uses a sweep gas on the permeate site or high pressures, as the permeation is proportional to the difference in the partial pressure of hydrogen (Seivert-Fick equation). A sweep gas, is a flow of gas that passes on the permeate side, removing hydrogen and reducing its partial pressure. In absence of sweep gas, H_2 partial pressure is 1 atm, thus requiring high pressures inside the membrane. The ideal sweep gas is steam, as it can be condensed afterwards giving a pure hydrogen stream.

Oxy-reforming at lower temperature may be employed in membrane reactors. Nevertheless, the coupling between oxidation and reforming has the drawback of hot spots

that can causes pinholes in the membrane. Thus, its application in membrane reactors is challenging compared to steam reforming one.

Hot-spots problems in a packed-bed can be partially avoided using catalyst supported on ceramic or metallic foam able to provide more flat axial profiles with temperature gradient decreased from 100 to 25°C, as reported by Kyriakides et al. [63] and better conversion due most likely to higher exit temperature. Further studies have been carried out by Patrascu et al. [64] using a Pt/Ni/CeO2 on SiC foam obtaining high conversion and selectivity.

Though, it is difficult to state the best operative conditions for a membrane reactor system and different set of parameters have been applied to membrane reactors for hydrogen production. For instance, different temperatures and pressures have been investigated in order to try to increase methane conversion, hydrogen yield and thus process efficiency. Some of the more relevant results at various temperatures and pressures obtained recently are treated in a review from Iulianelli et al. [65]. Nowadays, different membrane compositions were employed but a classification in this respect is challenging to make as different dopants in various percentages and various synthesis methodologies have been tried.

Applications involving temperatures ranging from 400°C to 550°C are the most interesting. In fact, they meet both the need of lowering operative temperature (which is over 900°C for industrial steam reforming) and the need of preserving the membrane from degradation. Moreover, the temperature is high enough to avoid the deactivation of the Pd sites from steam or carbon monoxide. Unfortunately, the equilibrium conversion of methane at this temperature is quite low and though very efficient membrane are needed in order to increase experimental conditions far above the equilibrium value to obtain acceptable yields.

In this regard, Basile and coworkers carried out different studies on methane and ethanol reforming at relatively low temperatures. In 2010, they performed methane steam reforming between 400°C and 500°C in a membrane reactor. This was composed by a Pd-Ag membrane synthesized by cold-rolling and diffusion welding. The Pd-Ag layer had a 50 μm thickness and a silver composition of 23% w/w. It was connected to stainless steel tubes

and a commercial Ni-Al_2O_3 catalyst was loaded inside the membrane. Finally, a sweep gas (N_2) flew in the permeate side in order to lower hydrogen partial pressure and favor the permeation. Best results were obtained at 450°C and a pressure of 3.0 bars and consisted in a methane conversion of 50% and a hydrogen recovery around 70%. In this case the best sweep factor (ratio sweep gas/methane feed) was found to be 1.6. The results seemed promising as the methane conversion in a fixed bed reactor was 6% in the same conditions [66]. Later, they performed the same reaction at 450°C in a membrane reactor of equal characteristics. However, a Ni-ZrO catalyst was chosen in this second study, in order to provide better thermal stability and resistance to coke formation. Best results were obtained at 450°C, with a pressure difference of 4.0 bar between permeate and retentate side. The sweep factor was maintained at 1.6. A methane conversion of 65% and a hydrogen recovery around 80% were obtained [67]. The difference in methane conversion (which raised from 50% to 65%) could be due to difference in the catalyst and pressure, while the increased hydrogen recovery is probably given by the different pressure.

Other works have been carried out employing higher temperatures, such as 500-550°C. In fact, this helps the reagent conversion due to the enhancement of the equilibrium value. The latter is given by the endothermic nature of the reaction. Moreover, membrane permeance is improved and this should allow for a higher flux of hydrogen toward the permeate side. On the opposite, problems can be found in membrane stability and carbon formation. Different catalysts and membranes were employed. For instance, 86% methane conversion and 70% hydrogen recovery were obtained by Lin et al. [68] who performed steam reforming over a commercial nickel catalyst in a palladium membrane supported on stainless steel. An increase in conversion (up to 86%) was obtained when the pressure was changed from 9 to 20 atm.

An even higher Temperature was employed by Way et al. [69], who tested methane steam reforming at 580°C and 2.9 MPa in a thick Pd–Ru membrane supported on a porous yttria-stabilized-zirconia/stainless steel substrate. In a membrane reactor configuration, they obtained methane conversions from 65% to 80%, while loading a commercial nickel catalyst. Interestingly, the membrane maintained good performances (93% purity of the permeate) for 1000 h of reaction at those conditions and at a S/C of 3. Regarding GHSV, it was found that methane conversion and hydrogen recovery dropped at too high values due to low

residence time of the mixture over the catalyst and in the membrane. On the other hand, concentration polarization effect occurred at low GHSV. Thus, a value of 300 h^{-1} was determined as the optimum one. A conclusion on the effect shown by different pressure is challenging as hydrogen flux through the membrane is influenced by the composition and the thickness of the membrane itself [70]. However, it seems that the bad influence that elevated pressure has on the equilibrium is overcame by the positive effect of the increased permeation when higher pressures are applied. This results in a higher hydrogen production.

Unfortunately, due to the employment of different catalyst types and loadings and different kind of membranes it is challenging to compare the results. However, it seems that higher temperatures produce an increase conversion for most of the membranes and catalysts. This is due to the thermodynamic and kinetic of the reaction which are both positively influenced by higher temperatures. However, this consideration can be biased by the different activity of the catalyst treated in the studies. Finally, it is worth noting that stability of the membrane may become an issue at higher temperatures. However, not all the works provided data about the durability of the membranes employed. On the opposite, Saric et al. [71] investigated the resistance of a bench scale membrane at 580°C and 28 bar and found out that it is stable for more than 1100 h, while obtaining a continuous 86% conversion of methane and 70% hydrogen recovery. The selected membrane was a palladium one made by electroless plating on an alumina support while the chosen catalyst was a nickel based one.

Membrane stability depends also on catalyst composition and membrane catalyst interaction in packed bed reactor, the migration of the transition metal present in the catalyst can be favored by the reductive hydrogen environment in which Fe, Zn, Cr or Ni can change the permeability of the Pd membranes by interdiffusion in the Pd lattice. Matsuka et al compared PdAg membrane with a V based layer coated with Pd on both side (1 μm). The latter showing better resistance to Fe migration while some Pd migration in the V layer was observed [72]. Generally speaking the problem can be solved using a coating layer on the Pd membrane. Usually Al_2O_3 is the most used but ZrO_2 has higher expansion coefficient and can be therefore more suitable for a stable Pd coating. The system requires

still further development in term of cost, long-term stability and pipes connection, all these aspects make the application in industrial scale challenging.

1.5. **Catalysts**

1.5.1. Reforming catalysts

Ni based catalyst have been traditionally used for the SR process due to their low cost and relatively good performances [73]. Also Ru [74,75], Rh [58,74], Pd [74], Pt [74,76] and Ir [57,74,77] are active in the reforming reaction, but seldom used on an industrial scale due to their high cost. Different studies on the order of activity have been carried out, starting from the Rostrup-Nielsen ones in 1970s [78]. An order of activity of Rh–Ru > Ni > Ir > Pd ~ Pt _ Co, Fe was proposed by Kikuchi et al for steam reforming of methane at 1 atm [79]. Both Rostrup-Nielsen and Quin studied MgO supported noble mtals and found the following order of reactivity: Ru, Rh > Ir > Ni > Pt, Pd [74,80]. In general, Rh and Ru are the most active catalyst although Rh is more stable toward sintering tan Ru. Ni and Ir have intermediate activity, followed by Pt and Pd. However, Active phase selection is not only related to catalytic activity but must also take in account the resistance of the metal to deactivation phenomena such as carbon formation and sintering.

1.5.2. Catalyst deactivation

1.5.2.1. Carbon formation

An unwanted process that occurs in steam reforming and catalytic partial oxidation is carbon formation. Carbon is formed by three reactions in methane steam reforming processes: methane decomposition, carbon monoxide disproportionation, also known as Boudouard reaction, and CO reduction (Eq. 8-10).

$CH_4 \leftrightarrows 2H_2 + C(s)$ (Methane decomposition) (ΔH^0_{298} = 75,6 kJ mol^{-1}) (Eq. 8)

$2CO \leftrightarrows CO_2 + C(s)$ (Boudouard reaction) (ΔH^0_{298} = -172,0 kJ mol^{-1}) (Eq. 9)$CO + H_2 \leftrightarrows H_2O + C(s)$ (CO reduction) (ΔH^0_{298} = 118,5 kJ mol^{-1}) (Eq. 10)These reactions are favoured in the reforming conditions, but their occurrence may

depend on the operative conditions employed. In particular, Boudouard reaction is an exothermic reaction while methane decomposition and CO reduction are endothermic. Thus, the former is favoured at relatively low temperatures, below 700°C, although too low temperatures would not cause its wide occurrence in a steam reformer due to the low amount of CO produced. On the opposite, methane decomposition is favoured at high temperatures, but can also occur in low temperature steam reforming due to the relevant presence of unreacted methane. CO reduction is also favoured at high temperatures where CO is produced in high amounts by steam reforming and not consumed by the water gas shift reaction that occurs at lower temperature. However, carbon formation can be avoided by increasing the amount of steam over the stoichiometric value, as steam is one of the reaction products. In general, carbon formation can be avoided by increasing the steam and hydrogen content. In fact, hydrogen can give methane back from carbon while water can gasify it to CO and hydrogen through the reverse CO reduction.

Finally, increasing pressure favours carbon or coke formation [81]. Nevertheless, carbon or coke are formed in the conditions when the rate of formation (r_f) is higher than the rate of gasification (r_g). Depending on the reaction that formed it the carbonaceous material can be called carbon or coke. In particular, carbon is the product of CO disproportionation, while coke derives from methane decomposition and consists of polymeric carbonaceous species and, upon the reaction conditions can vary from polyaromatics to graphite. Carbon and coke can block the reactants access to the active phase by strongly chemisorbing in a monolayer or physisorbing in multilayers; it can completely encapsulate a metallic particle or block the supports pore removing the particle inside it from the reaction environment. If big filaments are formed inside the pores, they can lead to complete breakage of the catalyst [82]. Different forms of carbon are created during this deactivation process [53,83,84]. In particular, methane or carbon monoxide dissociate on metal surface to give a reactive carbon (Cα), which is supposed to be atomic carbon [51,85]. This is then further converted back to methane, to CO product or can be transformed in a less reactive carbon species (Cβ) formed by carbon polymerization or rearrangement. Cβ can still be gasified but can also further polymerize on catalyst surface, leading to metal particle encapsulation. Moreover, it can dissolve inside the metal particle, especially when non noble metal active phases such as Ni are employed. After dissolution it can diffuse through Ni and nucleate at

the rear of the crystallite, initiating a continuous process that leads to whisker carbon formation [84]. When whisker carbon forms it actually grows between the Ni particle and support, but not completely covering the Ni particle. For this reason, this process can result in no deactivation, if no encapsulation occurs. However, whiskers can lead catalyst fragmentation, pressure drops and blockage of the reactor in cases of consistent formation. Coke formation can also occur in gas phase, but deactivation of the catalyst by this process is slow [84]. Pyrolytic carbon may deposit on reactor walls when high concentrations of hydrocarbons are present, which may lead to carburization of the reactor material.

Catalyst structure also influences the rate of carbon and coke formation. For instance, filamentous carbon forms on non-noble metals such as Co, Fe and Ni over 400°C. This can be avoided by using noble metal active phases such as Pt, Ru and Rh which are more active but do not favour the production of coke or carbon due to a reduced mobility and/or solubility of carbon in these metals, which slows carbon nucleation. However, noble metals are more expensive than transition metals. For this reason, doping of transition metals with noble one can be an option to reduce carbon formation rate [82]. In addition, crystal size seems to be an important parameter in carbon formation. In fact, this process is structure sensitive and will not occur when the crystallites are under a critical dimension [86]. In particular, crystallite size and coking formation rate have been correlated by Chen et al [87]. Moreover, increasing the steam adsorption properties of a catalyst diminish carbon formation and allows to work at lower S/C ratios. This can be done by using basic catalysts such as Mg-containing oxides. Another kind of support that can help to reduce carbon formation are Ce-based ones. In fact, Ce is able to rapidly shift form the 4+ to the 3+ oxidation state, oxidizing the eventually formed carbon present on the surface, being then re-oxidized back to 4+ state by steam. This in-situ regeneration is advisable compared to a classical carbon oxidation in air, as the latter would not only require to stop operation, but would also oxidize the metallic active phase. Finally, it is worth mentioning that specific sulphur poisoning of Ni based catalysts can reduce carbon formation and has been also developed to an industrial process [88]. When traces of H_2S are fed in the reaction stream, sulphur chemisorbs on Ni forming NiS. Even though this leads to an activity decrease toward steam reforming due to sulphur poisoning, it helps to reduce carbon formation. In fact, sulphur occupies a fourfold hollow site at low coverages on the (100) nickel face,

delimiting ensembled sites where sulphur is not adsorbed and delimiting metallic Ni domain. Steam reforming requires ensembles of 3-4 metallic atoms to occur, while 6 are required for Cβ formation, which are not found when Ni domain is delimited by NiS [89].

1.5.2.2. Sintering

Sintering is a deactivation process that provokes a loss of activity because of the loss of catalytic surface area. In particular, the metallic active phase can undergo crystallite grow, thus reducing the metal surface area. Moreover, sintering of the support can occur which causes collapse of the pores removing the active phase from the reaction environment. Finally, some chemical transformation of the active phase to an inactive one can occur. Mainly three mechanism have been proposed to describe sintering:

1. Particle migration
2. Atom migration (Ostwald ripening)
3. Vapor transport between particles

In the particle migration model, a particle migrates as a sole entity over the support surface and then unites with another particle. On the opposite, atom migration is characterized by the escape of the metal atom, followed by migration of such atom over the support surface, which is then captured by another particle. More in detail, together with emission, capture and diffusion over the support of metal particles, other processes may occur, such as adsorption of metal particle on the surface of the support, spreading of metal oxide particles, bridging of two metal particles, liquid formation and metal atom vaporization. This process provokes size decrease of small metal particle in favour of the growth of big ones, because the rate of the rate of loss of atoms is smaller than the rate of capture for large crystallites, while for small crystallites the rate of loss is greater than the rate of capture [90]. Sintering occurs at temperature higher than 500°C, but it is influenced by different parameters such as reaction time, temperature, molecules involved, catalyst structure and composition and support properties and morphology. Sintering temperature and reaction atmosphere are the most important parameters. Both steam presence and temperature raise favour the sintering process significantly [91]. In fact, sintering is kinetically slow at low temperatures and relatively faster when steam and catalyst with high steam adsorption

properties are present. This is also influenced by the starting particle size and the support characteristics [91–93].For instance, Ni particles can be stabilized with alkali or alkaline-earth promoters on alumina supported catalysts have been observed to have a stabilizing effect [94]. Sintering has been mainly studied over Ni particle, as this active phase is the most commonly employed in steam reforming, though most prone to sintering compared to noble metals [95]. In fact, metal nature also affects sintering. In particular, the rate of sintering can be reported as follows for some metal active phases employed in the reforming reactions: Ni > Pd > Pt > Rh [95]. As sintering is an irreversible process it is advisable to prevent it other than invert it, by accurate selection of the operative conditions and catalyst synthesis. Finally, it is important to note that also support sintering may occur, which leads to phase transformation, loss of surface area and pore volume due to pore collapse and grain boundary diffusion.

1.5.3. Supported Ce-Zr based catalysts

Among the supports employed in heterogenous catalysis, CeO_2 has peculiar properties and was thus widely employed for different applications [96]. In general, they provide mechanical and thermal stability, linked with redox properties thanks to the Ce^{3+}-Ce^{4+} redox couple. In fact, Ce oxides are able to store and release O atoms by changing their oxidation states. This properties have been exploited in automotive, catalysis and oxidations [96]. However, oxygen storage capacity and thermal stability can be enhanced by formig solid solutions of Ce oxide with other cations [97–102]. For example the addition of Zr can lead to higher surface area and oxygen storage capacity and mobility [100–102]. In fact, Zr presence promotes Ce reducibility. In this framework Menad et al. evidenced that the highest oxygen mobility was obtained when Ce an Zr were present in the oxide in a 1:1 ratio ($Ce_{0.5}Zr_{0.5}O_2$) [103]. The formation of mixed oxides is possibl thanks to the similar ionic radii of Ce and Zr cations (0.88 Å; = 0.82 Å)

When mixed CeZr oxides are synthesized, different phases can be obtained, as represented by the phase diagram in figure 18 [104–106].

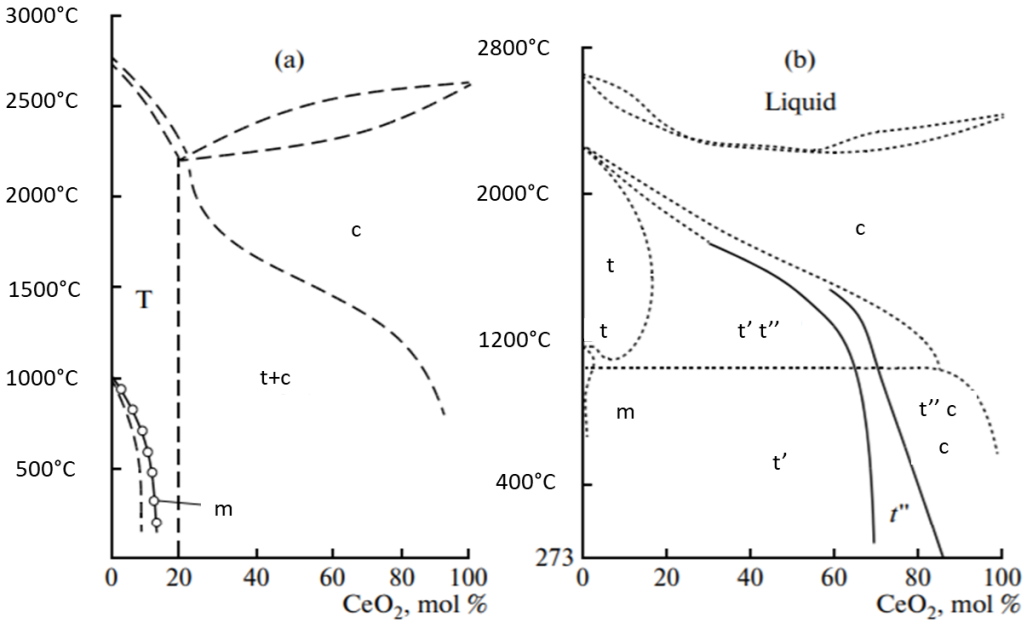

Figure 18: Ce-Zr phase diagrams, adapted from [104–106]

While CeO_2 has a cubic (c) structure and ZrO_2 is found in a monoclinic (m) of tetragonal one (t), the mixed oxides can be characterized by a mixture of these or some peculiar phases. According to Raman investigation also tetragonal metastable phases can be found: t' and t''. t' is a distorted tetragonal phase, while t'' is a tetragonal phase in which the oxygens are displayed in a cubic fashion.

The occurrence of these phases is mainly related to the synthetic method employed and the kinetic factors involved [107].

Moreover, the addition of a dispersed metal to the support further enhances its reducibility by spillover effect [96]. The oxygen mobility on oxide-supported metals was studied by 18O2 isotopic exchange and showed that the sequence involved are: (i) oxygen dissociative adsorption on the metal particle; (ii) O atom transfer from the metal to the support; (iii) surface migration of O atoms over the support; (iv) exchange of O atoms on the surface; (v) internal bulk O exchange; (vi) direct exchange of O2 with the support oxygen. Steps (v) and (vi) are relevant at high temperatures. The reverse steps are also involved.

Although the $Ce_{0.5}Zr_{0.5}O_2$ support was reported to have good oxygen exchange properties by Menad et al. [103], it is not easy to obtain such oxide. For this reason a water in oil microemulsion synthesis was selected in this work, which was reported to produce the desired oxide with increased propertied compared to a coprecipitated one [50].

In fact, microemulsions can be used to obtain oxide nanoparticles as reported in literature [108–111].

Microemulsion are a class of colloidal systems whose properties are related to the high dispersion and small micelle dimensions. The latter can vary between 5 and 100 nm [112]. The term microemulsion was first defined by Schulman and Friend in 1940 [113], and have found widespread applications since then. A microemulsion is characterized by a system in which aqueous phase, an organic phase and a surfactant are present. The latter must present both an hydrophile group and a hydrophobic group [114]. In general, when an aqueous and organic phase are mixed, they separate into two different phases, with traces of components soled in the other phase [115]. In the microemulsions the surfactant s used to diminish the interphase tension between the two phases. If a proper ratio between the two phases is used, the surfactants are able to create an interface, and if small amount of one phase is employed, micelles are formed, which characterize the microemulsion. Thus, oil in water (o/w) and water in oil (w/o) microemulsion can be formed. In the former case water is an excess and oil present inside the micelles, viceversa in the latter case. In this work water in oil microemulsions are treated. The formation of micelles is usually favoured by adding another surfactant, called co-surfactant. Microemulsion are characterized by thermodynamic stability and optical isotropy.

Inorganic oxide synthesis via microemulsions is usually carried out in water in oil microemulsions, i.e. water droplet dispersed inside an organic phase. These droplets are surrounded by a surfactant layer that stabilize them. In these droplets the metal salt precursors or a precipitating agent (for instance a base) are solved. When droplets containing the salt and the precipitating agent collide, a rapid and homogeneous precipitation occurs with the micelles that act as microreactors [108].

In this way particles with narrow size distribution in the nano-size range can be synthetized. Moreover, the homogeneous precipitation that occurs allows to avoid phase segregation and control the stoichiometric ratio obtained in the final oxide by simply adding an appropriate amount of reagents [50].

2. CHAPTER 2 – EXPERIMENTAL

2.1. **Catalyst preparation**

2.1.1. Water – in – oil Microemulsion

CeZr, Zr and CeZrPr supports are synthesized following the procedure reported by Martinez – Arias et al. [110]. The CeZrPr supports which were compared to the microemulsion one were synthesized as in [118]

An aqueous solution containing the same amount (0.25 M) of both Zr (precursor: $ZrO(NO_3)_2$* xH_2O – 99.00%, Sigma -Aldrich) and Ce (precursor: $Ce(NO_3)_3$*$6H_2O$ – 99.99%, Sigma-Aldrich) was prepared. An inverse microemulsion (water in organic) was prepared by mixing while stirring 8%wt of this aqueous solution with 58%wt of n – heptane (solvent, 99.00% – Sigma-Aldrich), 15%wt of 1 – hexanol (co-surfactant, 99.00% – Sigma-Aldrich), and 19%wt of a non – ionic surfactant (Triton X-1002 (TX-100), 99.00% – Sigma-Aldrich).The cationic emulsion was mixed while stirring with another emulsion having similar characteristics, except that the aqueous solution contains 1.5 M tetramethylammonium hydroxide pentahydrate (TMAH = (CH3)4NOH*5H2O), 97.00% – Sigma-Aldrich) instead of Ce and Zr salts. This approach, i.e. mixing the cationic and anionic aqueous solutions both dispersed in microemulsion is called double – mixed microemulsion method. Immediately

after the mixing, a brownish turbidity appeared, denoting reaction (precipitation in the aqueous phase micelles). The fluid was stirred for 24 h, after which the resulting suspension was filtrated; the remaining solid was washed with methanol. The solid is dried at 110°C overnight then grinded to obtain a fine powder.

2.1.2. Hydrotalcite synthesis

The synthesis was carried out by coprecipitation [119]. An aqueous solution containing nitrates salts of Ca, Ni, Mg, Al (Molarity=2) was dropped in an aqueous solution of sodium carbonate or sodium silicate (Molarity=1), kept at 60°C under vigorous stirring.

The following amount of reagents were used for the four synthesis:

Table 2: conditions used in the synthesis of the hydrotalcite precursors.

Sample	Ca^{2+} (mol)	Ni^{2+} (mol)	Mg^{2+} (mol)	Al^{3+} (mol)	$SiO3^{2-}$ (mol)	$CO3^{2-}$ (mol)	M^{2+}/M^{3+}	Final Ni^{0} % wt/wt
Ni10-C	0,0090	0,0034	0,0180	0,0101	/	0,0202	3	10,0
Ni20-C	0,0073	0,0068	0,0147	0,0096	/	0,0192	3	20,0
Ni10-S	0,0090	0,0034	0,0180	0,0101	0,0101	/	3	10,0
Ni20-S	0,0073	0,0068	0,0147	0,0096	0,0096	/	3	20,0

This solution was heated at 60° and kept at pH 10 (for carbonates) or 11 (for silicates) by addition of NaOH. Finally, the suspension was aged fo 1 h at 60°, then filtered, washed with warm water up to neutrality of the filtered solution and dried at 70°C overnight. The catalyst precursor was then calcined at 500°C for 1 h with a ramp of 10°C/min or at 650°C for 12 h with a ramp of 10°C/min.

2.1.3. Calcination procedure

The fine powders obtained both through w/o microemulsion and co – precipitation is thermally treated for obtain a mixture of oxide powder. The samples are placed in a temperature programmed oven in which the samples are maintained at 500 – 750 – 900°C for 5h. The set point is reached increasing the temperature 2°C/min. After 5h the sample is cold down to room temperature, both the weight and the volume are reduced.

2.1.4. Insertion of the active metal

The Rh or Pt precursors in the form of nitrate salt are dissolved in distilled water and their addition to the CeO_2 – ZrO_2 medium has been carried out by incipient wetness impregnation (IWI). The IWI is a method in which the amount of solution used for the supporting active phase is only the volume of solution corresponding to the volume of the pores of the support. The volume of solution needed for fill all the pores is called Water Uptake (WU), is different for each material and is necessary to be known before the impregnation in order to prepare the correct starting impregnation solution. The WU is measured by slowly dropping water (or a solvent used for the impregnation) on a known amount of support ensuring an homogeneous contact by mixing the powder. When the drop will form agglomerates, the liquid will not be adsorbed and this means that the pores are filled and the volume of water used is equivalent to the water uptake. The procedure for the production of the supported catalyst is as follows:

1. weight the support;
2. prepare the volume of solution with the correct amount of salt containing the precursor of the active phase;
3. drop slowly the solution mixing the powder in order to impregnate homogeneously all the pores;
4. drying the solid at 110°C overnight;
5. calcining the solid for 12h at 500°C, with a ramp of 2°C/min.

After this procedure the catalyst was pelleted, charged in the reactor and reduced overnight as stated below.

Table 3 reports the experimental conditions employed in the incipient wetness impregnation of the different active phases.

Table 3: experimental conditions employed in the impregnation of catalysts

Catalyst	Support	Wt of support (g)	Metal nitrate	Wt of metal precursor (g)	Vol of solution (ml)
Rh2.7-CZO	CZOm	6.995	Rh nitrate solution *	1,958**	1,960
Rh1-CZO	CZOm	2.000	Rh nitrate solution *	0,200**	0.510
Pt2-CZO	CZOm	3.000	$NH_3Pt(NO_3)_2$	0.119	0,760
PtRh0.7-CZO	CZOm	6.503	Rh nitrate solution*, $NH_3Pt(NO_3)_2$	0.609 (Rh)** 0.086 (Pt)	0,760
PtRh2.1-CZO	CZOm	6.900	Rh nitrate solution*, $NH_3Pt(NO_3)_2$	0.276 (Rh)** 0.117 (Pt)	1,740
Ru3-CZO	CZOm	2,996	Ru(NO)(NO)3 sol.	6,286***	5,870
Rh1-ZO	ZOm	1.500	Rh nitrate solution *	0,150**	0.300
Rh0.75-ZO	ZOm	7.500	Rh nitrate solution *	0.532**	1,870

* Rh nitrate solution containing 10% of metallic Rh (wt of Rh/wt of solution)

** wt of Rh solution.

*** Ru nitrate solution containing 1.5% of metallic Ru (wt of Ru/vol of solution)

**** wt of Ru solution

For the LTSR tests the IWI sample was compared with a catalyst obtained by depositing a Rh carbonyl cluster over the oxide support. In this case, sample manipulations were carried out using standard Schlenk techniques under carbon monoxide atmosphere to avoid the contact between the Rh carbonyl cluster and air. The synthesis of the clusters was carried out by the group "Cluster carbonilici dei metalli di transizione" of the Department of Industrial Chemistry "Toso Montanari" of the University of Bologna.

The deposition is carried out by dissolving the desired cluster (Rh_4CO_{12} or $[Rh_7(CO)_{16}]^{3-}$) in pure hexane an dropping the obtained solution to a slurry of the oxide support in hexane. The synthesis was stirred for 24 h at r.t. The slurry was then filtered, dried under vacuum and kept under CO atmosphere until the day o the catalytic tests. At that stage, the catalyst was pelletized, charged in the reactor and immediately heated up in nitrogen at 500°C in order to obtain the Rh active phase. In some cases, after the nitrogen pretreatment, the catalyst was cooled to 200°C, then reduced under a 10% (vol) flux of hydrogen in a temperature ramp up to 500°C and kept in these conditions overnight.

IR spectra were recorded on a Perkin Elmer SpectrumOne interferometer in CaF_2 cells with 1 mm thickness.

The CeZrPr samples were impregnated with Ni nitrate by wetness impregnation. Ni precursor (10% wt of metallic Ni/wt final catalyst) was dissolved in the least amount of water. The powder was then added to the solution and the suspension was stirred fo 15 minuts. Then it was dried in oven for 2 h at 120°C, then calcined at 500°C for 6 h with a ramp of 2°C/min.

2.1.5. Shaping of the catalysts

The calcined powders are pressed in a tablet than shaped in pellets within a granularity range between 30 and 60mesh or 60 and 80 mesh. This is done by breaking the tablet over sieves with the desired mesh dimension.

2.2. **Membranes preparation**

The membranes preparation is performed by the University of Messina, following the Electroless Plating Deposition (EPD) technique, which is based on the controlled autocatalytic reduction of a metallic salt on the substrate surface, through the use of a reducing agent. This technique allows the formation of dense and thin metallic films, even on non-conductive substrate, such as ceramic materials. The permeability and selectivity performances, as well as the membranes stability, are parameters strictly dependent on the film characteristics and, hence, they vary in function of the deposition technique adopted. The surfaces utilized for the deposition of thin Pd films are asymmetric porous α-Al2O3 tubes characterized by the presence of a macroporous layer (thickness ≈ 1.5 mm and average pores diameter ≈ 3 μm) and an internal microporous layer of a thickness at around 20 μm with an average porosity of 70 nm. The internal diameter (ID) of the tube is 0.7 cm, the outer diameter (OD) is equal to 1 cm and the tube length is 13 cm (figure 19).

Figure 19: membranes employed in this work.

The external extremities are constituted of a non-porous coating about 1.5 cm long, which guarantee the sealing with graphite rings, when the tube is finally placed into the reactor. The α-Al_2O_3 supports, before the Pd deposition, are tested in order to verify the homogeneity of the microporous layer, through the "bubbling test" procedure. This technique consists in the placement of the tubular supports inside of a plexiglass reactor, the sealing of which is guaranteed by a Viton o-ring. By means of a peristaltic pump, a liquid phase (H_2O or isopropanol) is fed to the external side of the ceramic tube; simultaneously, a flow ($\approx$ 180 mL/min) of an inert gas (N_2 or He) is fed into the tube. Varying the internal pressure of the tube within a range of 1 – 4 atm, is possible to observe the formation of bubbles on the support surface, index of the presence of macroporous defects on it. These defects highlight a non-homogeneous coating, thus it is not suitable for the deposition of a dense metallic film, therefore the supports for those is observed the formation of bubbles are classified as defective and then discarded. The suitable supports are cleaned up with a pure isopropanol washing, into an ultrasonic bath for 10 minutes, then they are dried at 110°C for 1 hour and later they are weighted with an analytical balance. At this point the ceramic support is ready for the Pd deposition through the EPD technique. Before the real Pd deposition, the plating procedure requires a first activation of the support surface. Practically, the EPD technique is characterized by two consecutive phases, i.e.:

1. the activation procedure consists in the deposition of Pd nanoparticles on the support surface. It is possible to carry out this step following different methodologies, but in this specific case it is conducted through Pd/hydrazine reduction into an ultrasonic bath;

2. the out-and-out plating procedure, i.e. the Pd film deposition is carried out through the reduction of Pd ions into an aqueous solution, putted in contact with the internal wall of the tubular α-Al_2O_3 support.

2.2.1. Activation step

The activation of the internal wall of the tubular porous ceramic support is performed following an innovative seeding procedure, optimized by the research group of Messina, based on the employment of Pd complexes. The conventional seeding procedure, provided a sequence of immersions, utilizing firstly an acid $SnCl_4$ solution, followed by an immersion in another acid solution in which is present the Pd salt. The result of this procedure is the formation of well–dispersed Pd nuclei, but the presence of Sn particles usually caused delamination problems during the tests at high temperature. The innovative procedure, instead, allows the formation of Pd nanocrystals, avoiding the presence of Sn.

Firstly, two aqueous solutions (50 mL each) are prepared: the first one (solution A) containing HCl (0.1 N) and $PdCl_2$ (2% w/w), while the second (solution B) is characterized by N2H4 in a molar concentration equal to 2 M. The α-Al_2O_3 is then externally covered with a parafilm layer in order to avoid that the Pd deposition occurs also in its external surface and then it is immersed into the solution A for 3 minutes into an ultrasonic bath. After a washing with distilled H2O, the support is immersed inside the solution B for further 3 minutes. This operation was cyclically repeated 5 times. At the end of the cycle, the support was dried at 110°C for 1 h and it was weighted with an analytical balance in order to determine the Pd amount deposited, through a weight difference with respect to the initial weight of the support.

2.2.2. Electroless Plating Deposition (EPD)

The EPD is an electrochemical process which involve redox reactions, with electrons transfer at the interface existing between the surface and solution. Therefore, it is an heterogeneous reaction during which occurs the autocatalytic deposition of the metal at the solid – liquid interface. The plating bath consists in a Pd ammino – complex solution stabilized with EDTA, with hydrazine as reducing agent. Furthermore, an excess of NH_4OH is necessary in order to stabilize the bath and maintain the pH of the solution equal to 11. The reaction is

carried out placing the activated support into the plating bath where the following reactions take place:

Cathodic metal deposition: reduction of the Pd ammino – complex:

$$2Pd(NH_3)_4^{2+} + 4e^- \leftrightarrows 2Pd^0 + 8NH_3 \qquad \text{(Eq. 11)}$$

Anodic reaction: hydrazine oxidation:

$N_2H_4 + 4OH^- \leftrightarrows N_2 + 4H_2O + 4e^-$ (Eq.12)The overall reaction can be written:

$$2Pd(NH_3)_4^{2+} + N_2H_4 + 4OH^- \leftrightarrows 2Pd^0 + 8NH_3 + N_2 + 4H_2O \qquad \text{(Eq.13)}$$

The reaction take place on the surface of the activated support, in proximity of the Pd nuclei. The initial reaction of N_2H_4 with OH^- forms N_2 and H_2O and it is accompanied by an electrons release. These electrons are transferred to the Pd complex, allowing its reduction to Pd^0 and its consequent deposition on the support surface. The deposition velocity increase in function of the number of nuclei formed on the surface. The deposition velocity is influenced significantly by parameters such as temperature, metal concentration, presence of complexing agents and the nature of the reducing agent. If the plating procedure is carry out too quickly, it will obtain a film characterized by big grains and then with an high roughness degree, while the main objective is the formation of thick and smooth films, in order to increase the H_2 permeability which the fundamental characteristic defining the quality of a Pd membrane for the gases separation. For these main reasons, the N_2H_4 addition is carried out very slowly, dripping its solution into the plating bath at a rate of 200 µL/h for a total time of 8 hours. At the end of this time, the membrane was washed with distilled H_2O and then dried at 110°C for 1 hour. Then, a sealing test with N_2 (180 mL/min) is carried out flowing the gas inside of the membrane until reaching a pressure of 4 bar, in order to exclude the presence of defects in the film or possible fractures of the support, that could be occurred during the preparation procedure. Finally, the membrane is placed into a reactor like those represented in figure 20.

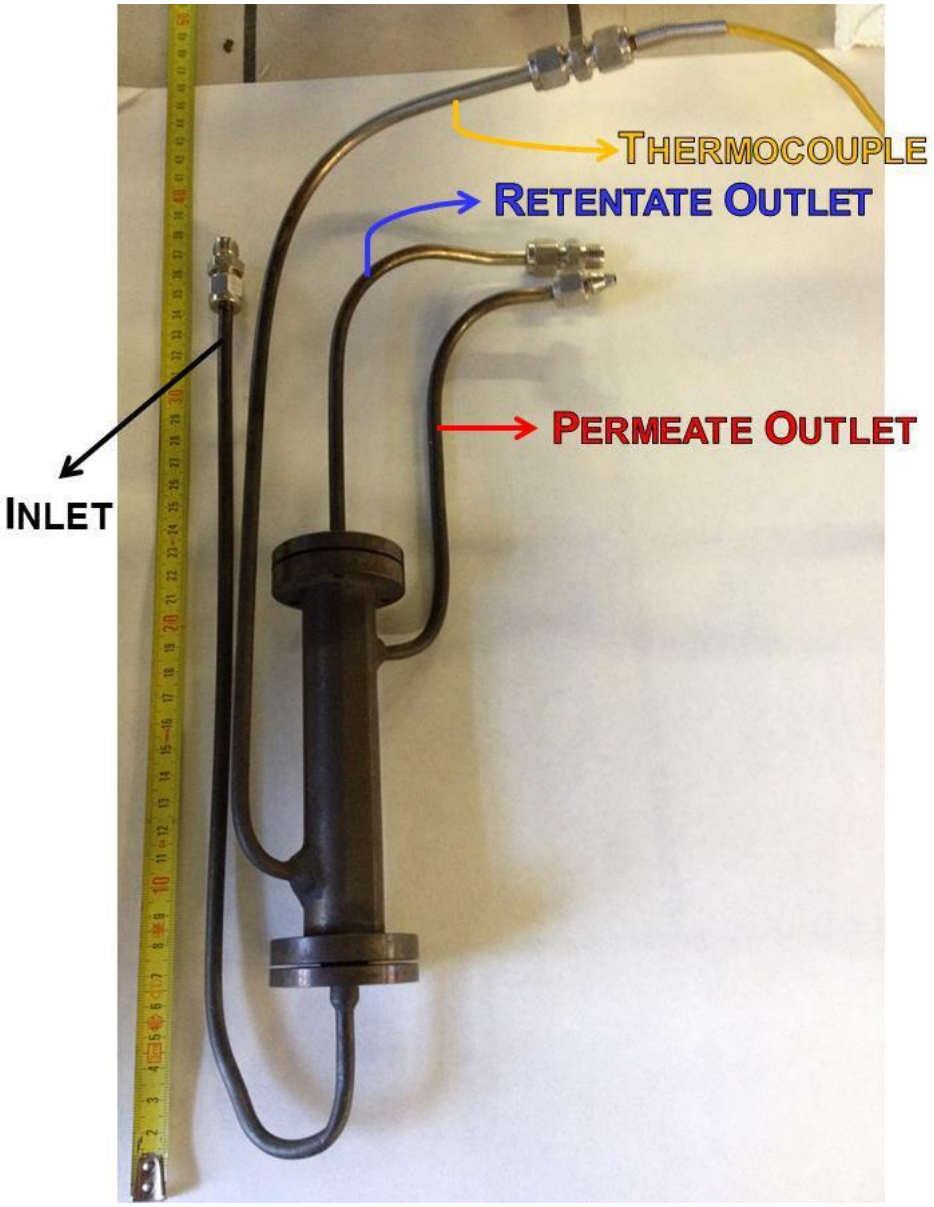

Figure 20: membrane module used in this work.

2.3. **Laboratory plant description**

Catalytic tests are carried out in a laboratory plant schematized in figure. 21. It is possible to divide this plant into three principal zones:

Zone 1 – Feeding zone: the cylinders of CH_4 and O_2 are connected to mass flow controllers by a two stage pressure regulator followed by a check valve; mass flow controllers are regulated by a central electronic unit. Deionized water is stored in a plastic vessel and pumped in a vaporizer by an HPLC pump then mixed with the hot O_2 stream. Methane is directly fed in the upper part of the reactor while the overheated vapor mixed with oxygen

is fed into the reactor in the part already filled with inert, in order to avoid explosion inside. H_2 and N_2 bottles are not connected to mass flow controller, but their flows are regulated, and maintained constant, through two different low – flow metering valves placed after each check valve. N_2 flow rate is regulated at about 400 – 440 mL/min and it is feed to the reactor when the reaction is stopped in order to maintain the catalyst always under a gas flow. The H_2 flow rate is regulated in function of the N_2 one, in order to obtain a gas mixture characterized by a 10% v/v of H_2 in N_2, to utilize for the "in – situ" reduction procedure of the catalyst.

Zone 2 – Reaction zone: the main part of this zone is characterized by the reactor, that is a 500mm long INCOLOY 800HT tube with an internal diameter of 10mm and an external diameter of 28mm; it can work up to 1000°C and 20 bar. The reactor is placed inside a tubular oven regulated by an external electric unit. The desired amount of catalyst is placed into the reactor in the isothermal zone, in which the temperature of the oven is defined and constant. An inert phase is added into the reactor before and after the catalytic bed and it solve three principal roles: it is a static mixer for fuel and oxidant, it prevent explosion because reduce the free spaces in which exist the possibility of explosive mixture formation and homogenize the temperature of gases. Inside the reactor is also inserted a thermocouple shell; type K thermocouple is putted inside rendering possible its sliding into the shell, useful for measure the temperature along the catalytic bed. At the end of this zone, after the reactor end, is possible to place a membrane module in order to separate H_2 from the others component of the reaction mixture. This module is maintained in temperature through the use of electric ceramic bands controlled by two thermocouples connected to two different temperature controllers.

Zone 3 – Post – treatment and analysis zone: the outlet stream is dried by passing through a gurgler placed in ice and then sent to a MicroGC.

The gas analysis system consist in a Micro C composed of two modules with two different types of columns. With the first module is detected the H_2 amount, instead with the second one are detectable CH_4, CO and CO_2. The typical carbon balance ranged between 90% and 110% due to random error. Values lower than 95% were also observed when carbon was formed over the catalyst. H balance was challenging to evaluate due to an incomplete recovery of the unreacted steam by condensation and was thus usually underestimated.

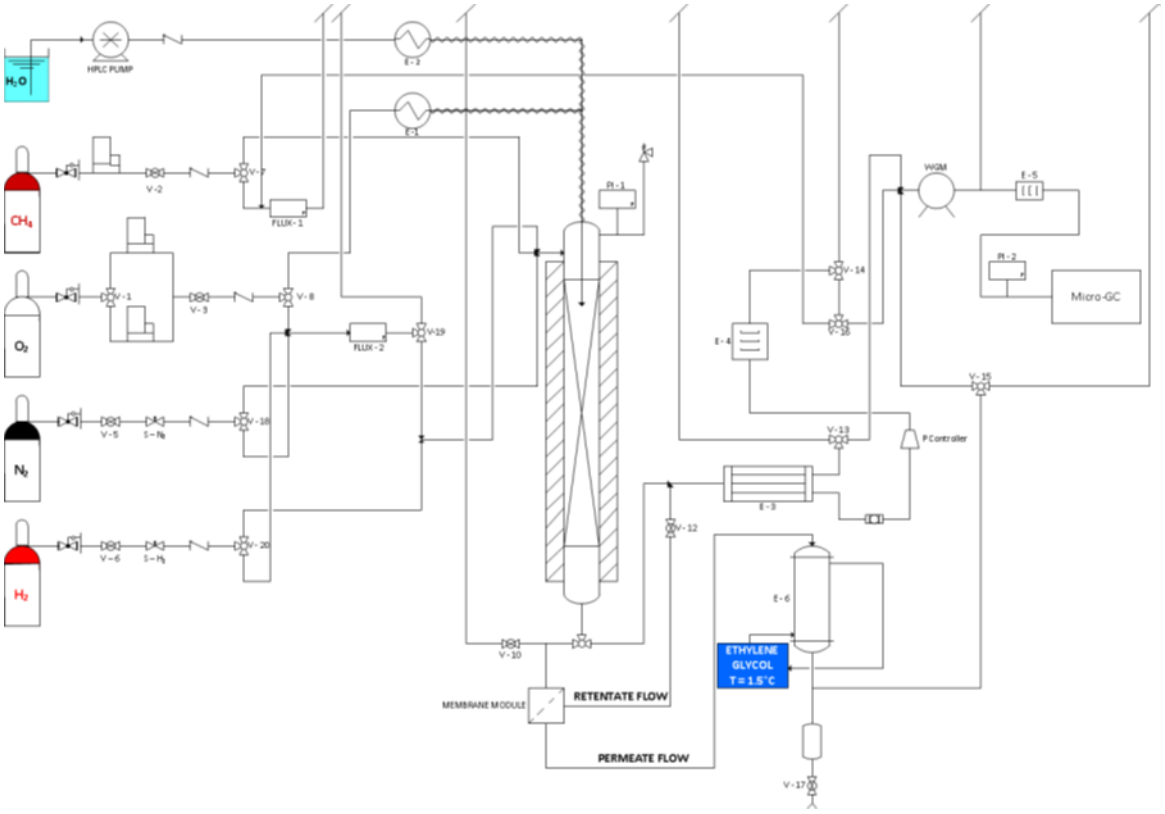

Figure 21: Flow sheet of the plant employed in this work

2.3.1. Description of the experiments

Different reactions are carried out on the catalysts tested. The oxy – reforming and the steam reforming reactions.

2.3.1.1. Oxy-reforming

1,00 g of catalyst was loaded in the Incolloy reactor described above. Before starting the reaction and proceed with all of the catalytic tests, is important to activate the catalyst, reducing the oxidized metals to its metallic active state. This was done by heating up the catalyst at 750°C under a flow of hydrogen 10% (vol/vol) in nitrogen and keeping it at this temperature overnight. Then the oxy-reforming tests were carried out.

The volumetric composition of the feed mixture of the oxy–reforming reaction, was decided in collaboration with Tecnimont KT simulating the real feed which will be used in the pilot plant and in the industrial plant. The selected feed composition involved sub-stoichiometric ratio of H_2O and O_2, namely an O_2/C molar ratio of 0.21 and a S/C (H_20/CH_4) molar ratio of

0.70.The O_2/C ratio is calculated considering only the free oxygen of the stream while the total amount of oxygen in the stream is considered, the O_2/C ratio becomes 0.57, a value typical for classical CPO reaction.

Generally, for all the catalysts tested, the same sequence of catalytic tests was followed. One test (reference test), generally the first one carried out on the fresh catalyst, was periodically repeated in order to evaluate the stability of the catalyst towards deactivation phenomena. For the oxy – reforming reaction the reference test was carried out at a Toven = 750°C, P = 1 atm and GHSV = 24000 h^{-1},

The parameters modified in the different catalytic tests were the steam to carbon ratio (S/C) (vol/vol) by increasing the steam flux; the GHSV, increasing all the fluxes, the oven temperature and total pressure (table 2). It must be noted that when steam flux was increased to evaluate the S/C effect, the GHSV raised, as evidenced by table 2. However, this variation was not as high as in the case in which the GHSV was changed at constant S/C. Thus, the GHSV value in the case of S/C modification was always indicated as 30000, to not confuse the reader.

Table 4: Conditions employed in the oxy-reforming tests.

	T (°C)	P (atm)	GHSV (h^{-1})	S/C	O_2/C	CH_4 in (ml/min)	H_2O in (ml/min)	O_2 in (ml/min)
Reference	750	1	2400	0,7	0,21	105	73	22
Effect of T	450	1	30000	2	0,21	105	210	210
Effect of S/C	500	1	27600	1	0,21	105	105	22
	500	1	33800	1.5	0,21	105	157	22
	500	1	40000	2	0,21	105	210	22
Effect of GHSV	500	1	50000	1	0,21	204	204	43
	500	1	100000	1	0,21	380	380	80
Effect of P	500	3	30000	1	0,21	105	105	22
	500	5	30000	1	0,21	105	105	22
Effect of O_2	500	1	50000	3	/	105	315	/

2.3.1.1. Steam reforming

The same Incolloy reactor used for the oxy-reforming was used and charged with 1,00 g of catalyst. The reduction of the active phase was carried out overnight at 750°C or 500°C with a 10% (vol/vol) hydrogen in nitrogen mixture. Then the steam reforming tests were conducted, investigating the effect of S/C, temperature, pressure and GHSV. A list of the performed tests is reported in table 5. The reference test was periodically repeated to evaluate eventual deactivation of the catalysts.

Table 5: Conditions employed in the low temperature steam reforming tests.

	T (°C)	**P (atm)**	**GHSV (h^{-1})**	**S/C**	**CH_4 in (ml/min)**	**H_2O in (ml/min)**
Reference	500	1	31200	1.5	105	157
Effect of S/C	500	1	25000	1	105	105
	500	1	37500	2	105	210
	500	1	50000	3	105	315
Effect of GHSV	500	1	70000	2	204	408
	500	1	130000	2	380	760
Effect of P	500	3	37500	2	105	210
	500	5	37500	2	105	210
	500	5	37500	2	105	210
Effect of T	450	1	50000	3	105	315
	400	1	50000	3	105	315
	350	1	50000	3	105	315
Effect of S/C at 10 atm	500	10	31200	1.5	105	157
	500	10	37500	2	105	210
	500	10	50000	3	105	315
Effect of S/C at 10 atm and 450°C	450	10	31200	1.5	105	157
	450	10	37500	2	105	210
	450	10	50000	3	105	315

Moreover, some stability tests were also conducted by running a test in the reference conditions (500°C, 1 atm, S/C 1.5 and 30000 h^{-1}) for 10 h.

2.3.1.2. Water gas shift and membrane reactor tests.

In the water gas shift experiments, the Incolloy reactor was filled with 1,00 g of Rh2.7CZOm750 catalyst and submitted to the oxy-reforming conditions at 750°C as listed in table 6. The refoming outlet was then sent to a water gas shift reactor in which 4,40 g of catalyst were mixed with inert quartz. The WGS reactor was heated at 400°C for all the tests involved. The outlet was then sent to the treatment and analysis zone.

Table 6: Conditions employed in the oxy-reforming reactor to generate the inlet mixture for the water gas shift tests.

	T (°C)	**P (atm)**	**GHSV (h^{-1})**	**S/C**	**O_2/C**	**CH_4 in (ml/min)**	**H_2O in (ml/min)**	**O_2 in (ml/min)**
Effect of S/C at 30000 h^{-1} and 3 atm	750	3	27600	1	0.21	105	105	22
	750	3	33800	1.5	0.21	105	157	22
	750	3	40000	2	0.21	105	210	22
Effect of S/C at 100000 h^{-1} and 5 atm	750	5	100000	1	0.21	380	380	80
	750	5	123000	1.5	0.21	380	570	80
	750	5	146000	2	0.21	380	760	80
Effect of P at 30000 h^{-1} and S/C 2	750	5	40000	2	0,21	105	210	22
Effect of P at 100000 h^{-1} and S/C 1	750	3	100000	1	0.21	380	380	80
Effect of GHSV at 3 atm and S/C 2	750	3	100000	2	0,21	380	760	80

The water gas shift reactor could be replaced by a membrane module (figure 20). In this case, the Incolloy reactor was just filled with quartz and used to pre-heat the reagents. The membrane module was composed by two inlet and two outlet streams. One inlet and outlet characterized the retentate, namely the inner part of the membrane tube, while the other two the permeate side. Nitrogen was fed to the permeate inlet to be used as sweep gas, while the reagents, namely methane and steam were fed to the retentate. The membrane was filled with 6,8 g of catalysts. Both outlets were alternatively sent to the treatment and analysis zone.

2.3.1.3. Formulas

The formulas used to express the results of the catalytic tests are listed below.

Methane conversion: $X_{CH4}=100*(\%COout + \%CO_2out)/(\%COout + \%CO_2out + \%CH_4out)$

CO selectivity: Sco 100*(%COout)/(%COout + $\%CO_2$out)

H_2/CO ratio: $H_2/CO=\%H_2out/\%COout$

Hydrogen production: H_2 prod= Litres of H_2out (STP)/hours of reaction

Carbon balance: $100*(\%COout + \%CO_2out + \%CH_4out)*flux\ out/(flux\ in*\%CH_4in)$

Hydrogen Recovery: $R_{H2}=\%H_2perm*flux\ perm/(\%H_2perm*flux\ perm+\%H_2ret*flux\ ret)$

CO conversion (WGS): $Xco=100*(\%COin*flux\ in-\%COout*flux\ out)/(\%Coin*flux\ in)$

CO_2 sel.(WGS): $Sco_2=100*(\%CO_2out*flux\ out-\%CO_2in*flux\ in)/(\%COin*flux\ in-\%COout*flux\ out)$

Hydrogen yield (WGS): $Y_{H2}=100*(\%H_2out*flux\ out-\%H_2in*flux\ in)/(\%COin*flux\ in)$

Sorbent conversion: 100*gCO_2 desorbed/theoretical CO_2 that can be adsorbed

Theoretical CO_2 that can be adsorbed refers to the amount of CO_2 that can be adsorbed by conversion of CaO to $CaCO_3$ and of the mixed oxide to hydrotalcite (1 mol of CO_2 for each mol of Al).

Methane Yield (methanation): $Y_{CH4}=100*(\%CH_4out + \%COout)/\%CH_4out$

The CEA-NASA software was used to calculate the outlet composition of the stream at the thermodynamic equilibrium. Form them the equilibrium conversion was calculated. The software provides the molar gaseous outlet composition, based on the feed composition in terms of molar percentage, the reaction temperature and pressure and considers all the reaction involved. For the equilibrium CO conversion in the WGS tests, only the water gas shit reaction was considered, and the equilibrium was calculated using the K_{eq}.

2.3.1.4. Nomenclature

The catalysts synthesised in this study were named as follows:

Pt2%-IWI-CZOm750-R750

Where Pt2% indicates a 2% wt/wt of support of Pt loading; IWI stands for Incipient Wetness Impregnation, which is the method used for the impregnation of the active phase; CZO is the $Ce_{0.5}Zr_{0.5}O_2$ support; m stands for microemulsion. which is the method used for the support synthesis; 750 represents the calcination temperature expressed in °C and R750 represents the temperature in °C at which the calcined catalyst was reduced. As some parameters for the synthesis were kept constant for most of the catalysts, the nomenclature may be simplified i.e. just specifying the active phase and the support (for instance Pt-CZO).

The operative conditions for the catalytic test will be expressed as follows:

750°C-30000h^{-1}-1atm-S/C0.7

Where 750°C is the set temperature of the oven in which reactor is placed; 30000h^{-1} is the selected GHSV (Gas Hourly Space Velocity); 1atm is the pressure inside the reactor; S/C0.7 is the Steam to Carbon ratio, expressed as: (steam flux)/(methane flux). It is be noted that the tests carried out different S/C actually have different GHSV, as methane flow is maintained constant while the water content is increased for higher S/C.

2.4. **Catalyst characterization**

X ray diffraction (XRD) analysis was carried out using a Philips PW1050/81 diffractometer equipped with a graphite monochromator in the diffracted beam and controlled by a PW1710 unit (Cu Kα, λ = 0.15418 nm). A 2θ range from 20° to 80° or from 5° to 80° was investigated at a scanning speed of 40°/h. Nitrogen adsorption-desorption isotherms were determined at liquid nitrogen temperature (−195 °C), using an automatic ASAP 2020 Micromeritics sorptiometer and analysed using a software operating standard BET and BJH methods. Raman analysis was carried out with a micro-spectrometer Renishaw Raman RM1000 interfaced to a microscope Leica DMLM (obj. 5×, 20×. 50×). The available sources were an Ar^+ laser (λ = 514.5 nm; Pout = 25 mW) and a diode laser (λ = 780.0 nm; Pout =

30mW). In order to eliminate the Rayleigh scattering, the system was equipped with a notch filter for the Ar^+ laser and an edge filter for the diode one. The network was a monochromator with a pass of 1200 lines/mm. The detector was a CCD one (Charge – Coupled Device) with a thermo-electrical cooling (203 K). Redox properties of the catalysts were studied carrying out temperature programmed reduction/oxidation (TPROR) cycles. These analyses are performed using a ThermoQuest Instrument TPD/R/O 1100 Catalytic Surface Analyzer. Before running any reduction/oxidation step, any sample (0.06–0.1 g) was subjected to a pretreatment, flowing He (30 mL/min) while the temperature was increased from room temperature to 150 °C and kept at this temperature for 30 min. After this isotherm, the sample was cooled down to 60 °C. Then TPR/O/R cycles was performed introducing into the system a 5% H_2/Ar (30 mL/min), while the operating temperature was increased from 60 °C to 950 °C at the rate of 10 °C/min. An isotherm at this final temperature of 30 min was performed. After the system was purged with He while the temperature reached 60 °C, TPR was followed by temperature programmed oxidation (TPO). A 5% O_2/He (30 mL/min) was introduced into the system and, similar to the TPR, the temperature was increases from 60 °C to 950 °C at the rate of 10 °C/min. After 30 min in which thetemperature was maintained constant at 950°C, the sample was cooled down to 60 °C in He, in order to perform the final step of reduction. H_2-TPD analyses were carried out by pulsing a mixture of H_2 10% in Ar over the sample at room temperature. The hydrogen adsorption was measured by TCD detector. Following the pulses, the temperature was increased to 900°C at 10°C/min, measuring the hydrogen desorption with a TCD. SEM/EDS analyses were performed by using an E-SEM Zeiss EVO 50 Series Instrument (Carl Zeiss, spa) equipped with an INCA Energy 350 EDS microanalysis system (Oxford Instruments Analytical) or with ZEISS GeminiSEM 500. The accelerating voltage was 20 kV and the spectra collection time 60 s. TEM analysis were carried out using a TEM/STEM FEI TECNAI F20 microscope combined with Energy Dispersive X – Ray Spectrometry (EDS), at 200 keV. A small quantity of powder (0,3 – 0,5 g) of calcined fresh catalysts, reduced fresh catalysts and spent catalysts were investigated in order to study the morphology, the dimensions and the size distribution of the active metal particles on the support and their interactions with it. The sample preparation was carried out suspending the powder in ethanol and treating it with ultrasound for 15 min. The suspension was

deposited on a “multifoil-carbon film” sustained by a Cu grid. Then the so prepared system was dried at 100 °C. With EDS it was possible to make an elementary analysis in some areas of the samples, therefore understanding the real composition of the catalyst.

CO_2 sorption analyses were carried out by charging the sample in a quartz reactor (0,100 g), heating up to sample under He to 800 to desorb and quantify the carbon dioxide already present in the sample. The temperature was then lowered to 600°C and submitted for 40 minutes to a flux of CO_2 20% in He. Then the temperature was raised to 800°C under He to measure the desorbed carbon dioxide which was taken as value for the sorption property. CO2 was detected with a Rosemount analytical XStream detector.

3. CHAPTER 3 - PREVIOUS STUDIES AND AIM OF THE WORK

The present work is a continuation of previous studies carried out in our laboratory by Barbera and Mafessanti [116,117]. These authors, in particular, studied the oxy-reforming (OR) reaction at 750°C, using two different catalyst systems. For this purpose, they synthesised active catalysts based on Rh-Mg-Al hydrotalcite precursor and on Rh deposited over $Ce_{0.5}Zr_{0.5}O_2$ support synthetized by microemulsion technique. Furthermore, in order to obtain pure hydrogen, they let the outlet stream of the oxy-reforming pass through a separation unit consisted of a Pd-based membrane. Thanks to the high permeability of the membrane, it was possible to get a high hydrogen separation. This process is based on the difference in hydrogen partial pressure between permeate and retentate side. In Mafessanti and Barbera works, the difference in partial pressure were found to be close to 0 atm at the end of the membrane. This, indeed entails no more driving force for separation inside the membrane. A further study in this regard [122] showed the possibility of increasing the driving force of separation and thus obtaining pure hydrogen outlet stream by filling the membrane with a WGS catalyst (Pt on $Ce_{0.5}Zr_{0.5}O_2$) in a membrane reactor configuration [118]. This permitted to increase the CO conversion

beyond the chemical equilibrium value in a fixed bed reactor configuration and to suppress the methanation reaction, which consumes hydrogen to produce methane.

With this background, the main goal of this thesis is to perform both reforming and water gas shift (WGS) reactions in the same membrane reactor, in order to produce pure hydrogen and increase its yield by removing it from the reaction environment. In this regard, the first part of the present work is focused on synthesising a new catalyst system with enhanced activity and improved stability against deactivation. The second part is related to the study of the oxy-reforming reaction at 750°C and its coupling with water gas shift reaction. The third part is related to the systematic study on oxy-reforming with an aim to optimize the reaction conditions as well as the catalyst system. The fourth part shifts the attention to Low Temperature Steam Reforming (LTSR), while the fifth part of this thesis relates to the membrane reaction operation.

In order to carryout both SR and WGS reactions inside the membrane reactor, the operative temperature (which is usually 750°C for the OR and even higher for steam reforming (SR)) must be lowered at least to 500°C, as the WGS is not favoured at higher temperatures and also the membrane can be used only at temperatures below 600°C due to its stability issues. On the contrary, this saves energy in the heating process. However, it must be noted that the methane conversion in SR and OR is thermodynamically unfavoured at temperatures below 750°C and that these reactions are necessary for both hydrogen production and WGS occurrence. Thus, very active catalyst must be selected in order to obtain conversions as close as possible to the equilibrium conversion.

However, when submitted to membrane operation, the removal of hydrogen should help to increase the conversion to values that overcome the equilibrium, thus making the process economically viable even at this temperature. Moreover, as charging and discharging as well as operating the membrane reactor is a time-consuming and delicate operation, it is essential to find a catalyst which is not only mechanically robust but also possess certain chemical stability, such as, e.g., stability against deactivation. The deactivation of the catalyst occurs mainly by three processes, namely carbon deposition, sintering and oxidation of the active metallic phase. Carbon deposition not only covers the surface of the catalyst but can also occur over the membrane, thus not only causing the catalyst to lose its activity but also

impeding hydrogen permeation. For this reason, the present study was started by selecting a catalyst support which was reported to possess high oxygen mobility and oxygen storage capacity, namely $Ce_{0.5}Zr_{0.5}O_2$ (CZO) [50]. These two properties play an important role in removing the carbon deposition.

This support was synthesized via microemulsion method, as the classical co-precipitation method was not able to provide the desired Ce/Zr ratio [50]. The catalytically active noble metal phases (namely, Pt, Rh and their mixtures which do not deactivate through sintering and oxidation, were selected and tested separately in both OR and WGS reactions. In particular, Pt has been reported to be an efficient WGS catalyst, while our group evidenced the good performances on Rh at 750°C for the OR reaction [116]. However, these catalysts have not been tested in the low temperature oxy-reforming (500°C) and WGS at 400°C. For this reason, they were selected for the catalytic tests of oxy-reforming (OR) and WGS. In all cases, the CZO precursor obtained by microemulsion was calcined at 750°C as this support has been proven to provide good performances in previous studies [116]. In a typical experiment, the active phases were deposited on the CZO support by incipient wetness impregnation (IWI), then submitted to calcination at 500°C to obtain the metal oxide from the nitrate precursor and finally reduced at 750°C under a 10% H_2/N_2 flow overnight.

Using the above-mentioned reactor configuration and catalytic system, the following parameters will be investigated:

(i) the methane conversion, compared to the methane conversion at the equilibrium value, which will give an indication of the activity of the catalyst and on how close to the equilibrium it is able to catalyse the reaction

(ii) H_2/CO ratio, which will give a hint on which reactions occur, as the CPO would provide a stoichiometric ratio of 2, the SR a ratio of 3, while the WGS would consume CO, increasing the ratio at even higher values; the CO_2 selectivity would give us an on indication of the WGS occurrence.

(iii) CO2 selectivity, which helps to understand the occurrence of WGS

(iv) Hydrogen production.

4. CHAPTER 4. SYNTHESIS, CHARACTERIZATION OF THE CeZr AND Zr OXIDE AND SYNTHESIS OPTIMIZATION

4.1. Introduction

This work focused on the study of catalytic systems based on two different supports (CeZr and Zr oxides). These were impregnated with Pt, PtRh, Rh or Ru active phases. This chapter treats the characterization of the two supports employed. These were $Ce_{0,5}Zr_{0,5}O_2$ and ZrO_2 synthetized by microemulsion, as reported in detail in the experimental part. The synthesis is based on the creation of micelles in which the aqueous solution containing the Ce and Zr cations are found. These micelles are dispersed in an oil phase, creating a microemulsion. This microemulsion is mixed with a similar one, which contains a base in place of the cation solution. Thus, a coprecipitation occurs when a micelle containing the cations hits and exchanges material with another one containing the base. This technique was able to provide homogeneous CeZr supports, with tailored composition and peculiar properties as reported in a previous work [50]. This chapter highlights the characterization of the supports obtained using this synthesis and then used as catalytic support in this work.

4.2. **Characterization of the supports**

4.2.1. XRD analysis

The CeZr and Zr based supports synthesized by w/o microemulsion were characterized after calcination by means of XRD analyses. Moreover, the effect of the calcination temperature on phase segregation was analysed on CeZr samples, by treating the hydroxide obtained after the microemulsion synthesis at temperatures between 500°C and 1100°C. Figure 22 reports the diffractograms of CZO-m supports calcined at 500 °C (CZO-m500), 750 °C (CZO-m750), 900 °C (CZO-m900), 1000 °C (CZO-m1000)and 1100 °C (CZO-m1100).

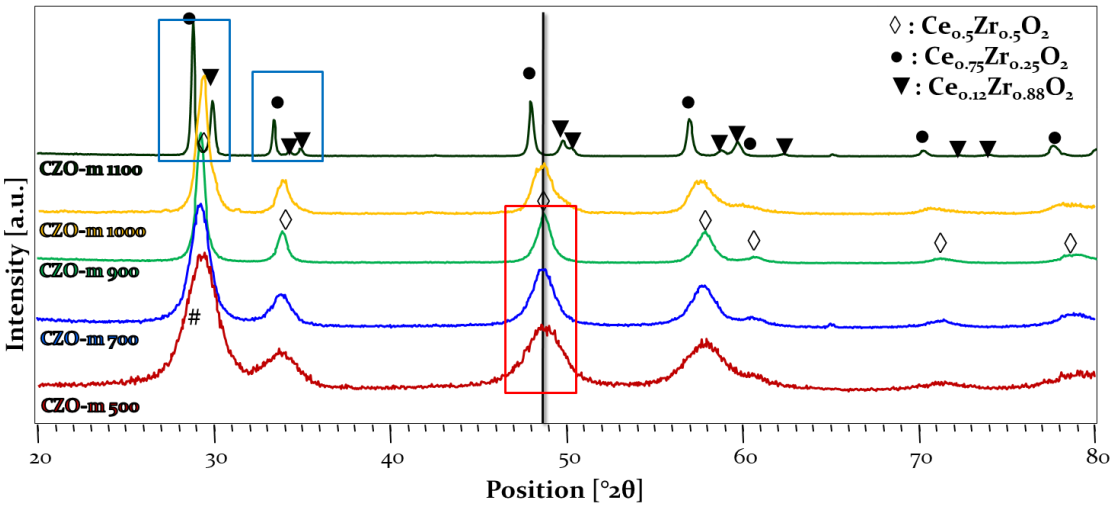

Figure 22: diffractograms of CZO-m supports calcined at 500 °C (CZO-m500), 750 °C (CZO-m750), 900 °C (CZO-m900), 1000 °C (CZO-m1000)and 1100 °C (CZO-m1100).

The analysis of the samples calcined at lower temperatures shows reflects ascribable to $Ce_{0.5}Zr_{0.5}O_2$ phase, thus indicating successful synthesis of the desired phase. This phase is stable up to 900°C, but phase segregation starts to occur at 1000°C, as detected by the enlargement of the peaks and it is complete at 1100°C where the sample is characterized by Ce-enriched ($Ce_{0.75}Zr_{0.25}O_2$) and Ce-depleted ($Ce_{0.12}Zr_{0.88}O_2$) phases [50]. This phenomenon limits the catalytic application of such supports to temperatures below 1000°C. With increasing calcination temperature, peak narrowing is observed, indicating the formation of larger particles due to sintering of the oxide. In fact, Debye Scherrer calculation on the peak

at lower 2θ showed an average crystallite dimension of 6 nm at 500 °C, 8 nm at 750°C and 14 nm at 900°C. The peak enlargement given by segregation at 1000°C made the calculation of crystallite dimension ineffective at this temperature, as the full width at half maximum in this case would be overestimated as it results from the overlay of two peaks of two different phases. At 1100°C, larger crystallites are formed after sintering and phase segregation with the two phases showing crystallite sizes of 62 nm for $Ce_{0.75}Zr_{0.25}O_2$ and 45 nm for $Ce_{0.12}Zr_{0.88}O_2$. These results suggest that the temperature at which the samples are submitted can modify their morphology and structure. For this reason, it was decided to use the CZOm sample calcined at 750°C for the tests of oxy-reforming and low temperature steam reforming as temperatures higher than 500°C could be developed during the occurrence of the oxy-reforming. Moreover, this sample proved to outperform the one calcined at 900°C during catalytic tests carried out in previous studies [116].

Even the ZrO_2 samples obtained by w/o microemulsion were calcined at 750°C and analysed by XRD analysis, that showed the formation of the sole tetragonal phase of zirconia, while the pattern relative to monoclinic phase was not present (Figure 23). The latter is associated with lower surface area [119–122]. This is an important feature of the microemulsion synthesis as a pure tetragonal phase is not easily obtained with other synthetic methods.

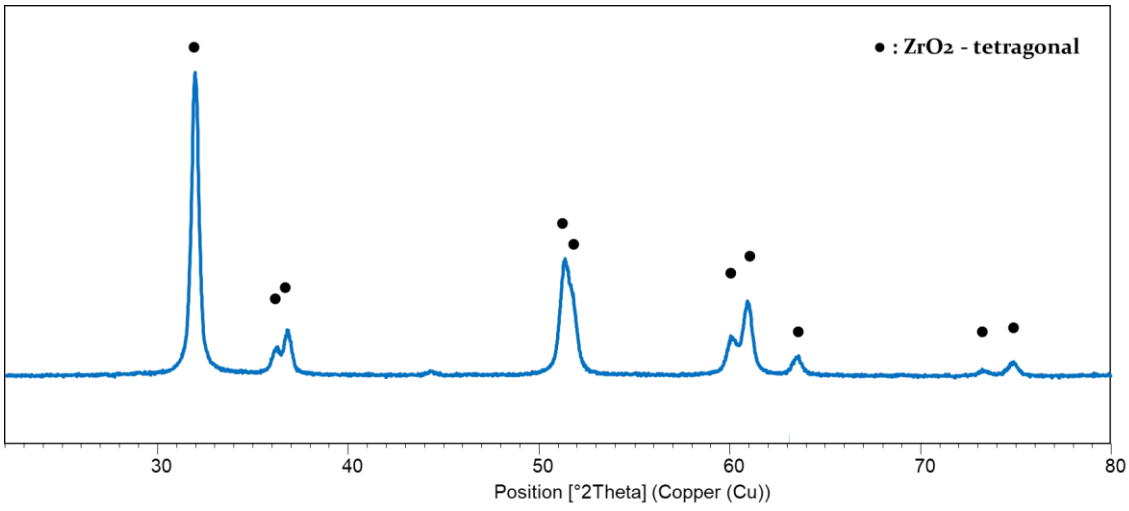

Figure 23: XRD of the ZOm sample synthesized by microemulsion and calcined at 750°C.

However, the tetragonal phase is unstable when submitted to harsh conditions. In fact, part of the tetragonal phase is converted into the monoclinic one after reduction at 750°C

overnight. This procedure was employed after impregnation with noble metal (Rh) to be used as steam reforming catalyst (chapter 7 and 8). The formation of a monoclinic phase was evidenced by XRD analysis as shown in figure 24. The absence of Rh phases (though present) is related to its low amount and high dispersion.

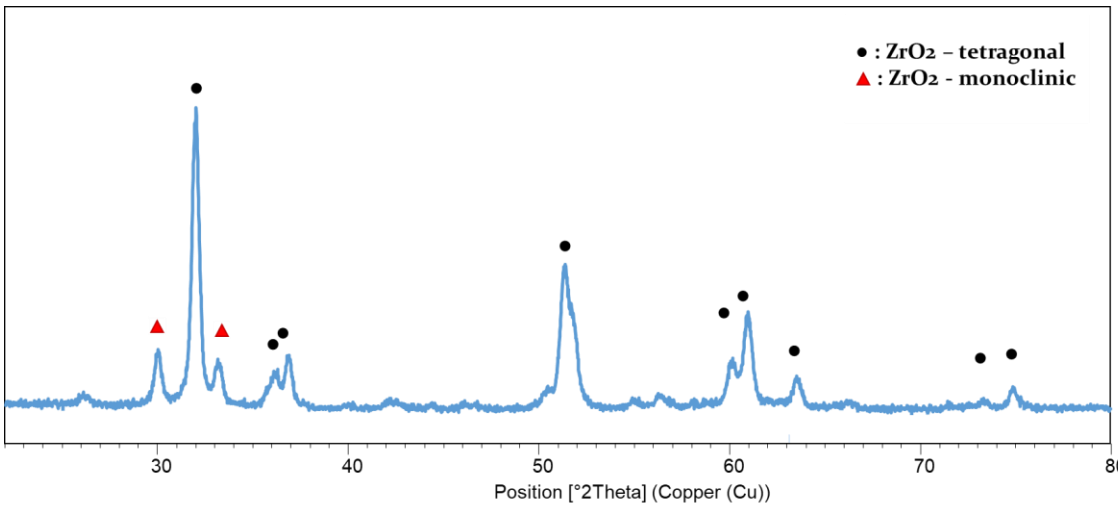

Figure 24: XRD of the ZOm sample synthesized by microemulsion and calcined at 750°C after reduction at 750°C.

4.2.2. Raman analysis

Raman analysis was carried out on CZO sample in order to further investigate the structure of this oxide synthesized by microemulsion. In fact, CeO_2-ZrO_2 binary oxides were found in different structures whose identification is not straightforward. In particular, the medium region of the Ce-Zr binary diagram is ambiguous because of the presence of a large number of metastable or stable phases, as discussed in different works [104,106].

In particular, one cubic phase (c), but three different tetragonal phases (t, t' and t'') can be found [106]. The most stable one is the cubic fluorite structure, typical for CeO_2 and Ce-rich oxides. The tetragonal phase is obtained in ZrO_2, when treated at high temperatures. When the tetragonal structure is distorted, t' and t'' phases are formed. In particular, t' has a lattice parameter ratio (c/a) of 1.01 and t'' of 1.00, compared to 1.4 of t phase. The t'' phase is composed by a tetragonal distortion of the oxygens inside a cationic cubic structure. Even though these differences seem to be small, they can highly affect the properties of the support, such as the oxygen storage capacity and oxygen mobility [50]. Raman was employed to evaluate the presence of these phases, as XRD is not sensible to oxygen atoms

when heavier elements are present, and it is thus not a suitable technique to distinguish between c and t'' phases, which both possess a cationic cubic displacement. The Raman spectra of the CZOm750 sample is shown in Figure 25.

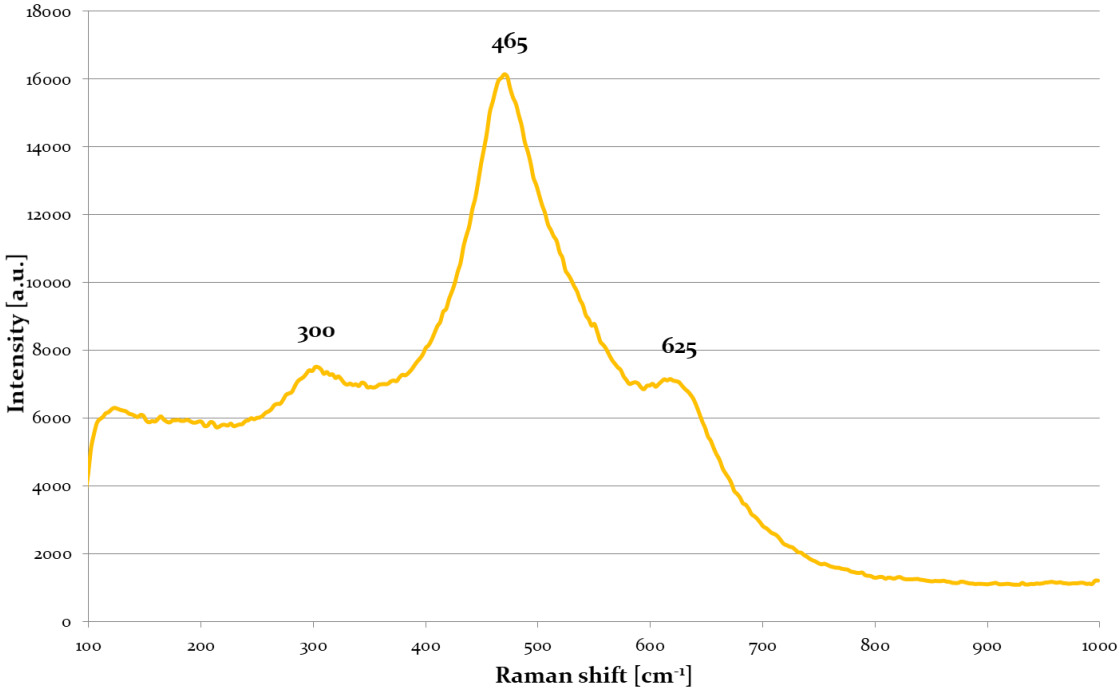

Figure 25: Raman spectra of the CZOm750 sample.

The main band at 465 cm^{-1} is due to the total symmetric stretching compatible with the presence of a cubic phase [123]. The small band detected at 300 cm^{-1} can be indicative of the t'' phase as reported by Zhang et al. [123] The presence of the t'' phase is further confirmed by the band at 625 cm^{-1}, which is due to the tetragonal lattice distortions of the cubic phase, that allow to break the selection rules. However, the formation of the t'' phase is not dependent only by the Ce/Zr ratio but it can be affected by many factors, such as the synthetic method. In fact, Roh et al. [101] reported the microemulsion synthesis of a $Ce_{0.5}Zr_{0.5}O_2$ oxide that showed the presence of solely cubic band (at 465 cm^{-1}). However, they used different solvent and surfactant, indicating that even slight modification in the procedure of the synthesis can change the properties of the obtained oxide.

The Raman analysis was also carried out on the zirconium oxide sample synthesized by microemulsion in order to further investigate the presence of tetragonal and cubic phases, which are not distinguishable by XRD (figure 26).

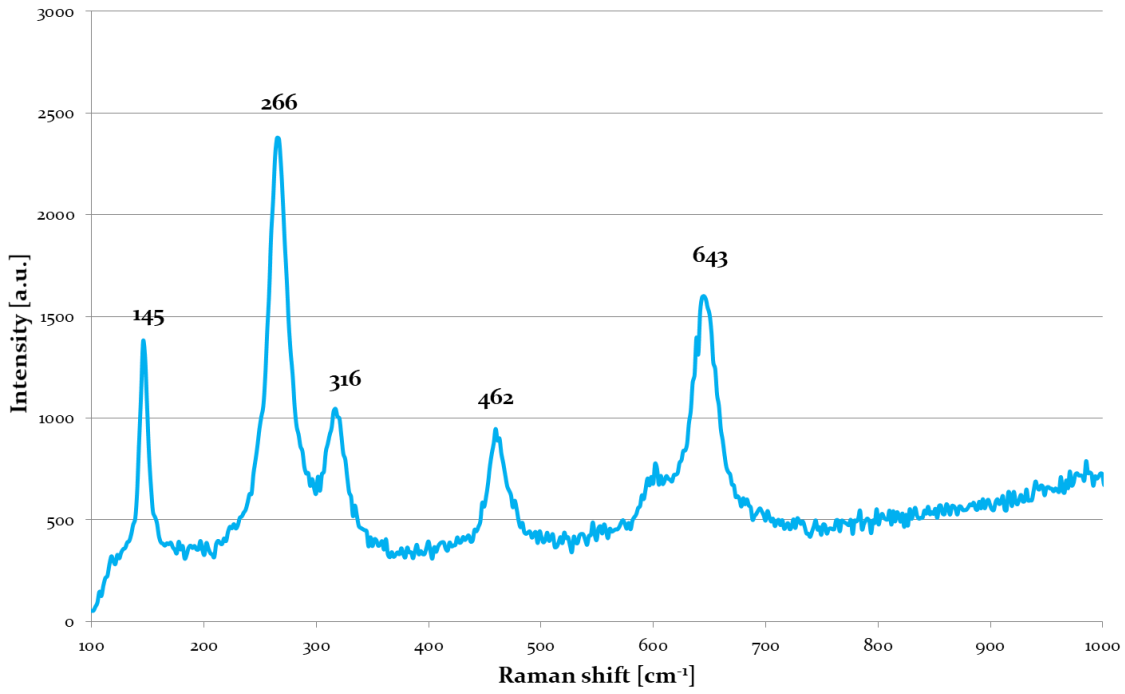

Figure 26: Raman spectra of the ZOm750 sample.

The samples present peaks centred at 145, 266, 316, 462 and 643 cm^{-1}. This pattern is consistent with the presence of a tetragonal phase, as reported in literature [119]. No bands relative to cubic phase (490, 579 and broad bands 595–660 cm^{-1}) were detected and thus a pure tetragonal phase can be assumed for this sample. This is another advantage of the microemulsion synthesis which is able to provide a homogenous pH inside the micelles, giving a phase which is not straightforward to obtain with classical synthesis methods [119].

The sample was also analysed after reduction of the deposited Rh phase, as structure modification was detected by XRD. The spectrum shows the presence of peaks at 145, 266, 316, 462 and 643 cm^{-1}, which confirm the presence of a tetragonal phase even after reduction at 750°C. The presence of the monoclinic phase detected by the XRD analysis

could be covered by the broad bands of the tetragonal phase, due to a higher presence of the latter.

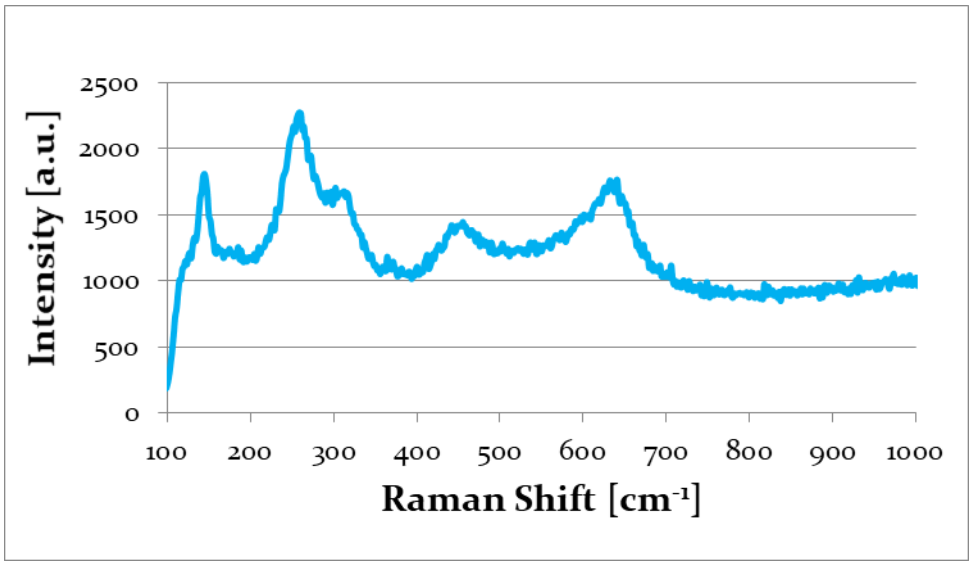

Figure 27: Raman analysis of Rh0.7%-ZOm after reduction at 750°C.

4.2.3. Nitrogen physisorption

Table 7 shows surface area, volume of the pores and average pore diameter analysed through nitrogen physisorption for CZOm750 and ZOm750 samples.

Table 7: Surface area, pores volume and average pores diameter of the CZOm750 and ZOm750.

	Surface Area (m2/g)	***Pores Vol. (cm3/g)***	***Avg. Pore Diam (nm)***
CZOm750	48.8	0.08	5.8
ZOm750	40.7	0.07	10.8

The Ce containing sample shows a higher surface area and a smaller average pore diameter. However, the total pore volume is similar for the two samples, suggesting that more and smaller pores are found in the CZOm750 sample. This is also confirmed by the pore size distribution that highlights the presence of smaller pores for CZOm750 (Figure 28). A higher number of pores centred between 8 and 12 nm is found in this sample, while ZOm750 possesses a wider pore distribution between 10 and 17 nm.

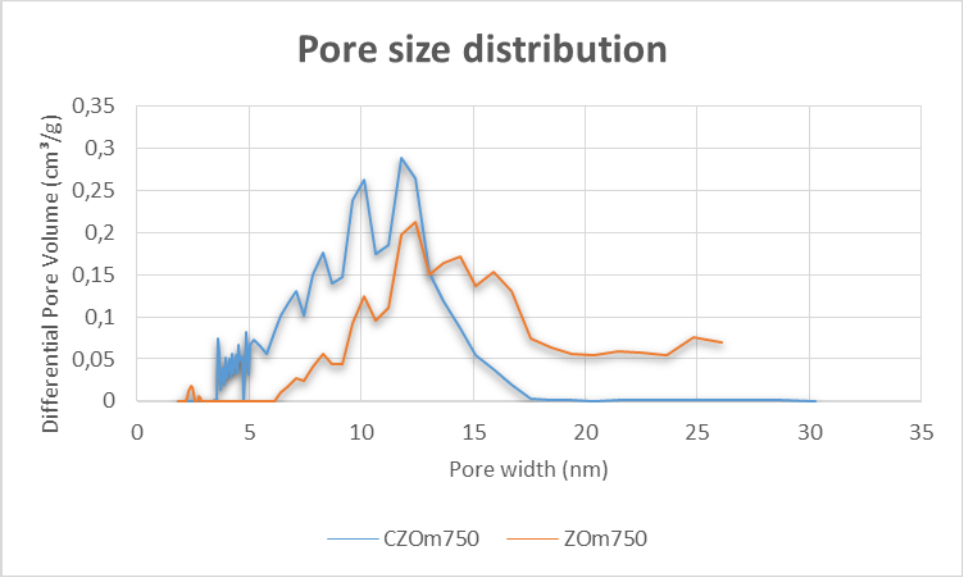

Figure 28: Pore size distribution for CZOm750 and ZOm750 samples.

Adsorption-desorption isotherms are presented in Figure 29.

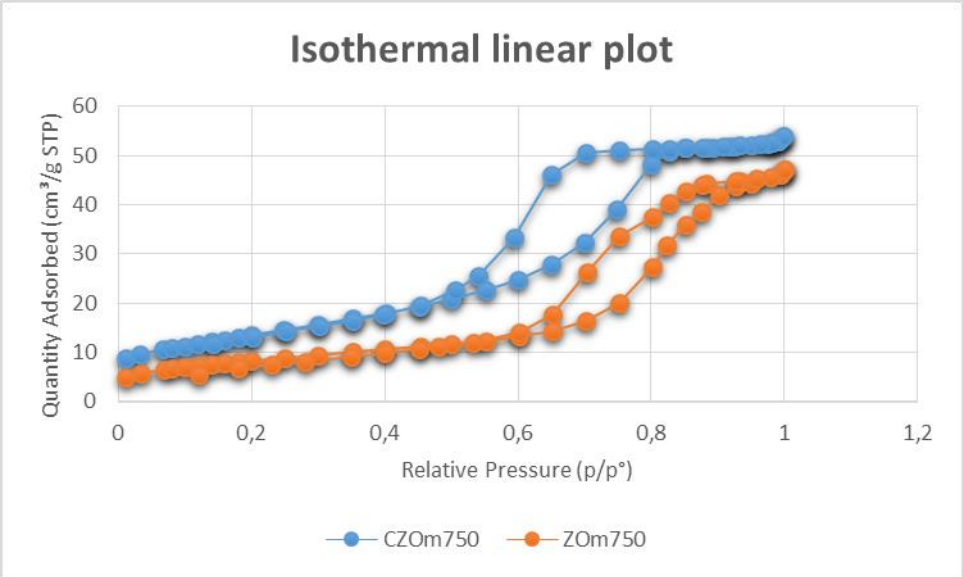

Figure 29: Isothermal linear plots of CZOm750 and ZOm750 samples.

In general, adsorption isotherms can be classified in mainly 6 types as reported by IUPAC and shown in figure 30 [124]. Both samples show a Type IV isotherm and an H2-type hysteresis loop.

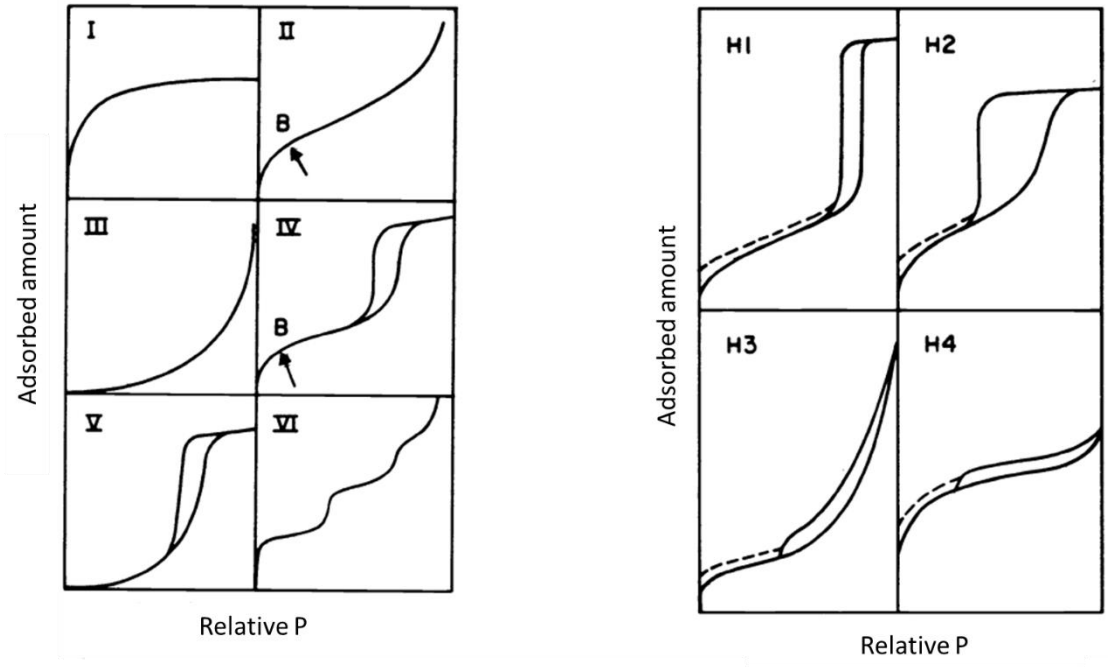

Figure 30: Classification of adsorption-desorption isotherms and hysteresis loops. Adapted from [124]

Type IV isotherms are characterized by the presence of hysteresis loop and a limiting uptake at high relative pressures that results in a trend parallel to the x axis. Point B (shown in figure 30), represents the stage at which the formation of a monolayer is complete and multilayer adsorption begins. Type IV isotherms characterizes mesoporous materials, which means that pores between 2 and 50 nm are present in both samples. In addition, the relative pressure at which the curve is found helps to understand the pore size. In particular curves found at higher relative pressure are found when bigger pores are filled. In fact, small pores are filled at lower relative pressure while large pore filling occurs at higher values. This is the case of zirconia, which displays bigger pores as also reported in Figure 28 and Table 8. Finally, the shape of the hysteresis can give information on the material morphology. The loop is caused by a difference in the adsorption and desorption processes. A classification of hysteresis loops was also provided [124]. The samples show the presence of an H2 hysteresis loop. This is no easy to interpreter. In the past it was said to be produced by a difference in the condensation and evaporation mechanism that occurred in ink bottle pores. These are pores with a narrow neck and a wide body, as an ink bottle indeed. However, this explanation was thought to be too simple [124]. Thus, the H2 hysteresis is usually associated to pores with broad size distribution and ill-defined shape.

Nitrogen physisorption was done even after reduction of the impregnated Rh-ZrO2 catalyst. A surface area of 29 m^2/g was observed together with wide pores (11.7) nm and a total pore volume of 0,10 cm^3/g. The smaller surface area compared to the not reduced support can be due to sintering, occurred during the reduction treatment. In fact, the sample was kept at 750°C overnight during the latter.

Table 8: Surface area, pores volume and average pores diameter of Rh0.75%-ZO.

	Surface Area (m2/g)	***Pores Vol. (cm3/g)***	***Avg. Pore Diam (nm)***
ZOm750	29.5	0.10	11.7

4.2.4. TEM analysis

The morphology and homogeneity of the synthesized oxides were analysed by TEM analysis to confirm the results obtained by XRD. The CZO sample synthesized by microemulsion is characterized by homogeneous and spherical crystals as can be seen from Figure 31. These have relatively small dimension that range between 10 and 40 nm. These properties are given by the microemulsion synthesis in which the micelles act as microreactors allowing the formation of small particles with round shape. Moreover, EDX analysis confirmed the composition of the Ce-Zr oxide, and the obtainment of an oxide with a Ce:Zr ratio close to 1. Small and round particles are also obtained in the case of zirconia thanks to the characteristics of the microemulsion synthesis. In this case, even smaller particles in the range of 10-20 nm are obtained.

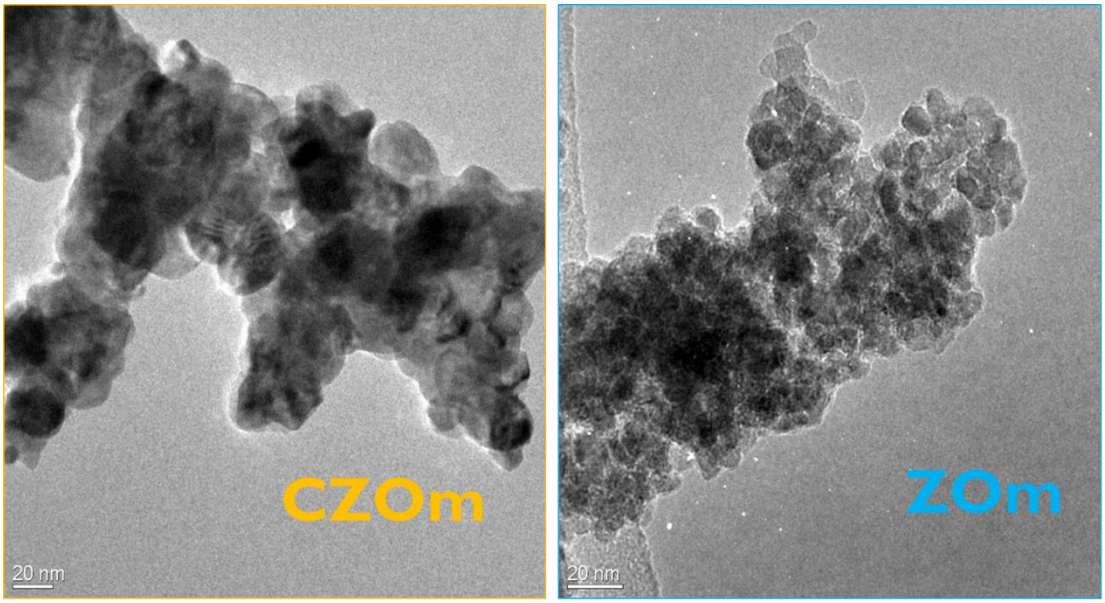

Figure 31: TEM images of the CZOm750 an ZOm750 samples

4.2.5. TPR analysis

The redox properties of the CZOm support were analysed by temperature programmed reduction and oxidation on the bare support. Even ZOm support was analysed but the absence of a reducible element resulted in no reduction or oxidation peak. For this reason, TPROR analysis on bare ZOm750 is not shown here. CZOm750 shows a broad reduction peak at 665°C (Figure 32).

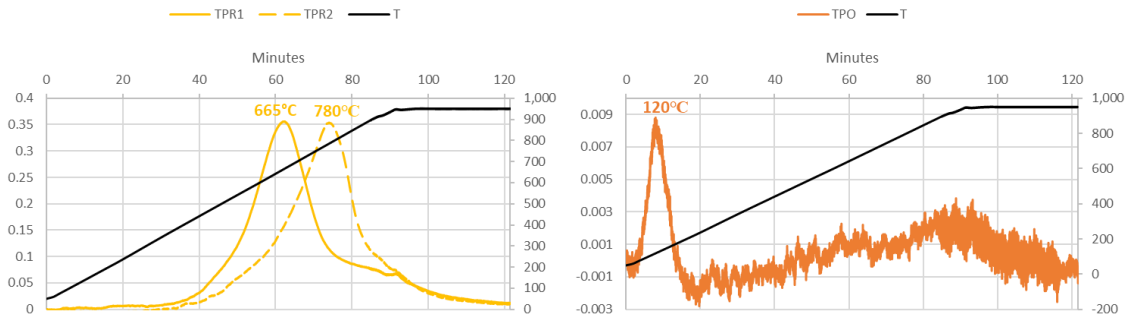

Figure 32:TPROR of the CZOm750 sample. Left: TPR1 and TPR2; Right: TPO.

Table 9: Hydrogen and oxygen consumption by TPR for CZOm750.

	TPR1	***TPO***	***TPR2***
Consumption (mmol/g)	1.28	0.09	1.33

Pure CeO_2 (not shown here) produces two reduction peaks which are due to the reduction of the surface (550°C) and of the bulk Ce (830°C) [98,129,130]. On the opposite, the $Ce_{0.5}Zr_{0.5}O_2$ obtained by microemulsion produces only one broad peak that is indicative of a more homogeneous reducibility given by this synthesis technique and an increased availability of bulk Ce, due to the increased oxygen mobility given by Zr addition in a 1:1 ratio. After oxidation, the reduction peaks are transferred to higher temperatures and centred around 780°C. This phenomenon has been reported by Fornasiero et al. [125] and may be caused by the reduction of surface area due to sintering, caused by the temperature programmed reduction up to 950°C. Noteworthy the hydrogen consumption is similar for the two TPR cycles (table 9), indicating that the amount of reducible material is kept constant even after a TPO cycle.

The oxidation peaks obtained during TPO are found at low temperatures because of to the high oxidation properties of the CZO sample.

4.3. **Optimization of the CZO microemulsion synthesis**

The microemulsion technique is a very useful synthetic method to obtain mixed oxides with peculiar properties. However, it is not straightforward to understand the parameters affecting the synthesis and few works about this can be found in literature. Thus, the influence on the oxide properties of the following parameters were investigated:

- Aging time
- Concentration of the base
- Rw (ratio between water and surfactant)

4.3.1. Aging time

In the classical synthesis, the microemulsion is stirred at room temperature for 5 h after the mixing of the reagents, before being filtered. In order to study the effect of this step, oxides were synthetized with an aging time of 1 and 24 h. Then the solid obtained was filtered, washed wit methanol to remove the surfactants and calcined at 500°C to obtain the mixed oxide. Even though the oxide employed in the catalytic test was calcined at 750°C, these

were treated at 500°C, as in this way it was easier to spot the differences in some properties such as the surface are, pore volume and pore diameter. These were analysed by nitrogen physisorption, which results are reported in table 10.

Table 10: nitrogen physisorption analysis of the samples with different aging time

Aging time (h)	S_{BET} (m^2/g)	Pore vol. (cm^3/g)	Pore diam. (nm)
1	83	0.11	4.39
5	127	0.13	4.22
24	137	0.14	3.49

Increasing the aging time, an increase in surface area is observed and this is particularly evident during the first hours of aging, where surface area increases from 83 to 127 m^2/g, in 4 h, while an increase of 10 m^2/g is obtained after further 19 h. Even the pore volume increases with aging time, from 0.11 to 0.14 cm^3/g, while the pore diameter is narrowed when time is raised. Thus, the support morphology is clearly affected by the aging time probably due to phenomena of re-dissolution and re-precipitation of the Ce/Zr hydroxide [132,133]. Favouring these phenomena by increasing the aging time allows the formation of a support with higher surface area and different pores, which are smaller but higher in number with respect to those obtained at short aging times.

XRD analyses were carried out to investigate the phases present in the obtained oxides. All the oxides present the characteristic phase of the desired $Ce_{0.5}Zr_{0.5}O_2$ indicating that the change of aging time does not affect the formation of an equimolar oxide, which is a useful property of the microemulsion synthesis. Sherrer equation was used to calculate the crystallites dimension of the obtained phases, as reported in table 11.

Table 11:Cristallites dimesnion as funcion of aging time

Aging time (h)	Crystallites dimension (nm)
1	8.0
5	9.7
24	10.2

The crystallite dimension increases with increasing aging time from 8 nm, obtained after 1 h, to 10,2 nm, which are found after 24h. Again, the biggest change occurs during the first hours of the synthesis as 9,7 nm crystallites are found after just 5 h. Thus, it is possible to

module the morphology of the oxide by varying the aging time. In particular, bigger particles are got after 24 h of aging, but they possess higher surface area thanks to high pore volume and narrow pores.

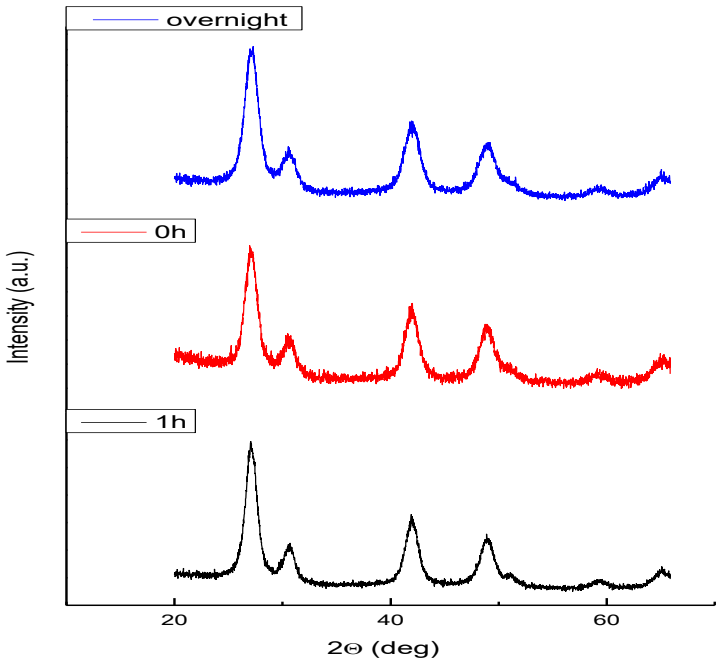

Figure 33:XRD of the samples synthetized at different aging times.

4.3.2. Concentration of the base

In this study the molar concentration of aqueous base solution found inside the micelles was increased from 1.56 M, which is the value of the classical synthesis, to 1.98 M and 2,61 M. In this way a faster precipitation may occur, modifying the properties of the final oxide. Finally, a test with a molar concentration of 1.25M was carried out. Nitrogen physisorption shows that slightly higher surface area is obtained with the classical molarity, namely 1,56. Both increasing or decreasing this value leads to a small drop in this property. At higher concentrations, lower surface area is linked with smaller pores with lower pore volume. However, the values obtained are close, and may fall within the experimental error

Table 12: Nitrogen physisorption analysis of the samples with different TMAH concentrations.

Conc TMAH (M)	S_{BET} (m^2/g)	Pore vol. (cm^3/g)	Pore diam. (nm)
1.25	120		
1.56	127	0.12	4.22
1.98	123	0.14	3.40
2.61	113	0.11	3.60

It is not straightforward to understand how the molarity affects the sample morphology. However, it can be hypothesized that high TMAH concentrations interfere with the formation of small micelles, which are not stable at high pH values[1]. Thus, the microemulsion with high TMAH concentration, presents an environment which is closer to that of a coprecipitation than the one of microemulsion. This is confirmed by DLS analysis that shows the formation of micelles bigger than those compatible with a stable microemulsions at high pH values [116]. This may have worsen the support properties as the microemulsion samples were found to perform better than the co-precipitated samples in a previous study from our group [50].

This is further confirmed by XRD analysis that showed the formation of a Ce-enriched phase at 2.61M, while the desired $Ce_{0.5}Zr_{0.5}O_2$ was obtained at lower TMAH concentrations. In particular, a pattern compatible with $Ce_{0.6}Zr_{0.4}O_2$ phase was observed. This confirms the hypothesis highlighted above, i.e. the environment at high pH is closer to a coprecipitation synthesis than a microemulsion one. In fact, this phase is obtained by coprecipitation as reported previously [54].

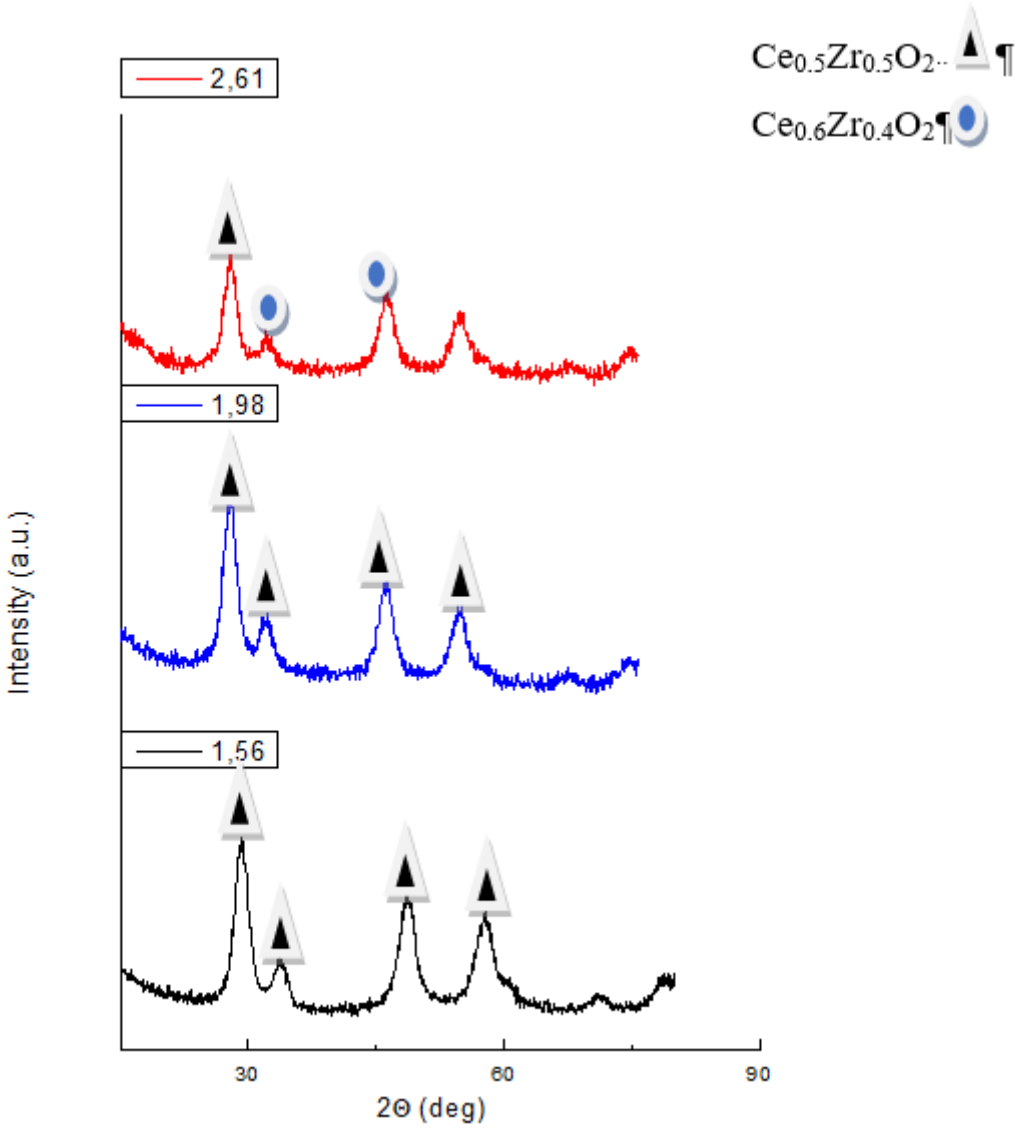

Figure 34:XRD analyses of the supports obtained at different concentration of TMAH

4.3.3. Variation of Rw

Finally, the Rw value of the TMAH microemulsion was modified to module the properties of the microemulsion and the derived oxide. The Rw corresponds to the ratio between water moles and surfactant moles (Triton X-100 in this case). This parameter is important as by increasing it is possible to increase the micelles dimension and viceversa. However, micelles are not formed at too high or too low Rw.

In a previous study the Rw of the TMAH microemulsion between 1 and 14 were investigated, showing that micelles of 10 nm are got between 1 and 5 and that over the

value of 7 the micelle dimension are not compatible with a microemulsion [116]. However, it is worth noting that the classical value employed is 14, and this implies that the TMAH mixture is actually not a proper microemulsion, as it is not thermodynamically stable. However, it was and will be called microemulsion for matters of simplicity. In this study the Rw was further increased to the value of 20, by increasing the amount of water in the aqueous phase containing the TMAH. Thus, also TMAH concentration was modified to smaller values.

Nitrogen physisorption shows a decrease in surface area from 127 m^2/g given by Rw 14 to 116 m^2/g. This is due to the higher dimension of the micelles which can lead to the formation of bigger particles and it is also compatible with the decrease in concentration of TMAH as discussed above. Even in this case, thus, the environment shifts from that of a microemulsion synthesis in which the small micelles work as microreactors and allow to get the desired $Ce_{0.5}Zr_{0.5}O_2$.

4.4. **Conclusions**

The characterization of the CeZr and Zr supports synthetized by microemulsion was treated in this chapter. This synthesis was able to provide oxides with peculiar properties. In fact, the use of micelles as microreactors provided different advantages such as: (i) the obtainment of the desired $Ce_{0,5}Zr_{0,5}O_2$; (ii) the synthesis of a tetragonal ZrO_2; (iii) the production of oxides with mesoporous structure and small and round particle dimension, templated by the micelles of the microemulsion; (iv) the presence of an homogeneous reduction of bulk and surface Ce, in the case of the CeZr oxide.

The synthetic parameters were modified in order to understand their influence on the oxide properties. In particular, particle dimension and surface area can be moulded with aging time. A sharp rise is observed from1 to 5h of aging time while a slighter one is obtained if the mixture is aged for 24 h. Regarding base concentration, 1.56 M was found to be the optimal value. In fact, surface area is lowered if base concentration is both reduced or increased, Moreover, if concentration is too high, conditions similar to classical coprecipitation were obtained that lead to the formation of $Ce_{0,6}Zr_{0,4}O_2$ over the desired $Ce_{0,5}Zr_{0,5}O_2$. This phenomenon was also observed while increasing the Rw value, namely the

amount of water in the micelles. When bigger micelles are created, a $Ce_{0,6}Zr_{0,4}O_2$ due to an environment similar to the coprecipitation synthesis.

5. CHAPTER 5 - HIGH TEMPERATURE OXY-REFORMING

5.1. **Introduction**

The following chapter focuses on the investigation of the performances of the synthesized catalysts in the high temperature oxy-reforming. The aim was to evaluate the activity of different metals (Pt and Rh) in this reaction. For this reason, the CZO support was impregnated with platinum nitrate (Pt-CZO) or Rh nitrate (Rh-CZO). Following calcination, the final catalyst was obtained by reduction at 750°C carried out overnight in the same reactor used for the oxy-reforming tests. These were conducted a 750°C and with a standard O/C ratio of 0,21. The other parameters namely S/C, GHSV and pressure were changed to investigate their effect on the catalytic activity of the investigated catalysts.

5.2. **Pt on CeZr oxide**

5.2.1. Characterization of Pt on CeZr oxide

Pt-CZO catalyst was obtained by incipient wetness impregnation (IWI) of a Pt nitrate aqueous solution on the $Ce_{0.5}Zr_{0.5}O_2$ support as reported in the experimental section. After

drying at 120°C and calcination at 500°C, to decompose the nitrate precursor to the relative oxide, the sample was characterized by means of temperature programmed reduction (TPR), reported in figure 35.

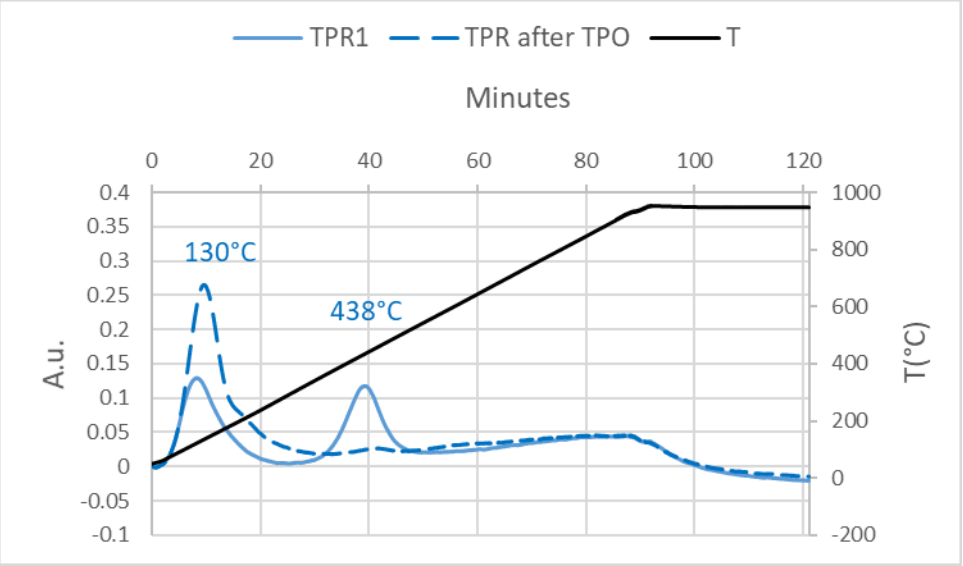

Figure 35: TPR of Pt-CZOm750

Table 13: Hydrogen consumption by TPR for Pt-CZOm750.

	TPR1	***TPR2***
H_2 consumption (mmol/g)	0.31	0.37

The first reduction cycle evidenced the presence of two reduction peaks around 130°C and 438°C. The first can be assigned to the reduction of Pt and surface Ce, which is reduced thanks to the hydrogen spillover effect given by the presence of Pt, able to break the H-H bond. The second one is related to the reduction of bulk Ce, which is more difficult to be reduced. Nevertheless, both surface Ce and bulk one are reduced at lower temperature than that in the case of the bare support shown above, thus confirming the positive effect of metal deposition over Ce-based oxides, as already reported in literature [126]. However, after a temperature programmed oxidation is carried out, the TPR shows only one broad peak which can be assigned to the reduction of Pt as well as surface and bulk Ce, which occur altogether around 130°C. This is also confirmed by the similar total hydrogen uptake in the two TPR cycles, which suggests that both Pt and Ce are reduced together in TPR2. This indicates the presence of a homogeneous reduction given by a good metal-support

interaction and a high hydrogen spillover. These properties are favourable in catalytic reactions such as WGS in which both the metal and the support act as active sites [127].

The Pt-CZO catalyst reduced at 750°C was submitted to TEM analysis. The results demonstrated that the incipient wetness impregnation technique over the CeZr oxide obtained by microemulsion allows to synthesize a catalyst possessing small metal particles with narrow size distribution (figure 36).

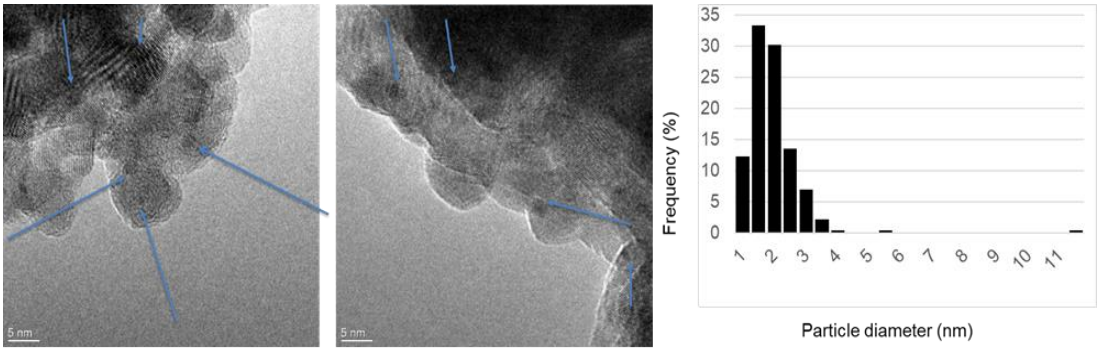

Figure 36: TEM images and particle size distribution of Pt-CZOm750

The Pt particle dimension and size distribution were found to be between 1 and 3 nm with average particle size distribution of 1.95 nm. STEM analysis helped to further distinguish Pt nanoparticles evidencing a large number of them present on the support (figure 37). Moreover, the porous nature of the CZO support was more evident through this analysis.

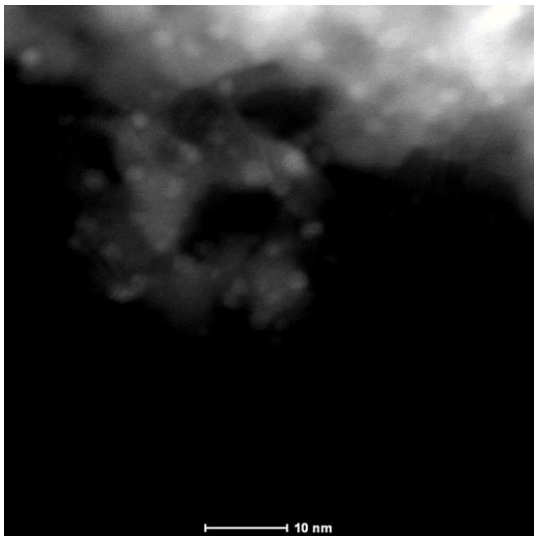

Figure 37: STEM image of Pt-CZOm750.

5.2.2. Catalytic oxy-reforming on Pt on CeZr oxide

Given the successful synthesis of Pt on $Ce_{0.5}Zr_{0.5}O_2$ (Pt-CZOm750), this catalyst was also tested in the OR at 750°C under different conditions. The first test was conducted at 30000 h^{-1}, 1 atm and a S/C of 0.7.

At first, the effect of the Gas Hourly Space Velocity (GHSV) was studied by increasing it from 30000 to 100000 h^{-1} and keeping the other parameters constant, namely oven temperature of 750°C, pressure of 1 atm and a S/C of 0.7 (figure 38). At high contact times, CH_4 shows a conversion of 79%, which differs from the equilibrium by less than 10%. However, decreasing the contact time, methane conversion decreases. In fact, at these conditions the reaction is under kinetic control and Pt is not able to catalyse the reaction to the equilibrium value. CO selectivity decreased from 82% to 62% at high GHSV probably due to the occurrence of fast parasitic reactions such as combustion. This reaction is in fact supposed to be the first step of CPO reaction by some authors [128], followed then by steam and dry reforming which converts methane, the produced steam and carbon dioxide into hydrogen and CO. However, the reaction temperature of the catalytic bed slightly decreased from 737°C, to 732°C and 731°C by increasing the GHSV. Thus, a slightly predominant effect of steam and dry reforming over exothermic reactions seem to occur at lower contact times.

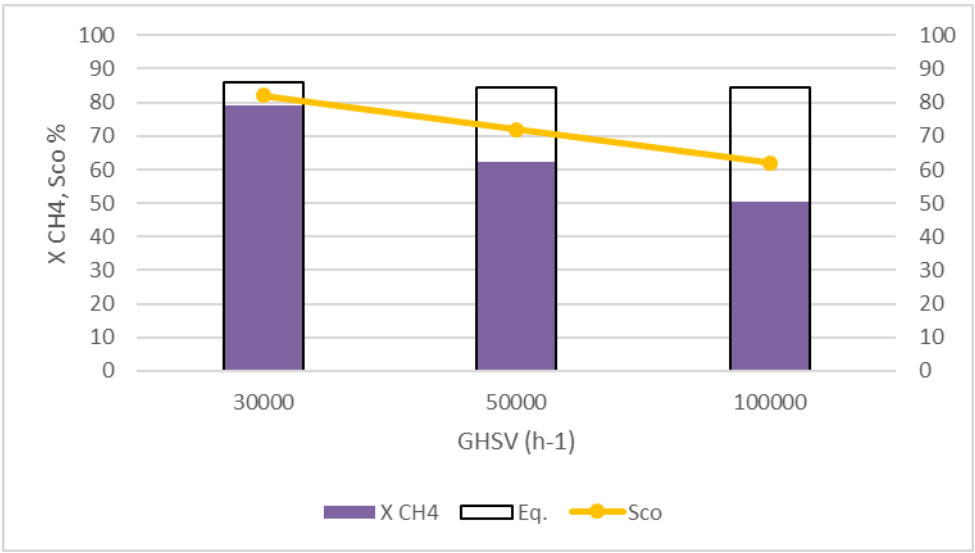

Figure 38: effect of GHSV on the activity of Pt-CZO at 750°C, 1 atm and S/C 0.7

In the following test the S/C was increased from 0.7 to 1 to evaluate if higher conversions can be obtained by increasing the amount of the steam (figure 39). This influenced the

equilibrium value which increased to 92% but did not change the experimental conversion, suggesting that the kinetic of SR is not influenced by the amount of steam, but only by the rate determining step of methane decomposition, as reported in literature [57]. This may indicate that a kinetic regime is present even at high contact times, i.e. at low GHSV, and shows the advantage of the selected conditions which allow for a performance comparison of different catalysts, as the equilibrium is reached only by catalysts with high activity.

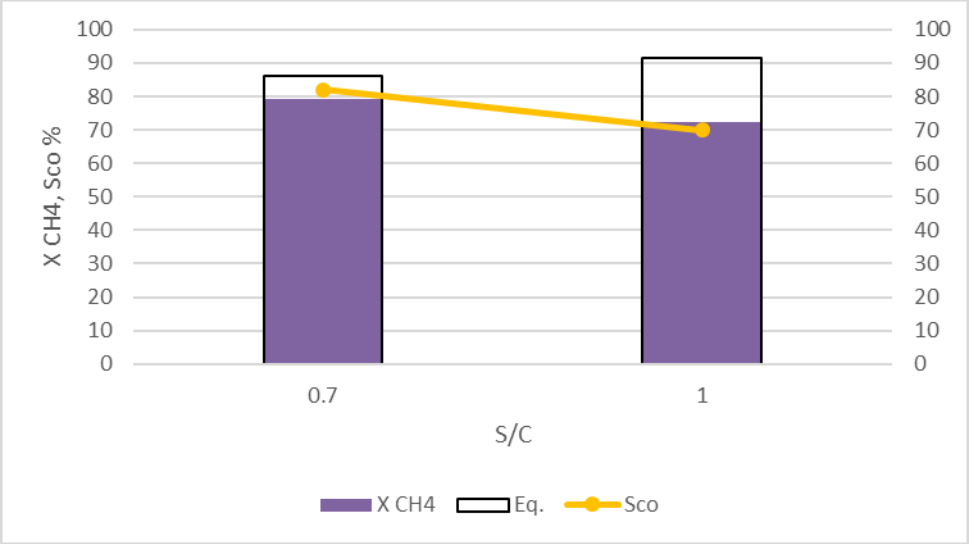

Figure 39: effect of S/C on the activity of Pt-CZO at 750°C, 1 atm and 30000 $^{h-1}$.

An increase in pressure provided a decrease in methane conversion due to a lower value of equilibrium conversion, as reported in figure 40. In fact, the latter lowers to 74% at 3 atm and 65% at 5 atm. However, the experimental conversion is closer to the equilibrium value in these cases, with the values of 67% at 3 atm and 63% at 5 atm, as the kinetics of the reforming are increased by higher methane partial pressure. CO selectivity decreases at higher pressures probably due to the occurrence of parasite reaction such as Boudourad reaction which is positively influenced by pressure.

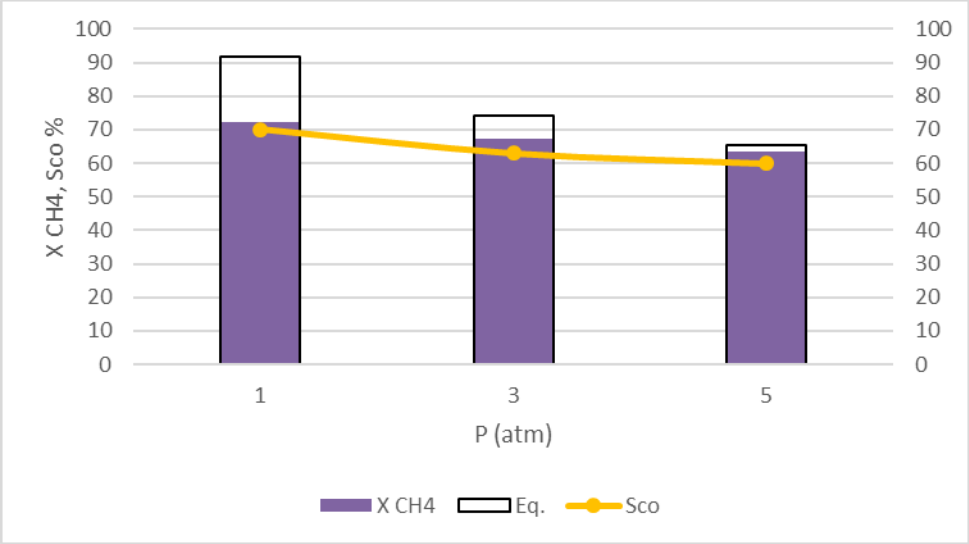

Figure 40: effect of P on the activity of Pt-CZO at 750°C, S/C 1 and 30000 h^{-1}

Finally, a deeper study on the influence of S/C was carried out at 5 atm and a GHSV of 100000 h^{-1} and is reported in figure 41. Again, the thermodynamic equilibrium is influenced by the presence of steam and equilibrium methane conversion increases with S/C. However, no significant increase in the experimental methane conversion is observed as the kinetic of SR is not related to steam partial pressure. The slight decrease observed can be related to the dilution effect of steam over methane partial pressure at high S/C. CO selectivity, on the opposite, is influenced by steam to carbon ratio and a decrease in this value is observed with increasing the latter. This is due to a higher occurrence of the WGS reaction which is influenced by steam presence.

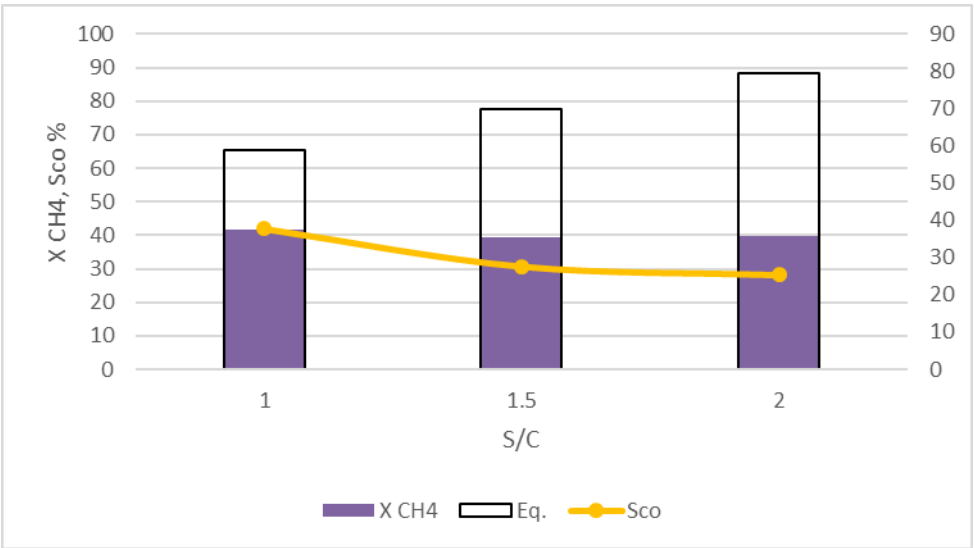

Figure 41: effect of S/C on the activity of Pt-CZO at 750°C, 5 atm and 100000 h^{-1}

5.3. **Comparison between Pt and Rh on CeZr oxide**

5.3.1. Characterization of Rh on CeZr oxide

Pt-CZO activity was compared with that of Rh on $Ce_{0.5}Zr_{0.5}O_2$ (Rh-CZOm750), which was the best performing catalyst in the oxy-reforming up to now [120].This was synthetized by impregnation and calcination of Rh nitrate by incipient wetness impregnation.

The H_2-TPR profiles of Rh2.7IWI-CZOm750 are shown in figure 42. The first reduction ramp highlights the presence of two peaks, centred at 115°C and 230°C, while no peak at temperatures higher than 600°C is found, which could be indicative of bare Ce reduction. In fact, Ce is reduced by hydrogen spillover from Rh to the support and thus the first reduction peak is lowered to 115°C for Rh and surface Ce and 230°C for bulk Ce. Noteworthy, the spillover effect is more intense on Rh than on Pt, as the second peak was found at higher temperature in that case, namely at 438°C. The second reduction ramp, carried out after a TPO shows the presence of a sole peak, evidencing a more homogenous reduction and interaction between Rh and Ce. This is also confirmed by the hydrogen consumption, which is also four times higher than in TPR1 (table 14), suggesting a higher reduction of the Ce contained in the support. However, in this case, Pt also showed only one peak but at lower temperature (130°C) indicating a higher reducibility after a TPR-TPO cycle compared to Rh.

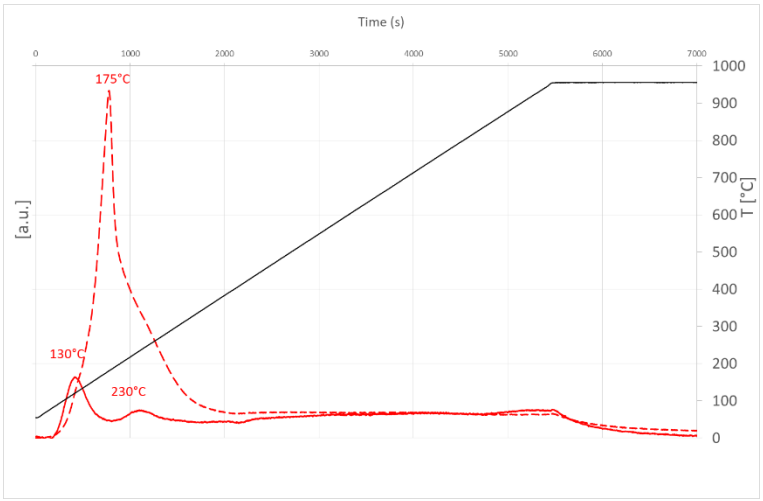

Figure 42: TPROR of Rh2.7-CZOm750

Table 14: Hydrogen consumption by TPR for Rh2.7-CZO.

	TPR1	***TPR2***
H_2 consumption (mmol/g)	0.22	0.86

The catalyst was also investigated by TEM analysis after reduction at 750°C. A TEM image and the particle size distribution are reported in figure 43. Small and well-distributed particles are obtained with a narrow particle size distribution mainly centred between 1 and 2 nm.

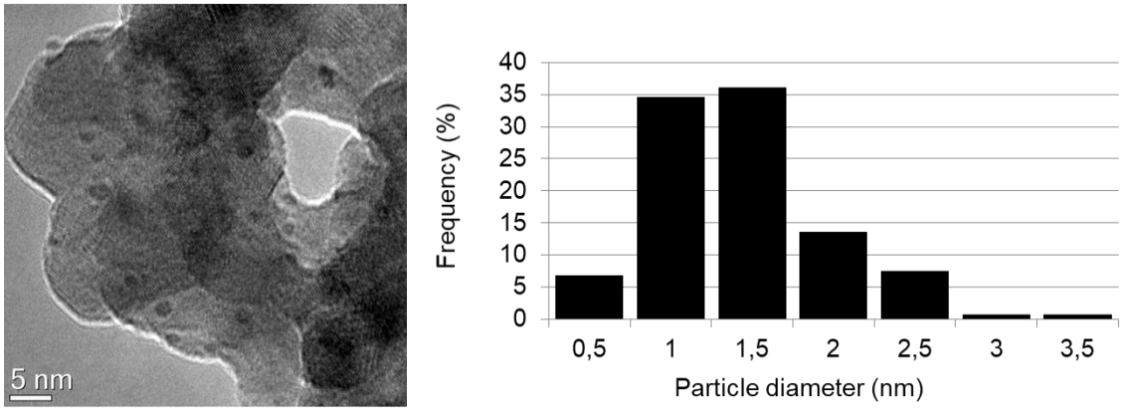

Figure 43: TEM analysis on Rh2.7-CZOm750

5.3.2. Catalytic oxy-reforming on Rh on CeZr oxide

The performance of Pt based catalysts was compared with that of Rh based at 750°C, S/C 0.7, 1 atm and different values of GHSV. Rh-CZOm750 provided higher methane conversion due to its higher activity in both SR and CPO reactions (figure 44). The conversions as shown by both catalyst systems almost equalized at high GHSV, but Rh still outperformed Pt in terms of hydrogen production, indicating selectivity toward SR and CPO compared to Pt. The difference between the two catalysts in terms of hydrogen production increases with increasing GHSV, showing a faster kinetics for hydrogen production for the Rh catalyst. The difference in performances between the two catalysts can be ascribed to the higher activity and selectivity of Rh toward steam reforming [81] and CPO [137] with respect to Pt, as also reported in literature [81,137]. A further insight was provided by a computational study on methane dissociations and syngas production over different metals [138]. Here the authors calculated the total dissociation energy for the CH4 decomposition

to C and 4H on Ir, Pt, Os, Rh, Ru and Pt. This process was found to b exothermic for Rh, slightly endothermic on Ir and Ru and rather endothermic on the other metals. This indicates that methane decomposition is thermodynamically favoured on Rh, which showed to lowest total dissociation energy. The trend for dissociation energies followed the order: Rh<Ru<Ir<Os = Pt<Pd. However, the presence of oxygen can modify the dissociation energy needed for methane decomposition. In fact, surface oxygen promotes methan dehydrogenation by hydroxyl formation following the mechanism [138]:

$$CH_{x;s} + O_s \rightarrow CH_{x-1;s} + OH_s \,. \qquad (x = 4; 3; 2; 1)$$

Again this process was more favoured on Rh rather than on Pt.

The general increase in hydrogen production with GHSV is due to the increased flux that counts in the hydrogen production equation. Finally, Rh shows higher hydrogen selectivity than Pt. This was shown by the hydrogen production obtained at low contact time, where methane conversion was similar for the two catalyst. This can be computationally explained by the difference ability of the two metals to perform the following reaction [138]:

$$H_s + O_s \rightarrow OH_s$$

This reaction was calculated to be endothermic, thus disfavoured on Rh, while exothermic on Pt. This disfavours H_2 production on Pt, lowering hydrogen selectivity.

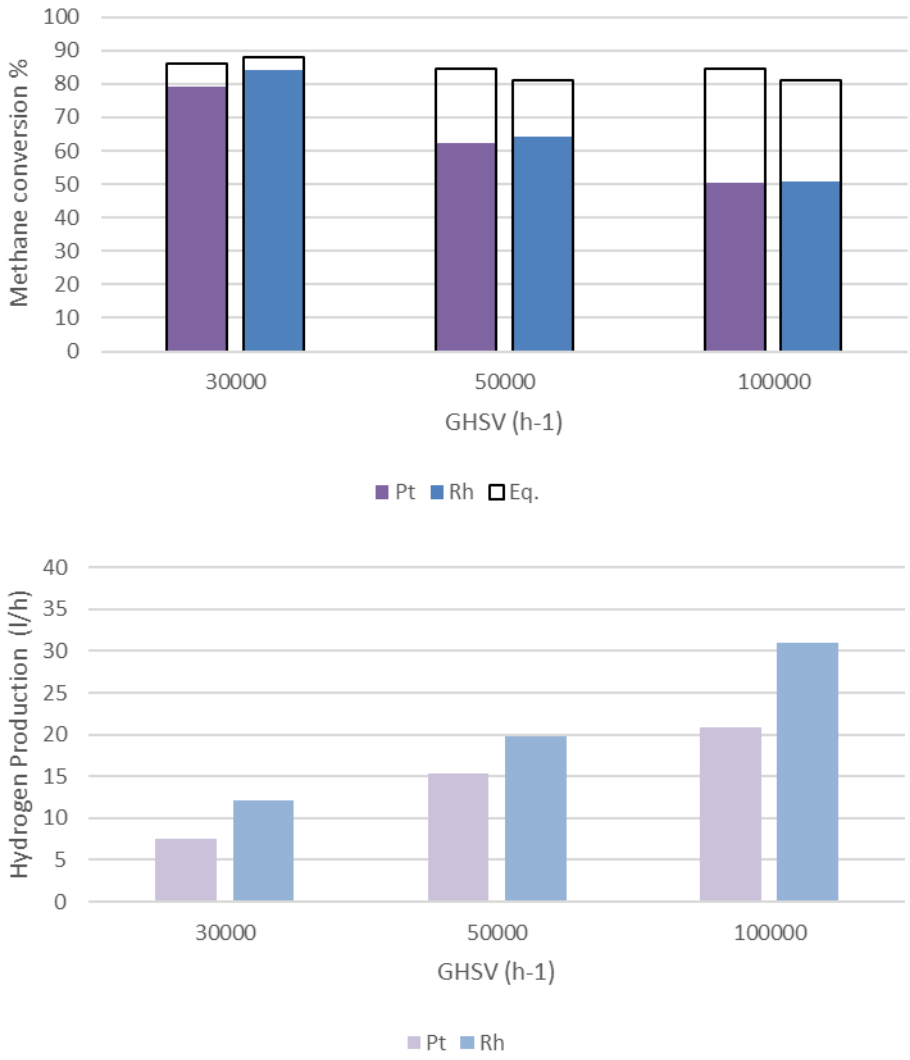

Figure 44: Methane conversion and hydrogen production over Pt and Rh on CZO at 750°C, 1 atm S/C 1 and different GHSV.

Moreover, Rh showed an increased stability under the reaction conditions chosen for these tests. This was assessed by periodically performing tests at the same conditions as that of the first test, carried out on the fresh catalyst (i.e. 750°C, 30000 h^{-1}, 1 atm and S/C 0.7), and comparing the resulting conversions (figure 45). These tests were called return tests. A slight drop in methane conversion is observed by the Rh based catalyst which showed a conversion of more than 80% after the third return test. On the opposite, Pt conversion dropped from 79% to 60% from the first to the third return test. This may be due to sintering or to carbon deposition. The latter was in fact, evidenced by Raman spectroscopy on the spent catalyst by two bands at 1350 and 1550 cm^{-1}. These are called D and G bands and are indicative of amorphous and ordered carbon. Thus, a weaker synergy between Pt and the

CZO support is observed compared to Rh, which does not allow removing the formed carbon and leads to deactivation.

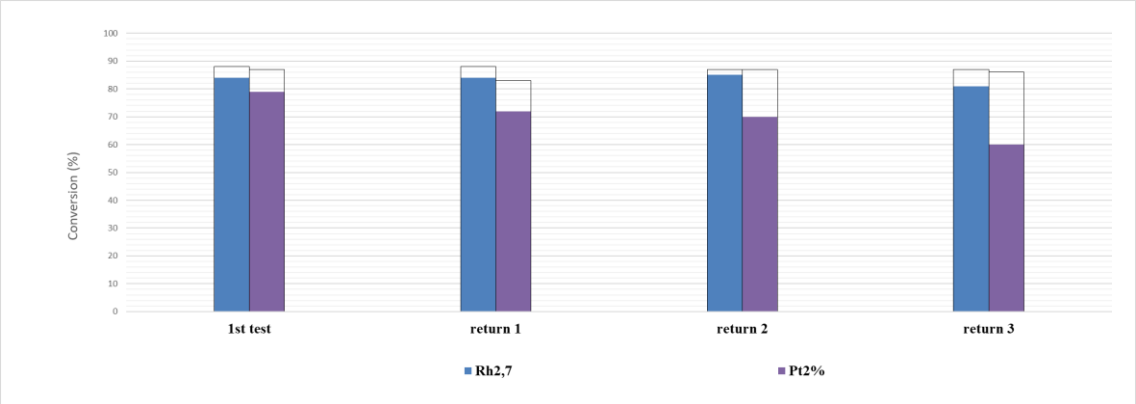

Figure 45: deactivation tests on Pt and Rh over CZO carried out at 750°C, 30000 h^{-1}, 1 atm and S/C 0.7.

5.4. **Conclusions**

Pt and Rh based catalysts supported on CZO were tested in the oxy-reforming reaction at 750°C (Toven) under different operative conditions. The occurrence of the endothermic steam refoming lowered the reactor temperature to 737°C and 740°C for Pt and Rh respectively. However, these values were close to the oven temperature, thanks to the co-occurrence of CPO, which produced the heat needed for SR, reducing the temperature gap. In general, the steam to carbon ratio seemed to slightly influence the experimental conversion, suggesting that methane decomposition over the active phase is the limiting step in these conditions. An increase in GHSV provided a decrease in methane conversion due to the lower contact time between the reagents and the catalyst. Higher pressures gave lower equilibrium and experimental conversions as suggested by thermodynamics. However, the experimental and equilibrium values were closer at these conditions.

Finally, Rh-CZO outperformed Pt-CZO due to a higher selectivity toward reforming and catalytic partial oxidation. Moreover, it was more stable, given an improved synergy between the metal and the support, which allowed the removal of deposited carbon.

Thus, Rh was selected as reference catalyst for the high temperature oxy-reforming and it was employed in this process to produce a reformate stream that was then submitted to the water gas shift reaction under different conditions. The study of the water gas shift process will be the focus of the next chapter.

6. CHAPTER 6 - WATER GAS SHIFT ACTIVITY OF Pt, Rh AND Pt-Rh BIMETALLIC ACTIVE PHASES OVER CeZr OXIDE

6.1. Introduction

The water gas shift reaction is usually carried out on the outlet stream of a steam reformer to increase the hydrogen content and decrease the CO one. This process can also be applied to the oxy reforming outlet stream. In particular, Rh-CZO was employed in the oxy-reforming reactor that was object of the previous chapter and the produced stream was submitted to another reactor to carry out the water gas shift. This chapter highlights the results obtained in this combined process over different catalysts.

Other than Pt-CZO, two more catalysts containing a mixture of Pt and Rh were synthesized with the aim of providing an active catalyst for both WGS and reforming reactions by combining the properties of Pt and Rh. These catalysts were obtained by impregnating the CZO support with a solution containing the solved precursors of both Pt and Rh in two different ratios, namely Pt/Rh molar ratio of 0.7 and 2.1.

Finally, the Rh-CZO catalyst was also tested to investigate the WGS activity of its active phase. For this purpose, a WGS reactor was filled with different catalysts, namely Pt, Rh and to two Pt-Rh bimetallic catalysts.

6.2. **Pt on CeZr oxide**

6.2.1. Water gas shift activity of Pt on CeZr oxide

Pt-CZO was studied at first in the water gas shift reaction. The water gas shift tests were carried out at 400°C and 3 or 5 atm pressure for different S/C and GHSV. It is important to note that the S/C is fixed before the oxy-reforming reactor and thus the steam that is fed to the WGS reactor is what is not consumed in the reforming reactor.

In particular, the effect of S/C was studied at various conditions and showed significantly different results based on the contact time and the pressure employed. Figure 46 shows the effect of S/C at low GHSV (30000 h^{-1}) and pressure (3 atm) and at high GHSV (100000 h^{-1}) and pressure (5 atm).

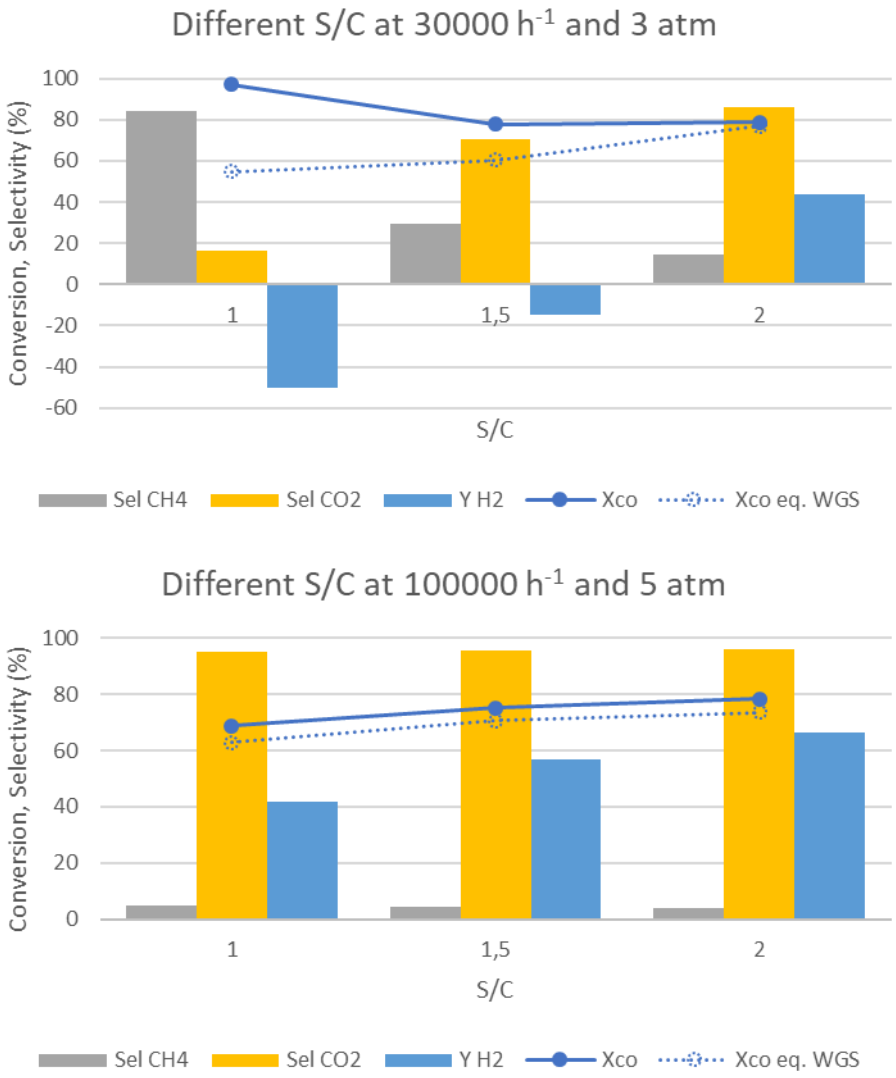

Figure 46: effect of S/C on CO conversion, methane and carbon dioxide selectivity and hydrogen production on Pt-CZO. Equilibrium CO conversion calculated on WGS reaction only.

Figure 47 reports equilibrium and experimental CO conversion, methane and carbon dioxide selectivities and hydrogen yield obtained by varying the S/C at 3 and 5 atm. It must be noted that the equilibrium conversion is not calculated with the CEA NASA software in this case, which takes in account all the possible reactions, but it only considers the occurrence of WGS. Thus, undesired CO-consuming reaction as methanation are not taken in account. Nevertheless, this reaction occurs in the investigated conditions, as evidenced by methane selectivity and literature [139]. Thus, the experimental conversion can be found higher than the equilibrium one due to the contribution of methanation. Equilibrium conversion calculated with CEA NASA is not reported but approached 100% in all

investigated conditions. At low values of S/C, pressure and GHSV, a high CO conversion is obtained which decreases with increasing S/C at constant GHSV and pressure. This is not consistent with the only occurrence of the water gas shift reaction. In fact, this reaction should be favoured when the steam amount is increased, as for the equilibrium conversion. Steam is indeed a reagent for the water gas shift reaction. It is thus unexpected to see a conversion fall at higher S/C. Moreover, the equilibrium conversion for the WGS is lower than the experimental one, suggesting that another reaction is also consuming CO. A better understanding of the process can be obtained by looking at the values of methane and carbon dioxide selectivities and hydrogen yield. In fact, at low S/C, a negative hydrogen yield is obtained with high methane and low CO_2 selectivity. This can be explained by the occurrence of methanation instead of WGS. Thus, if high contact times are used with low S/C the reverse steam reforming reaction is favoured at relatively high temperature of 400°C. Methanation can be inhibited by increasing the S/C ratio, as steam is both a reagent of WGS and a product of methanation. This is confirmed by the increase of CO_2 selectivity observed at high S/C. The observed decrease in CO conversion is not due to a decreased occurrence of WGS but to the inhibition of methanation. At higher GHSV and pressure, methanation occurs to a lower extent and the effect of steam on the WGS reaction is more evident, with an increase in hydrogen production and CO conversion. It thus seems that methanation is disfavoured at low contact times. In fact, by increasing the GHSV at high S/C, low methane selectivity is observed with an increasing CO conversion and hydrogen production (figure 47).

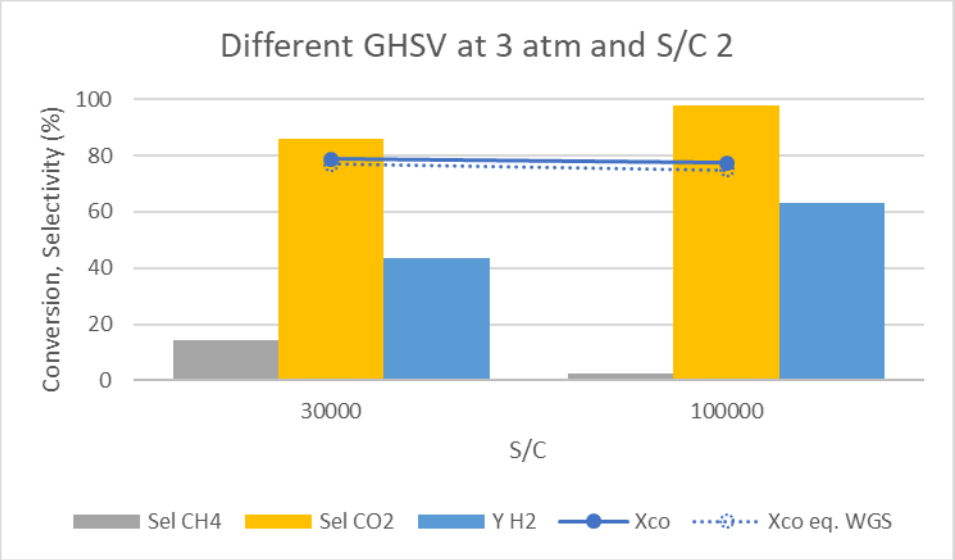

Figure 47: effect of S/C on CO conversion, methane and carbon dioxide selectivity and hydrogen production on Pt-CZO. Equilibrium CO conversion calculated on WGS reaction only.

This suggests that methanation reaction occurs subsequently to WGS on Pt-CZO, as it is not detected at low contact times, but it is observed at higher ones. In fact, in the latter case, the CO adsorbed over Pt is consumed first to give carbon dioxide, thus leaving Pt free to decompose hydrogen and perform CO_2 methanation, thanks to the carbon dioxide adsorption on support sites. When S/C is increased, the support active sites are saturated by steam and thus are not available for the methanation reaction. It is thus hypothesized that the methanation reaction occurs on carbon dioxide instead directly on CO. CO equilibrium conversion is similar at different contact times as this parameter does not influence the thermodynamics of the reaction.

The methanation occurrence at high contact times (30000 h^{-1}) is further confirmed by analysing the effect of total pressure on the system (figure 48).

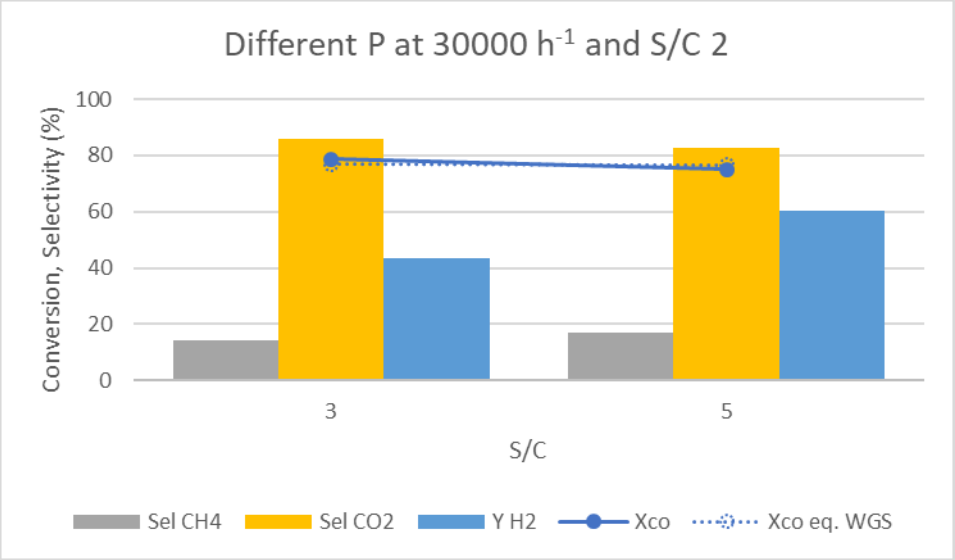

Figure 48: effect of P on CO conversion, methane and carbon dioxide selectivity and hydrogen production on Pt-CZO at 30000 h^{-1} and S/C 2. Equilibrium CO conversion calculated on WGS reaction only. In this case, a S/C of 2 was selected in order to favour the WGS activity. However, a slight increase in methane selectivity is observed. In fact, this reaction produces a decrease in the moles number between reagents and products and is thus favoured at higher pressures. However, hydrogen yield is also increased because of the improved kinetic of the catalyst given by the increase of partial pressures of the reagents.

This trend is also confirmed at lower contact times, hence higher GHSV (100000 h^{-1}), as reported in figure 49.

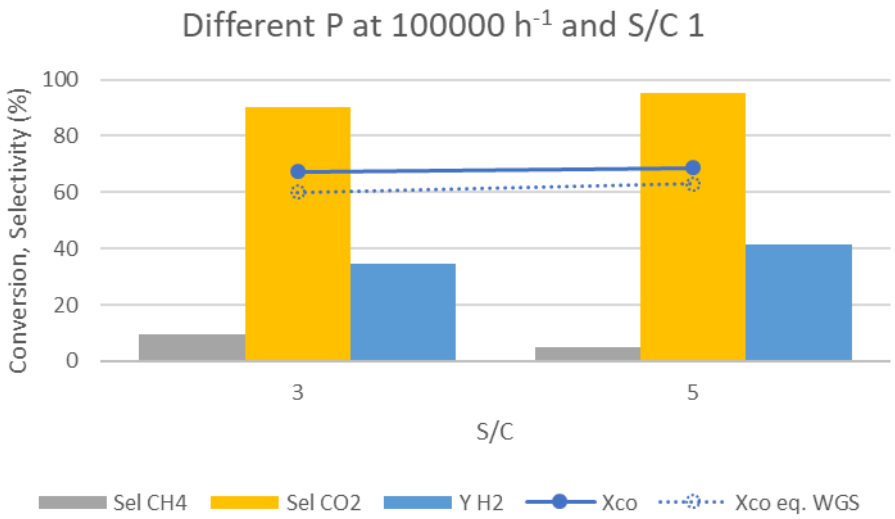

Figure 49: effect of pressure on CO conversion, methane and carbon dioxide selectivity and hydrogen production on Pt-CZO at 100000 h^{-1} and S/C 2. Equilibrium CO conversion calculated on WGS reaction only.

Methanation is just slightly decreased by changing pressure from 3 to 5 atm as the high GHSV disfavoured this consecutive reaction. Moreover, higher hydrogen yields than the tests at lower GHSV are obtained for the same reason. As WGS is not influenced by pressure, the experimental and CO conversions are similar for the two conditions.

Given the good results obtained with Pt-CZO this catalyst was used as a reference to compare the Pt-Rh and Rh catalysts.

6.3. **Bimetallic Pt-Rh on CeZr oxide catalysts**

6.3.1. Characterization of bimetallic Pt-Rh catalysts

The CZO support synthesized by microemulsion was used to prepare the Rh and Pt-Rh catalysts. It was impregnated with Rh nitrate (Rh-CZO) or two mixtures of Pt and Rh nitrate in different ratio, namely 0.7 (mol/mol) (PtRh0.7-CZO) and 2.1 (mol/mol) (PtRh2.1-CZO). These catalyst precursors were characterized by means of TPR and TEM analyses (figure 50, and 51).

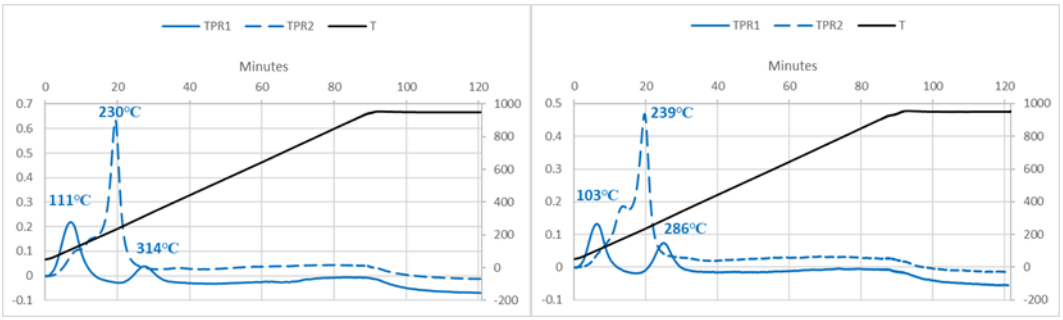

Figure 50:TPROR of PtRh2.1 (left) and PtRh 0.7 (right).

Table 15: Hydrogen consumption by TPR for PtRh2.1-CZOm750 and PtRh0.7-CZOm750.

H_2 consumption (mmol/g)	***TPR1***	***TPR2***
PtRh2.1-CZOm750	0.31	0.62
PtRh0.7-CZOm750	0,22	0.54

The TPR results were similar for the two samples: both of them showed the presence of two reduction peaks in the first TPR cycle. The first peak was found at low temperature (103°C and 111°C) and the second one at 286°C and 314°C for PtRh0.7 and PtRh2.1 respectively. These were analogous to those obtained for monometallic Pt and Rh samples and were supposed to be related to metal and surface Ce reduction and Ce bulk reduction. The peaks of the first TPR cycle were found at lower temperature than Rh1 and Pt, indicating a synergic effect for the mixed catalysts. Moreover, the two reduction peaks are closer for the bimetallic catalysts in the second TPR cycle (with the first peak which is delayed and the second one anticipated). This may indicate a more homogeneous reduction of Pt, Rh and Ce and the formation of bimetallic nanoparticles. These particles seem also to increase the spillover effect, hence the amount of reducible Ce as evidenced by a higher hydrogen consumption in the second TPR cycle (table 15)

These were confirmed by TEM-EDS analysis carried out on PtRh2.1 in which well dispersed and small nanoparticles were observed over the CeZr support (figure 51). Moreover, EDS analysis evidenced the presence both Pt and Rh in the nanoparticles, suggesting the formation of a bimetallic active phase.

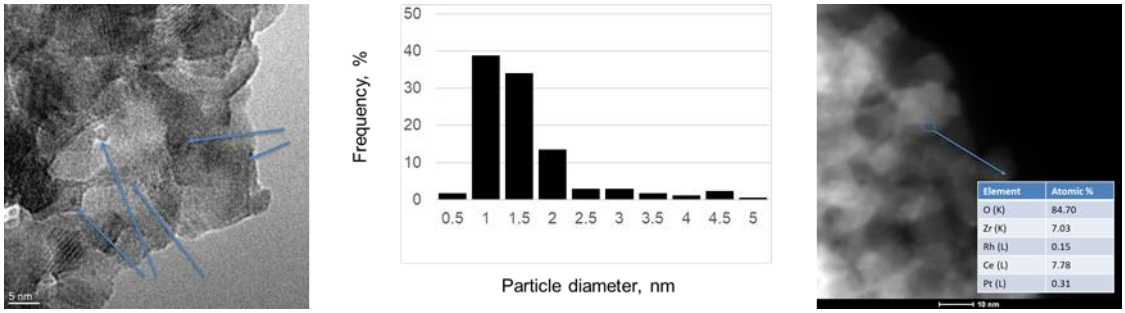

Figure 51: TEM image and particl size distribution of PtRh2.1.

6.3.2. Water gas shift activity of Rh and bimetallic Pt-Rh catalysts and comparison with Pt-CZO

The synthesized catalyst (Rh and PtRh mixtures over CZO) were also tested in the water gas shift reaction. This was carried out in a reactor placed downstream another tubular reactor in which the oxy-reforming reaction was performed over Rh2.7-CZO.

The obtained results were expressed as CO conversion, methane, carbon dioxide selectivity and hydrogen yield, and compared with those obtained on the monometallic Pt-CZO catalyst. The effect of S/C on the catalytic activity of these catalysts is reported in figure 52.

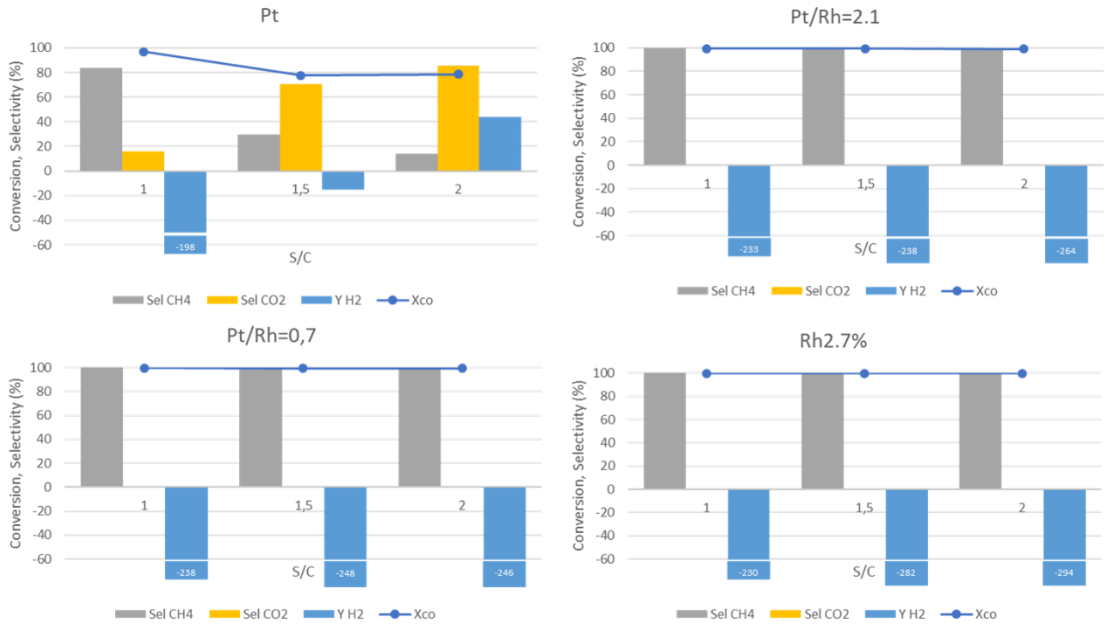

Figure 52: Effect of S/C at 30000 h^{-1} and 3 atm on different M-CZO catalyst (M=Pt, Rh or Pt-Rh active phases).

The Rh containing catalyst reached an almost total CO conversion which was higher than that of Pt. However, by looking at methane selectivity and hydrogen yield it is evident that

this is due to the unwanted methanation reaction and not to the desired WGS. In particular, hydrogen yield resulted in a negative value which indicated that the hydrogen that was obtained by oxy-reforming was consumed instead of being enriched. Although this is observed even for the Pt catalyst at low S/C, hydrogen production can be obtained for this catalyst by saturating the supports active sites with a higher amount of steam. This phenomenon is not observed for the Rh containing catalyst and, on the opposite, an increase in the hydrogen consumption is observed. This suggests that even for the Rh containing catalyst, the consecutive carbon dioxide methanation is responsible for methane production and hydrogen consumption, rather than simple CO methanation. In fact, at higher S/C, the WGS is favoured, producing an increased amount of CO_2, which then consumes an increased amount of hydrogen. Methanation reaction is in fact catalysed by Rh based catalyst [140] and the highest hydrogen consumption was obtained by the monometallic Rh catalyst.

In order to further understand the WGS-methanation process, tests at different GHSV were carried out at constant S/C (2) and pressure (3 atm) (figure 53).

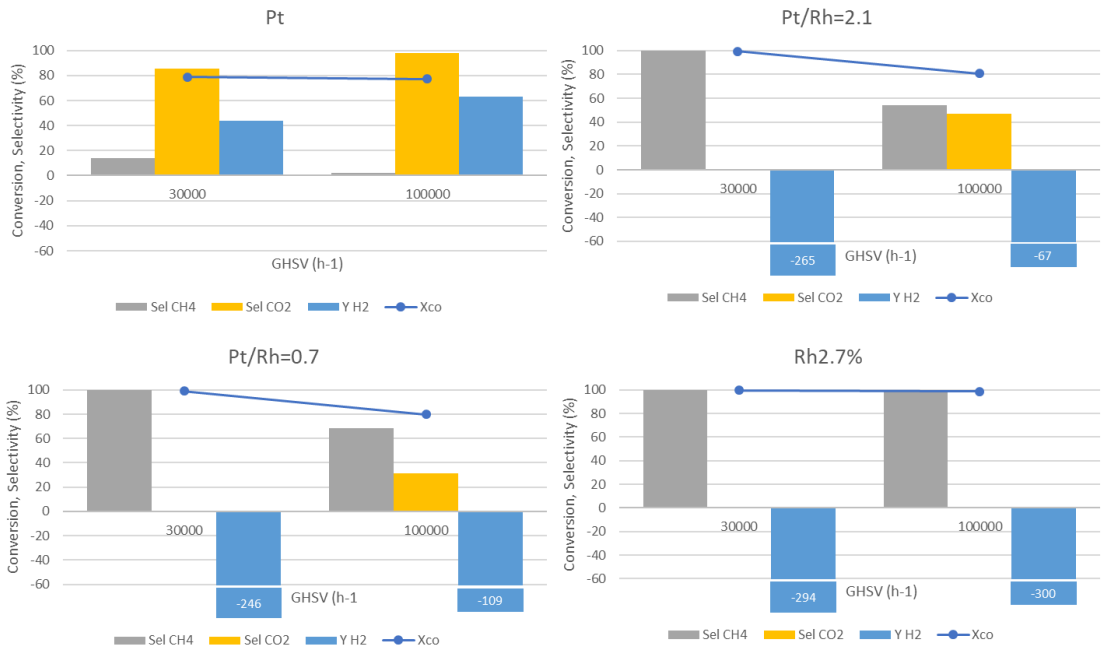

Figure 53: Effect of GHSV at S/C 2 and 3 atm on different M-CZO catalyst (M=Pt, Rh or Pt-Rh active phases).

In these conditions, Pt was able to provide hydrogen production and good selectivity toward carbon dioxide. Both these parameters were increased by decreasing the contact time, at the expenses of methane selectivity. An analogous trend was observed for the Pt-

Rh catalysts, where hydrogen consumption and methane selectivity decreased at 100000 h^{-1} in favour of carbon dioxide production by WGS. In particular, the increased WGS selectivity was consistent with the Pt content of the sample. This also resulted in a lower CO conversion as most of this value is increased by the occurrence of methanation. In the case of Rh-CZO, only slight variation of the results were observed, suggesting a very fast kinetics for the methanation reaction for this catalyst.

Finally, the influence of pressure was analysed at high GHSV (100000 h^{-1}) (figure 54). Given the low WGS activity of Rh-CZO, only Pt and Pt-Rh catalysts were studied in these conditions.

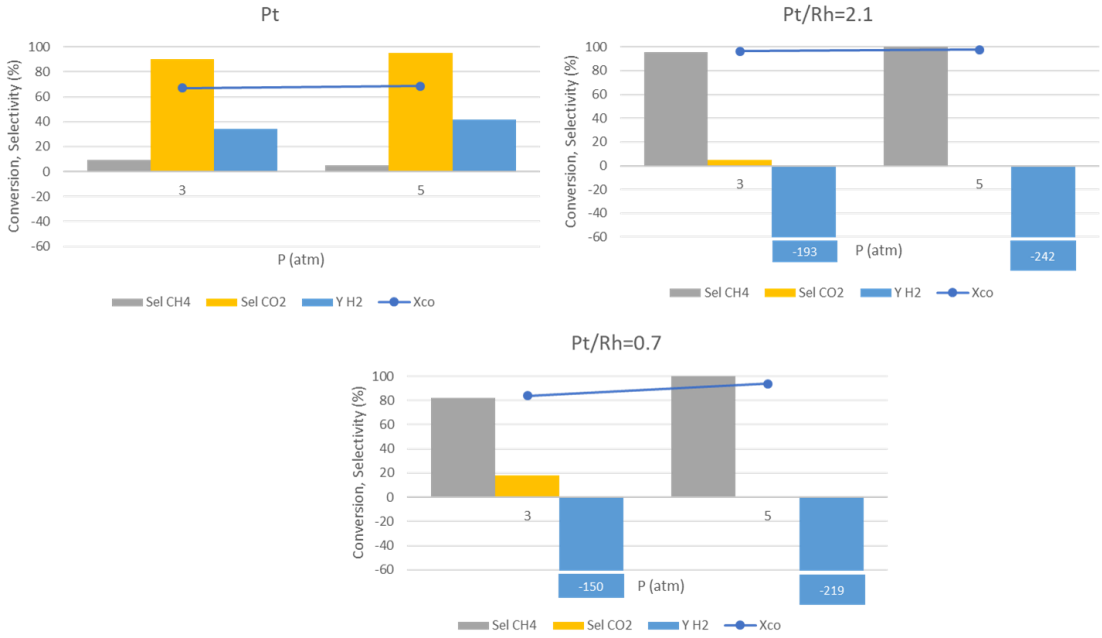

Figure 54: Effect of pressure at 100000 h^{-1} and S/C 1 on different M-CZO catalyst (M=Pt or Pt-Rh active phases).

In the case of monometallic Pt, a slight decrease in methanation is observed in favour of the WGS reaction, suggesting a faster kinetics of the latter at 5 atm. This resulted in a higher hydrogen yield. This is not the case for the Rh-containing catalysts. In fact, a higher methanation activity is observed together with a higher hydrogen and CO consumption. This is probably related to the high kinetics of Rh in the methanation reaction and Pt in the WGS one. In fact, CO conversion to CO_2 by Pt is faster at 5 atm, as also confirmed by the results of the monometallic catalyst. However, the presence of Rh, quickly converts carbon monoxide to methane, consuming hydrogen. Thus, form the results of these tests it is suggested that the WGS is the rate determining step of the process and carbon dioxide is

readily converted to methane once it is formed. Moreover, it is suggested that the production of methane is easier to perform over CO_2 rather than CO, and thus a mechanism which not involves CO desorption during methanation reaction is suggested [129].

The reported results indicate that Rh-containing catalysts are not suitable to perform the WGS reaction to increase the hydrogen yield. However, they showed high methanation activity even at high GHSV and could be thus useful for applications in which high amounts of CO and CO2 have to be transformed into methane such as the case of methane production from biogas [130].

Moreover, as methanation is the inverse reaction of steam reforming, the Rh containing catalyst should be able to provide high reforming activity as also suggested by the results obtained in the high temperature oxy-reforming. For this reason, they were also tested, together with Pt, in the low temperature oxy-reforming.

6.4. **Conclusions**

The water gas shift reaction was carried out on reformate outlet using different catalysts. Pt-CZO gave the best results. In particular, high S/C at the reforming inlet were needed to favour the water gas shift reaction over methanation. In fact, hydrogen was consumed to give methane over the Pt catalyst at S/C 1. Moreover, increasing the contact time favoured methanation over water gas shift. This suggested that water gas shift is the fastest reaction and that methanation occurs on the CO_2 produced by it, without a CO desorption step in this reaction.

7. CHAPTER 7 - LOW TEMPERATURE OXY-REFORMING

7.1. Introduction

Steam reforming and catalytic partial oxidation are usually carried out at high temperature to favour the thermodynamic of the processes and boost catalytic activity and methane conversion. Thus, also the oxy-reforming process was carried out at 750°C as reported in a previous chapter. However, this temperature would not be suitable for its employment in a Pd based membrane reactor, as the membrane is not stable at temperature higher than 600°C. For this reason, the operative temperature of the process was lowered to 500°C. Having assessed the high activity of Pt in the WGS reaction, its performances were studied in this process, with the aim of developing an optimal catalyst for the membrane reactor. In this way both reforming and WGS may be performed at low temperature in the same reactor.

7.2. Pt on CeZr oxide activity in low temperature oxy-reforming

The effect of the operative parameters on the catalytic performances was evaluated by varying the S/C, GHSV and pressure. However, before the tests were performed at 500°C, a preliminary test at 450°C was carried out in order to understand if the catalyst was able to catalyse these reactions even at lower temperatures (figure 55). These would imply mild conditions, a decreased thermal stress on the catalyst and eventually a minor thermal stress on the membrane. Methane conversion decreases at lower temperature, due to a less favoured thermodynamic equilibrium as highlighted by the lower equilibrium methane conversion. The high CO_2 selectivity at 450°C (reported in tabl 6), which is almost 100% indicates the occurrence of WGS. This reaction is likely to happen as it is favoured at this temperature and as Pt is known to be an active WGS catalyst. However, the occurrence of combustion may also have contributed to the production of CO_2 and cannot be completely excluded. The same consideration applies to the test at 500°C., even though both experimental and equilibrium methane conversions are higher due to enhanced thermodynamics and kinetics at higher temperature. From the CO_2 selectivity (99%) and H_2/CO ratio (20), it can be seen that the WGS happens readily, as soon as some CO is produced, thanks to the good activity of Pt in the WGS at these conditions.

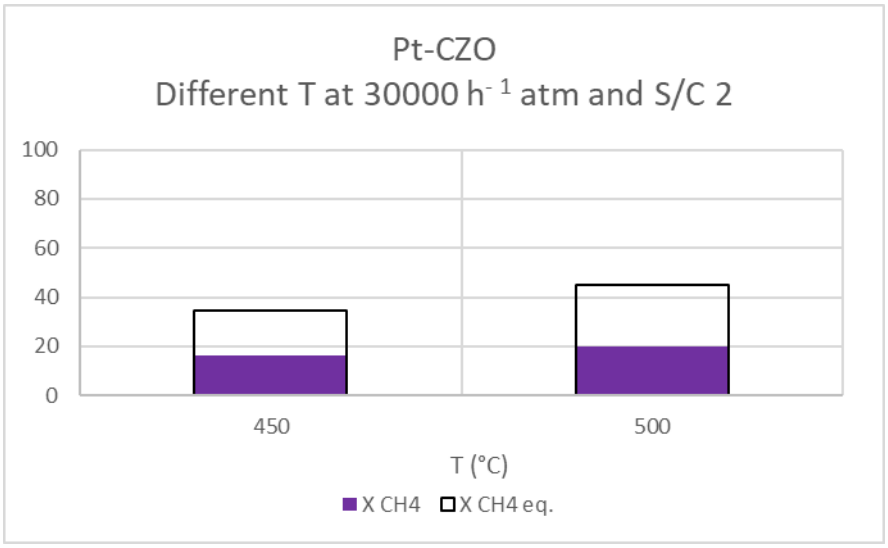

Figure 55: Effect of oven temperature on methane conversion, carbon dioxide selectivity and hydrogen yield on Pt-CZO.

Table 16:Summary of the results of tests at 450 °C - 30000 h^{-1} - 1 atm - 0.21 O_2/C - 2 S/C and 500 °C - 30000 h^{-1} - 1 atm - 0.21 O_2/C - 2 S/C.

T	X CH4 (eq) [%]	H_2 dry out (eq.) [%]	S_{CO2} [%]	C-balance [%]	H_2 pressure [atm]	T_{min} [°C]	T_{max} [°C]
450	16 (34)	13 (48)	99	88	0.04	450	457
500	20 (45)	22 (57)	98	93	0.08	500	504

Different S/C over the Pt catalyst were also studied in order to assess how an excess of water influences the OR and carbon formation as reported in figure 56.

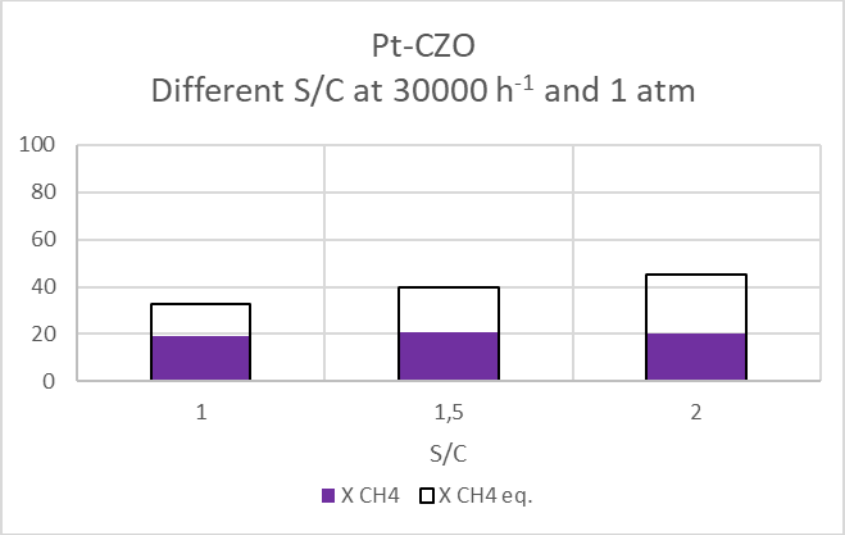

Figure 56: Effect of S/C on methane conversion, carbon dioxide selectivity and hydrogen yield on Pt-CZO.

Table 17:Summary of the results of tests with a S/C ratios of 2; 1.5 and 1 performed under the conditions 500 °C - 30000 h^{-1} - 1 atm - 0.21 O_2/C.

S/C	X CH4 (eq) [%]	H_2 dry out (eq.) [%]	S_{CO2} [%]	C-balance [%]	H_2 pressure [atm]	T_{min} [°C]	T_{max} [°C]
1	19 (33)	20 (48)	96	88	0.10	497	500
1.5	21 (40)	22 (53)	97	89	0.09	500	505
2	20 (45)	22 (56)	98	93	0.08	500	504

Both methane conversion and carbon balance only slightly decrease while lowering the S/C. However, it must be noted at S/C 1, carbon deposition is favoured, as shown by a carbon balance lowered by 6 points by shifting from S/C 2 to 1. Thus, these conditions seem to be not favourable, as catalyst deactivation can occur. In general, the catalyst is not able to reach the equilibrium at these conditions which suggests that the reaction is under kinetic

control at these conditions and it is driven by methane decomposition as rate determining step, which is related to methane partial pressure and is independent of steam concentration. Working with a lower amount of water would be favourable as this would allow not diluting the reagents, not diluting hydrogen in the membrane reactor operation and decrease the cost of steam. However, carbon formation on tis catalyst limits the employment of these conditions.

Different GHSV were also tested in order to analyse the kinetic behaviour of Pt at low temperature (figure 57). Increasing the GHSV at 500°C does not affect conversion of methane and the results obtained are quite similar for all the three GHSV tested. This indicates that Pt is working at its kinetical maximum at this temperature even at high GHSV. This can be useful as more hydrogen can be produced per unit of time.

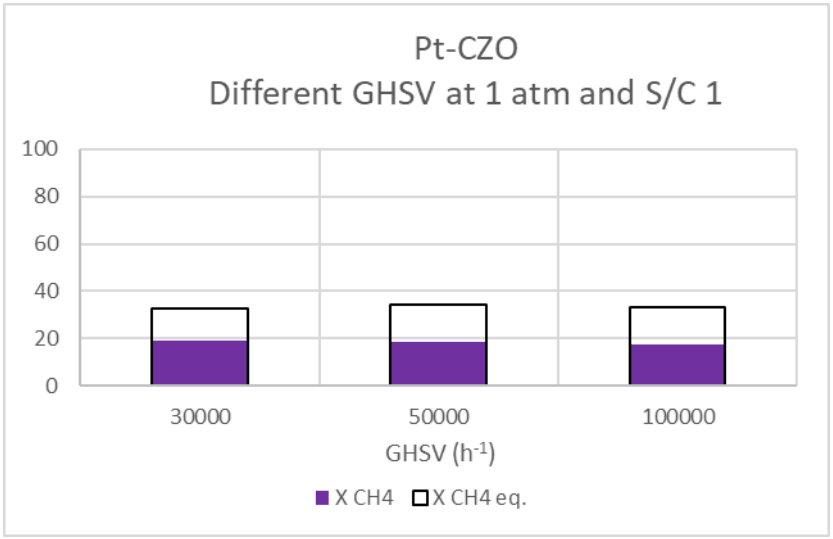

Figure 57: Effect of GHSV on methane conversion, carbon dioxide selectivity and hydrogen yield on Pt-CZO.

Table 18:Summary of the results of tests with a space velocity of 30000 h^{-1}, 50000 h^{-1} and 100000 h^{-1} under the reaction conditions 500 °C - 1 atm - 0.21 O_2/C – 1 S/C.

GHSV (h^{-1})	X CH4 (eq) [%]	H_2 dry out (eq.) [%]	S_{CO2} [%]	C-balance [%]	H_2 pressure [atm]	T_{min} [°C]	T_{max} [°C]
30000	19 (33)	20 (48)	96	88	0.10	497	500
50000	18 (34)	18 (50)	96	87	0.09	500	510
100000	18 (33)	15 (49)	97	86	0.07	500	502

Finally, the effect of pressure on Pt activity was evaluated and reported in figure 58. Increasing pressure to 3 or 5 atm provides only a slight decrease in methane conversion, while the equilibrium conversion decreases, and is thus closer to the experimental one, as both CPO and SR are disfavoured at high pressures. This is positive as higher pressures are suitable for efficient membrane reaction operations. Low CO selectivity at all pressures was observed thanks to the occurrence of WGS which is not affected by pressure.

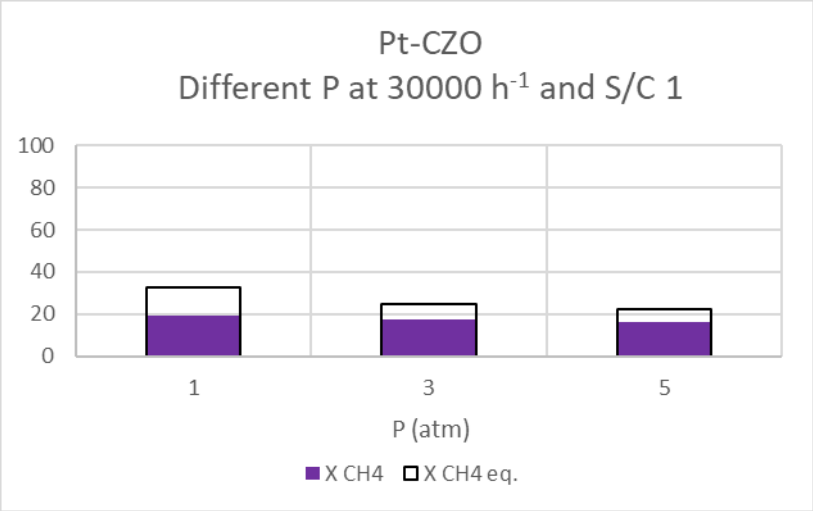

Figure 58: Effect of pressure on methane conversion, carbon dioxide selectivity and hydrogen yield on Pt-CZO.

Table 19: Summary of the results of tests a pressure of 1 atm, 3 atm and 5 atm under the conditions 500 °C - 30000 h^{-1} - 0.21 O_2/C – 1 S/C.

P (atm)	X CH4 (eq) [%]	H_2 dry out (eq.) [%]	S_{CO2} [%]	C-balance [%]	H_2 pressure [atm]	T_{min} [°C]	T_{max} [°C]
1	19 (33)	20 (48)	96	88	0.10	497	500
3	17 (24)	16 (35)	97	87	0.24	497	500
5	16 (22)	13 (30)	98	87	0.32	496	500

The contribution of SR to the OR process over the Pt catalyst was studied by removing oxygen from the reagents and performing a test feeding methane and steam (figure 59). However, it must be noted that removing CPO, even its exothermic contribution is eliminated, which helped the endothermic SR to occur.

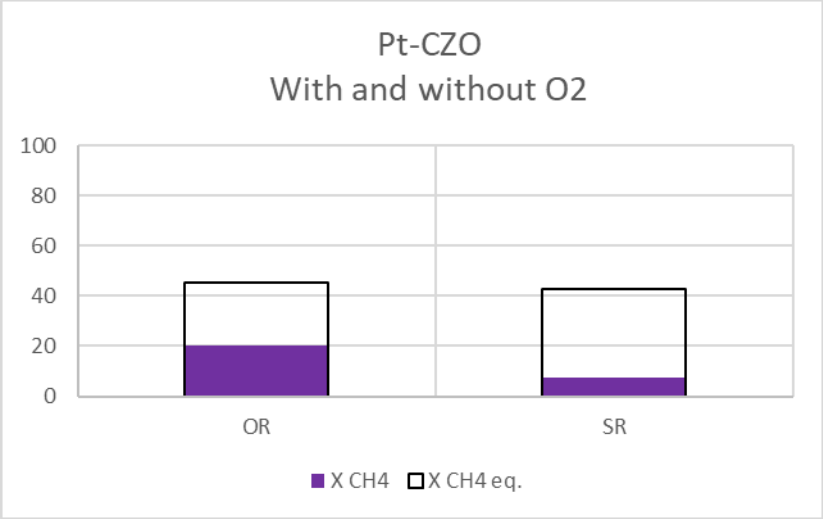

Figure 59: Comparison between oxy-reforming (OR) and steam reforming (SR) on Pt-CZO.

Table 20:Summary of the test performed without O_2 under the conditions 500 °C - 30000 h^{-1} - 1 atm - 0 O_2/C – 3 S/C.

	X CH4 (eq) [%]	H_2 dry out (eq.) [%]	S_{CO2} [%]	C-balance [%]	H_2 pressure [atm]	T_{min} [°C]	T_{max} [°C]
SR	8 (43)	20 (62)	98	91	0.06	496	500

Comparing the test carried out at the same conditions with and without oxygen, it was found that SR occurs, but it is able to convert only 8% of the methane, while a conversion of 19% was given by the oxy-reforming, evidencing that CPO and combustion contributes to more than half of the total conversion. However, CO_2 selectivity shows that Pt is active in the WGS. Though, SR seems to be the limiting step of the process and thus small amounts of Rh will be substituted to part of the Pt in next studies to increase the steam reforming activity.

7.3. **Comparison between Pt and Rh in low temperature oxy-reforming**

Rh-CZO was also tested in the low temperature oxy-reforming and compared with Pt to understand if the difference in activity observed at 750°C is kept even at lower temperatures (figure 60 and table 21). In fact, Rh-CZO was found to be the best performing catalyst in a previous study from our group [120]. At these conditions, however, the methane conversion of the two catalysts was different than at higher temperature, with Rh

providing much higher values than Pt, thanks to its higher activity at low temperature. In particular, this catalyst is able to reach the equilibrium conversion at almost all conditions that were tested. Furthermore, different conversions were obtained at different S/C with Rh always outperforming Pt, reaching the equilibrium value. The Rh catalyst provided conversions close to the equilibrium also at high GHSV, showing a high activity even in discriminant conditions at this relatively low temperature. Finally, the equilibrium was reached by increasing pressure, thanks to the more favoured thermodynamics and kinetics. In general, from these tests, it was clear how Rh at 500°C is a much better oxy-reforming catalyst than Pt, and for this reason it is working under thermodynamic conditions, providing methane conversions close to the equilibrium values. This can be explained by the different activity and selectivity of the two active phases, already discussed in chapter 5.

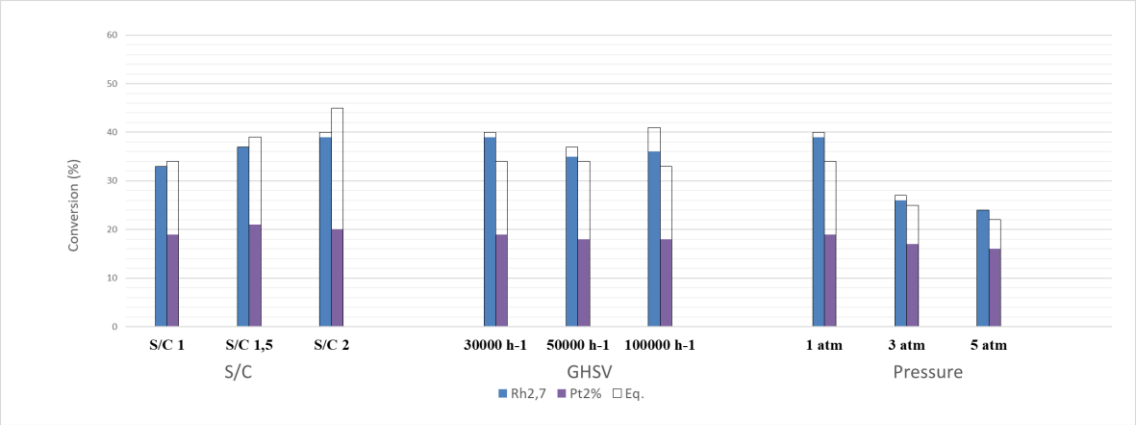

Figure 60: Methane conversion obtained in low temperature oxy-reforming in different conditions at 500°C, over Rh2.7-CZO and Pt-CZO.

Table 21: results of the test carried out on Rh2.7-CZO at 500°C under different conditions.

	X CH4 (eq) [%]	**H_2 dry out (eq.) [%]**	**S_{CO2} [%]**	**C-balance [%]**	**H_2 pressure [atm]**	**T_{min} [°C]**	**T_{max} [°C]**
S/C							
1	33 (33)	39 (47)	86	95	0.26	495	503
1.5	37 (37)	44 (51)	90	96	0.25	488	505
2	39 (40)	46 (53)	91	98	0.23	481	504
GHSV							
30000h^{-1}	33 (33)	39 (47)	86	95	0.26	495	503
50000h^{-1}	35 (38)	41 (53)	86	87	0.25	500	526
100000h^{-1}	36 (41)	41 (56)	80	95	0.25	500	540
P							
1	33 (33)	39 (47)	86	95	0.26	495	503
3	26 (27)	32 (39)	93	89	0.59	500	517
5	24 (24)	29 (34)	94	89	0.92	495	518

However, it must be noted that Rh was loaded on the CZO support in a higher amount than Pt. In particular, a 2.7% weight of Rh per weight of support was employed, while 2% of Pt was deposited. Moreover, Rh molecular weight (102,9) is much lower than Pt one (195,1 g/mol), thus more moles are deposited in the case of Rh even at same weight loading. For this reason and to reduce the cost of the synthesis, a catalyst with a lower Rh amount was produced in order to have comparable loading in terms of moles (i.e. of 0.01% moles of metal/grams of support) between the Rh and Pt catalysts. This catalyst will be called Rh1-CZO, as the Rh weight over weight of support was close to 1%.

A comparison between the conversion of Pt and Rh is shown in figure 61.

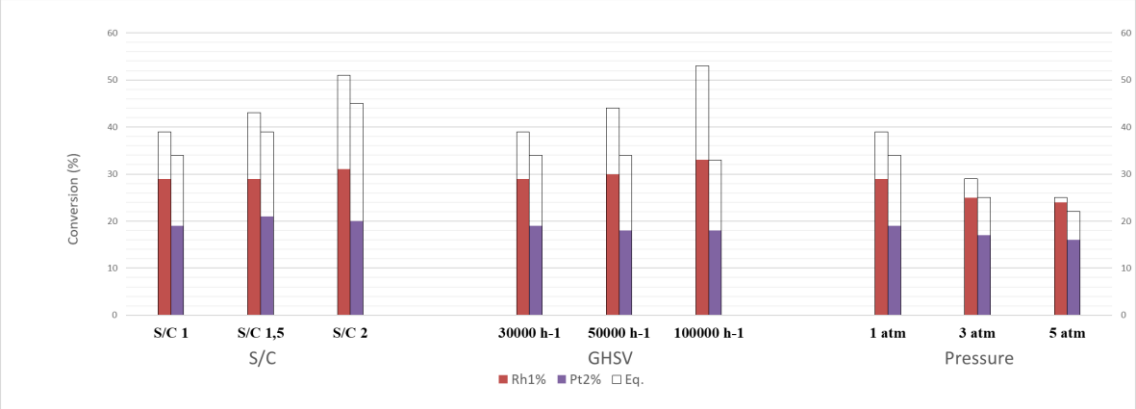

Figure 61: Methane conversion obtained in low temperature oxy-reforming in different conditions at 500°C, over Rh1-CZO and Pt-CZO.

The catalytic activity of Rh-CZO shows that it still outperforms Pt-CZO at all conditions even at lower metal loading. However, as expected, lower conversions are obtained compared to Rh2.7%-CZO, due to a lower Rh amount in this sample.

The H_2/CO ratio produced by the two catalysts was analysed to understand the effect of the water gas shift reaction and is reported in table 22.

Table 22: H_2/CO ratio of Pt and Rh catalysts under different conditions.

	S/C			GHSV (h^{-1})			P (atm)		
	1	1.5	2	30000	50000	100000	1	3	5
Rh1%-CZO	16	24	30	16	16	12	16	23	24
Pt-CZO	35	45	58	35	31	35	35	47	56
Rh2,7%-CZO	14	22	27	14	14	10	14	25	29
Equilibrium	16	21	27	16	13	11	16	17	20

The hydrogen to carbon monoxide ratio is influenced by the S/C ratio as the water gas shift reaction is favoured by the presence of steam, which is a reagent of this reaction. On the opposite, it is almost not influenced by the contact time, showing that this reaction is not kinetically limited. Finally, an increase of pressure increases the hydrogen to CO ratio. This may be attributed to a lower CO production by oxy-reforming, which is more influenced by pressure than WGS. However, Pt provided much higher H_2/CO ratios at all tested conditions, indicating its high activity in the WGS reaction but lower activity toward reforming. In fact, the values obtained for Pt are found to be higher than the equilibrium

one calculated by CEA-NASA: The software in fact considers an equilibrium among all the reaction involved. The high selectivity in WGS displayed by Pt produces a decrease in CO and an increase in hydrogen which raises the H_2/CO ratio over the value predicted by the software.

Nevertheless, a different trend in the equilibrium conversions is observed for Rh1%-CZO compared to Rh2.7%-CZO and Pt-CZO, which makes a direct comparison difficult. In fact, the equilibrium conversion trend is opposite than in the case of Rh2.7%-CZO, which is lowered by increasing the S/C. This is caused by a different average catalytic bed temperature for the two Rh samples (table 23 and figure 62).

Table 23: Catalytic bed temperature on Rh1 and Rh2.7-CZO under different S/C, 30000 h^{-1}, 1 atm and Toven 500°C.

	S/C 1	**S/C 1.5**	**S/C 2**
Rh1%-CZO	528°C	527°C	526°C
Rh2.7%-CZO	501°C	490°C	483°C

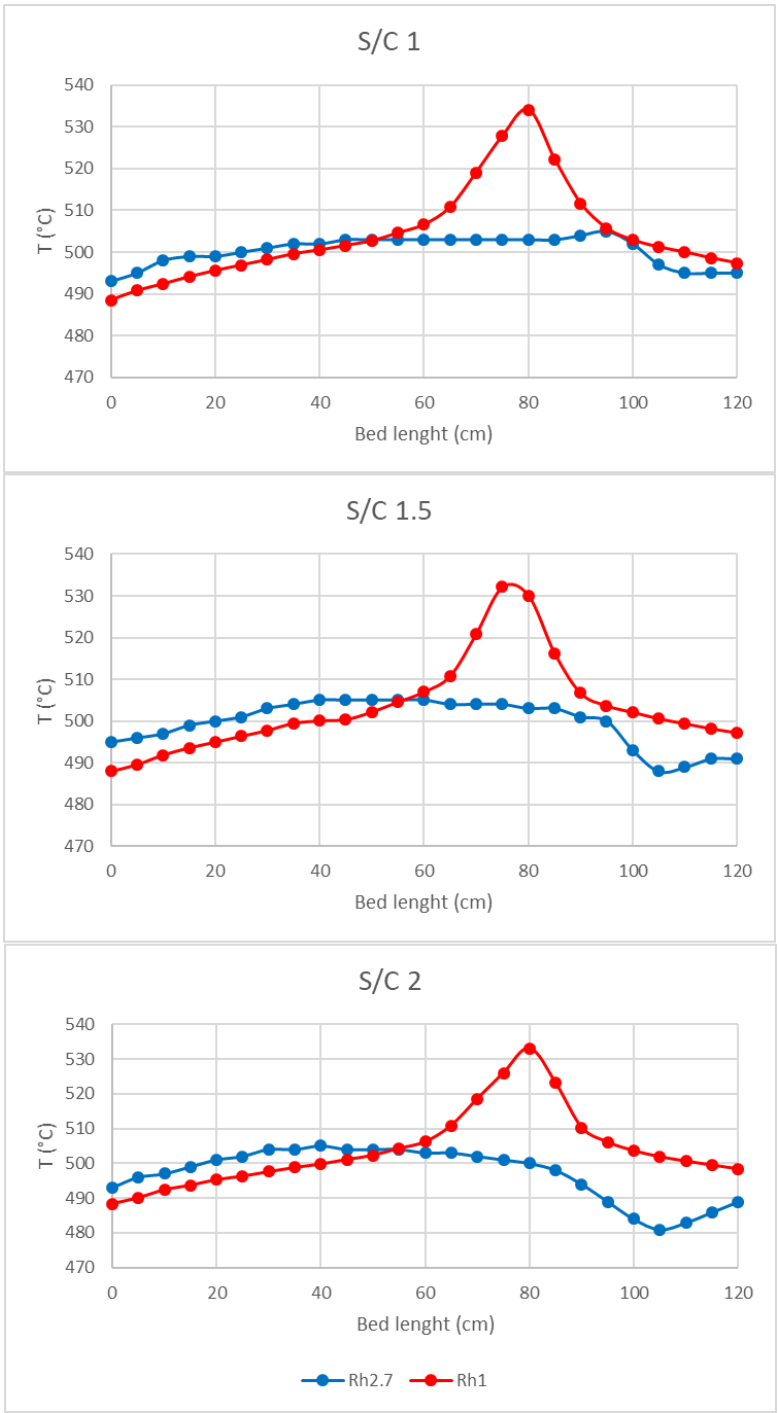

Figure 62: Temperature profile of the catalytic bed on Rh1 and Rh2.7-CZO under different S/C, 30000 h-1, 1 atm and Toven 500°C.

In fact, the catalyst with higher metal loading shows an endothermic peak in the temperature profile of the reactor, indicative of the occurrence of the SR reaction (figure 62). On the opposite, Rh1%-CZO is characterized by an exothermic peak which could be related to the consumption of oxygen in exothermic reactions such as CPO (figure 62). It

can be thus supposed that the latter reaction is predominant when fewer Rh metal atoms are present on the catalytic surface, while it is followed by SR at higher Rh loadings, which uses the heat produced by CPO, thus decreasing the temperature of the catalytic bed. Though, an interesting finding of these tests may be the possibility to perform both SR and CPO at low temperature, without the development of high endothermic or exothermic peaks, when intermediate metal loadings are used. This can be useful to provide a more energy efficient process and to help catalysts comparison. In fact, the most active catalysts provide sharper endo or exothermic profiles compared to the least active ones in in classical CPO or SR at low temperature. This modifies the thermodynamic equilibrium, making catalyst comparison difficult.

Given the different behaviour of Rh1% compared to Rh2.7%, a deeper analysis of the activity of Rh1-CZO under different conditions will be treated in the next chapter.

7.4. **Rh1%CZO**

7.4.1. Characterization of Rh1%CZO

The Rh1%CZO catalyst was characterized after the impregnation of the active phase by means of TPR and TEM analysis. Figure 63 shows the results of the temperature programmed reduction.

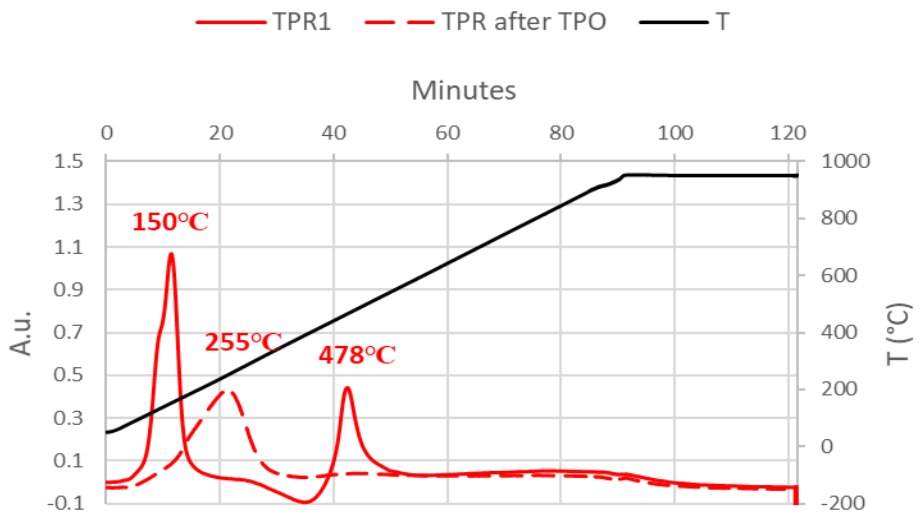

Figure 63: TPROR of Rh1-CZO catalyst.

Table 24: Hydrogen consumption by TPR for Rh1-CZO.

	TPR1	***TPR2***
H_2 consumption (mmol/g)	0.89	0.68

The first reduction cycle of the monometallic Rh catalyst shows two peaks at 150°C and 478°C, which can be related to the reduction of Rh and surface Ce and bulk Ce respectively. These are found at higher temperatures than the Rh2.7-CZO catalyst (115° and 230°C) (figure 42). This is due to the lower amount of active phase which slightly shifts the reduction peaks. The larger shift observed in the second peak highlights that bulk Ce is available for reduction by spillover at low temperature only if high amount of metal is employed. In fact, lower hydrogen consumption was evidenced in the TPR2, differently to what was observed for Rh.27-CZO (table 24)

At first, the influence of S/C on Rh activity was studied (figure 64 and table 25)

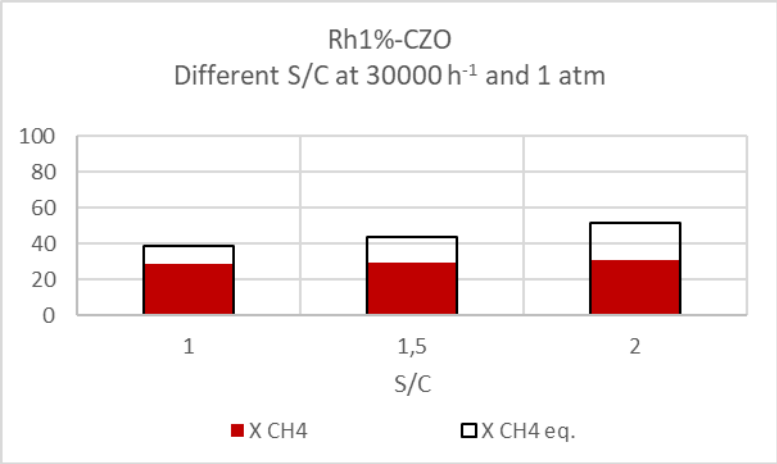

Figure 64: Effect of S/C on methane conversion, carbon dioxide selectivity and hydrogen yield on Rh1-CZO.

Table 25: Summary of the results of tests with a S/C ratios of 2, 1.5 and 1 performed under the conditions 500 °C - 30000 h^{-1} - 1 atm - 0.21 O_2/C.

S/C	**X CH4 (eq) [%]**	**H_2 dry out (eq.) [%]**	**S_{CO2} [%]**	**C-balance [%]**	**H_2 pressure [atm]**	**T_{min} [°C]**	**T_{max} [°C]**
1	30 (52)	36 (56)	92	90	0.20	534	500
1.5	30 (52)	36 (56)	92	91	0.18	532	500
2	31 (51)	38 (60)	93	90	0.17	533	500

Differently from Rh2.7%, Rh1% is not able to reach the equilibrium at 1 atm, even when the S/C is increased, because of the lower Rh amount in the sample. Both methane conversion and carbon balances are constant while lowering the S/C. However, a bigger distance between experimental and the equilibrium methane conversion is observed at S/C 2. This is due to the increase in the equilibrium conversion provided by the effect of steam amount, which is a reagent of the SR, on the thermodynamic equilibrium.

Another operative condition that highly influences the catalytic bed temperature is the contact time. Thus, the results of the tests conducted at different GHSV are reported in figure 65.

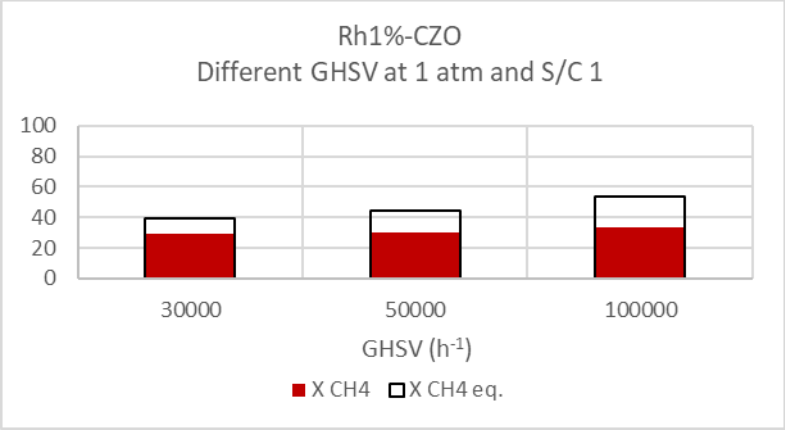

Figure 65: Effect of GHSV on methane conversion, carbon dioxide selectivity and hydrogen yield on Rh1-CZO.

Table 26: Summary of the results of tests with a space velocity of 30000 h^{-1}, 50000 h^{-1} and 100000 h^{-1} under the reaction conditions 500 °C - 1 atm - 0.21 O_2/C – 1 S/C.

GHSV (h^{-1})	X CH4 (eq) [%]		H_2 dry out (eq.) [%]	S_{CO2}[%]	C-balance [%]	H_2 pressure [atm]	T_{min} [°C]	T_{max} [°C]
30000	30 (52)	36 (56)	36 (56)	92	90	0.20	534	500
50000	30 (44)	36 (57)	38 (58)	88	95	0.22	560	500
100000	33 (53)	39 (61)	38 (62)	84	95	0.24	594	510

At these conditions, the temperature increase for the Rh1%-CZO catalyst is even more pronounced by increasing the GHSV, as the CPO reaction is faster than SR and thus favoured over it at lower contact times. This provides a slight increase in methane conversion regardless the discriminant conditions. The equilibrium conversion increased with decreasing contact time as the average catalytic bed temperature (which is used to calculate the equilibrium conversion) raised.

Increasing the pressure, methane conversion decreased due to the effect of the thermodynamic equilibrium, but it was able to reach it at 5 atm. At 5 atm, a hydrogen partial pressure of 1.01 atm, was developed, which however, is not enough for membrane operation. This suggests that the employment of higher pressures or of a sweep gas is needed to perform membrane reactor tests. For instance, it was estimated with CEA NASA software for equilibrium calculations that a test at 10 atm would give 1.88 atm of hydrogen partial pressure which would allow the separation of hydrogen form a membrane even in the absence of a sweep gas.

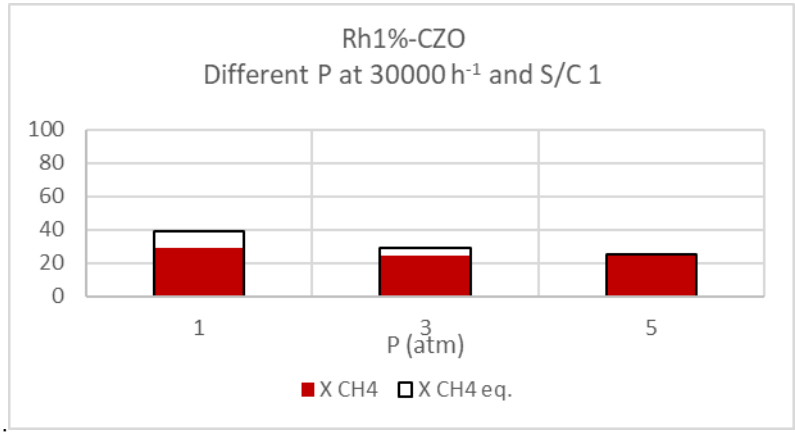

Figure 66: Effect of pressure on methane conversion, carbon dioxide selectivity and hydrogen yield on Rh1-CZO.

Table 27:Summary of the results of tests a pressure of 1 atm, 3 atm and 5 atm under the conditions 500 °C - 30000 h^{-1} - 0.21 O_2/C – 1 S/C.

P (atm)	X CH4 (eq) [%]	H_2 dry out (eq.) [%]	S_{CO2}[%]	C-balance [%]	H_2 pressure [atm]	T_{min} [°C]	T_{max} [°C]
1	30 (52)	36 (56)	92	90	0.20	534	500
3	25 (29)	30 (41)	93	95	0.64	537	500
5	24 (25)	29 (35)	93	95	1.01	529	500

Finally, a test without oxygen was carried out to estimate the performances of Rh1%-CZO in the SR reaction (figure 67). This test shows decreased conversion but similar hydrogen concentration in the outlet stream. However, a deeper comparison of the two tests is difficult due to the different temperatures developed on the catalytic bed, even though the tests were carried out at the same oven temperature of 500°C. In fact, a catalytic bed temperature of more than 530°C characterizes the oxy-reforming while SR produces an endothermic phenomenon and a catalytic bed temperature of 485°C. Such a high difference influences both the equilibrium conversion and the kinetics of the catalysts, making a proper comparison challenging.

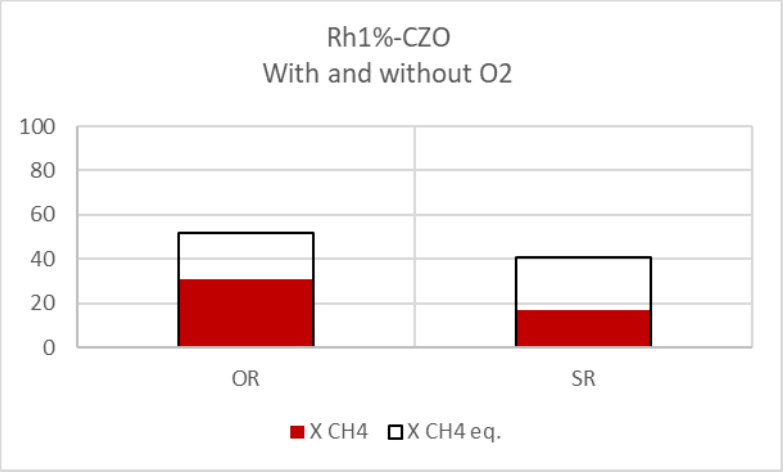

Figure 67: Comparison between oxy-reforming (OR) and steam reforming (SR) on Rh1-CZO

Table 28:Summary of the test performed without O_2 under the conditions 500 °C - 30000 h^{-1} - 1 atm - 0 O_2/C – 3 S/C.

Test #	X CH4 (eq) [%]	H_2 dry out (eq.) [%]	S_{CO2} [%]	C-balance [%]	H_2 pressure [atm]	T_{min} [°C]	T_{max} [°C]
SR	17 (40)	39 (61)	95	100	0.13	485	499

7.5. **PtRh bimetallic catalysts activity in oxy-reforming**

Given the good results of Pt in WGS activity and Rh in oxy-reforming, the two catalysts containing both Pt and Rh (PtRh 0.7 and PtRh2.1) were tested in the low temperature oxy-reforming reaction. Rh1%-CZO will be used a reference for Rh based catalysts, as these two

were synthetized employing a similar total metal to support ratio, namely 0,01% moles of metals per gram of support.

In order to have a more comprehensive understanding of the catalytic activity of these samples, they were initially tested in the oxy-reforming at 750°C, just before the low temperature tests (figure 68). The selected conditions were 750°C, 30000 h^{-1}, 1 atm and S/C 0.7.

At these conditions, the Rh1% catalyst was not able to reach the thermodynamic equilibrium and gave a similar conversion as compared to Pt. Interestingly the mixed catalysts gave higher conversions than the monometallic catalysts, being the Pt/Rh2.1 the best performing one, reaching the equilibrium conversion. Improved performances of the bimetallic catalyst were also reported in autothermal reforming process [143]. The test at 750°C test was repeated for twice after the tests at low temperature, in order to assess the stability of the investigated catalysts (first and second return tests).

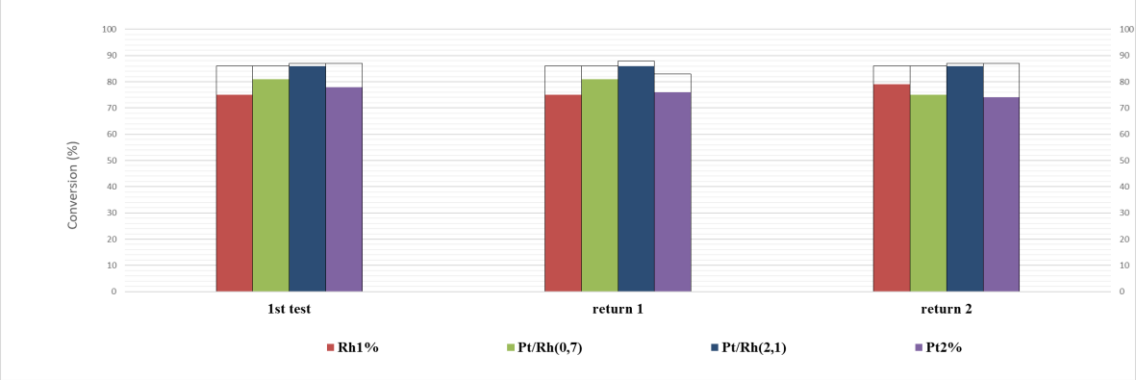

Figure 68: Stability tests carried out on Pt, Rh and PtRh catalysts on CZO at 750°C, 30000 h^{-1}, 1 atm, S/C 0.7.

The higher activity of the mixed catalyst can be explained by the formation of bimetallic Pt-Rh particles which helps to link the oxidation activity of Pt with the SR activity of Rh [81,144]. The presence of bimetallic nanoparticles was evidenced by TEM-EDS analysis which showed the presence of small particles with narrow size distribution (Figure 51) as discussed in chapter 5. Moreover, an improved metal support interaction is observed when bimetallic particles are present. In fact, by looking at the TPR profiles, it can be noted that the peak of bulk Ce reduction is found at lower temperature (314°C and 286°C) (figure 50) than in the case of Rh (478°C) (figure 63).

A high stability was shown by PtRh 2.1 catalysts which was also the best performing one in all the test and did not show any loss in conversion, confirming its high activity in high temperature oxy-reforming. Rh was also stable and showed an increase in conversion in the last test. This can be related to an increased reduction, dispersion or interaction with the CZO support, that occurred thanks to the conditions employed in the tests at low temperature between the first and second return tests. Finally, Pt and PtRh 0.7 showed a decrease in conversion in the last return test which could be due to deactivation phenomena such as sintering or carbon formation, which was favoured in the high pressure tests carried out at low temperature between the first and second return tests.

Given the good results obtained by the bimetallic catalysts at high temperature, they were also tested at 500°C under different conditions. The results, reported in figure 69, highlights that the bimetallic catalyst provide methane conversions similar to those of the Rh monometallic catalyst. This suggests that the Rh activity is particularly predominant in these conditions and are not linked to those of Pt in a synergic effect The S/C seem not to influence the conversion of the catalyst with the Rh containing samples providing higher values than Pt. In order to further discuss the catalytic activity of these samples, the hydrogen production was reported in figure 70. It shows a similar trend to methane conversion regarding the S/C ratio. On the opposite, hydrogen production was influenced by the space velocity. In fact, decreasing the Rh content of the catalyst (while increasing the Pt one), lower methane conversions and hydrogen productions were observed when contact time was decreased. This demonstrates a faster kinetic behaviour of Rh compared to Pt, thanks to its higher activity toward reforming reactions [79]. This behaviour is observed even at higher pressures where Rh outperformed the other catalysts in terms of hydrogen production and Pt provided the lowest conversion and hydrogen production.

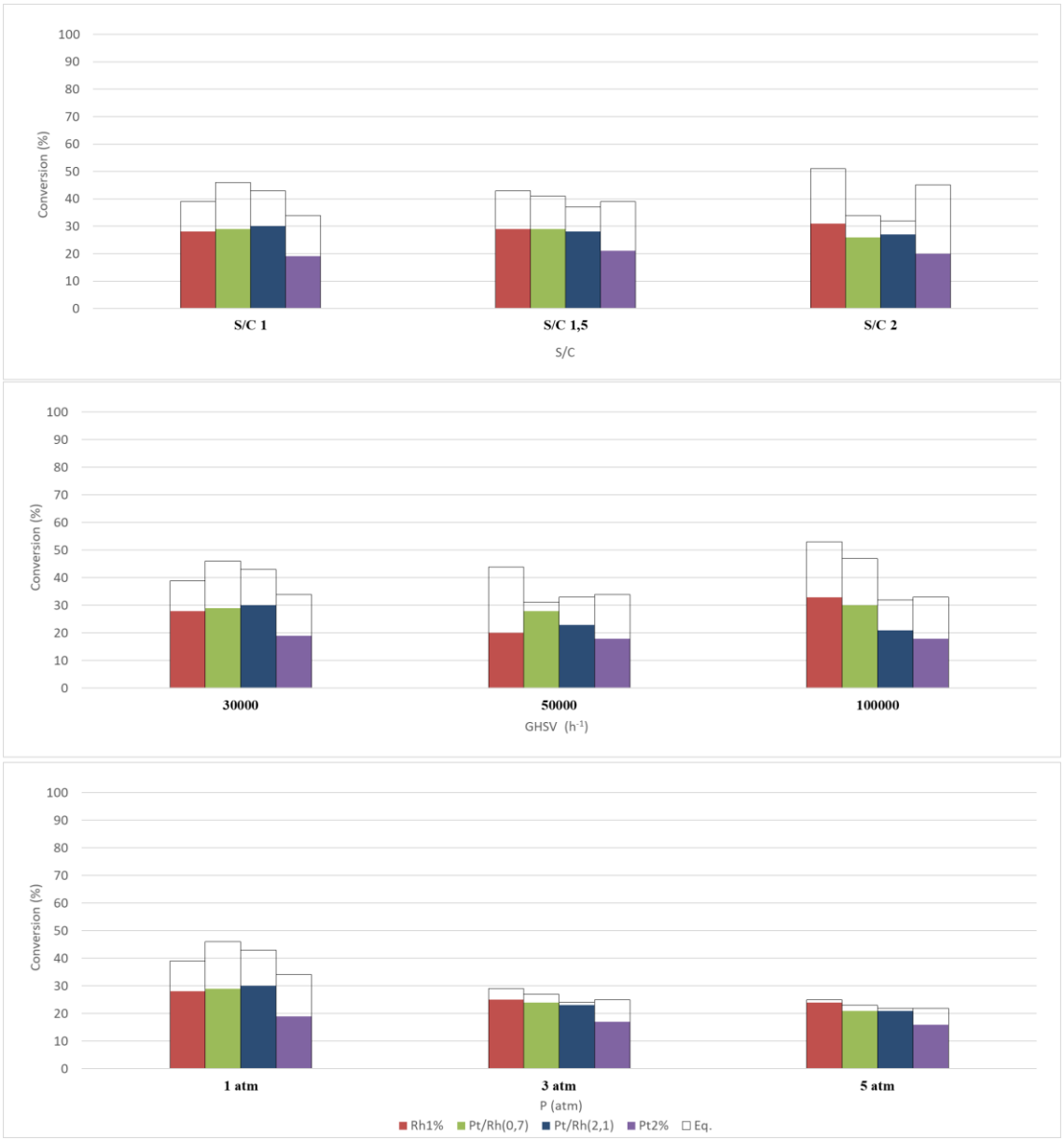

Figure 69: Methane conversion obtained in low temperature oxy-reforming in different conditions (500°C, 1 atm, 30000 h^{-1}, S/C 1), over Rh1-CZO PtRh0.7-CZO, PtRh2.1-CZO and Pt-CZO.

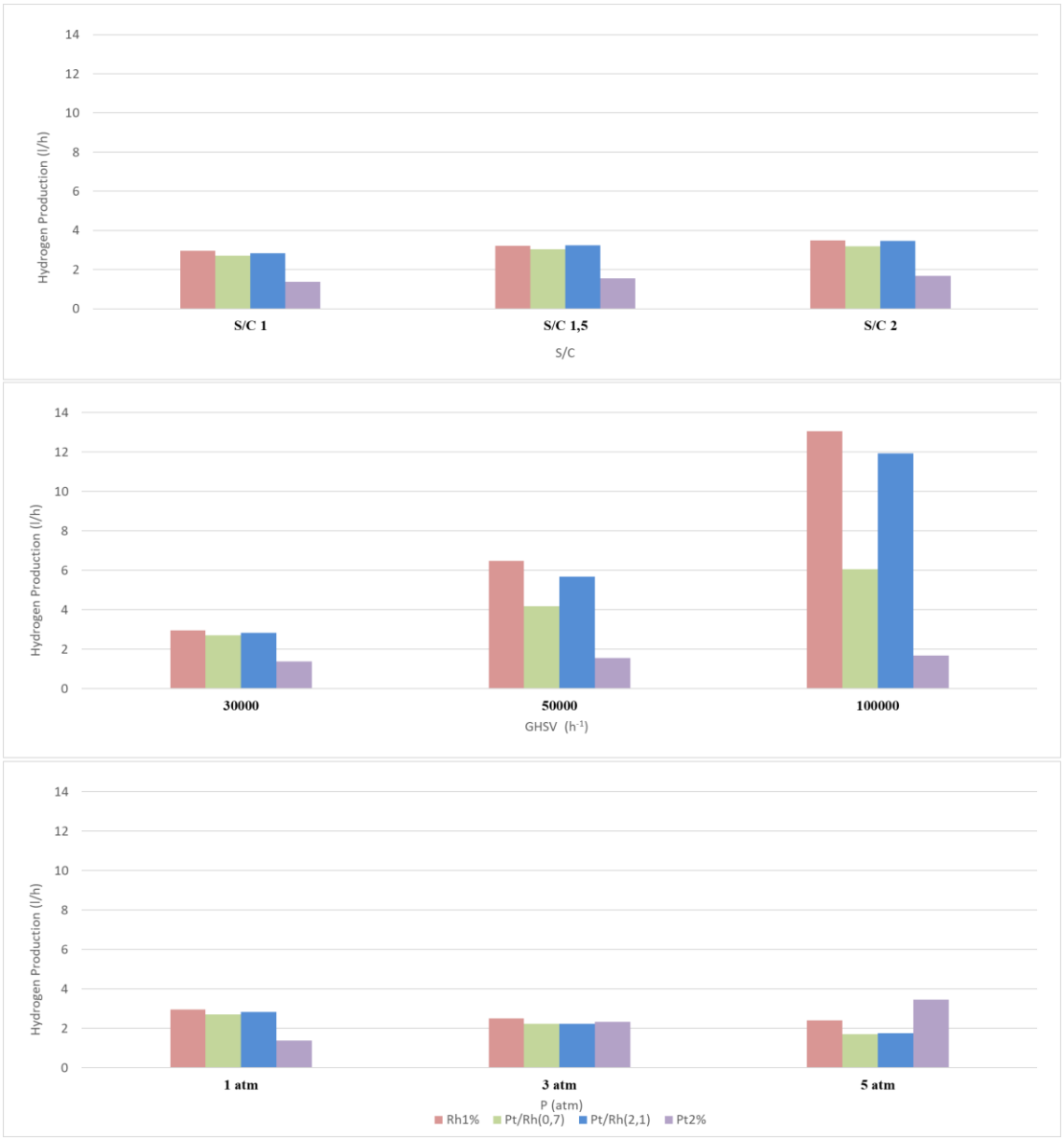

Figure 70: Methane conversion obtained in low temperature oxy-reforming at different conditions (500°C, 1 atm, 30000 h^{-1}, S/C 1), over Rh1-CZO PtRh0.7-CZO, PtRh2.1-CZO and Pt-CZO.

Finally, an analysis of the H_2/CO ratio further confirmed the predominance of Rh character in these conditions, although the copresence of Pt. In fact, hydrogen to CO ratios similar to those of monometallic Rh were obtained showing a minor WGS activity compared to monometallic Pt for the Rh containing samples.

Table 29: H_2/CO ratio obtained over Rh1, PtRh0.7, PtRh2.1 and Pt under different conditions.

	S/C			GHSV (h^{-1})			P (atm)		
	1	**1.5**	**2**	**30000**	**50000**	**100000**	**1**	**3**	**5**
Rh1%	16	24	30	16	16	12	16	23	24
Pt/Rh 0.7	18	24	30	18	16	11	18	21	26
Pt/Rh 2.1	18	24	31	18	19	27	18	27	33
Pt	35	45	58	35	31	35	35	47	56

7.6. **Ru on CeZr oxide activity in low temperature oxy-reforming**

Having shown that Rh was the best performing catalyst in the low temperature oxy-reforming conditions, it was decided to evaluate the activity of a Ru catalyst in comparison to it. Even though Rh might be more active, Ru is cheaper as active phase and could provide a more economical catalyst. Thus 3% of Ru was impregnated over the CZO support.

7.6.1. Characterization of Ru3%-CZO

TPROR analyses were carried out on the impregnated Ru catalyst to assess its redox properties (figure 71). The first TPR cycle showed three reduction peaks centred at 115°C, 249°C and 468°C. This highlights a non-homogeneous reduction and the presence of different reducible species on the catalyst precursor. The first one is related to the reduction of Ru, while the second and third one may be caused by surface and bulk Ce reductions. One main peak was observed in the second TPR cycle at 249°C. This suggests a homogeneous reduction of both Ce and Ru after the TPO. However, this peak is found a similar temperature with respect to Rh (255°C) and suggest that similar redox behaviour after the first TPR is obtained on Ru.

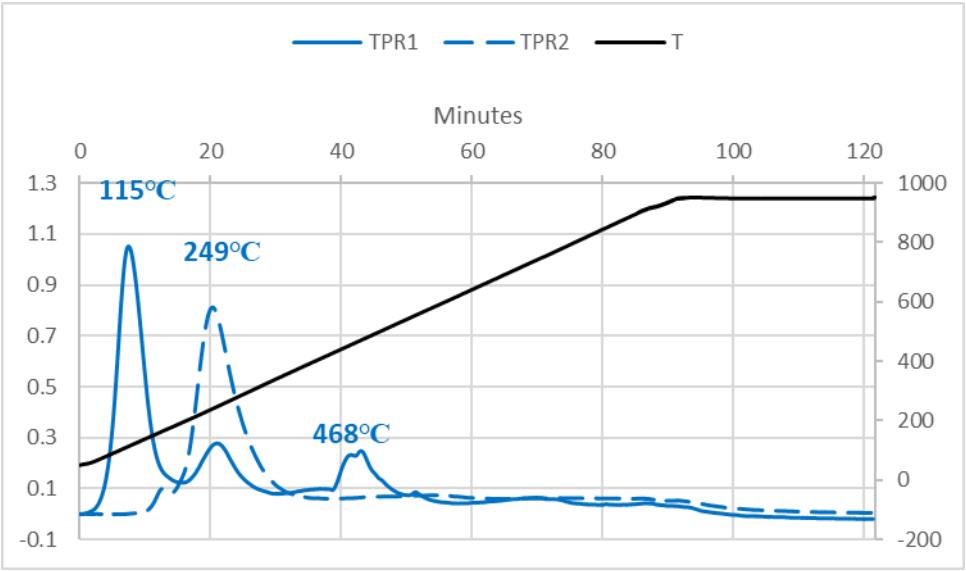

Figure 71: TPROR of the Ru3IWI-CZO catalyst.

Table 30: Hydrogen consumption by TPR for Ru3IWI-CZO.

	TPR1	***TPR2***
H_2 consumption (mmol/g)	1.68	1,16

TEM analysis of the reduced catalyst evidenced the presence of Ru particles with a wide size distribution, with most of the particles with dimensions between 5 and 25 nm (figure 72). This can be due to a sintering process occurred during the calcination after impregnation and the reduction at 750°C. In general, Ru gave bigger particles than other noble metals, which were even wider than support pore size in some cases. Thus, some metallic particles were constrained on the support surface, reducing the metallic dispersion, which possible influences the catalytic activity.

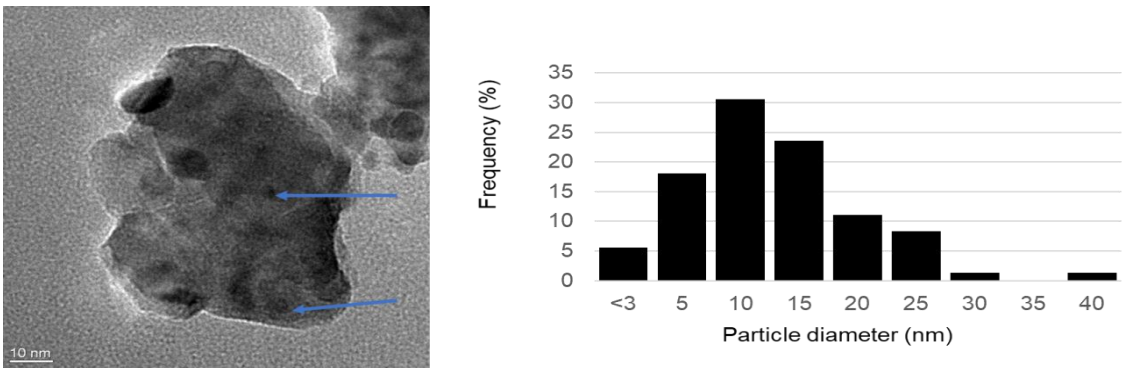

Figure 72: TEM image and paticle size distribution of Ru3IWI-CZO catalyst.

7.6.2. Catalytic activity of Ru3%-CZO

The catalytic results obtained with Ru were compared with those obtained by Rh2.7-CZO. In fact, these two catalysts have a similar metal loading. However, it must be noted that Rh is much more expensive than Ru, and thus an active Ru catalyst would provide a cheaper system. Methane conversion and hydrogen production at different S/C and GHSV are reported in the figures below.

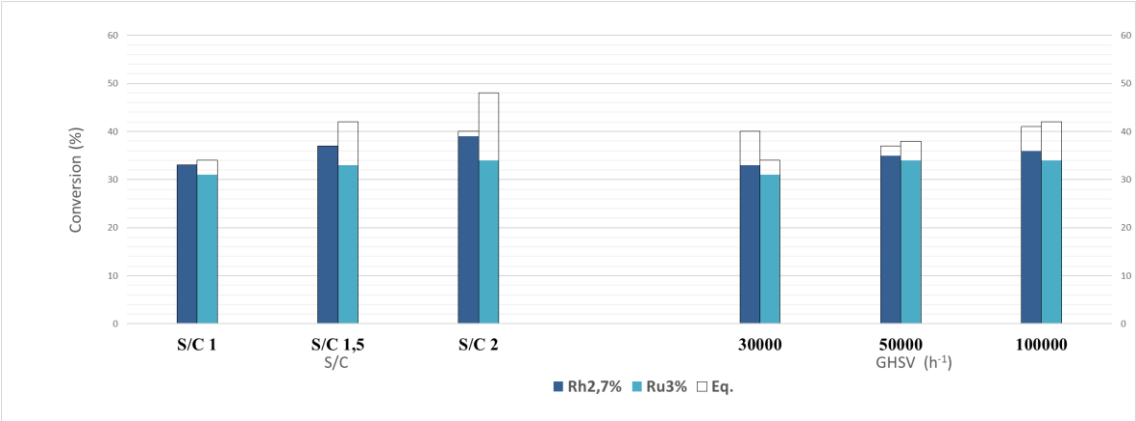

Figure 73: Methane conversion obtained in low temperature oxy-reforming in different conditions at 500°C, over Rh1-CZO and Ru3-CZO.

Changing the S/C produced an increase in methane conversion due to a wider occurrence of the steam reforming reaction. Rh was able to reach the equilibrium, giving higher conversion than Ru. Interestingly, the equilibrium value was higher for the latter, as Ru favoured the occurrence of exothermic reactions, increasing the bed temperature, hence the equilibrium conversion value, which is calculated taking in account the average catalytic bed temperature. Higher hydrogen production was obtained o Rh catalyst thanks to its high activity and selectivity toward steam reforming. The trend observed for the Ru catalyst methane conversion as function of S/C was also found in the hydrogen production value (figure 74).

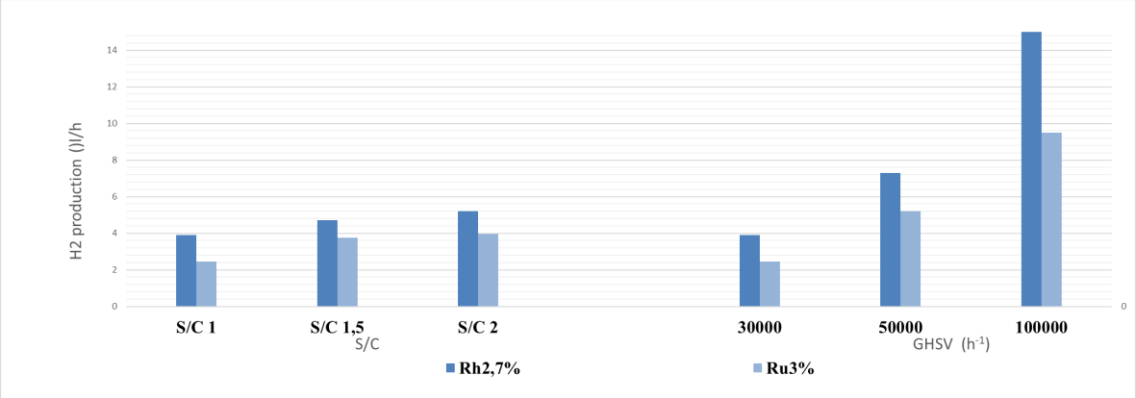

Figure 74: Hydrogen production obtained in low temperature oxy-reforming in different conditions at 500°C, over Rh1-CZO and Ru3-CZO.

An increasing trend for methane conversion was obtained by increasing the GHSV on the Ru catalyst. However, this is again linked with a catalytic bed temperature increase. This is further confirmed by the hydrogen production values which are lower than the Rh catalysts at higher GHSV regardless the similar methane conversion provided by the Ru one.

In general, Rh catalyst gave higher conversions and hydrogen productions. This is due to the higher activity of Rh active phases compared to Ru, and also to the smaller particle size as evidenced by TEM (figure 43 and 72). This also resulted in a better interaction with the support as evidenced by TPR were peaks at lower temperature for both metal and Ce were observed in the case of Rh. This may affect the catalytic properties. In order to provide smaller Ru particles and lower the sintering of the active phase, a Ru catalyst was synthetized by the bulk microemulsion technique, as explained in the next paragraph.

7.6.3. Characterization of Ru3%Bulk-CZO

An issue found in Ru active phases is deactivation due to sintering of the metallic active phase. Therefore, a Ru-CeZr catalyst was produced by bulk microemulsion synthesis, which may provide more stable metallic particles thanks to a different interaction between the metal particles and the support. In fact, the Ru precursor was inserted in the microemulsion together with the precursors of Ce and Zr rather than impregnated after the obtainment of the oxide support. In this way the metallic particles got closely linked to the support oxides. This may give a lower Ru particles mobility during the sintering process.

The catalyst was characterized by TPROR, reported in figure 75.

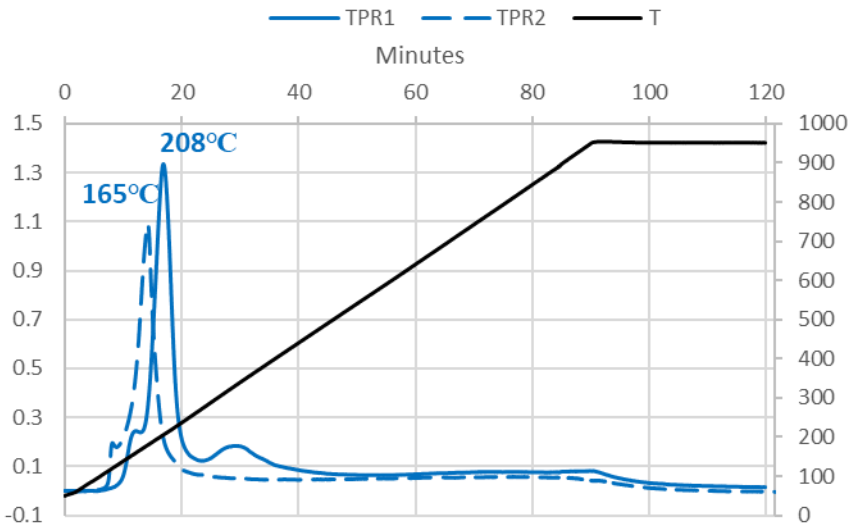

Figure 75: TPROR of the Ru3bulk-CZO catalyst.

Table 31: Hydrogen consumption by TPR for Ru3bulk-CZO.

	TPR1	***TPR2***
H_2 consumption (mmol/g)	1.24	0.84

The first reduction cycle shows a peak centred at 208°C and a smaller one at higher temperature. The first one can be related to Ru and surface Ce reduction while the second one to the bulk Ce reduction. However, the first TPR shows a more homogeneous reduction than the impregnated Ru, which highlights a more homogeneous interaction between Ru and Ce thanks to the bulk synthetic technique. The second reduction is more homogeneous and occurs at lower temperature. This is probably due to the different form of the oxidized ruthenium that is reduced in TPR1 and TPR2. In fact, the first reduction involves Ru oxide species present in the framework of the CeZr oxide structure, hence less available on the surface and less reducible. This process leads to the extraction of Ru ions from the oxide structure and the formation of flat metallic nanoparticles in close relation with the support [116]. Instead the Ru reduced during the second TPR is supposed to be Ru oxide in the form of particles on the surface, obtained after the oxidation of the metallic nanoparticles which have been formed during the TPR1. On the opposite, the insertion of Ru in the structure provides a lower overall reducibility of the catalyst, due to uncomplete reduction

of Ru, which is inserted in the CeZr structure. This affects the spillover effect, hence the hydrogen consumption in the TPR cycles, which results lower than for the impregnated catalyst (table 30 and table 31).

TEM analysis sowed the presence of small particles with narrow size distribution between 2 and 7 nm (figure 76). These were noteworthy smaller than those obtained by impregnation. In fact, the close link between Ru and the support disfavour sintering phenomena during calcination and reduction. However, it must be noted that part of Ru may still be not reduced, trapped in the oxide structure.

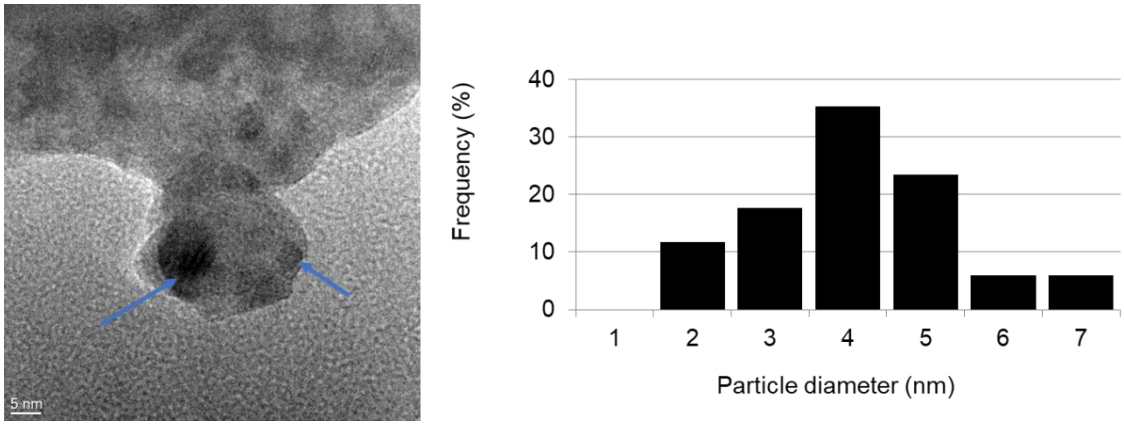

Figure 76:TEM image and paticle size distribution of Ru3Bulk-CZO catalyst.

7.6.4. Catalytic activity of Ru3%Bulk-CZO

A comparison of methane conversion and hydrogen production between the impregnated (IWI) and bulk Ru catalyst on CZO is reported in figures 77 and 78.

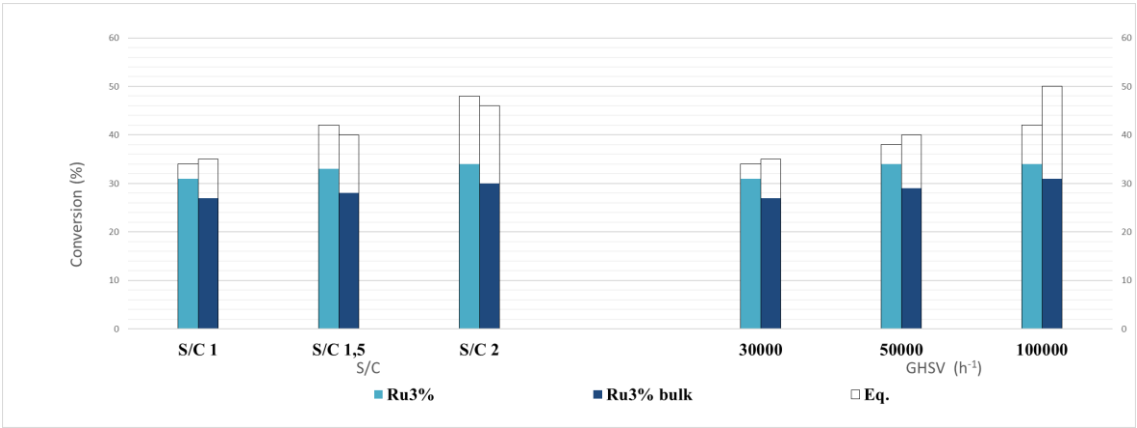

Figure 77: Methane conversion obtained in low temperature oxy-reforming in different conditions at 500°C, over Ru3IWI-CZO and Ru3bulk-CZO.

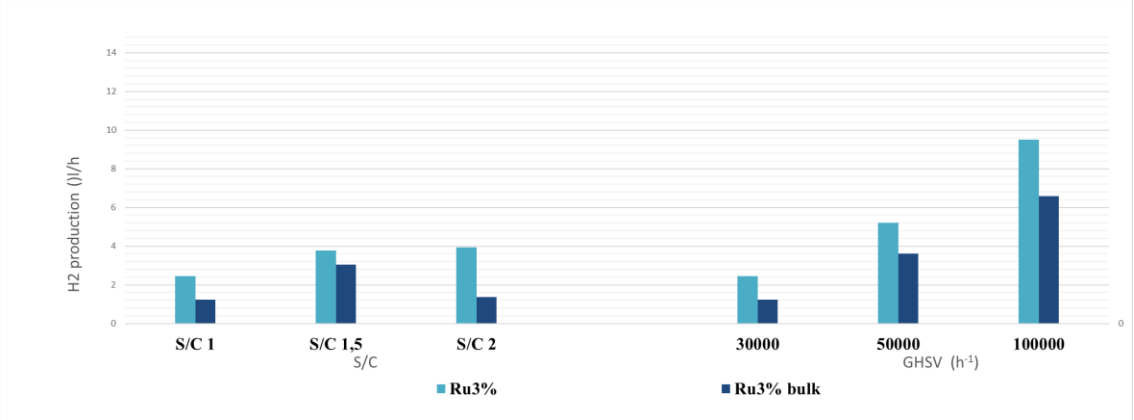

Figure 78: Hydrogen production obtained in low temperature oxy-reforming in different conditions at 500°C, over Ru3IWI-CZO and Ru3bulk-CZO.

The conversion trends for the two catalyst are very similar and showed an increase in conversion at increasing S/C. However, the bulk catalyst provided lower conversion and hydrogen production values than the IWI due to a lower availability of metallic Ru over the surface, given by a lower mobility of the Ru ions in the support framework, hence a lower reducibility. At higher GHSV an increase of methane conversion and hydrogen production are observed but the bulk catalyst was still outperformed by the impregnated one. The increased conversion was due to an increase in the equilibrium conversion for the occurrence of exothermic reactions, which favoured the endothermic SR.

The stability of the two catalysts was also compared by performing return tests at 750°C (figure 79).

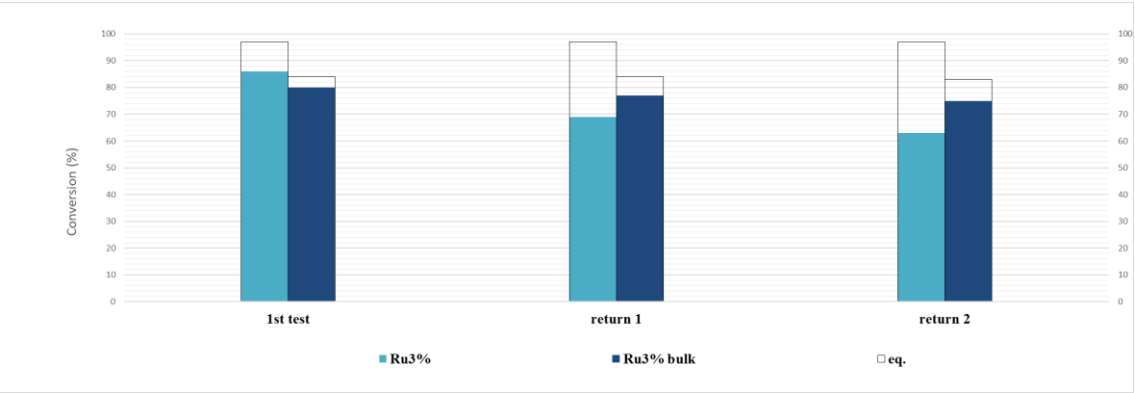

Figure 79: Stability of the IWI and Bulk Ru catalysts.

In the first test a higher activity of the impregnated catalyst was observed, due to the increased availability of metallic Ru on the surface as discussed above. However, the return

tests show a sharp deactivation of this catalyst probably due to sintering of the active phase that decreased the metallic surface area. On the opposite, a much slower deactivation was observed for the bulk catalyst, thanks to a positive interaction between Ru and the support, given by the more homogeneous metal insertion method of the bulk synthesis [49].

This was confirmed by TEM analysis of the used catalysts (figure 80), that showed the formation of big Ru particles in the IWI sample, with diameters up to 125 nm together with a broad size distribution which indicates that big particles were formed during the reaction. On the opposite a narrower size distribution was observed for the bulk sample, linked with the absence o big particles. In particular, most of the particles were found to be smaller than 10 nm. This highlights the good interaction between Ru and support in the case of the bulk sample that is able to slow down the sintering process.

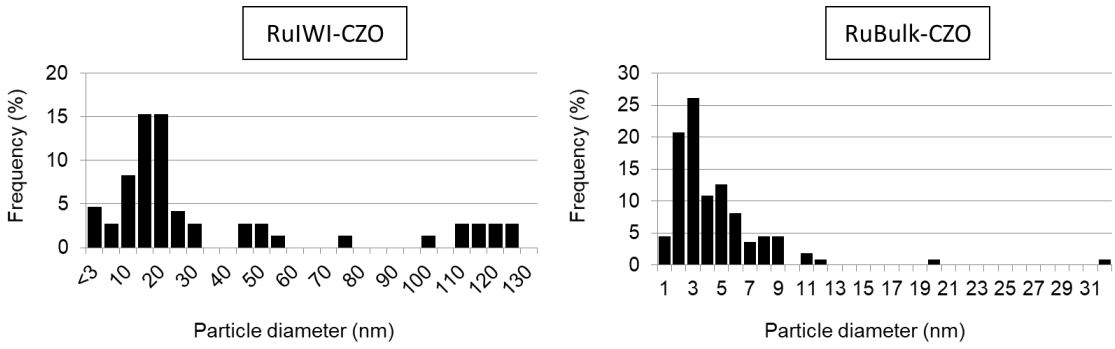

Figure 80:Particle size distribution obtained by TEM on the Ru IWI and bulk spent samples.

Thus, the bulk method is a valid procedure to stabilize Ru toward sintering, given a cheaper catalyst with a good stability. However, this lowers the conversion due to a lower reducibility of the Ru precursor. In order to increase it, a different pre-treatment method, which consists of a calcination at low temperature, then a reduction and finally a thermal treatment in nitrogen at higher temperature could be employed to increase the Ru availability on the surface. This method was in fact able to increase bulk Rh reducibility in an ex-hydrotalcite catalyst [53].

In conclusion, the Ru catalyst can be seen as an effective and cheaper alternative to the Rh one, as it can provide similar conversion and hydrogen productions, which were even higher than the latter S/C of 1.5 or 2. However, this performances were linked with high

increase in the catalytic bed temperature (as high as 600°C), which discouraged the employment of Ru in a membrane reactor.

In general, the low temperature oxy-reforming can provide very sharp exothermic profiles due to CPO as evidenced by the tests with Rh1%-CZO which can make catalyst comparison difficult. Moreover, hot spots may be formed in the catalytic bed even if not detected from the thermocouple. This would cause membrane stability problems in a membrane reactor setup as the Pd thin film is damaged at temperatures higher than 500°C. For these reasons also the Low Temperature Steam Reforming (LTSR) was studied in this work as treated in the following chapter.

7.7. **Conclusions**

Different active phases impregnated on the CZO support were tested in oxy-reforming at 500°C. Pt was found to be active, though was not able to reach the equilibrium conversion and was overcome by Rh2.7-CZO which showed a higher activity. It reached the conversion equilibrium in most conditions. Rh based catalysts outperformed platinum also when the Rh loading was lowered to 1%, to provide a similar metallic molar content to the Pt catalyst.

An interesting trend was observed on the Rh-CZO catalysts (Rh2.7 and Rh1). In fact, an endothermic catalytic bed profile was developed on Rh2.7 while and exothermic one was shown decreasing the Rh amount. This affected the catalytic bed temperature and thus the equilibrium conversions. This was probably related to a predominance of CPO reaction when low number of Rh atoms are present on the catalyst surface. This reaction is in fact faster than steam reforming. On the opposite, steam reforming takes place to a high extent at higher Rh loadings, using the heat developed by CPO. Thus, an optimal catalytic bed temperature may be obtained by tuning the Rh loading, reducing both the exothermic and endothermic profiles.

Bimetallic catalyst (PtRh) were also employed and showed synergy between the two metals at 750°C, where the equilibrium conversion was reached. This was ascribed to the link between the oxidation properties of Pt and the reforming activity of Rh. However, this was

not the case at lower temperature (500°C) were Pt was not able to provide oxidation ability and the Rh character was predominant.

Finally, Ru based catalysts were selected to reduce the cost of the active phase. Ru provided similar conversion than Rh, especially when the S/C was high. In fact, S/C seemed to influence catalytic activity of Ru-CZO suggesting that steam participated to the kinetic equation. This was not the case for Rh, where methane decomposition is the rate determining step. However, Rh outperformed Ru at all the conditions. Moreover, stability due to sintering is an issue in Ru catalysts. Thus, a Ru-CZO catalyst was produced by inserting Ru in the support synthesis step. This allowed for an increased interaction between the metal and support after the reduction of the active phase. It provided lower conversion compared to impregnated Ru but increased stability, reducing sintering of the active phase.

8. CHAPTER 8- LOW TEMPERATURE STEAM REFORMING

Part of this chapter was published in:

Highly Active Catalysts Based on the $Rh_4(CO)_{12}$ Cluster Supported on $Ce_{0.5}Zr_{0.5}$ and Zr Oxides for Low-Temperature Methane Steam Reforming [132].

8.1. Introduction

The Steam reforming reaction was studied in a fixed bed configuration at different temperatures and conditions in order to find an optimal catalyst for the membrane reaction operation. A new type of active phase was developed in collaboration with the group "Cluster carbonilici dei metalli di transizione" of the Department of Industrial Chemistry "Toso Montanari" of the University of Bologna.

This was obtained after depositing a Rh_4CO_{12} cluster over the CeZr or Zr oxides supports and compared with a classical impregnated Rh catalyst to assess if an active phase is formed and its catalytic activity.

8.2. **Synthesis and Characterization of the cluster-based catalysts**

The two supports have been analysed through IR spectroscopy on nujol mull before and after the deposition of the $Rh_4(CO)_{12}$ cluster. Both of them with no active phase deposited showed νCO at 2100 (w), 2031 (s) and 1892 (w) cm^{-1}. The cluster compound was then deposited in two different concentrations, (0.6% and 1.0% wt/wt) on CZOm750 and just at 0.05% on ZOm750, by reacting an hexane solution of $Rh_4(CO)_{12}$ with a slurry of the desired support in the same solvent, for 24 hours, under CO atmosphere, because of its instability in air. The nujol mull spectrum recorded after the deposition of the neutral cluster on the CZOm750 exhibited peaks at 2078 (sh), 2051 (s), 2019 (sh), 1803 (sh), 1797 (w) cm^{-1}, while the one of the same compound deposited on ZOm750 showed different peaks at 2068 (w), 2038 (s), 1990 (s) and 1774 (w) cm^{-1}.

Later on, both catalysts were pelleted and treated under pure N_2 at 500 °C. After this operation new nujol mull spectra have been recorded in order to evaluate if there still were carbonyl ligands in the catalysts. It is interesting to see how the ZOm750 supported catalyst exhibited peaks at 2023 (w) and 1874 (w) cm^{-1}, while the CZOm750 supported one displayed the same peaks shown by the support before the deposition [133]. As for the compounds treated in hydrogen flow at 500 °C, none of the catalysts showed anymore the presence of carbonyl ligands related to a possible carbonyl metallic species, but only the bands associated to the supports.

XRD analysis of the samples did not show any Rh phase due to the low amount of this element in the samples. However, an XRD of the pure cluster heated in nitrogen in one case and heated in He then reduced showed the formation of metallic Rh upon these treatments due to cluster decomposition. This suggests that the cluster-based catalyst could provide an active phase. Moreover, the advantage of employing such precursor may rely in the different interaction that is established between the support and the Rh phase and the formation of small Rh particles given by the small dimension of the four atoms, Rh cluster. In fact, the cluster deposition is different form the classical impregnation and is based on reaction between the cluster and the support in which the former loses a CO to react with a

surface OH of the support. This provides a Rh cluster in which one atom is bonded directly to an oxygen of the oxide support. After heating up in He, some of the carbonyls are lost and only one CO is supposed to be left as evidenced by drift analysis [134].

During reduction the last CO is removed. This was confirmed during the pretratment carried out before TPR experiments that shows the production of CO and CO_2 due to cluster decomposition during the heating ramp in inert gas and by the results of the IR analysis.

The catalysts obtained in this way were called Rhxx-CL-R-CZO for the reduced cluster-based catalyst and Rhxx-CL-N-CZO for those just heated in nitrogen, where xx is the metal loading expressed as weight %

8.3. **Catalytic tests on Rh0.6-CL-R-CZO**

The cluster-based catalyst with a metal loading of 0.6% deposited on $Ce_{0.5}Zr_{0.5}O_2$ (Rh0.6-CL-R-CZOm) was treated onvernight under H_2/N_2 stream at 500°C and tested in different conditions The effects of the S/C (Steam/Carbon) ratio, temperature, pressure and GHSV (Gas Hourly Space Velocity) were studied. The precursor was charged in the reactor and heated under N_2 at 500 °C, and after cooling down to 200 °C, the sample was heated at 500 °C under H_2 to obtain the final active catalyst. The analyses of the reaction parameters have been carried out with the aim of studying the conditions with which the catalyst could maximize both syngas and hydrogen productions.

At 500 °C, the increase of the S/C ratio had a positive effect on the methane conversion (X CH_4), as shown in Figure 81. In particular, at low S/C ratios, the methane conversion was 19% at S/C 1 and 22% at S/C 1.5, very close to the equilibrium values (19% and 24%, respectively). A further increase in S/C up to 2 and 3 resulted in higher conversions of 23% and 26%, though not enough to meet the increase of the equilibrium values (29% and 36%, respectively), deriving from higher steam concentration, showing a kinetic limitation of the steam reforming reaction. The H_2/CO ratio was also considered to analyze the contribution of the water gas shift reaction (WGSR). In all conditions, the ratio was higher than the stoichiometric value of 3, due to the occurrence of the WGSR. Thus, an advantage of low temperature steam reforming is the possibility of carrying out the two reactions together, as opposed of conducting them in three different reactors (one for steam reforming, a high-

temperature shift reactor and a low-temperature shift one), which is the usual procedure. For instance, a H_2/CO ratio of 28 was obtained at S/C 1. When the S/C ratio increased, the H_2/CO raised thanks to an augmented contribution of the WGSR, reaching the values of 35, 43, and 63 at S/C 1.5, 2 and 3, respectively. Indeed, the high amount of steam reacted with CO and produced a major amount of hydrogen. This was also confirmed by the CO selectivity (sCO), which decreased when increasing S/C, falling from 13% (at S/C 1) down to 6% at S/C 3.

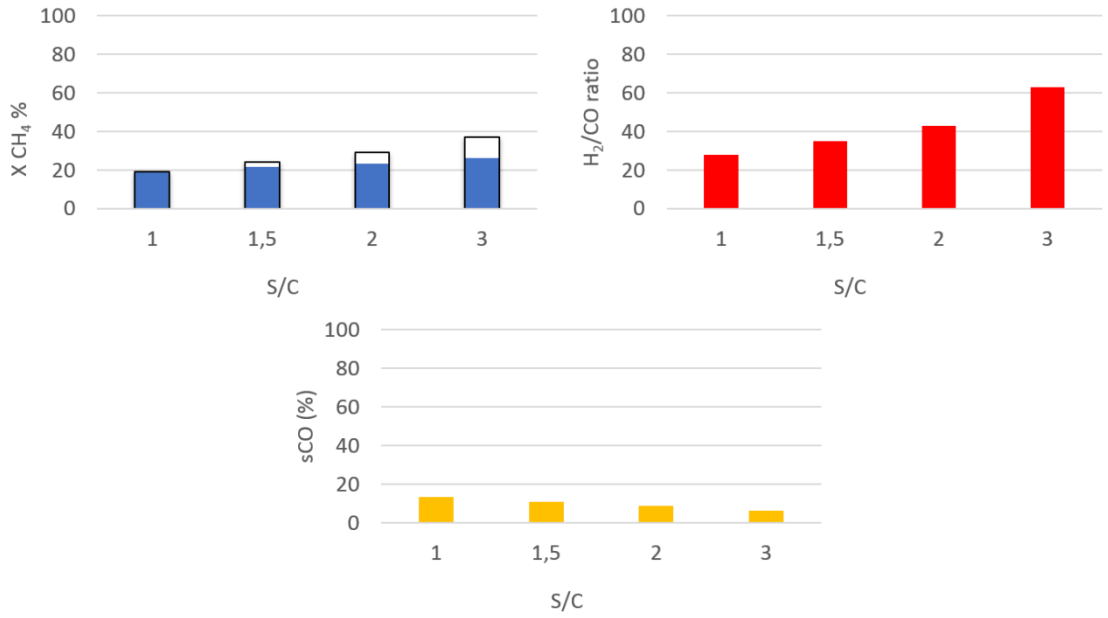

Figure 81: Comparison among tests carried out on Rh0.6-CL-R-CZOm at 30000 h^{-1}, 1 atm and 500 °C. The graphs report the methane conversion (blue) with respect to the equilibrium values (white bars with black frames), H_2/CO ratio (red), and CO selectivity (yellow) versus different S/C ratios.

Figure 82 highlights the effect of the temperature on the catalytic conversion of methane at 30,000 h^{-1}, S/C 3 and atmospheric pressure. In all conditions, the methane conversions were far from the equilibrium values (indicated by the empty bars). In general, experimental and equilibrium methane conversions increase with temperature as both steam reforming thermodynamics and kinetics are favored at high temperature. In fact, a conversion of 4% was observed at 350 °C, far from the equilibrium value of 11%, which increased to 9% and 17 % at 400 and 450 °C, but they were both still far from the equilibrium conversions (18% and 26%, respectively). The equilibrium value was not reached even at 500 °C, where the observed experimental conversion was 26% and the equilibrium one 36%. However, a

sharply decreasing trend was observed for the H_2/CO ratio. The WGS and SR reactions are favored in opposite conditions; therefore, at 350 °C water gas shift was predominant, and the as-produced CO was directly converted into hydrogen, resulting in a final gas composition with CO concentration of 75 ppm. Conversely, at 500 °C the water gas shift is less favored, and an increased rate of steam reforming consumed water, further depressing the WGSR. Overall, this resulted in a decrease of the H_2/CO ratio from 1700 at 350 °C to 63 at 500 °C, and in an increase of the CO selectivity with temperature up to 6%.

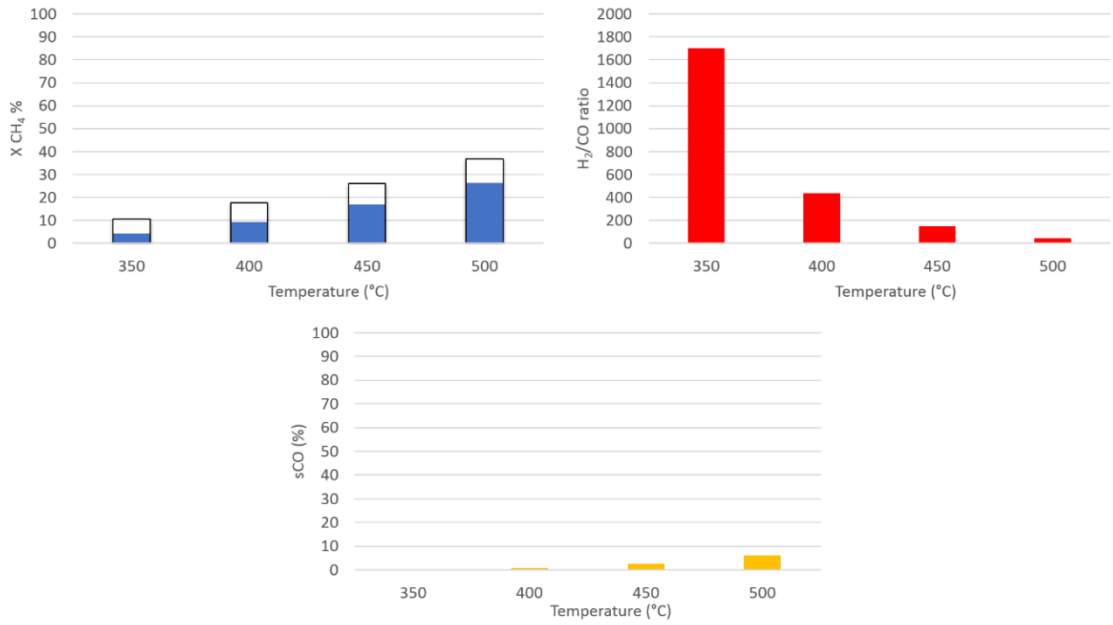

Figure 82: Comparison among tests carried out on Rh0.6-CL-R-CZOm at 30000 h^{-1}, 1 atm and S/C 3. The graphs report the methane conversion (blue) with respect to the equilibrium values (white bars with black frames), H_2/CO ratio (red), and CO selectivity (yellow) versus different T. The Y scale related to the H_2/CO-ratio graph is very different from the others due to the large values.

An increase of the GHSV caused a decrease in the methane conversion from 23% at 30,000 h^{-1}, to 17% at 50,000 h^{-1} and 13% at 100,000 h^{-1}, which also resulted in lower hydrogen production (Figure 83). Moreover, the conversion values were far from the equilibrium ones, which were set at 29%, 28%, and 25%, respectively. This was due to the minor contact time between the gas stream and the catalyst. In these conditions, in fact, the reaction appeared to be strongly limited by kinetics, and the catalyst gave conversion results that were far from the thermodynamic equilibrium. The lower methane conversion is accompanied by a higher water partial pressure, which decreased the CO amount due to WGSR and, overall,

increased the H_2/CO ratio from 43 at 30,000 h^{-1}, to 66 at 50,000 h^{-1} and 91 at 100,000 h^{-1}. This catalyst behavior showed the predominance of the WGSR in determining the H_2/CO ratio, suggesting a faster kinetics for the WGS reaction over the steam reforming one. However, it is difficult to offer a complete comparison among the different tests as lower catalytic bed temperatures are developed at higher GHSV, due to decreased conversions. In fact, lower temperatures decrease the equilibrium conversion and steam reforming activities.

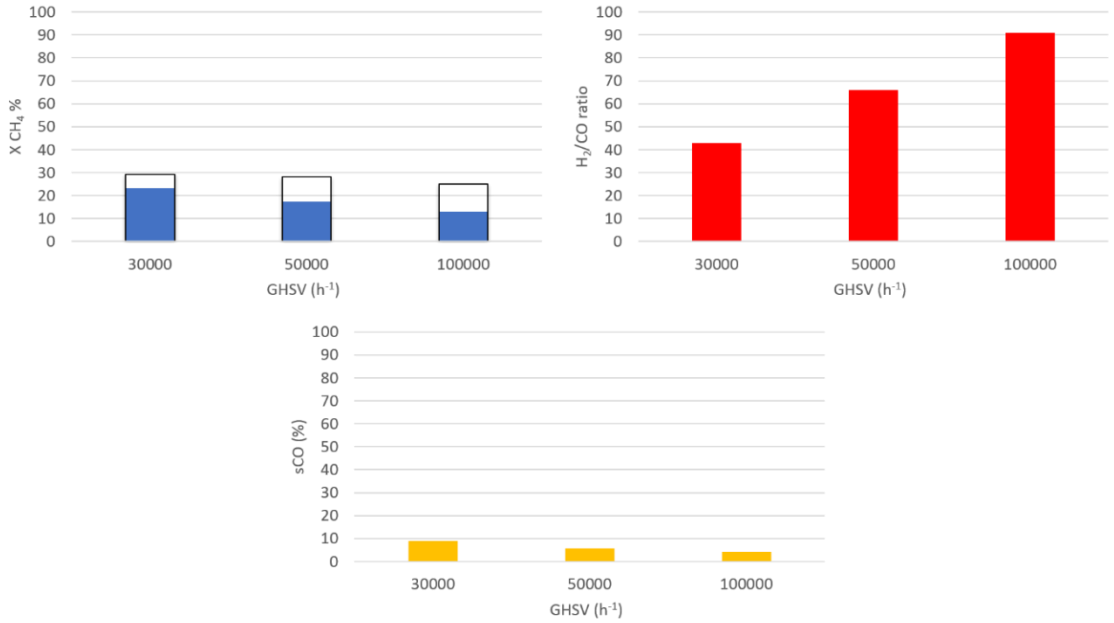

Figure 83: Comparison among tests carried out on Rh0.6-CL-R-CZOm at 1 atm, S/C 2 and 500 °C. The graphs report the methane conversion (blue) with respect to the equilibrium values (white bars with black frames), H_2/CO ratio (red) and CO selectivity (yellow) versus different Gas Hourly Space Velocity (GHSV).

At higher pressure, lower methane conversions were observed (from 29% at 1 atm, to 20%, 17%, and 13% at 3, 5, and 10 atm, respectively) (Figure 84), owing to a decreased thermodynamic equilibrium of the SR reaction. However, the equilibrium conversion was close to the experimental conversion at 5 atm (17%) and reached it at 10 atm (13%). In analogy with what observed above, a lower methane conversion is associated with a higher residual amount of water, which enhances the WGSR and, in turn, the H_2/CO ratio, which raised from 43 at 1 atm to 108 at 10 atm.

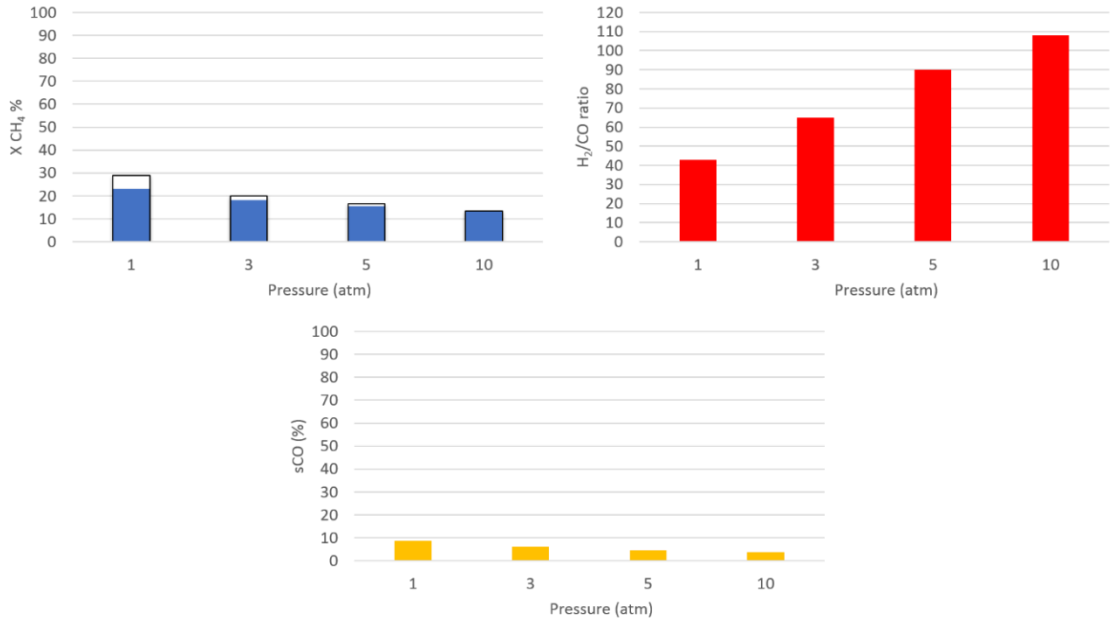

Figure 84: Comparison among tests carried out on Rh0.6-CL-R-CZOm at 30000 h^{-1}, S/C 2 and 500 °C. The graphs report the methane conversion (blue) with respect to the equilibrium values (white bars with black frames), H_2/CO ratio (red) and CO selectivity (yellow) versus different GHSV. The Y scale related to the H_2/CO-ratio graph is slightly different from the others due to higher values.

The effect of the S/C ratio was investigated at 500 °C and 10 atm (Figure 85). In these conditions, the methane conversion increased with S/C, reaching the equilibrium values up to S/C 2 (9% at S/C 1, 11% at S/C 1.5 and 13% at S/C 2), and the experimental conversion (15%) close to equilibrium value (17%) at S/C 3. The highest conversion was observed at S/C 3 thanks to the increased equilibrium values at higher S/C ratios.

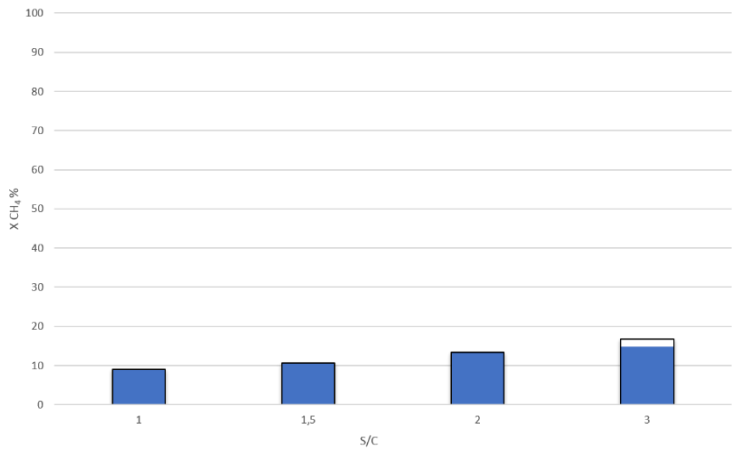

Figure 85: Comparison among tests carried out on Rh0.6-CL-R-CZOm at 30000 h^{-1}, 10 atm and 500 °C. The graph reports the methane conversion (blue) with respect to the equilibrium values (empty bars with black frame) versus different S/C ratios.

The same tests were also conducted at lower temperature, namely 450 °C (Figure 86). In these operative conditions, the experimental methane conversion was close to the equilibrium values up to a S/C ratio of 2, however, it remained distant from it a S/C 3 due to the lower catalytic activity at this temperature. In particular, conversions of 5%, 6%, 7%, and 8% were, respectively, observed by increasing the S/C, while equilibrium conversions concurrently increased from 5% to 7%, then 9% and 12%.

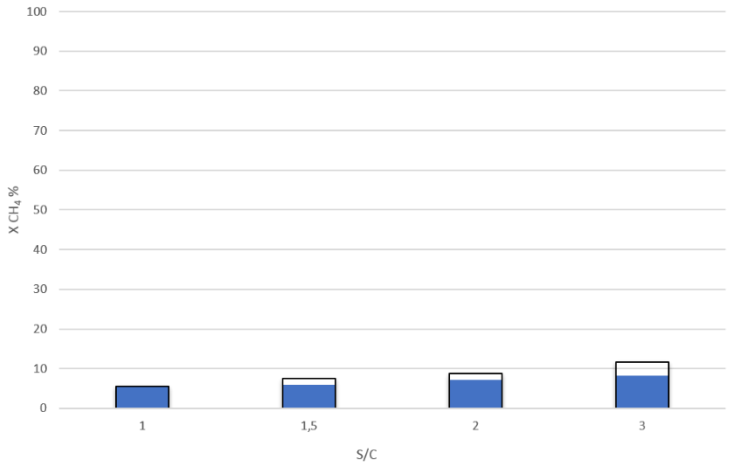

Figure 86: Comparison among tests carried out on Rh0.6-CL-R-CZOm at 30,000 h^{-1}, 10 atm and 450 °C. The graph reports the methane conversion (blue) with respect to the equilibrium values (empty bars with black frames) versus different S/C ratios.

Finally, in order to evaluate the stability of the catalysts in the operative conditions, a test with the same parameters as the first one (500 °C, 30,000 h^{-1}, 1 atm and S/C 1.5, Figure 87) was periodically conducted after every three tests carried out in different conditions, giving rise to the so-called return tests. The results indicate a rather high catalyst stability towards methane conversion. However, a conversion drop of 4% was observed in the last return test, which was carried out after those conducted at low temperature and high pressure.

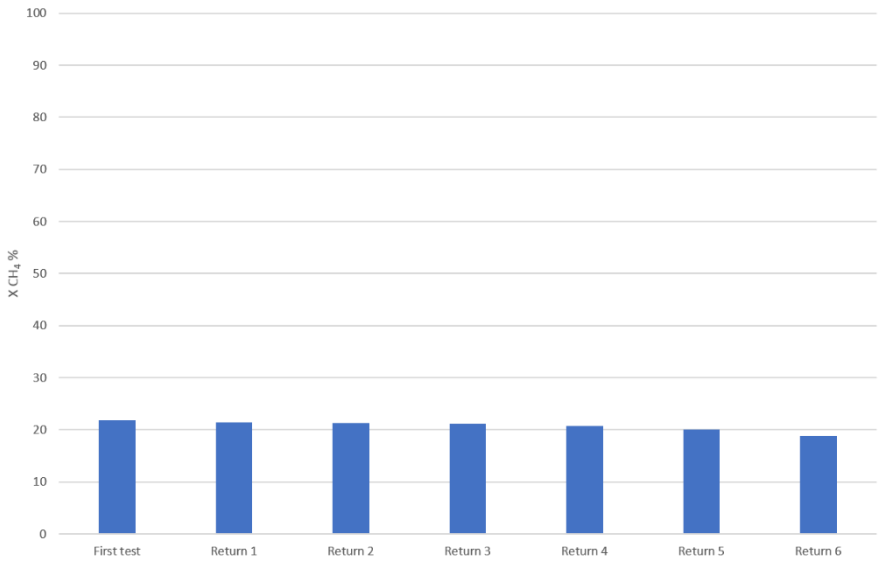

Figure 87: Methane conversion in deactivation tests carried out at 500 °C, 1 atm, 30,000 h^{-1} and S/C 1.5.

This deactivation could be due to the formation of carbon on the active site, owing to Boudouard reaction, which in fact is favored at low temperature and high pressure. The Raman analysis on the spent Rh0.6-CL-R-CZOm catalyst (Figure 88) showed two very small peaks related to the presence of carbon. In particular, the bands detected at 1350 and 1580 cm^{-1} could be attributed to the D-band and G-band of carbon, respectively [135–137]. In general, the G-band derives from the stretching of sp^2 carbon bonds in planes of graphene type [28], while the D-band is caused by the vibrations of carbon atoms in disordered species, such as amorphous carbon [138]. Both bands are rather broad and weak even after a long time on stream and different reaction test conditions, demonstrating the properties of the $Ce_{0.5}Zr_{0.5}O_2$ support synthetized by microemulsion in retarding carbon formation, which was also reported previously [50]. Considering the weakness of the bands, other phenomena, such as the re-oxidation of the catalyst during high-pressure tests, where high water partial pressure is present, need to be taken into account. In those conditions, especially in the first part of the catalytic bed where the presence of hydrogen is still very low, the gas mixture had a higher oxidative potential that could affect the oxidation state of the Rh.

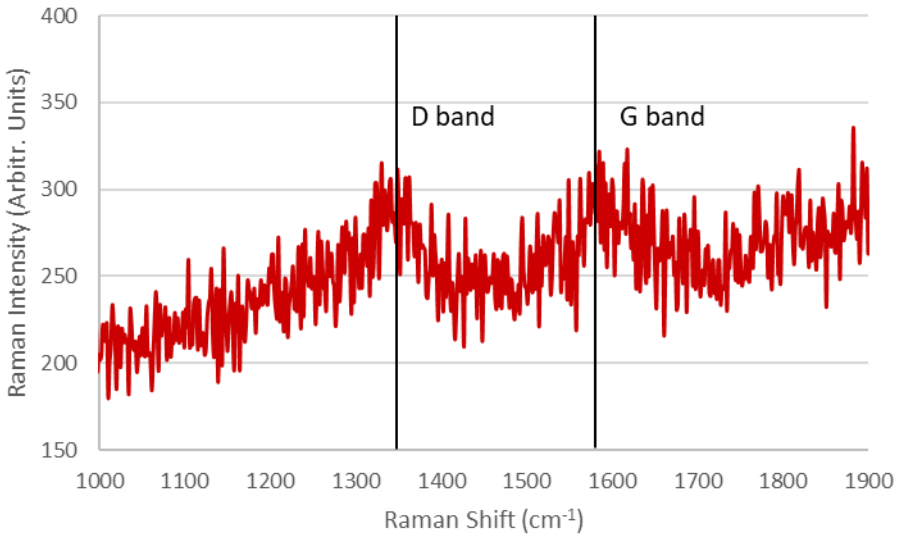

Figure 88: Raman analysis carried out on the used Rh0.6-CL-R-CZOm catalyst. The two bars indicate the presence of carbon.

8.4. **Comparison with a Rh0.6-IWI-CZO catalyst**

The same tests were carried out on a Rh 0.6% (w/w) catalyst obtained by impregnation on CZO. the results were very similar to those shown by the cluster-based catalyst at the same concentration and thus it was difficult to assess if the different precursor provided an better intrinsic catalytic activity. In general, the conditions employed and the high amount of active phase, made the catalyst work close to the thermodynamic equilibrium, which further disfavoured an easy discrimination between catalytic performances. So, the loading of the two active phases was decreased to 0.05% to work in kinetically controlled conditions and stress the differences between the two catalysts. To do that, impregnated and cluster-based catalysts were produced at a concentration of 1% (w/w) and physically diluted by mixing them with bare support in order to reach a concentration of 0.05% (w/w).

8.5. **Catalytic tests on diluted clusters and impregnated catalysts.**

The catalysts with a lower Rh loading were prepared diluting the 0.6% sample down to 0.05% wt/wt for further tests, to allow a better evaluation of the activity in a kinetic regime and a better understanding of the deactivation phenomena and metal support effects. Furthermore, the study of catalysts with low amounts of active phase is interesting for some

specific applications, such as structured catalysts, membrane reactors, and microreactors, where the active phase may be deposited or coated in thin layers or on low-surface-area supports.

Catalysts with a low % of active phase (0.05% wt/wt) on the two different supports (CZOm and ZOm) were prepared and treated in two different ways: either just heated under N_2 or treated firstly under inert gas and then hydrogen. The four produced catalysts were named as follows:

- Rh0.05-CL-N-CZOm (the cluster-based catalyst deposited on CZOm was heated under nitrogen before the tests).
- Rh0.05-CL-R-CZOm (like the previous catalyst, also treated under H_2).
- Rh0.05-CL-N-ZOm (the cluster-based catalyst deposited on ZOm was heated under nitrogen before the tests).
- Rh0.05-CL-R-ZOm (like the previous catalyst, also treated under H_2).

Tests were carried out at fixed experimental conditions (GHSV = 30000 h^{-1}, P = 1 atm, T = 500 °C, S/C 1.5) to compare the different catalysts' performances.

Before the catalytic tests, a preliminary screening was carried out to compare the Rh-particle size and distribution on the not-reduced (only heated under nitrogen) CZOm and ZOm-supported catalysts. The TEM (Transmission Electron Microscopy) analyses performed on both supports evidenced the presence of small Rh particles (1-2 nm) with narrow size distribution (Figure 89). However, it is important to note that the identification of particles below 1 nm is difficult and may be strongly underestimated.

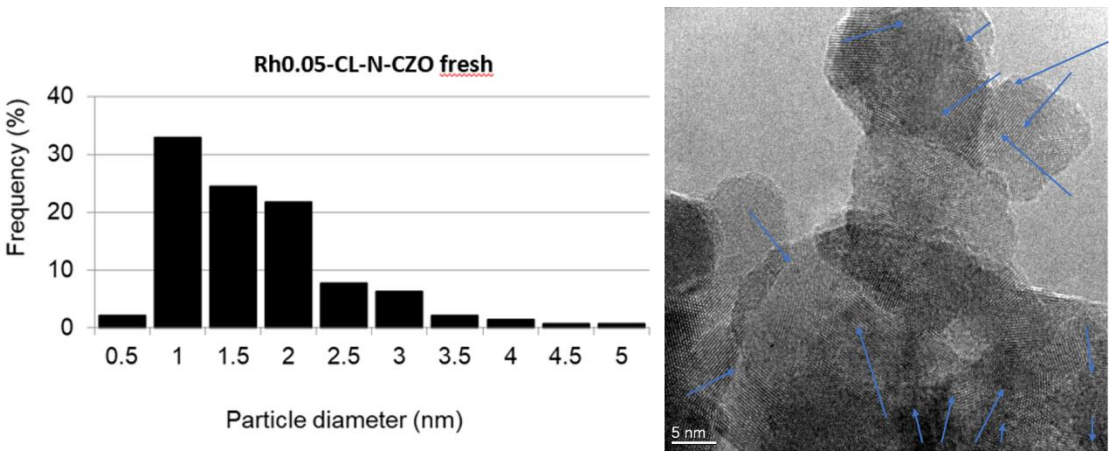

Figure 89: Rh particle-size distribution of the Rh cluster deposited on CZOm support determined by Transmission Electron Microscopy (TEM) analysis.

Figure 90 shows the results obtained with the cluster-based catalysts deposited on CZOm in tests carried out at high temperature (750°C). An initial conversion around 35% was observed for the catalyst not treated in hydrogen, with a decreasing trend in the first hour and an almost constant value of 30% during the reaction time. This result is in agreement with the fact that, when using such cluster-derived samples, active species are obtained even without the need of a reduction step (hydrogen treatment). The deactivation of the first part was probably due to the fast sintering of the reactive small particles evidenced by TEM analysis. The sample treated under H_2 was able to produce a higher conversion (40%) with stable results over 300 minutes.

The same test was conducted on an Rh-impregnated catalyst on the same CeZr oxide and reduced at 500 °C (Rh0.0.5-IWI-R-CZOm), which represents the best catalyst in oxy-reforming reaction [19] (Figure 91). This test showed an initial methane conversion of 36% with a slightly deactivation trend towards 34%. These results were lower than those obtained with Rh0.05-CL-R-CZO, indicating a higher activity for the cluster-derived catalyst and a readily stable conversion. This could be related to a better dispersion of the Rh cluster on the oxide support.

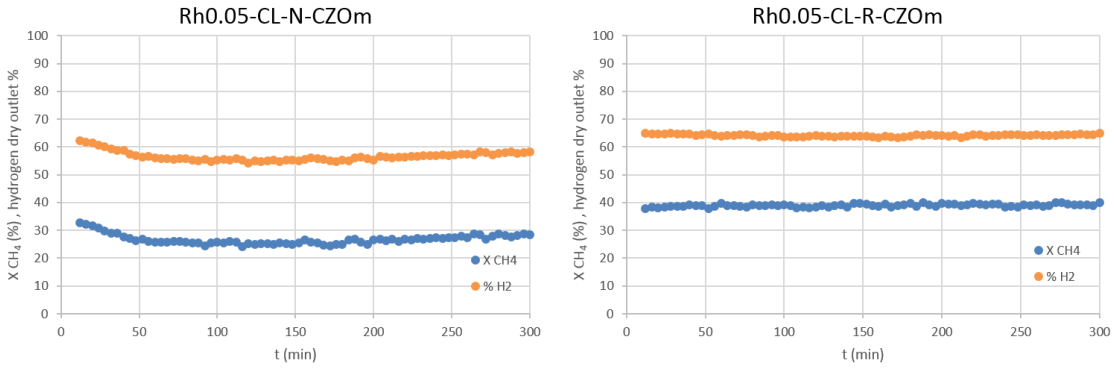

Figure 90: Methane conversion and hydrogen dry outlet percentage obtained on Rh0.05-CL-N-CZOm (left) and Rh0.05-CL-R-CZOm (right) tested at 750 °C, 30,000 h^{-1}, 1 atm and S/C 1.5.

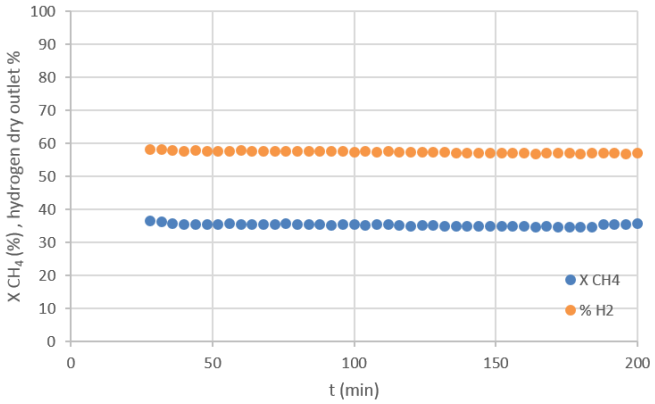

Figure 91: Methane conversion and hydrogen concentration in the dry gas obtained on Rh0.0.5-IWI-R-CZOm tested at 750 °C, 30,000 h^{-1}, 1 atm and S/C 1.5.

The same test was also conducted on the cluster-based catalyst supported on zirconia (Rh0.05-CL-R-ZOm, Figure 92) and treated under H_2, which gave a lower methane conversion (around 33%) with respect to the analogous cluster on CZOm. This is probably related to the effect of the Ce(IV)/Ce(III) couple in the sample that acts as steam-dissociating site, and by the higher oxygen mobility in the $Ce_{0.5}Zr_{0.5}O_2$ phase obtained with the microemulsion synthesis [50,139–142].

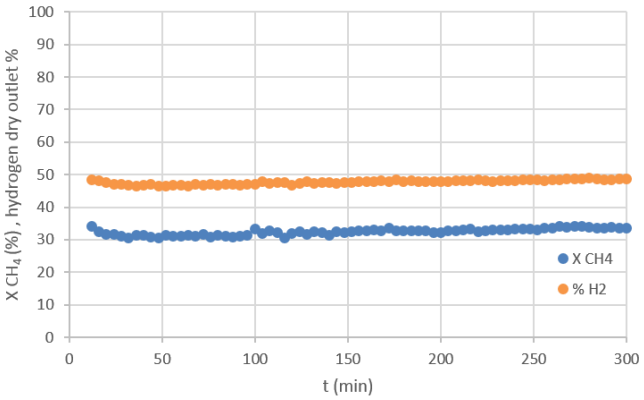

Figure 92: Methane conversion and hydrogen dry outlet percentage obtained on Rh0.05-CL-R-ZOm tested at 750 °C, 30,000 h^{-1}, 1 atm and S/C 1.5.

Having assessed the higher conversion of the cluster-based catalysts at 750 °C, the tests were also conducted at 500 °C. Figure 93 highlights the methane conversion and hydrogen dry outlet concentration versus the reaction time on the two CZOm-supported catalysts.

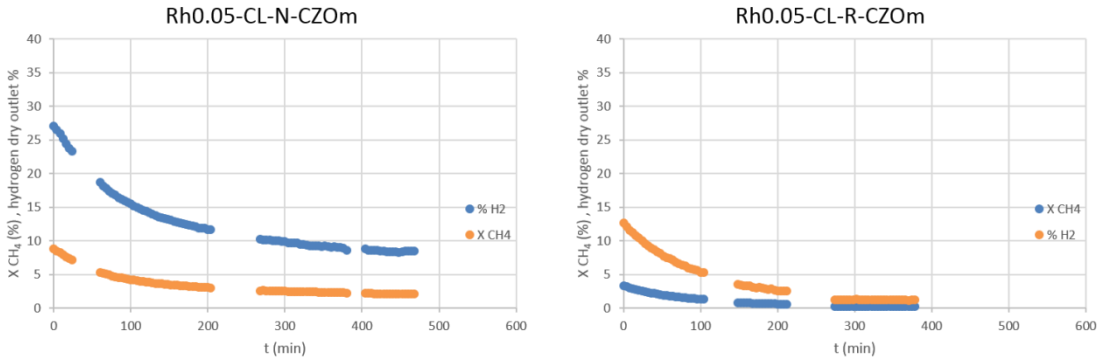

Figure 93: Methane conversion and hydrogen dry outlet percentage obtained on Rh0.05-CL-N-CZOm (left) and Rh0.05-CL-R-CZOm (right) tested at 500 °C, 30000 h^{-1}, 1 atm and S/C 1.5.

The unreduced catalyst provided an initial conversion of circa 9%, while the reduced one gave an initial lower conversion (3%). It has been experimentally demonstrated that hydrogen treatment favors the formation of larger particles [133], and this phenomenon could explain the lower activity of the reduced catalyst with respect to the not-reduced one. In order to explain the deactivation phenomena that took place in both catalysts, it is important to consider that the reaction environment at low temperature is an oxidizing one due to: i) the low amount of produced hydrogen related to lower kinetics of the catalyst, and also related to the low amount of active phase; ii) the high concentration of water. All this could favor the oxidation of Rh, which is faster when small particles are present, i.e., in the unreduced sample. The oxidation is very likely favored by the presence of Ce(IV) and the high oxygen mobility. The possibility to ascribe the deactivation to sintering of the active phase during reaction can be excluded, since small Rh particles were still found on the unreduced spent catalyst, as evidenced by TEM, where it is clear that the Rh metal particles are only slightly larger (centered between 1.5 and 2.5 nm, Figure 94) than those found on the fresh catalyst.

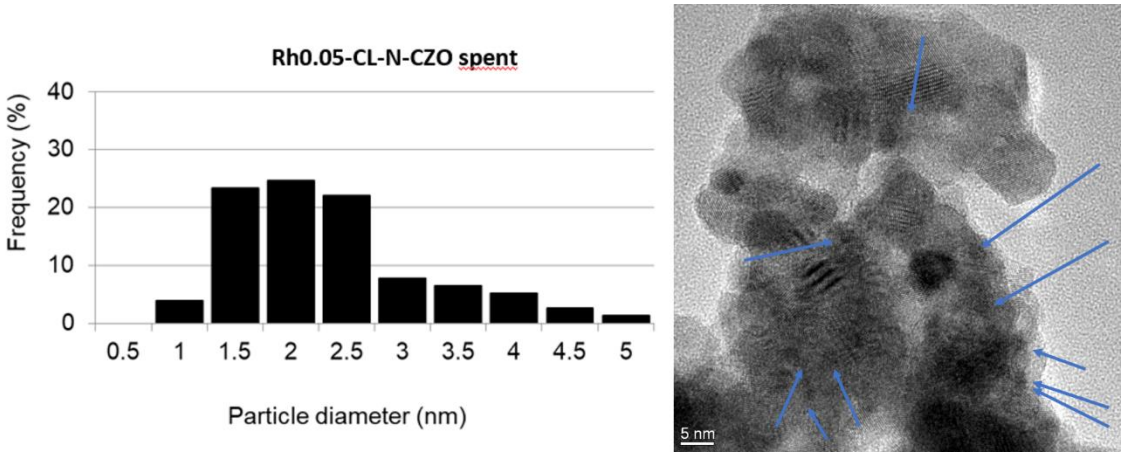

Figure 94: Particle size distribution of the spent Rh0.05-CL-N-CZOm determined via TEM analysis.

The catalytic performances of the Rh cluster deposited on ZOm, both not reduced and reduced (Rh0.05-CL-N-ZOm and Rh0.05-CL-R-ZOm), are shown in Figure 95.

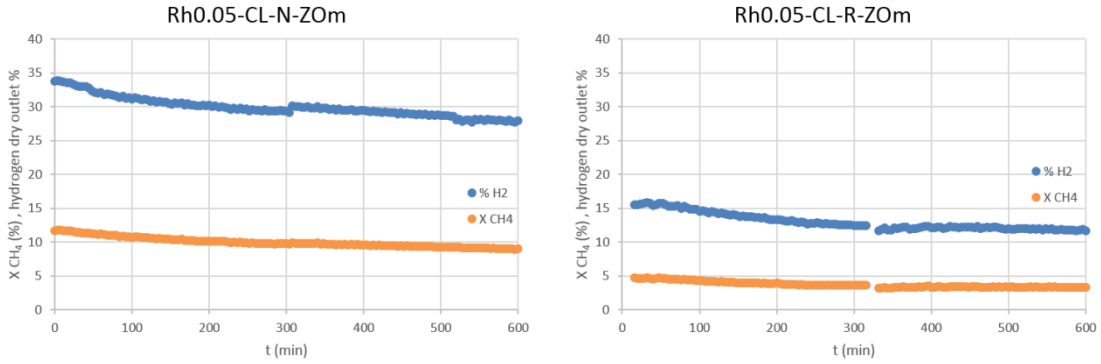

Figure 95: Methane conversion and hydrogen dry outlet percentage obtained on Rh0.05-CL-N-ZOm (left) and Rh0.05-CL-R-ZOm (right).

The initial conversion of the not-reduced catalyst (10.2%) was higher than the one reached with the CZOm-deposited cluster. Moreover, the fast deactivation that characterized the CZOm-based catalysts was not observed in this case, indicating that the presence of Ce favors the oxidation of the Rh. The reduced catalyst was stable too, but produced a lower conversion than the unreduced one, owing to the larger particles formed during the reduction step [133].

8.5.1. Investigation on Deactivation

It is particularly interesting to elucidate the mechanism of catalyst deactivation, since no such investigation on carbonyl cluster-derived catalyst is reported in literature, since very

few low-temperature studies have been carried out. Having observed that the deactivation was related to the presence of Ce and the oxidizing environment, its cause was further investigated by TEM and EDS (Energy Dispersive X-ray Spectrometry) analyses. Having also excluded deactivation by sintering, and assessed the absence of carbon formed over the surface by TEM and Raman analyses, it was hypothesized that the deactivation was caused by the oxidation of the active particles favored by Ce, which is able to provide oxygen to the active phase thanks to its redox properties, enhanced by the oxygen mobility of the microemulsion catalyst [19].

This phenomenon benefits from the oxidizing environment found in the low-temperature SR conditions, in which a relatively low amount of hydrogen is produced together with high concentrations of unreacted steam. SAED (Selected Area Electron Diffraction) analyses were carried out during TEM on the Rh particles of the unreduced CZOm- and ZOm-supported catalysts, after reaction at low (500°C) and high (750°C) temperature with the same Rh loading (0.05% wt/wt). In all samples, the presence of Rh in the analyzed particles was evidenced by the EDS analyses. The spent ZOm-supported samples, both at 500 °C and 750 °C, showed the presence of metallic Rh, as well as the CZOm-supported catalyst after reaction at high temperature (Figure 96). Experimental d-values of 2.25 and 1.84 Å, in fact, could be attributed to the metallic Rh phase, while those at 3.10 and 2.61 Å are related to the support.

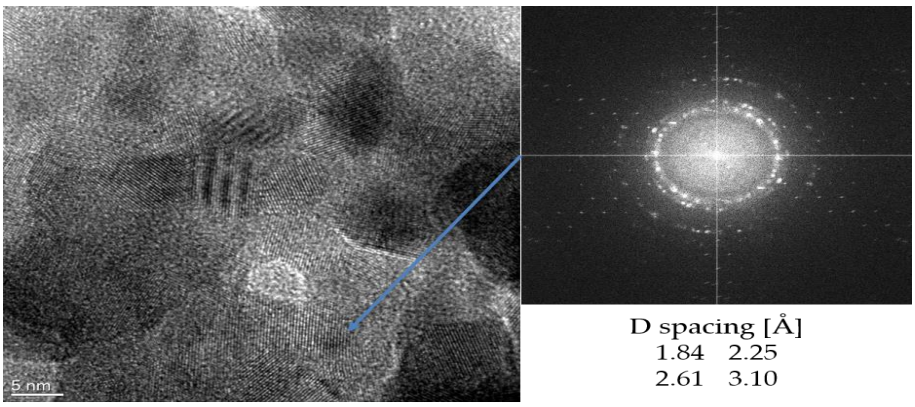

Figure 96: Selected Area Electron Diffraction (SAED) and TEM analyses carried out on an Rh containing area of the spent not-reduced CZOm supported catalyst after reaction at high temperature.

However, no such phase was observed in the spent CZOm-supported catalyst after reaction at low temperature (Figure 97); the measured d-values of 2.65 and 3.05 Å were attributed to the tetragonal phase of $Ce_{0.5}Zr_{0.5}O_2$. It was not possible to detect the presence of Rh oxide because its reflexes overlapped those of the support. Nonetheless, all these evidences can be confidently seen as an indirect confirmation that oxidation of Rh only occurred on the CZOm-supported catalyst after reaction at low temperature, which is the only one that showed deactivation.

The hypothesis of the oxidation of Rh is also substantiated by a computational study on metallic Rh clusters on CeO_2, which showed that they are stable in reducing conditions such as those obtained in the high temperature steam reforming, but that the relative oxide is formed in oxidizing ones [146].

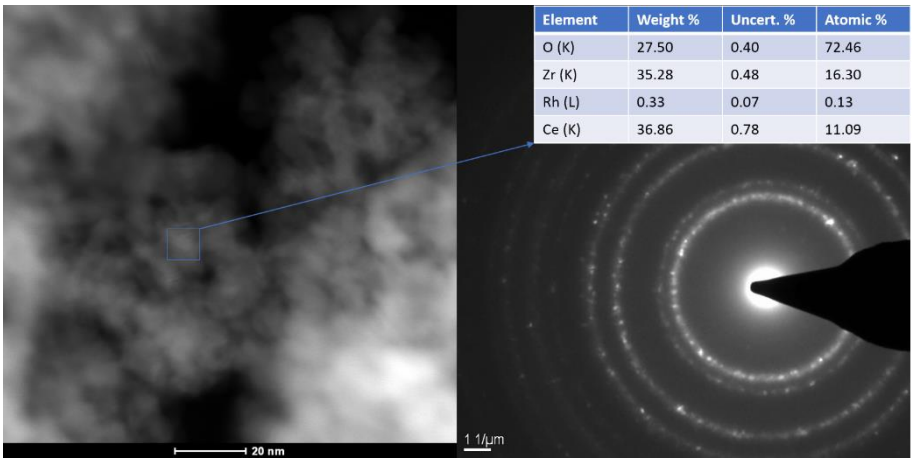

Figure 97: SAED and Energy Dispersive X-ray Spectrometry (EDS) analyses carried out on an Rh containing area of the spent not-reduced CZOm supported catalyst after reaction at low temperature.

Finally, a new catalyst was prepared by deposition of another cluster containing a higher amount of Rh atoms, namely $Rh_7(CO)_{16}K_3$. After the deposition the catalyst was just heated in nitrogen as this pretreatment gave better in the low temperature steam reforming than reduction in the previous tests. The results of the catalytic test, shown in figure 98 highlight an even faster deactivation of the cluster and a lower catalytic activity.

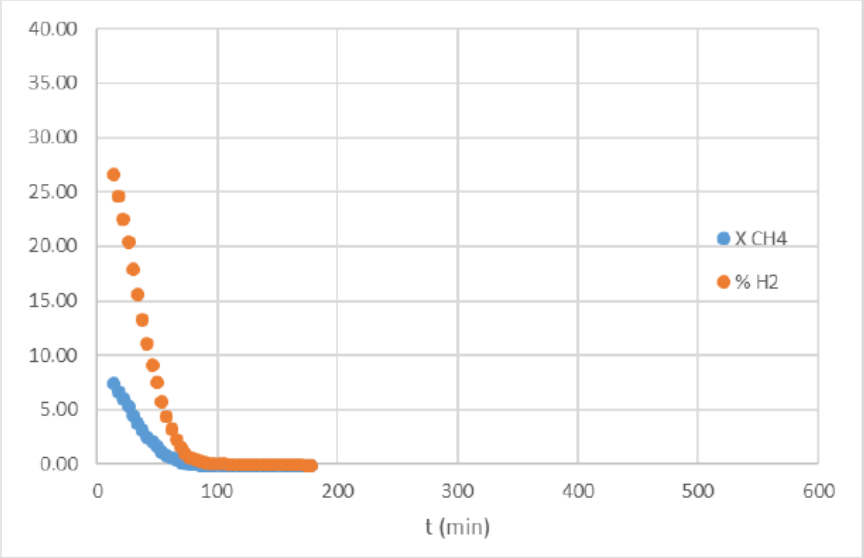

Figure 98: Methane conversion and hydrogen dry outlet percentage obtained on the catalyst obtained from the deposition of $Rh_7CO_{16}K_3$.

Again, the nature of the cluster itself seemed to play a role in the deactivation process. It was thus supposed that the deactivation may be due to the different interaction between the support and Rh which is found after the reactive deposition of the cluster compared to classical impregnation.

8.6. **Low temperature Steam Reforming on impregnated catalyst**

8.6.1. Effect of support composition and reduction temperature

The steam reforming reaction was also tested on impregnated catalysts (on CZO and ZO) at 500°C. Two reduction temperatures were selected and investigated for both Rh supported catalysts, namely 750°C and 500°C. The results of the test are shown below.

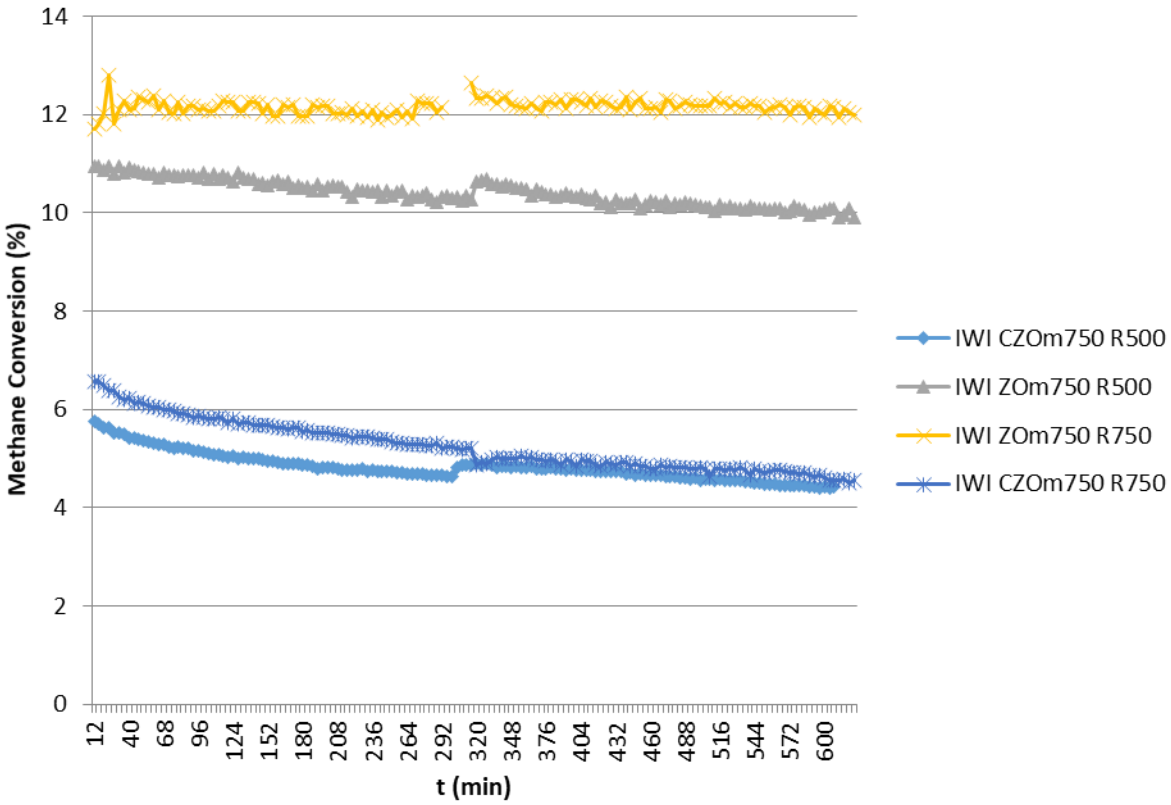

Figure 99: Methane conversion for the Rh0.05% catalyst impregnated on CZO and ZO and reduced at 500 or 750°C.

As in the case of low temperature tests on cluster-based catalysts, the ZO based ones outperformed those impregnated on CZO. In fact, an initial conversion of 12% and 11% was observed for the ZO catalyst reduced at 750°C and 500°C respectively, while only 7% and 6% initial methane conversions were given by the CZO catalysts. Noteworthy, the conversion obtained by the ZO impregnated catalyst is similar to that given by the cluster-based ones treated in the previous paragraph. On the opposite, the initial conversion of the CZO impregnated systems were lower than those of the clusters, but a higher stability was observed in this case. The improved activity of the ZO catalyst can be explained by looking at the TPR analyses of the ZO and CZO samples reported in the figure below. Actually, this analysis was done on the impregnated catalyst with a rhodium loading of 1%, which was then diluted to 0.05% in the final catalyst, as peak identification in the latter was difficult because of the low amount of reducible Rh present.

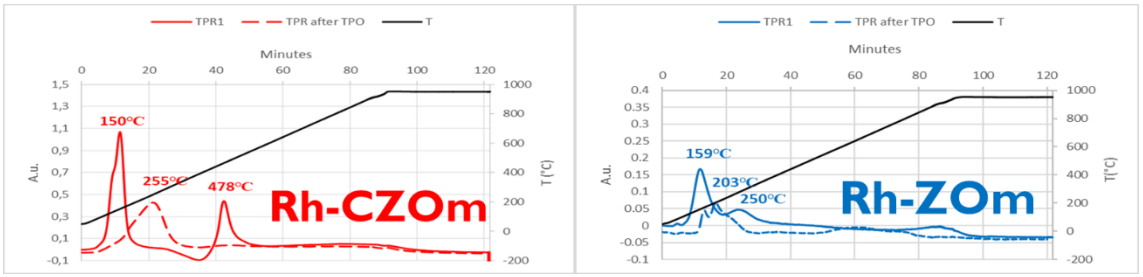

Figure 100: TPR analysis of Rh1%-CZOm750 and Rh1%-ZOm750

Table 32: Hydrogen consumption by TPR for Rh-CZOm and Rh-ZOm.

H_2 consumption (mmol/g)	***TPR1***	***TPR2***
Rh-CZOm	0,89	0.68
Rh-ZOm	0.28	0.12

Even though the CZO based sample displays the first reduction peak at a slightly lower temperature than the ZO supported sample, the trend is inverted after the TPO, where the latter displays peaks at lower temperatures, due to a shift of the reduction peaks of the CZO sample caused by the homogeneous reduction between Ce and Rh. This kind of metal support interaction seems to lower the redox properties of Rh. The hydrogen uptake for the CZO based catalyst is higher than the ZO one due to the presence of Ce, which is reducible and reduced during the analysis.

Regarding the reduction temperatures the obtained conversions were quite similar, but a slight increase could be obtained by reducing the catalyst at 750°C. This is due to a more homogeneous reduction obtained at higher temperatures which provided an increased surface metal availability.

Finally, the deactivation observed in the CZO samples was thought to be related of a strong metal support interaction between the support and the metallic active phase. In order to investigate this phenomenon TPR-TPO cycles were carried out on the catalyst precursor before reduction (figure 101). The results of the TPR show a modification of the reducibility of the sample after multiple TPR-TPO cycles, with a decrease in the temperature at which the reduction start. On the opposite, the hydrogen consumption is constant through the cycles, suggesting that the amount of surface Rh decreases but not its spillover property.

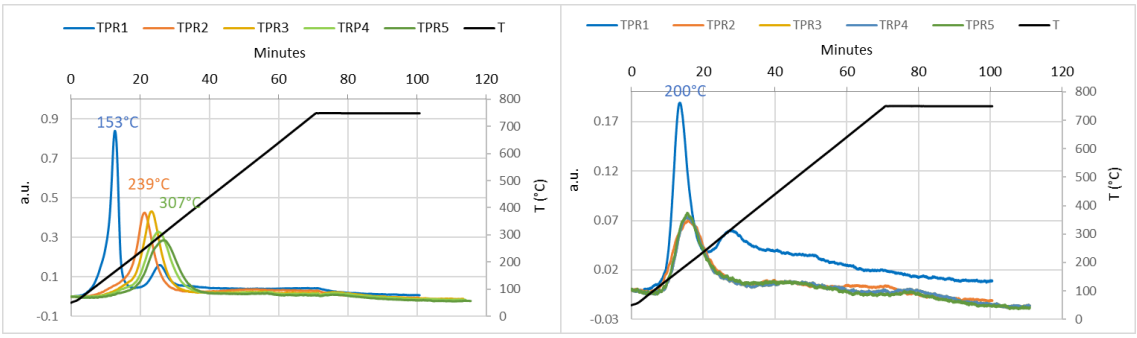

Figure 101:Repeated TPR cycles analyses on of Rh1%-CZOm750 and Rh1%-ZOm750.

Hydrogen consumption by TPR for Rh-CZOm and Rh-ZOm.

H_2 consumption (mmol/g)	***TPR1***	***TPR2***	***TPR3***	***TPR4***	***TPR5***
Rh-CZOm	0.56	0.50	0,51	0.51	0.50
Rh-ZOm	0.36	0.14	0.14	0.16	0.14

The SMSI was confirmed by TEM analysis on the sample treated in the TPR cycles repeated five times. The analysis showed that some metallic particles have been decorated by the CeZr support, as shown in figure 102. The partial encapsulation of metal particle by the support decreases the metallic surface area and leads to deactivation.

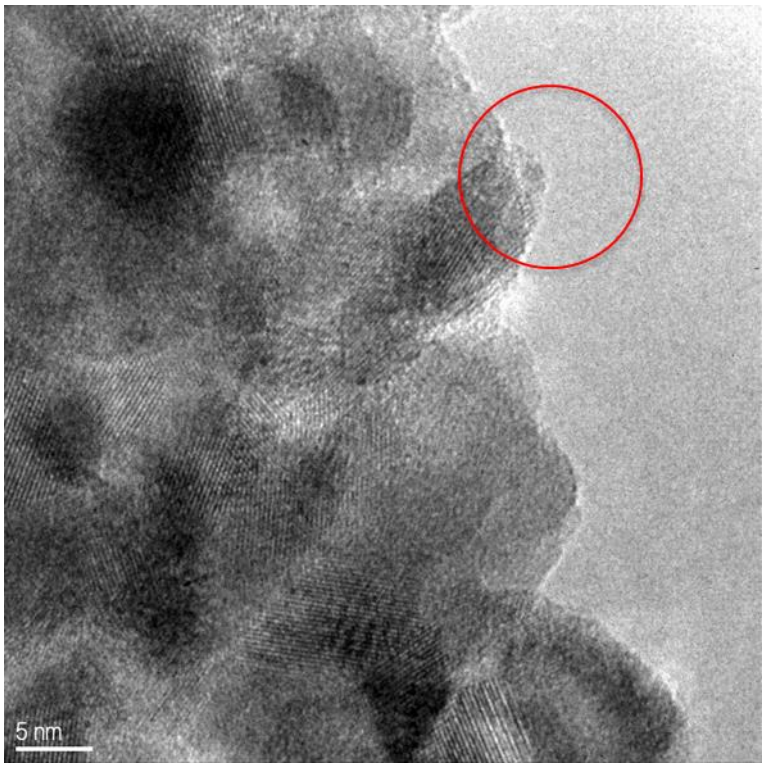

Figure 102: TEM analysis on the sample treated in the TPRORORORORORcycle.

8.6.2. Investigation of the fluid dynamic parameters

The Rh0.05% impregnated over zirconia was selected as catalyst for the membrane reactor due to its good performances and stability in the screening tests. However, this catalyst was not able to reach the equilibrium conversion because of the low amount of active phase employed and worked then under a kinetic regime. However, the obtained results were used to estimate the amount of active phase that is needed in the membrane reactor to obtain a sufficient hydrogen partial pressure for separation. In particular, the catalyst turnover frequency can be derived and then used to estimate the needed amount of active phase to employ in the membrane reactor. TOF can be calculated only if transport limitations and temperature gradients over the catalyst are avoided as these may contribute to the conversion value, thus not allowing such calculation. For this reason, a fluid dynamic study was carried out to exclude the occurrence of such phenomena, modifying the fluid dynamic parameters. In particular, tests were conducted:

1. Reducing pellets dimensions from 30-60 mesh to 60-80 mesh
2. Halving the mass of charged catalyst from 1,0 to 0,5 g and concurrently halving the space velocity.
3. Diluting part of the Rh0,05%-ZO used catalyst with pure zirconia to make a Rh loading of 0.025% and halving the space velocity.

If similar conversions are obtained, it means that these parameters do not significantly affect the methane conversion, which is thus only related to Rh amount.

8.6.2.1. Different pellets dimension

The methane conversion (experimental and equilibrium) obtained after reducing the pellets dimension is shown in figure 103. Different conditions were investigated at 450°C, both atmospheric pressure and 10 atm, changing the S/C from 1.5 to 2. At atmospheric pressure and different S/C, the conversions obtained were very close indicating that no transport limitations occur in these conditions. Moreover, changing the pellets dimensions, also changes the temperature distribution over the pellets. However, conversion is not influenced by this phenomenon in this case.

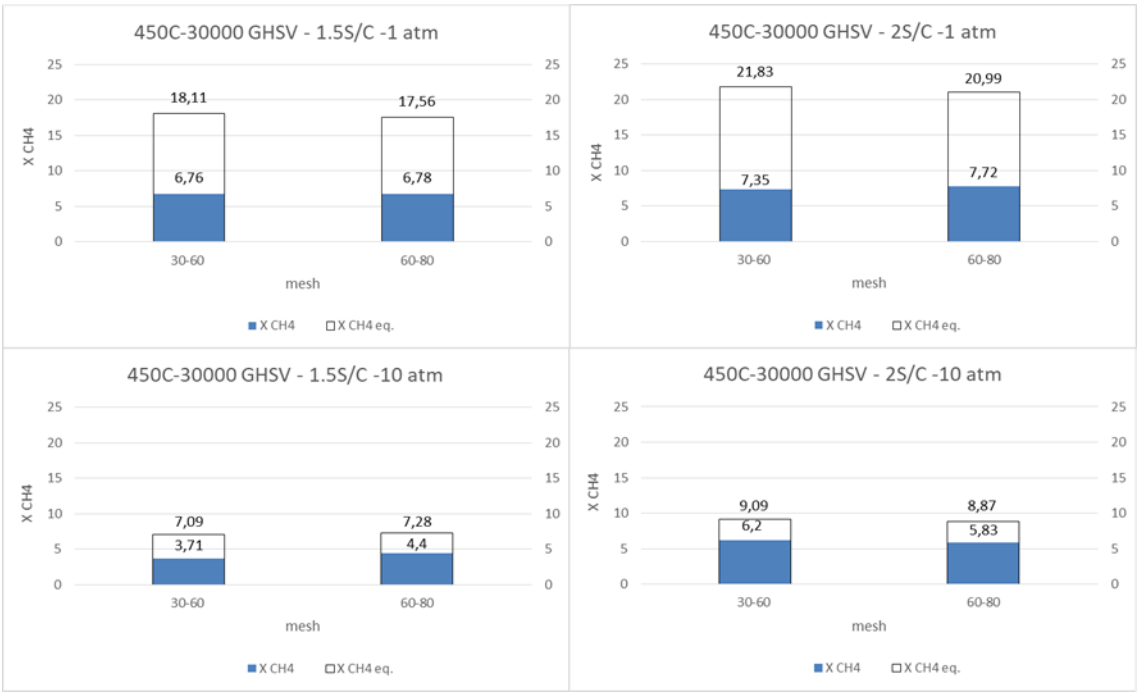

Figure 103: Experimental and equilibrium conversions under different conditions for the catalyst with pellets dimension of 30-60 mesh and 60-80 mesh.

8.6.2.2. Different catalytic bed length

In this second series of tests catalysts with 60-80 mesh and 0.05% of Rh were investigated. In particular, one test was conducted over 1.0 g of catalyst while another on 0.5 g, thus reducing the catalytic bed length. However, the inlet flow was halved in the test on 0.5 g of catalysts thus maintaining the same GHSV. By halving the grams of catalyst, similar conversions are obtained at atmospheric pressure. At higher pressures, a higher conversion was obtained for the standard sample (1.0 g), which again suggests that mass transfer phenomena may affect the experimental methane conversion. However, it must be noted that such small changes in methane conversion may also be related to mass flow controller imprecision as small fluxes at high pressures are sent, which may affect its accuracy.

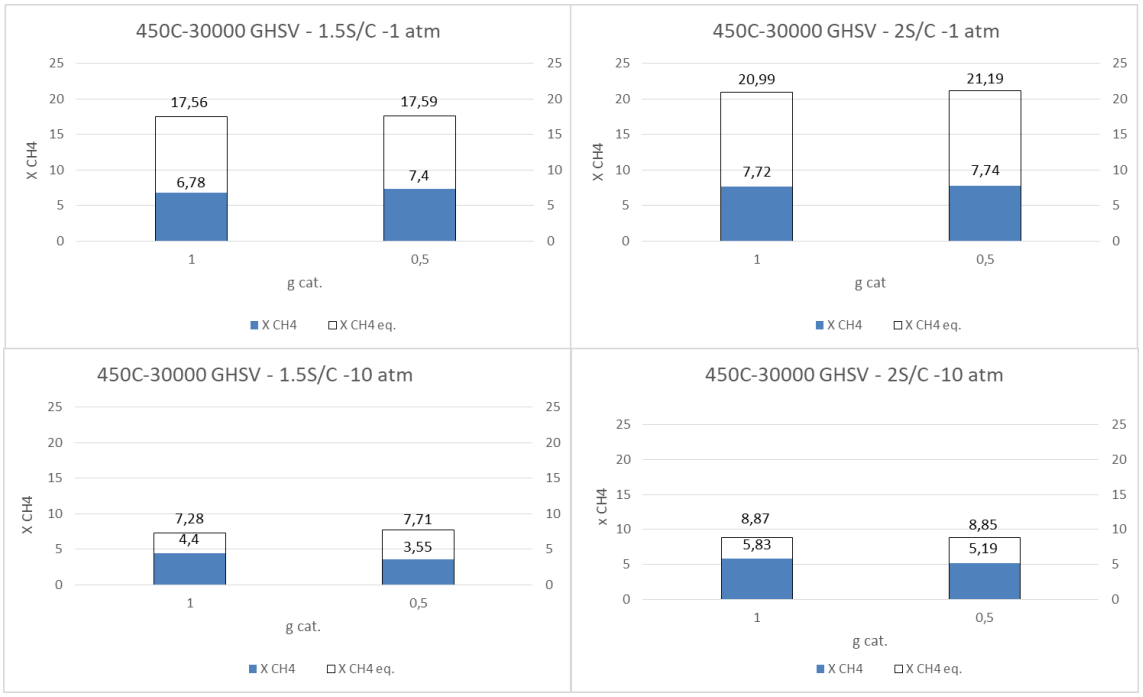

Figure 104: Experimental and equilibrium conversions under different conditions at same GHSV for 1.0 and 0.5 grams of catalyst.

Thus, limitations given by the fluid dynamics of the catalytic bed can be excluded. Moreover, also the temperature distribution is different in the two tests but the presence of temperature gradients that influence the methane conversion and catalytic performances can be excluded. In fact, a comparison of the catalytic temperature profiles for the test shows a slight difference, which is caused by the difference in the catalytic bed length (figure 105). However, the conversion is not consistently influenced by this difference.

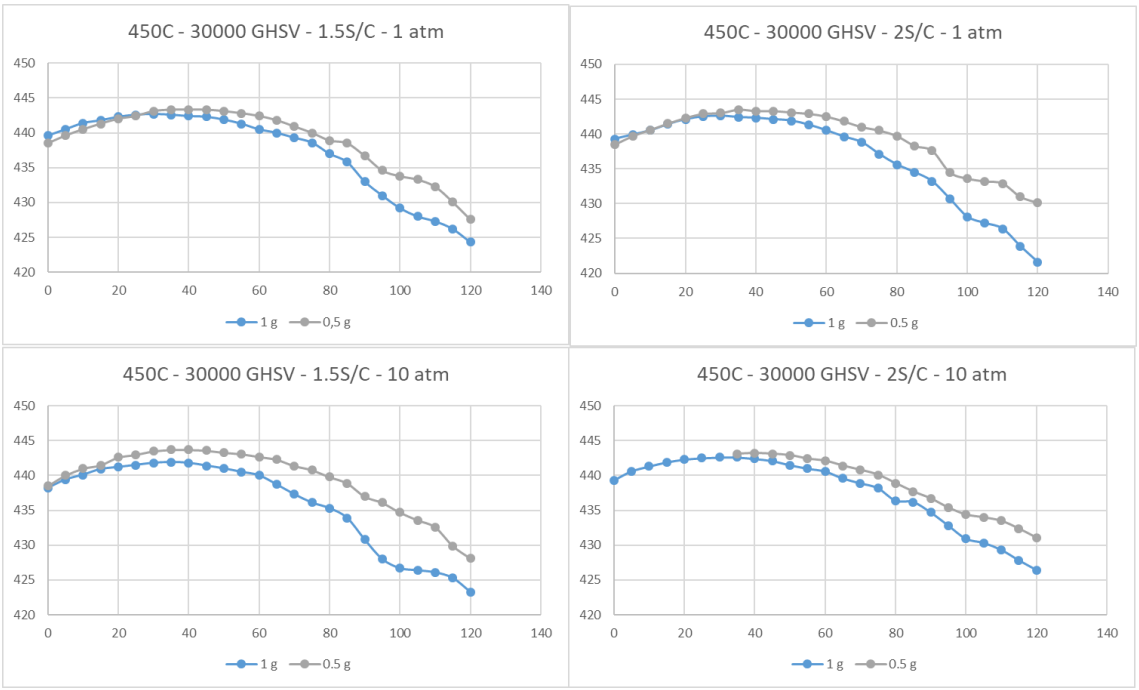

Figure 105: Temperature profile of the catalytic bed for the test conducted under different conditions at same GHSV for 1.0 and 0.5 grams of catalyst.

8.6.2.3. Effect of dilution

Finally, a spent catalyst from the previous tests was diluted with pure zirconia to get a total Rh loading of 0.025% and tested halving the inlet flow. In this case, lower conversions were obtained which may indicate that Rh distribution over the catalytic bed affects the fluid dynamic behaviour of the catalyst, hence its apparent activity. However, the decrease in conversion may also be due to the occurrence of slight deactivation over the used catalyst or to impurities related to mixing with the quartz used as inert material in the reactor which is not easy to detect and separate from the discharged catalyst.

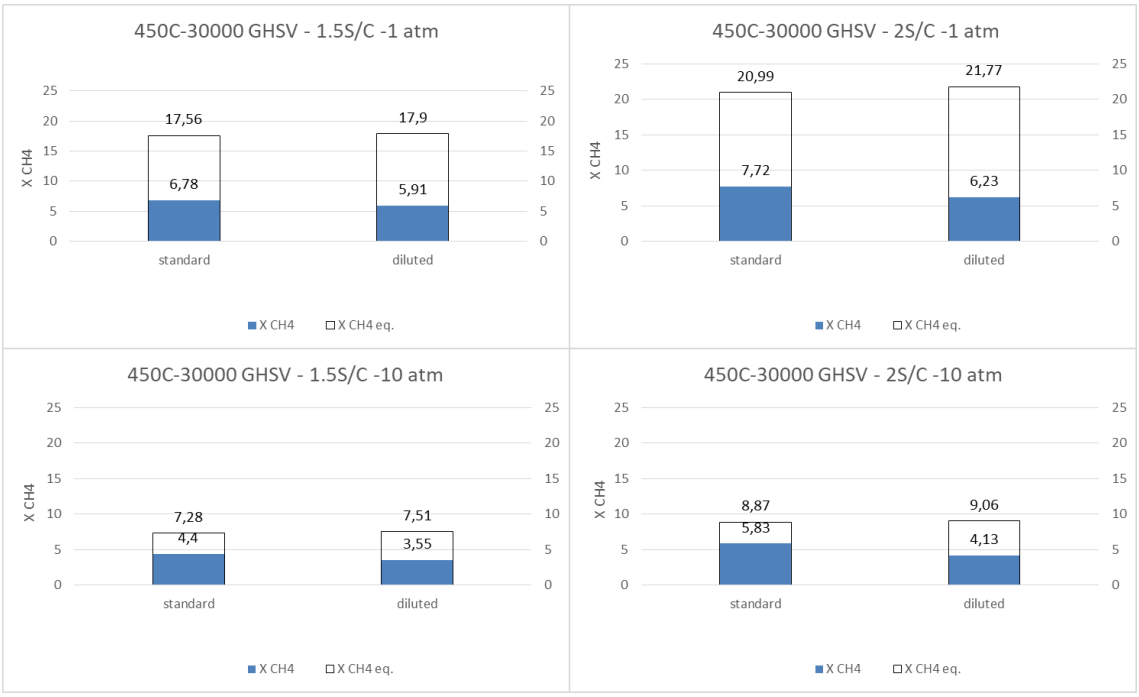

Figure 106: Experimental and equilibrium conversions under different conditions at constant GHSV calculated on Rh amoun for the catalyst at 0.05% and diluted to 0.025%.

In general, it can be affirmed that the fluid dynamic parameters only slightly affect the methane conversion and thus, a turnover frequency value for the Rh-ZO catalyst can be calculated with some approximation relate to the fluid dynamic behaviour at high pressure.

The calculated TOF are reported below:

Table 33: Turnover frequencies calculated in different conditions.

Conditions	TOF [(mol conv. CH4)/(mol Rh*s)]
450°C-30000 h^{-1}-S/C 1.5-1 atm	0.99
450°C-30000 h^{-1}-S/C 2.0-1 atm	1.08
450°C-30000 h^{-1}-S/C 1.5-10 atm	0.65
450°C-30000 h^{-1}-S/C 2.0-10 atm	0.85

The TOF was used to calculate the Rh loading to impregnate on zirconium oxide to obtain a sufficient conversions in the membrane reactor. This value was found to be 0.75% wt/wt. Thus, a Rh0,75%IWI-ZOm catalyst was synthetized. However, it must be noted that an

assumption was used in this calculation, i.e. that the TOF does not vary with the metal loading.

8.7. **Conclusions**

Rh-based catalysts were obtained by using the $Rh_4(CO)_{12}$ neutral cluster the active-phase precursor. In particular, the preparation method allowed the reactive deposition of the cluster on the surface of $Ce_{0.5}Zr_{0.5}O_2$ and ZrO_2 supports, which were synthetized by w/o microemulsion technique. The catalysts were found to be active in the low-temperature steam reforming process for syngas production. At high Rh loadings (0.6%) the CZOm-supported catalyst was active even at 350°C and was able to reach the equilibrium conversion, especially at low S/C ratio or at high pressures at 450 and 500°C. At lower concentrations (0.05%) and high temperature, the CZOm-supported cluster sample showed better results with respect to the analogous ZOm-supported one and to a classical Rh-impregnated CeZr catalyst. At low temperature, a deactivation effect was observed for the CZOm-supported catalyst, which could be overcome by employing a ZOm support. A detailed analysis provided evidences that the oxidation of the Rh promoted by Ce and high oxygen mobility was responsible for the fast deactivation. In these conditions, it was also observed that the cluster-based catalyst which had not been treated with hydrogen at 500°C was more active than the treated one, due to the sintering of the Rh particles. Finally, the unreduced 0.05% Rh cluster deposited on the ZrO2 support showed significant activity at 500°C.

The low temperature steam reforming was also investigated on CeZr and Zr impregnated catalysts using Rh as active phase. Rh on zirconium oxide provided higher conversion and stability than the CeZr one. This was related to a decrease of the redox properties of Rh over CZO due to strong metal-support interaction given by the presence of Ce. For this reason, zirconium oxide (ZO) was selected as support to be used in the membrane reactor. The turnover frequency of Rh-ZO was calculated using low Rh amounts, after assessing the absence of mass transfer phenomena with a fluid dynamic study. The turnover frequency was used to calculate the optimum amount of Rh to be employed in the membrane reactor under steam reforming conditions, which resulted to be 0.75% wt/wt. This loading was

higher than 0.6%, which was able to reach the equilibrium in the fixed bed tests. In fact, the presence of the membrane reactor allows to shift the equilibrium value. The 0.75% loading was calculated taking this in account.

9. CHAPTER 9 - CATALYTIC STEAM REFORMING IN A MEMBRANE REACTOR

9.1. Introduction

Having calculated the TOF of the Rh-ZO catalyst, this value was used to estimate the amount of active phase necessary to provide the membrane reactor with the desired amount of hydrogen. In particular, this was done by taking into consideration a particularly favourable condition, i.e. 10 atm S/C 2 and 450°C, with a sweep gas flow that allowed to have a hydrogen partial pressure of 0.2 atm at the permeate side. From these data a Rh loading of 0.75% was evaluated to be necessary to allow efficient permeation in those conditions.

9.2. Catalyst characterization

The Rh0.75%-ZO catalyst was reduced at 750°C overnight and then characterized by means of XRD analysis, nitrogen physisorption and TEM.

XRD analysis showed that the tetragonal phase obtained for zirconia with the microemulsion synthesis is unstable when submitted to harsh conditions (figure 107). In

fact, part of the tetragonal phase was converted into the monoclinic one after reduction at 750°C overnight. The absence of observable Rh phases is related to its low amount and high dispersion.

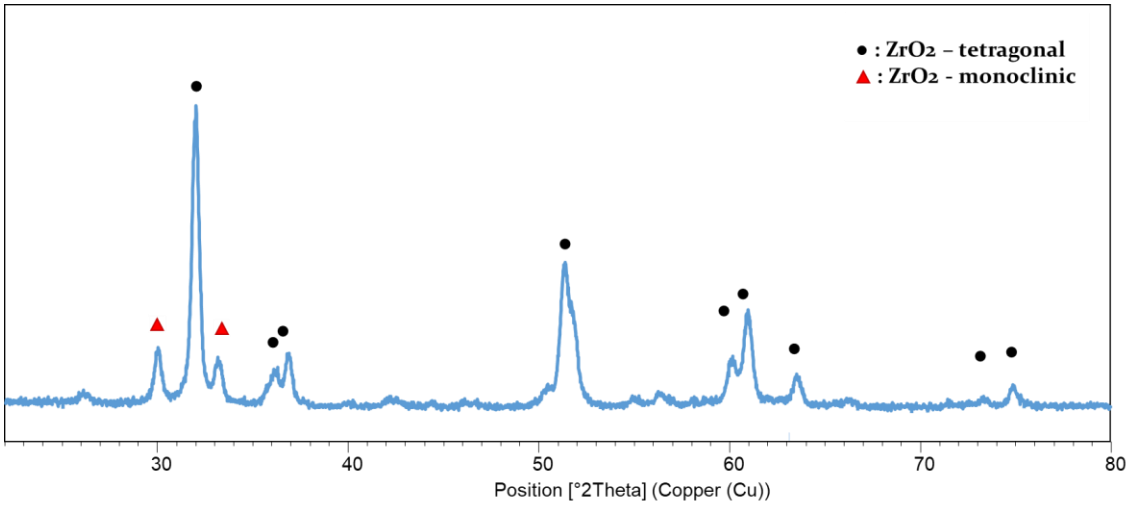

Figure 107: XRD of the ZOm sample synthesized by microemulsion and calcined at 750°C after reduction at 750°C.

As also reported in chapter 4, nitrogen physisorption analysis showed that the reduced catalyst possessed a surface area of 29 m^2/g, with wide pores of 11.7 nm and a total pore volume of 0,10 cm^3/g. A slight sintering of support may have occurred due to the reduction treatment during which the sample was kept at 750°C overnight.

Table 34: Surface area, pores volume and average pores diameter of Rh0.75%-ZO.

	Surface Area (m2/g)	***Pores Vol. (cm3/g)***	***Avg. Pore Diam (nm)***
ZOm750	29.5	0.10	11.7

Finally, TEM analysis was conducted on the reduced catalyst (figure 108). The obtained images showed the presence of well-dispersed, small particles. Particle size distribution was narrow and centred between 1 and 2 nm.

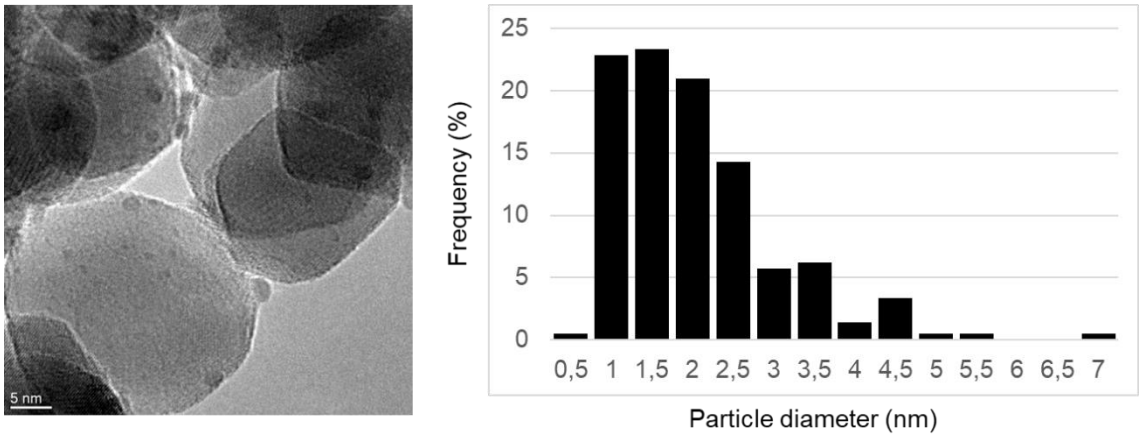

Figure 108: TEM analysis conducted on the reduced Rh0.75%-ZO catalyst.

9.3. **Membrane characterization**

6.8 g of this catalyst weas loaded inside the tubular membrane, which was mounted in a stainless-steel module, represented in the experimental (figure 20) The module was then heated up to 400°C and maintained at this temperature during the period of the tests. To avoid a different expansion between the alumina support and the Pd layer, which could lead to membrane damage due to crack formation, the preheating process was carried out at 1°C/min.

The membrane works with the mechanism as represented in figure 109 The inlet gas passes inside the tubular membrane, where the catalyst has been placed. There the reaction occurs, and the thus produced hydrogen permeates through the membrane walls in the permeate side. The unseparated hydrogen, unconverted methane and steam and CO and CO_2 exit the tubular membrane outlet, which is called the retentate stream.

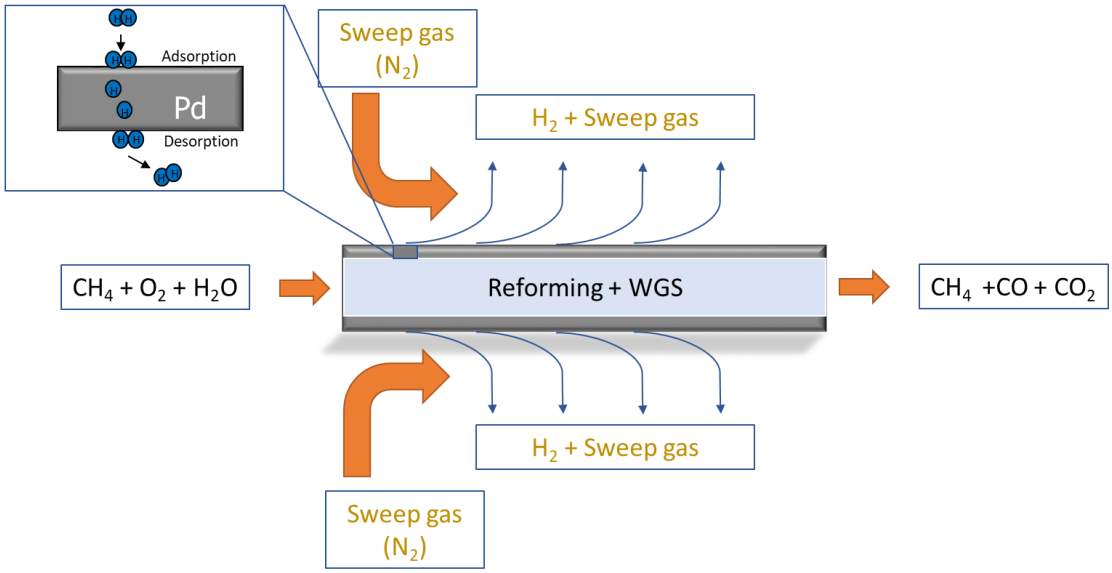

Figure 109: Schematic representation of the membrane reactor

Before activity tests, nitrogen permeation tests were carried out by fluxing a stream N_2 at pressures between 1.5 and 6 atm and calculating the flow at the permeate side. This was found to be negligible at all the conditions thus ruling out the presence of any defect in the Pd layer, which could allow the passage of the reaction mixture in the permeate.

Hydrogen permeance was evaluated by analysing the permeate flow at different pressures after sending a high flux of hydrogen (2 l/min) inside the membrane at different pressures (from 1.5 atm to 2.75 atm, increasing the pressure by 0.25 atm after each test). The hydrogen permeance was evaluated at 400, 425 and 450°C.

At a given temperature, the hydrogen permeation occurs through the following steps [157,158]: (i) adsorption of hydrogen; (ii) dissociation of hydrogen molecules into atoms, (iii) diffusion of hydrogen atoms from the Pd surface layer, through the membrane bulk, to the other side of Pd surface layer; (iv) recombination of hydrogen atoms to form hydrogen molecules; (v) desorption of hydrogen molecules from Pd surface. This process follows the equation:

$$JH2 = \frac{Pe_{H2}(p^n{}_{H2},\mathrm{ret} - p^n{}_{H2},\mathrm{perm})}{\delta}$$

where JH2 is the hydrogen flux permeating through the membrane, Pe_{H2} the hydrogen permeability, p_{H2},ret and p_{H2},perm the hydrogen partial pressures in the retentate and permeate sides, n (ranging within 0.5 and 1) the dependence factor of the hydrogen partial

pressure and d the membrane thickness. The “n” factor is used as an indicator for the rate-controlling step of the permeation. If the diffusion of atomic hydrogen through the dense metal layer is rate limiting, the equation above becomes the Sieverts-Fick’s law [159], where the hydrogen permeating flux is directly proportional to the hydrogen partial pressure (elevated at 0,5) difference between the two sides of the membrane:

$$JH2 = \frac{Pe_{H2}(p^{0.5}{}_{H2},\mathrm{ret} - p^{0.5}{}_{H2},\mathrm{perm})}{\delta}$$

The results of the permeability tests are reported in the figures below. In particular, J_{H2} was obtained experimentally by measuring the permeate hydrogen flux, while P_{H2} in retentate and permeate was set by the experiment conditions, hence the reactor pressure.

To confirm that the membrane was working under the Sievert Fick law, the n value was experimentally evaluated by plotting the obtained data of J_{H2} as function of (p^{n}_{H2} ret – p^{n}_{H2} perm), using different n values. The n value to be used to calculate the permeance was obtained by looking at the R^2 value and choosing the plot with the highest one. This resulted to be n=0.5 as show in figure 110. This confirms that diffusion of atomic hydrogen through the dense metal layer is rate limiting

The permeance (indicated as Q= Pe_{H2}/ δ) was thus evaluated using the Sievert Fick law: It was estimated as the slope of the obtained curve. A high permeance of 110.91 $mL \cdot cm^{-2} \cdot min^{-1} \cdot atm^{-0.5}$ was calculated.

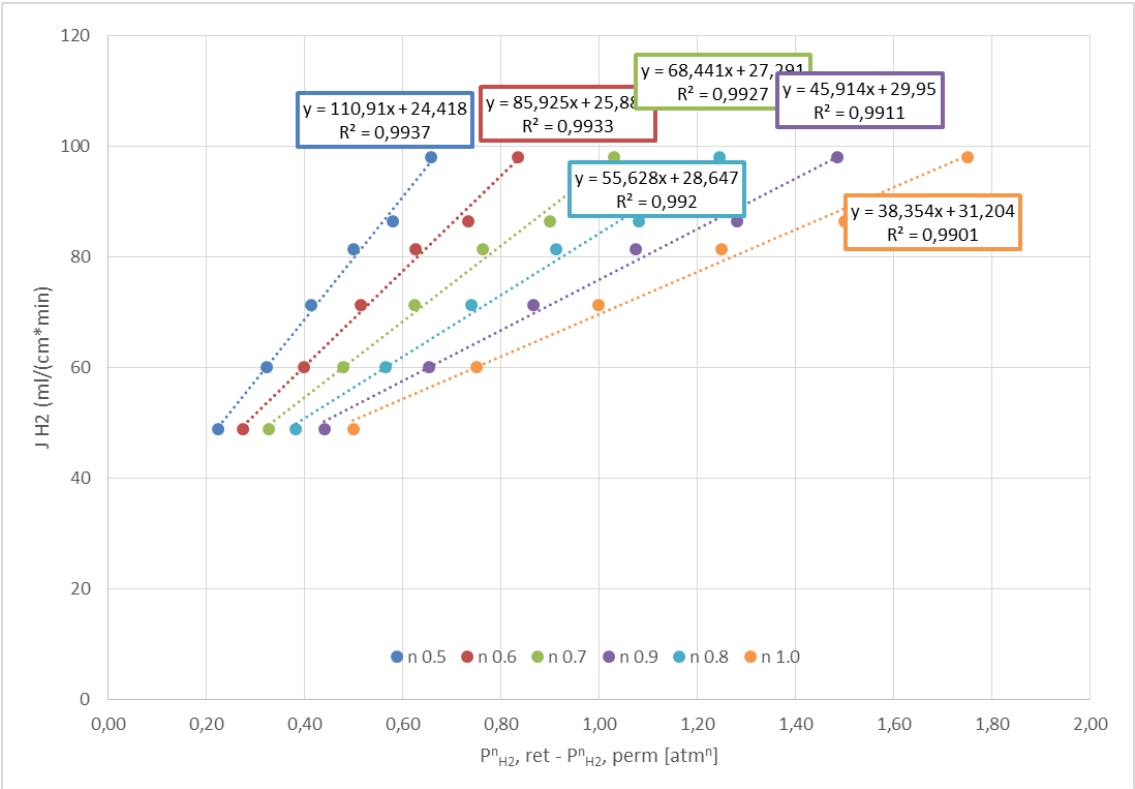

Figure 110: Membrane hydrogen permeance at 400°C.

The relation between the membrane temperature and permeance was evaluated by increasing the membrane temperature to 425°C. In this case a very similar permeance was obtained with a value of 109.07 $mL \cdot cm^{-2} \cdot min^{-1} \cdot atm^{-0.5}$.

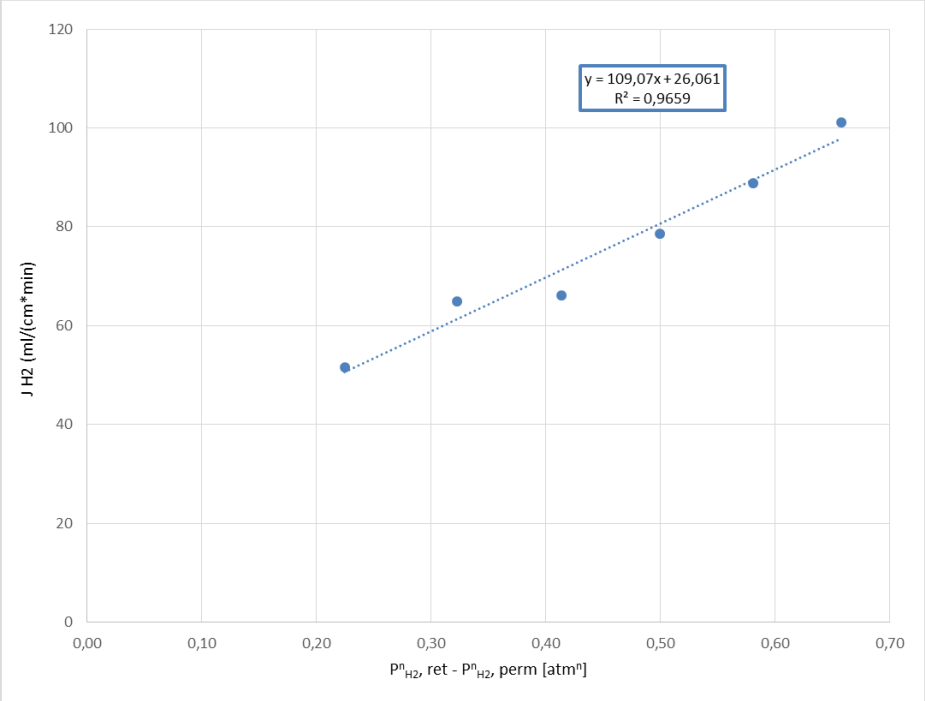

Figure 111: Membrane hydrogen permeance at 425°C.

However, the membrane permeance could be further increased by raising the temperature to 450°C. In this case, a permeance of 120.10 $mL \cdot cm^{-2} \cdot min^{-1} \cdot atm^{-0.5}$ was calculated.

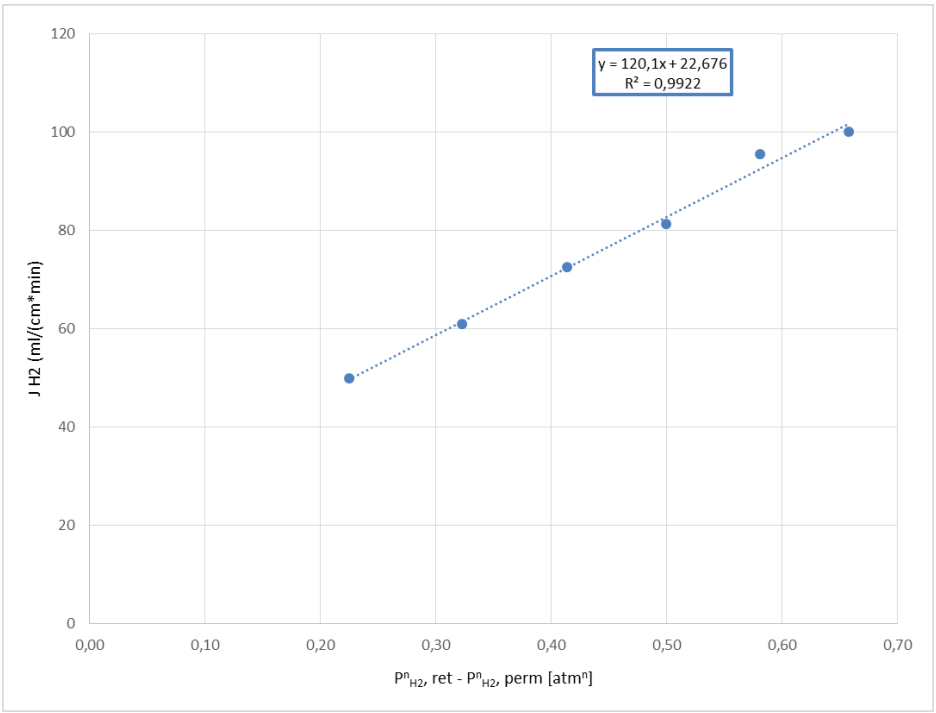

Figure 112: Membrane hydrogen permeance at 450°C.

These tests were repeated after the catalytic tests to evaluate if they caused any decrease in membrane performances. It was demonstrated that no drop in membrane performances occurred during the tests, regardless of the operative conditions.

9.4. Catalytic tests in a membrane reactor

At first the catalytic tests were performed at 400°C to avoid the degradation of the membrane which could occur at higher temperatures due to crack formation. The effect of pressure was investigated at first by increasing it from 3 to 5 and finally to 10 atm. However, the latter test was done after investigating the effect of sweep gas at 5 atm. The membrane showed a total selectivity toward hydrogen and no other gas was detected in the permeate.

In general, the increase of total pressure in the retentate has two opposite effects: a decrease of equilibrium conversion due to the thermodynamics of methane steam reforming and an increase in hydrogen partial pressure. The latter raises the separation driving force and produces a shift effect which increases the hydrogen production and methane conversion due to the removal of one of the products.

The results of the tests at different pressures are reported in figure 113. It shows a positive effect of pressure when this was increased from 3 to 5 atm, with the methane conversion increasing from 43% to 62%

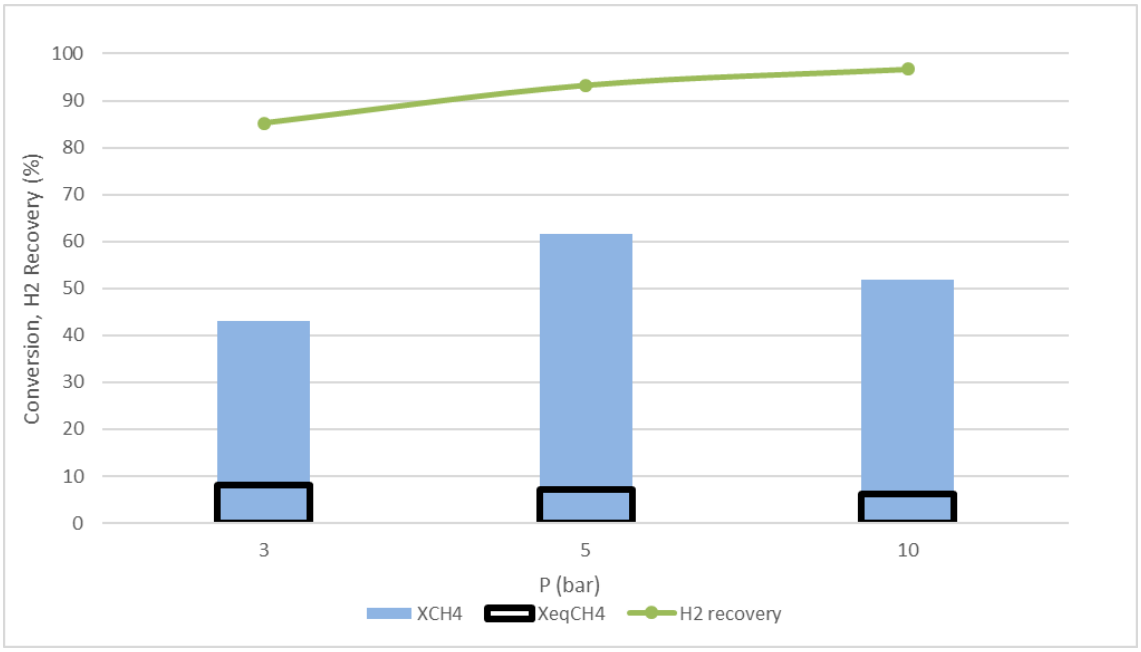

Figure 113: Effect of pressure on methane conversion and hydrogen recovery in the membrane reactor at 400°C, 2400 h^{-1}, sweep factor 10.5 and S/C 2.

The experimental conversion was found to be over the equilibrium value for a fixed bed reactor thanks to hydrogen removal from the reaction environment, which favoured the reaction thanks to the Le Chatelier principle and the creation of a dynamic equilibrium. Thus the positive effect of the equilibrium shift given by the increased partial pressure overcame the disadvantageous equilibrium drop that was given by the higher total pressure. This allowed to increase the pure hydrogen production rate. This was observed in all the membrane reaction tests where higher conversions than the equilibrium value (of a fixed bed reactor) were obtained. Nevertheless, the employment of sweep gas was fundamental to allow permeation, as the hydrogen partial pressure developed inside the retentate was lower than 1 atm. A sweep gas is a gas that passes in the permeate, removing hydrogen and reducing its partial pressure. It affects the last step of permeation, namely hydrogen desorption from the Pd surface. Thus, it helps to increase the permeation driving force.

The membrane was able to separate all the hydrogen possible and showed an outlet hydrogen partial pressure difference that approached 0.1 atm, indicating low driving force at the end of the membrane. This resulted in very high hydrogen recoveries of 85% at 3 am and 93% at 5 atm.

Surprisingly the conversion dropped to 52% at 10 atm. This seemed related to a deactivation phenomenon which lowered the catalytic activity and did not allow to increase further the methane conversion in spite of the higher driving force for separation given by the increased total pressure. In fact, the membrane was able to separate hydrogen with recovery of 97%, showing a low difference in pressure at the end of the catalytic bed and a high hydrogen recovery. The occurrence of deactivation was confirmed by repeating the test at 5 atm and sweep factor 10.5, which in this case provided a lower methane conversion of 51%. (figure 117), instead of 62%.

On the opposite a hydrogen permeability tests showed no decrease in membrane separation properties after the catalytic tests. Thus, the catalyst was found to be limiting at these conditions. In fact, the membrane was not completely exploited and a similar partial pressure between the permeate and retentate was observed at the end of the membrane module. This could be inverted by reducing the separation driving force, by lowering the sweep ratio from 10.5 to 1 (figure 114).

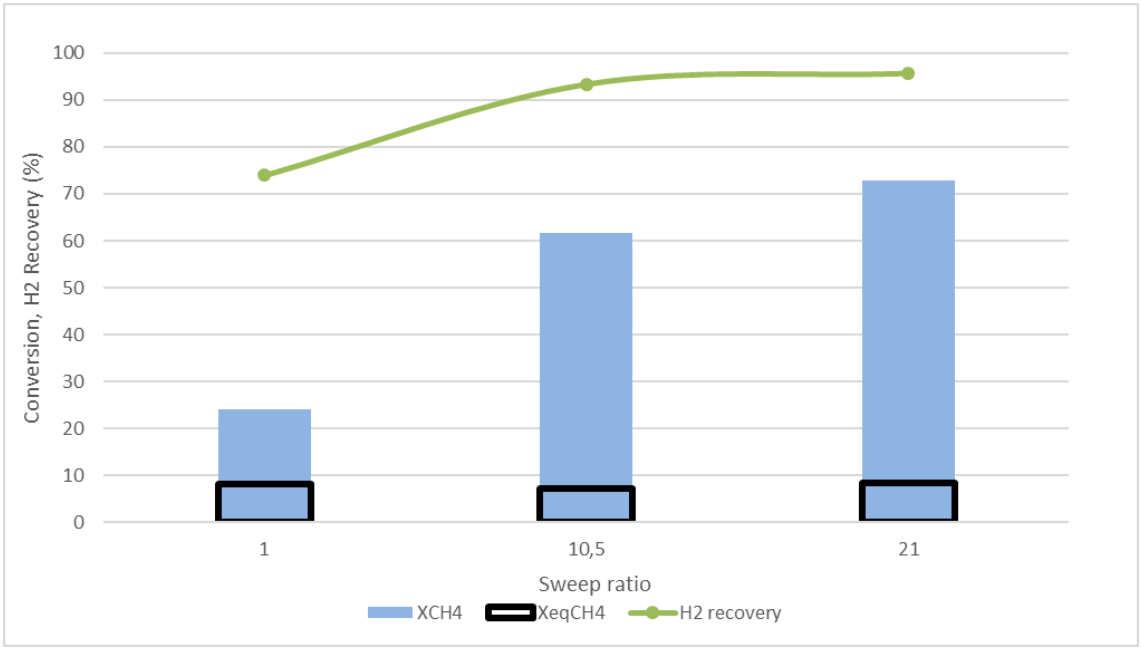

Figure 114: Effect of sweep factor on methane conversion and hydrogen recovery in the membrane reactor at 400°C, 2400 h^{-1}, 5 atm and S/C 2.

In this case, a lower conversion was obtained (24%) due to a lower driving force. Here the process was limited by the membrane separation. In fact, a lower hydrogen recovery (74%) and a difference of 0.47 atm in hydrogen partial pressure between retentate and permeate

was observed. Nevertheless, hydrogen permeated through the membrane and allowed to give a conversion higher than the equilibrium calculated for an analogous fixed bed reactor. This tests highlighted the importance of sweep gas in catalytic steam reforming carried out in membrane reactors. Sweep gas is in fact needed to generate a high separation driving force.

On the opposite, doubling the sweep factor to 21 allowed to further increase the methane conversion to 72% thanks to an increased hydrogen permeability given by the higher driving force which was provided by the dilution of the hydrogen in the permeate.

In order to increase the catalytic activity of the Rh-ZO catalyst, which showed to be rate determining, the membrane reactor was heated to 450°C (figure 115). In fact, a higher reaction temperature affects positively both methane conversion and hydrogen permeation.

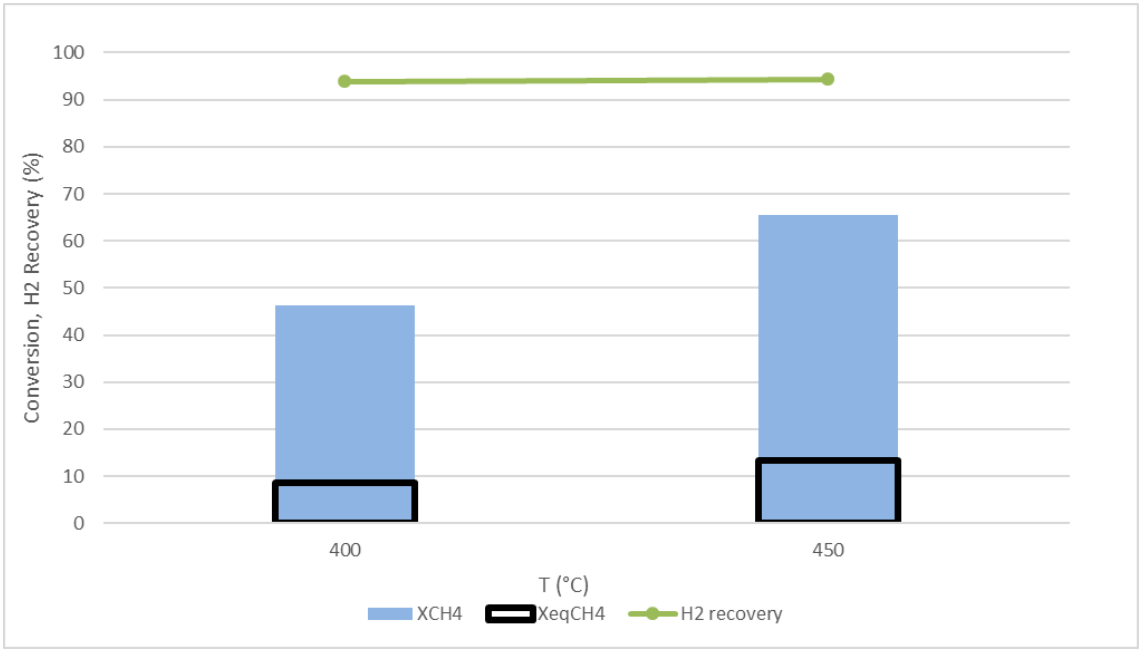

Figure 115: Effect of temperature on methane conversion and hydrogen recovery in the membrane reactor at 5 atm, 2400 h^{-1}, sweep factor 10.5 and S/C 2.

A catalytic test was carried out at 450°C, 5 atm and sweep factor of 10.5. It gave a methane conversion of 65% and a hydrogen recovery of 94%. Unexpectedly, the methane conversion was just slightly higher than in the test at 400°C. This was probably due to further deactivation of the catalyst. Halving the sweep factor to 5.75 provided a methane conversion of 61% and a hydrogen recovery of 93% (figure 116). The methane conversion

just slightly decreased indicating that the sweep gas flow may be reduced without decreasing the membrane reactor performances, This would provide a more economical process in industrial conditions where steam have to be used as sweep gas to be easily separated from the hydrogen and is associated with a vaporization cost. A further decrease of the sweep factor to 2.6 led to a drop in conversion to 53% and a hydrogen recovery of 90% This was due to a decreased driving force given by the lower sweep ratio.

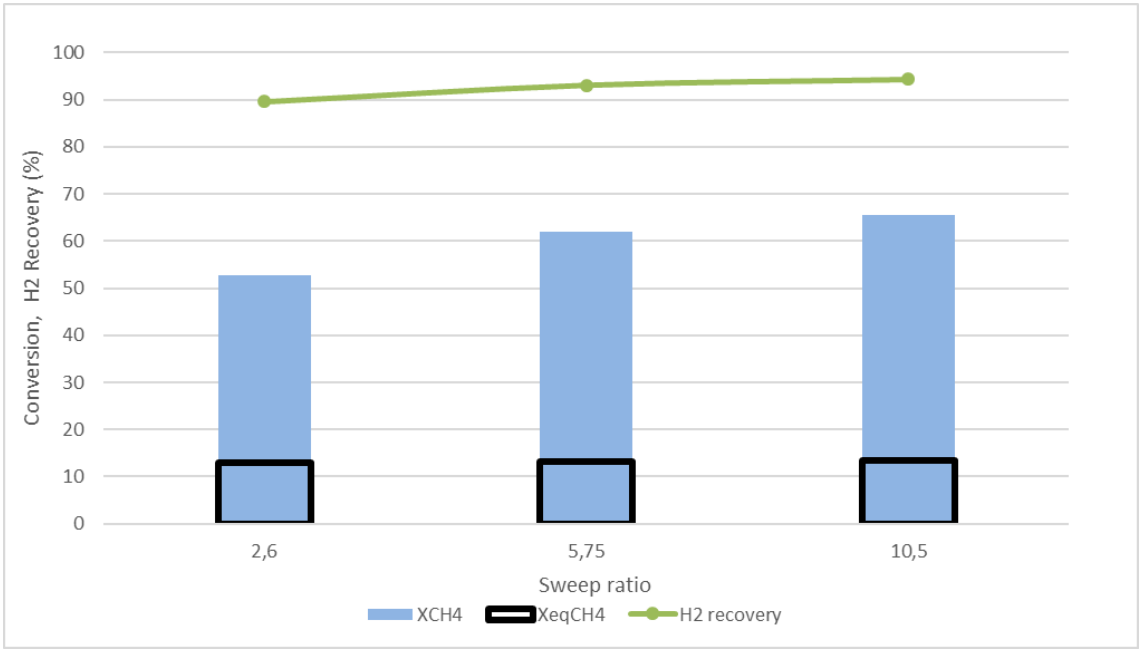

Figure 116: Effect of sweep factor on methane conversion and hydrogen recovery in the membrane reactor at 450°C, 2400 h^{-1}, 5 atm and S/C 2.

Another return test carried out to investigate catalytic stability showed a methane conversion of 40% indicating further deactivation of the catalyst. For this reason, the membrane module was dismounted and the catalyst analysed to understand the reason of the deactivation.

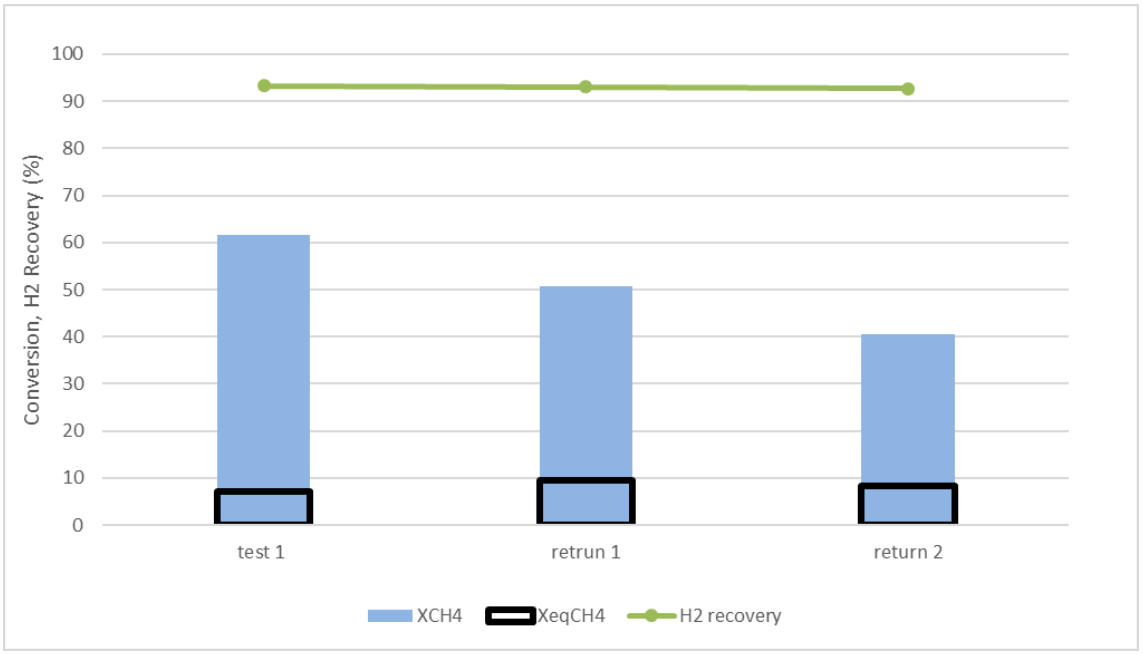

Figure 117: Stability evaluation tests carried out in the membrane reactor at 400°C, 2400 h^{-1}, sweep factor 10.5, 5 atm and S/C 2.

Regardless the deactivation the main results of the work show the possibility of obtaining high methane conversions which overcome the equilibrium value of a fixed bed reactor, due to the shift effect given by the hydrogen separation. Moreover, it is demonstrated the possibility to obtain high fluxes of CO_x free H_2, with very high recoveries.

9.5. **Characterization of the used catalysts**

In order to investigate the cause of the deactivation, the membrane reactor was discharged and the catalyst analysed by means of XRD, Nitrogen physisorption, Raman and TGA analysis. During the discharging operation it was noticed that part of the catalyst moved during the tests and was found in the stainless-steel tube that is placed before the membrane. Only 5.2 grams were found inside the membrane, while 6.8 had been charged at the beginning. This is one of the causes of the decreased conversion that was observed at higher pressure. In fact, the catalyst movement has probably occurred during the pressure increase steps.

XRD analysis of the used catalyst is shown in figure 118. The pattern relative to zirconium oxide is observed. In particular, the main phase is composed by tetragonal zirconia, while a smaller amount of monoclinic phase is also present. This resembles the phases of the fresh

catalyst, obtained after the reduction (figure 107). The absence of observable Rh phases is related to its low amount and high dispersion. The broad peak observed at 23 °2Theta is related to amorphous silica, and is associated to the presence of quartz wool, which was used to seal the catalyst inside the membrane, inside the spent catalyst.

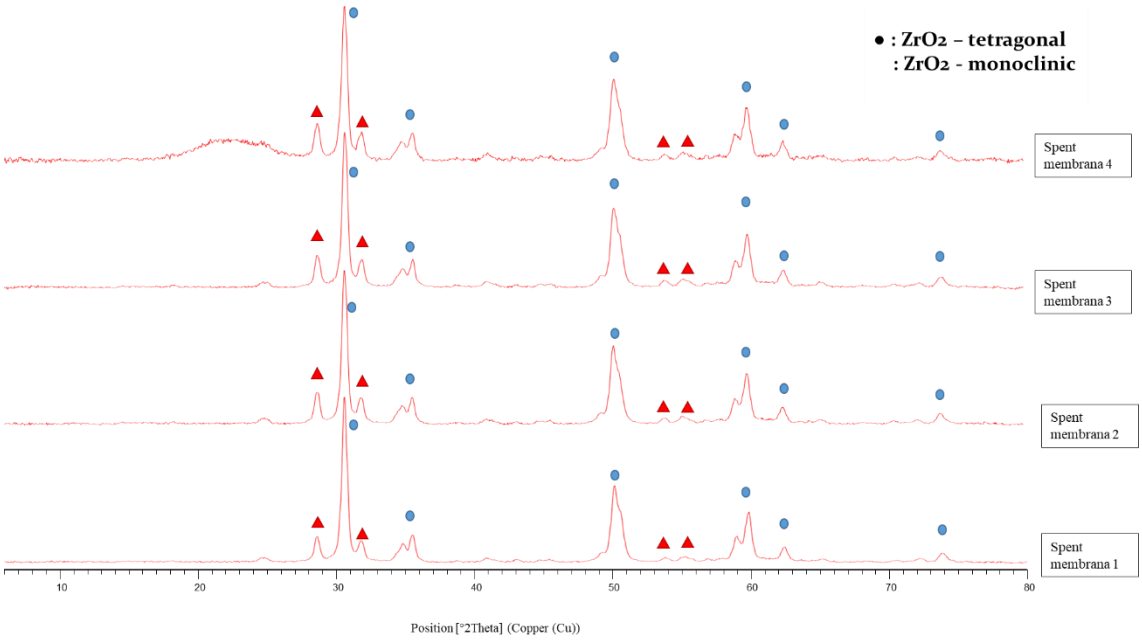

Figure 118: XRD analysis carried ou on the spent catalyst.

Raman analysis was carried out on four fractions of the catalyst which were respectively collected in four different regions of the membrane. This analysis can be used to evidence carbon formation over the catalyst as two band at 1350 cm^{-1} and 1550 cm^{-1} are usually observed when carbonaceous deposits are present in the sample. These bands were not found on the catalysts used in the membrane reactor indicating the absence of deposited carbon over the catalyst. A thermodynamic analysis was carried out with the CEA NASA software to further understand the carbon formation process. In particular, the input given to the software were the conditions at the inlet of the membrane (hence the reaction mixture fed) and the conditions at the retentate outlet, after reaction and hydrogen separation has occurred. The analysis evidenced that carbon formation is not thermodynamically favoured in the first part of the membrane. However, when a mixture enriched in CO_2 and with low hydrogen and steam is obtained thanks to the high conversions and hydrogen separation provided by the membrane, carbon formation becomes favoured. However, no carbon was observed by Raman analysis, showing a good

stability of the selected catalyst even at the harsh conditions of the membrane reactor. Carbon absence was also confirmed by TEM analysis (figure 119 and 120). Moreover, small particles were still observed on the used catalyst, with narrow size distribution centred between 1 and 2 nm. This indicates that the active phase was stable toward sintering in the selected conditions.

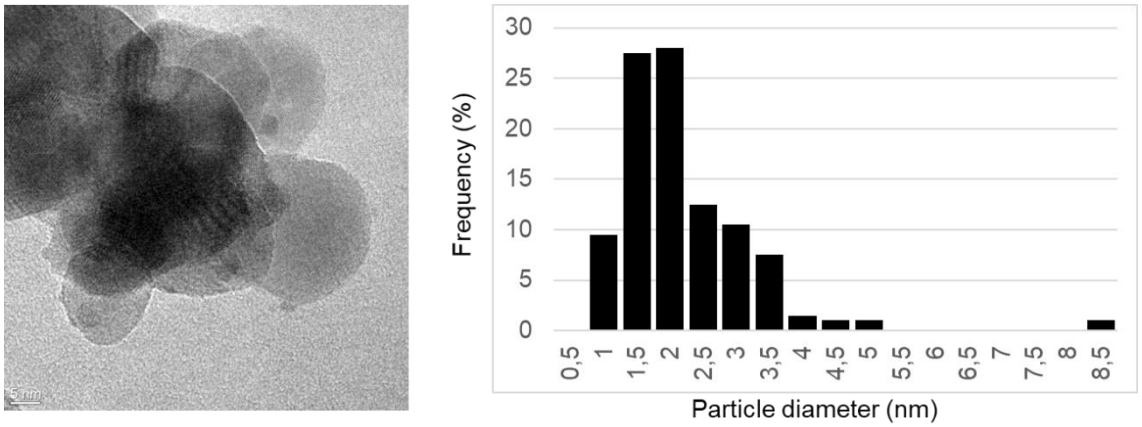

Figure 119: TEM analysis carried out on the first fraction of the used catalyst.

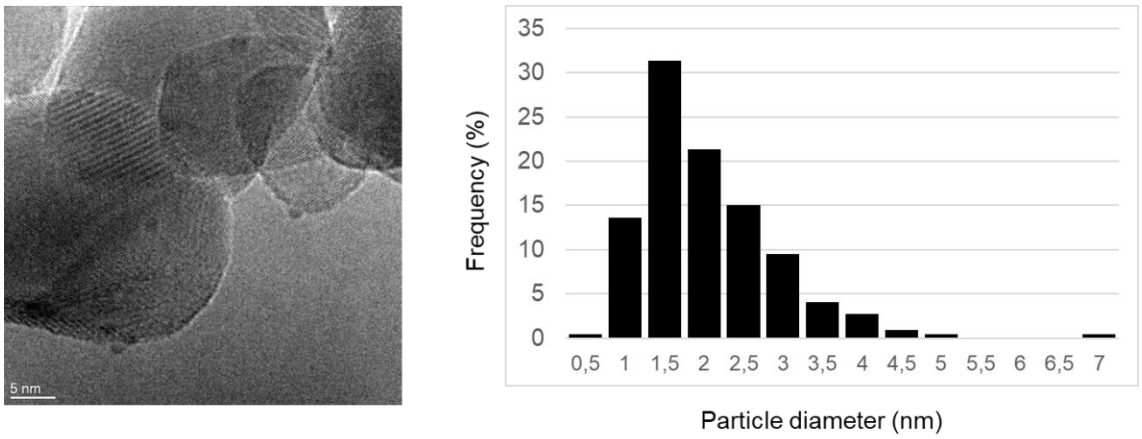

Figure 120: TEM analysis carried out on the fourth fraction of the used catalyst.

Moreover, TGA analysis was carried out on the first and fourth fraction of catalyst discharged from the membrane reactor. The results are reported in figure 121. No loss related to carbon oxidation was present. In fact, only a small weight loss (around 1.5%) is observed over 100°C, which is related to the loss of water adsorbed over the catalyst.

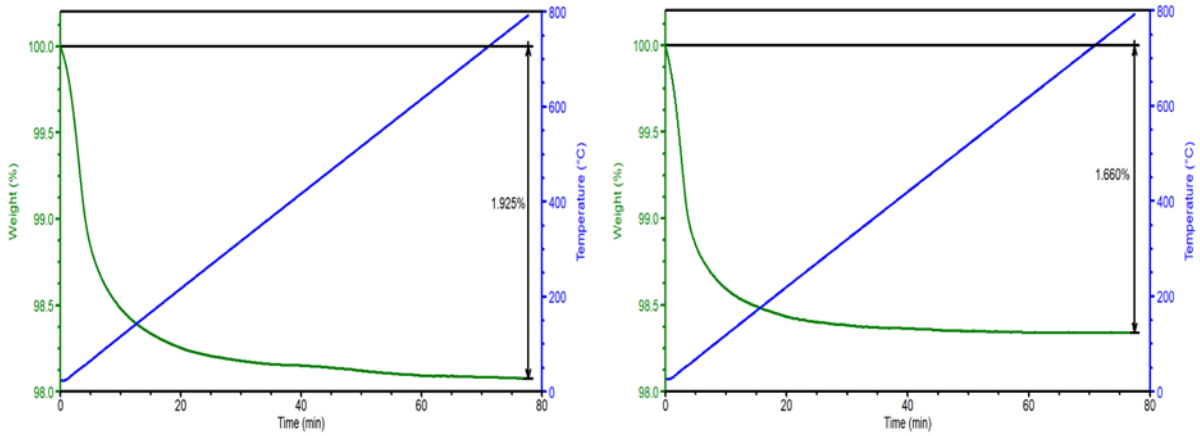

Figure 121: TGA analysis was carried out on the first and fourth fraction of catalyst discharged from the membrane reactor

Nitrogen physisorption analysis was carried out to investigate any change in the catalyst morphology. Table 35 shows the surface are values obtained for te fresh (reduced) catalyst and the used catalyst. A decrease in surface area was observed, from 28 to 23 m^2/g. This was probably caused by the sintering of the support

Table 35: Surface area of the fresh and used catalyst.

Samples	**Surface area (m^2/g)**
Reduced catalyst	29
Used catalyst	23

In order to further study the loss of performances observed, part of the used catalyst was diluted with pure zirconia in order to obtain a Rh loading of 0.05% and then tested in low temperature steam reforming to be compared with the catalyst used to calculate the turnover frequency. The results of the comparison are reported in figure 122.

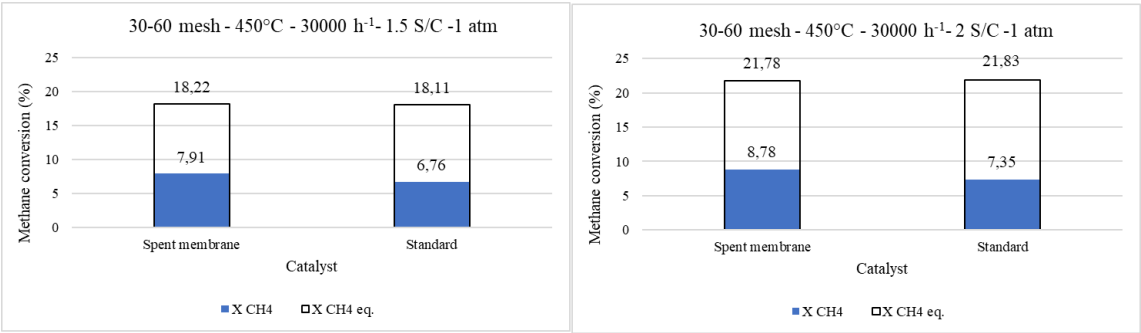

Figure 122: Methane conversion obtained on he used catalyst diluted to a Rh content of 0.05% and compared with a fresh catalyst.

The used catalyst was found to be still active in low temperature steam reforming and provided methane conversions even higher than those given by the fresh catalyst. This indicates that the catalyst deactivation is not the cause of the performance loss of the membrane reactor. The higher activity observed after the membrane tests can be related to an increased degree of reduction of the catalyst. In fact, it was submitted to different fluxes of hydrogen at 400°C, which were employed during the hydrogen permeability test which were used to characterize the membrane and periodically repeated to assess its stability.

Thus, even though a loss of catalyst surface area is observed after the prolonged tests in the membrane reactor, the catalyst was still found to be active and surface area loss cannot be pointed out as cause of the performance loss observed during the tests. It was thus hypothesized that this was caused by a movement of the catalytic bed in the tubes downstream the membrane. Thus, the catalyst amount inside the membrane tube reduced, lowering the synergy between the catalyst and the membrane and the performances of the membrane reactor. This movement was caused by the high pressures employed and was probably occurring during the pressure raise or lowering between the tests. Thus, quartz wool was not sufficient to create a fixed catalytic bed and it will be substituted in future studies with a SiC monolith, that may better seal the membrane.

9.6. **Conclusions**

The steam reforming reaction was carried out at low temperature (400-450°C) inside a Pd-based membrane reactor. The membrane was characterized before the reactivity tests and

showed high permeability. In the catalytic tests, hydrogen was readily separated by the Pd membrane. The permeation was allowed by a difference in hydrogen partial pressure between the inner and outer part of the membrane. This was provided by hydrogen generation on the catalyst and the use of sweep gas at the permeate side. Different conditions were investigated and high methane conversions and hydrogen recoveries were obtained thanks to the high permeability of the membrane reactor which allowed to shift the equilibrium due to the Le Chatelier principle. Noteworthy, the methane conversion was higher than the equilibrium conversion of a fixed bed reactor operated in the same conditions. However, a decrease in methane conversion was observed over time. No decrease in membrane permeability was observed. Thus, the catalyst was discharged and characterized. During this operation it was observed that part of the catalyst moved from the membrane reactor to the tubes placed before and after it. This was caused by the change in pressure during operation. The characterization showed the absence of deactivation phenomena such as sintering and carbon formation. The used catalyst was tested in a fixed bed reactor ad its performances were compared with that of a fresh one. Thus, catalyst deactivation was excluded and the reduction of methane conversion was associated to the movement of the catalyst out of the membrane reactor. This reduced the synergy between catalyst and membrane. A new configuration will be employed in future studies to avoid this movement.

10. CHAPTER 10 - ENHANCED STEAM REFORMING WITH CARBON DIOXIDE CAPTURE

The study treated in this chapter was carried out at ICPEES -Strasbourg (FR) under the supervision of Prof. Claire Courson.

10.1. Introduction

Methane steam reforming is an endothermic reaction whose conversion is limited by the thermodynamic equilibrium at low temperatures. A way to increase the methane conversion over the equilibrium value thanks to the Le Chatelier principle is to remove the one of the products which is formed during the steam reforming and water gas shift reactions, namely CO2. This can be done by capturing it with a solid material called sorbent. Among them, this work focused on hydrotalcites, or layered double hydroxides and their derived oxides. They are reported to be promising adsorbents for carbon dioxide capture, especially in lower temperature range (200°C-500°C) compared to classical reforming reaction and could be then applied to low temperature steam reforming[160–165]. They are

characterized by low energy requirement in the regeneration, multicycle stability, fast adsorption and desorption kinetics and the possibility to work in a water containing environment. These characteristics make them suitable for the application in sorption enhanced steam reforming and water gas shift (SESR and SEWGS). These properties are related to the structure of the hydrotalcites and they related mixed oxides and the possibility of reconstructing the hydrotalcite structure once the mixed oxide is in presence of water and carbon dioxide.

Layered double hydroxides (LDH) are class of hydroxides with the general formula [(M2+)1-x(M3+)x (OH)2]x+ [(An-)x/n) mH2O]). These materials possess a structure which resembles that of brucite, namely an octahedral disposition of Mg2+ (surrounded by 6 OH-), that share edges to form a continuous structure. However, the presence of a M3+ cation (for instance Al3+), which is found in place of some of the Mg2+ in the LDH structure, provokes a positive charge excess in the octahedral structure, which has to be balanced by a counterion. Thus, a layered structure is found in which sheets of Mg/Al mixed hydroxide are interlayered with anions, such as carbonate, as shown in figure 123. Noteworthy, Mg and Al can be substituted with other M2+ or M3+ cations and also ternary or quaternary mixed oxides can be obtained[166]. Moreover, different anions can be intercalated in the LDH structure[166].

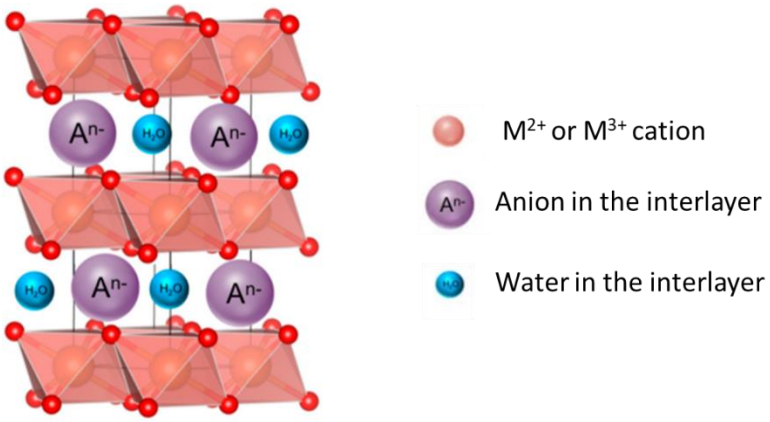

Figure 123: Layered double hydroxide structure. Adapted from [167].

Layered double hydroxides are usually also generally called hydrotalcites (HT). However, it must be specified that this name is related to the Mg6Al2(OH)16CO3.4H2O layered double hydroxide, while the other LDHs should be called hydrotalcite-like compounds (HTc).

However, it is possible, both in this work and in the existing literature, that hydrotalcite is used to name HTc compounds in general.

The possibility of employing different cations and anions to produce the hydrotalcite precursors make them versatile materials which are employed in different applications from polymer and medicinal chemistry, to water treatment and catalysis[166]. Moreover, mixed oxides can be obtained by calcination of the LDH precursor which possess interesting properties from a catalytic point of view. In fact, the employment of the LDH precursor allows to obtain a material with a homogeneous mixture of oxides (mixed oxide) with small crystal size, with a tuneable composition depending on the reagents employed in the LDH synthesis. This also allows to tune the basic properties of the mixed oxide or to insert a metal precursor, which can be then reduced to get the final active phase[53]. Moreover, the obtained oxide possesses a high surface area, thanks to the "cratering" mechanism in which the carbonate decomposition and the collapse of the LDH structure during calcination provides a porous material[166]. Finally, the so called "memory effect" is a properties of these materials, which allows to reconstruct the LDH structure for the corresponding mixed oxide in presence of water and an anion or carbon dioxide[166].

This property, linked with high surface area, can be used to capture CO2, by reconstructing a carbonate containing LDH, which can then be transformed again in the mixed oxide in a second moment, regenerating the starting material[166].

It is considered that the absorption of carbon dioxide on LDH-derived oxides occurs like a chemisorption through the following steps: (i) diffusion of carbon dioxide into the surface and pores, (ii) reaction with the active sites and formation of carbonate layer on the surface. However, as the latter forms, diffusion of CO2 becomes impeded to the inner part of the pores. Thus, also surface area and pore structure is a key parameter to consider for this application, as also reported in literature[168]. For instance "sand rose" like morphologies were observed in some LDH, which provides an abundance of pores between the "petals", favouring the absorption[168].

Moreover, the carbon dioxide capture depends on the characteristic of the hydrotalcites derived materials itself. For example, the effect of Al content was investigated[169]. However, only a slight increase in carbon dioxide capture was observed at higher Al

contents. It was thus suggested that the increase of Al content provided an increase in the positive charge that can be compensated by a carbonate absorption, but this also decreases the interlayer spacing and thus lowers the accessibility of the absorption sites. Moreover, the absorption capacity depends on the nature of the trivalent cation and on its calcination temperature, as demonstrated by a work that compared LDH derived material with different trivalent cations (Mn, Ga, Fe, Al)[170]. Al containing sample showed to have highest absorption capacity among them. Moreover, this study also showed that the calcination temperature influences the absorption capacity, with Mn showing best performances when calcined at 250°C, Fe at 300°C, Ga at 350°C and Al at 400°C. However, this property rapidly decreases for Mn, Ga, and Fe containing samples, if the calcination temperature is decreased. Thus, these samples can be used only for low temperature applications. On the opposite, absorption capacity only slightly increased in Al containing samples if the calcination temperature is increased, making this kind of materials appropriate for high temperature applications.

The effect of the divalent cations and interlayer anions were investigated da Hutson et al.[171], who showed that the highest absorption was provided by MgAl-CO3 sample. In addition, the effect of carbon chain lengths of the interlayer anions was investigated using C2 to C16 carboxylic acids. The results showed that the CO2 adsorption did not consistently increase in the range C2-C10 but raised for C11-C16, being the best performing sample the one intercalated with the C16 counter anions. This occurred because the decomposition of long carbon chain anions provided cracks in the LDH layers increasing the basicity, it lowers the degree of crystallinity and leads to a more stable structure.

Finally, the addition of calcium in the LDH reagents can lead to the formation of a mixed oxide and a calcium oxide or carbonate phase. The presence of the latter increases the carbon capture properties of the material[172]. In fact, CaO can undergo and exothermic reaction to provide CaCO3, which can be then retransformed to CaO by calcination.

$$CaO + CO2 \rightleftharpoons CaCO3$$

Calcium oxide possesses the best sorbent properties among the oxides, as it can work at different temperatures and with easy regeneration over 800°C[173]. The latter step is a fundamental one because it has to give back the starting material to allow multi-cycle

operation. However, for CaO sorbents a loss of sorption ability during successive cycles is observed. This is caused by sintering and surface area loss[174]. For instance, the fresh CaO, shrinking of the particles does not allow a complete carbonation and new CaO grains are formed an agglomerated after cycling. This leads after more cycles to the formation of a rigid network that allows only its outer part to be recarbonated. Thus, the insertion of calcium into the LDH structure or its dispersion over an LDH can provide higher surface area for this material and lower the sintering phenomena.

10.2. Synthesis and characterization of the sorbent materials

Different catalyst precursors were synthetized by co-precipitation with the aim of obtaining layered double hydroxides that can be transformed to mixed oxides after calcination. In order to obtain active catalysts which also possess carbon dioxide sorption properties Ni, Mg, Al and Ca nitrates were used as precursors. These were dropped in a carbonate or silicate containing solution in order to obtain a LDH with these anions in the interlayer. These cations were selected as Mg and Al are typically used to form LDH and as supports in the steam reforming reaction[53], Ca was selected to improve the sorption ability of the material while Ni0 was the desired active phase, that can be obtained after reduction of the mixed oxide. Form the anion side, carbonates are classical anions used to synthetize LDH catalyst precursors, as their decomposition to carbon dioxide through calcination leads to the formation of a porous mixed oxide with high surface area[166]. However, when the Mg/Ni ratio is low, Ni2+ ions reducibility decreases due to its low concentration in the (Ni/Mg)O solid solution[175]. For this reason, silicates were also incorporated in the structure as interlayer anions. In fact, their decomposition during calcination does not lead to the formation of volatile species and silicon forms a forsterite-like phase with Al, which increases thermal and mechanical strength [175–177]. Moreover, the presence of silicon as a third element to Mg and Al, changes the correlation between Mg and Al, hence the Ni2+ ions distribution and reducibility.

The following catalyst precursors were synthetized, all possessing a M2+/M3+ ratio of 3 and a Mg/Ca ratio of 2:

- Ni(10% wt/wt)MgCaAl interlayered with carbonates, which will be called Ni10-C

- Ni(20% wt/wt)MgCaAl interlayered with carbonates, which will be called Ni20-C
- Ni(10% wt/wt)MgCaAl interlayered with silicates, which will be called Ni10-S
- Ni(20% wt/wt)MgCaAl interlayered with silicates, which will be called Ni20-S

The synthesis was carried out by coprecipitation. An aqueous solution containing nitrates salts of Ca, Ni, Mg, Al was dropped in an aqueous solution of sodium carbonate or sodium silicate. This solution was heated at 60° and kept at pH 10 (for carbonate) or 11 (for silicates) by addition of NaOH. Finally, the suspension was aged fo 1 h at 60°, then filtered and dried at 70°C overnight.

10.2.1. Catalyst characterization

The catalysts were characterized by means of XRD analysis, BET analysis, SEM and CO2 sorption ability.

The diffractograms of the as-synthetized Ni10-C and Ni20-C catalysts are shown in figure 124.

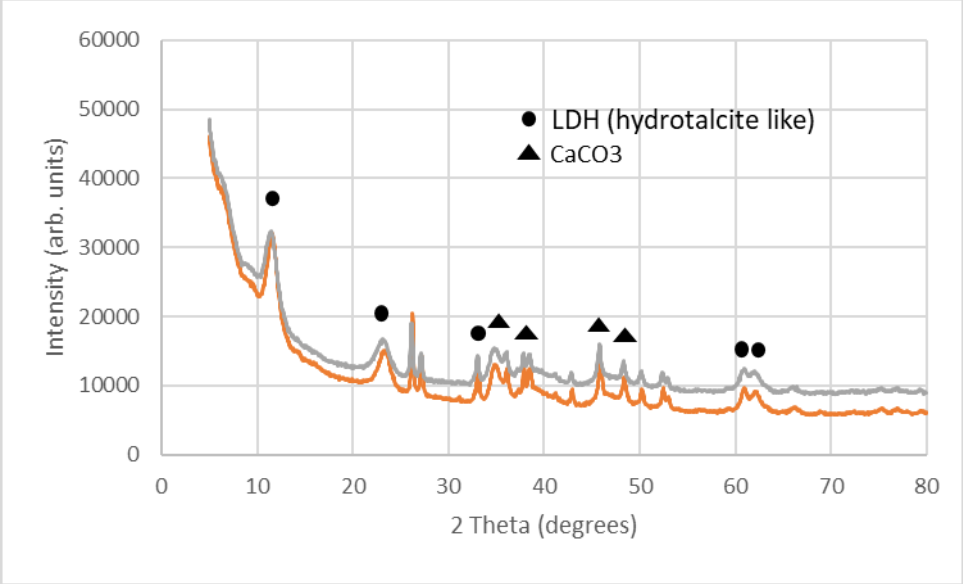

Figure 124: XRD analysis on the as-prepared Ni10-C (grey) and Ni20-C (orange).

The analysis shows the presence of an LDH structure before calcination. However, another segregated phase is observed which was assigned to calcium carbonate, formed by the carbonation reaction with Ca2+. This was favoured by the ionic radius of Ca which is bigger than those of the other cations and thus disfavours the insertion of Ca2+ in the hydrotalcite

structure. However, calcium carbonate dispersion over the LDH surface may lead to high specific surface area of this phase and thus high Ca availability for carbon dioxide sorption and desorption.

The XRD of the samples calcined at 500°C (figure 125) show the presence of segregated Ca oxide and calcium carbonate, together with a peak that can be ascribed to the presence of Ni-Mg-Al mixed oxides. Noteworthy part of the calcium may have been incorporated inside the LDH and mixed oxides structure but its identification with this technique is challenging.

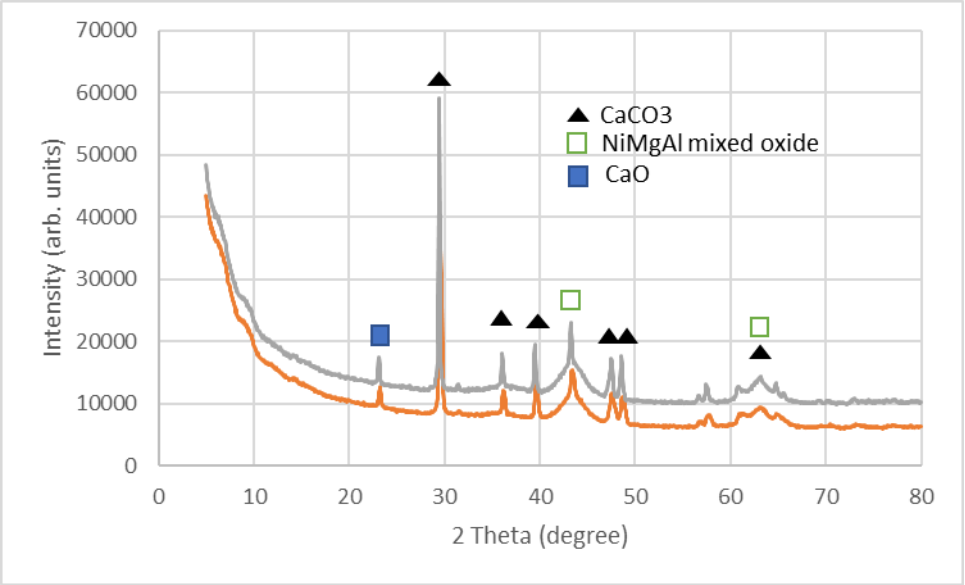

Figure 125: XRD analysis Ni10-C (grey) and Ni20-C (orange) calcined at 500°C for 1 h with a ramp of 10°C/min.

Increasing the calcination temperature and time to 650°C and 12 h, gives similar phases (figure 126). Again a mixed oxide phase is observed, together with segregated CaCO3.

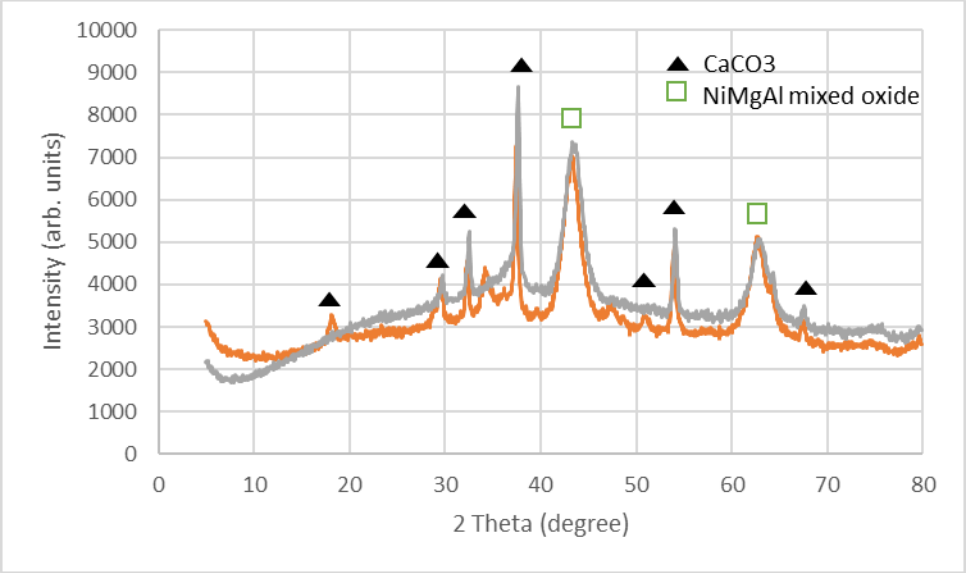

Figure 126: XRD analysis Ni10-C (grey) and Ni20-C (orange) calcined at 650°C for 1 h with a ramp of 10°C/min.

The diffractograms of the as-synthetized Ni10-S and Ni20-S catalysts are shown in figure 127.

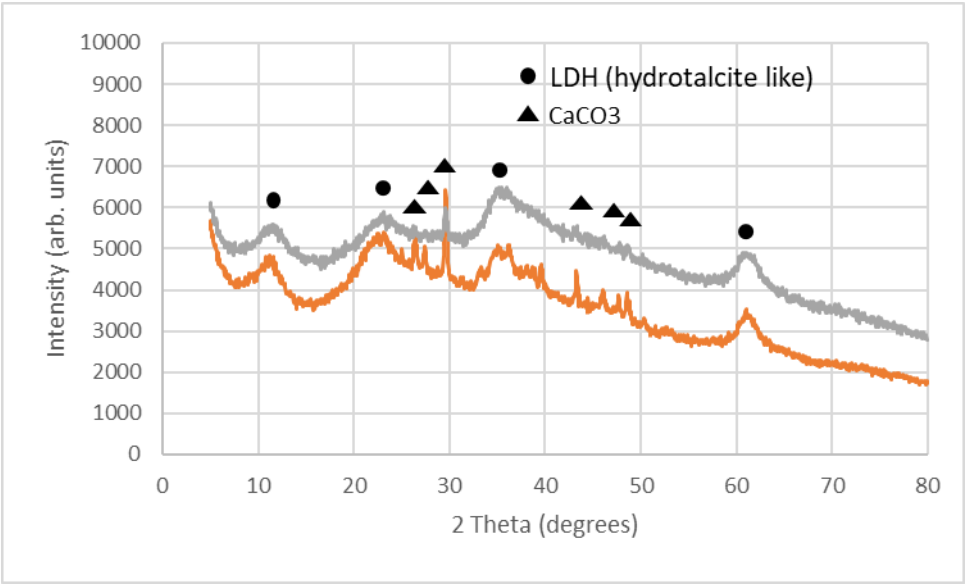

Figure 127: XRD analysis on the as-prepared Ni10-S (grey) and Ni20-S (orange).

The obtained pattern shows the presence of LDH characteristic peaks. However, they are broad and of low intensity, suggesting a low crystallinity of the material or the presence of small particles. Moreover, in a classical LDH structure, the peak at 10 2teta should be the most intense of the spectra. It is supposed that the silicates are intercalated in the LDH interlayer to balance the charge excess provided by Al ions. In fact, no Si segregated phase

was observed. On the opposite, the presence crystalline calcium carbonate is observed. Thus, it is supposed that Ca was not completely englobed in the hydrotalcite structure. However, the sample was calcined at 500°C and 650°C as in the case of the carbonate-containing samples.

The diffractograms of the Ni10-S and Ni20-S catalysts calcined at 500°C for 1 h are shown in figure 128.

As in the case of Ni10-S and Ni20-S, it is observed the presence of segregated calcium carbonate, together with a peak that can be ascribed to the presence of Ni-Mg-Al mixed oxides and were part of the calcium could be englobed. Finally, the baseline increase observed around 20 2teta is related to the presence of some amorphous phase. As this was not observed, in the carbonate-containing samples, it can be due to a segregated Si-containing phase.

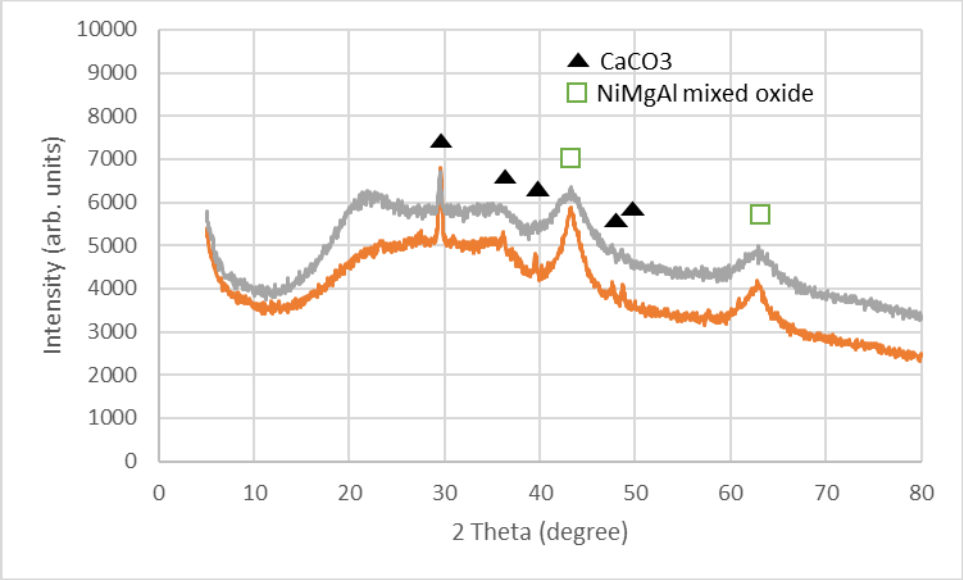

Figure 128: XRD analysis Ni10-S (grey) and Ni20-S (orange) calcined at 500°C for 1 h with a ramp of 10°C/min.

Calcining the samples in harsher conditions (650°C for 12 h) slightly changes the phase distribution. In fact, a higher intensity and sharper peaks are observed. This is related to an increase particle size dimension of the oxide, given by sintering of the material. The mixed oxide average particle size was calculated by Sherer equation on the main peak at 43 2teta. It resulted to be 4,7 and 3,1 nm for Ni10-S and Ni20-S calcined at 500°C respectively. The value slightly decreased to 4,4 for the sample with lower Ni amount and increased to 3,7 for

the other one. The particle dimension of the calcium carbonate phase was challenging to calculate due to the presence of an amorphous material that increased the baseline in the area of the reflect of this phase and covered part of the peaks.

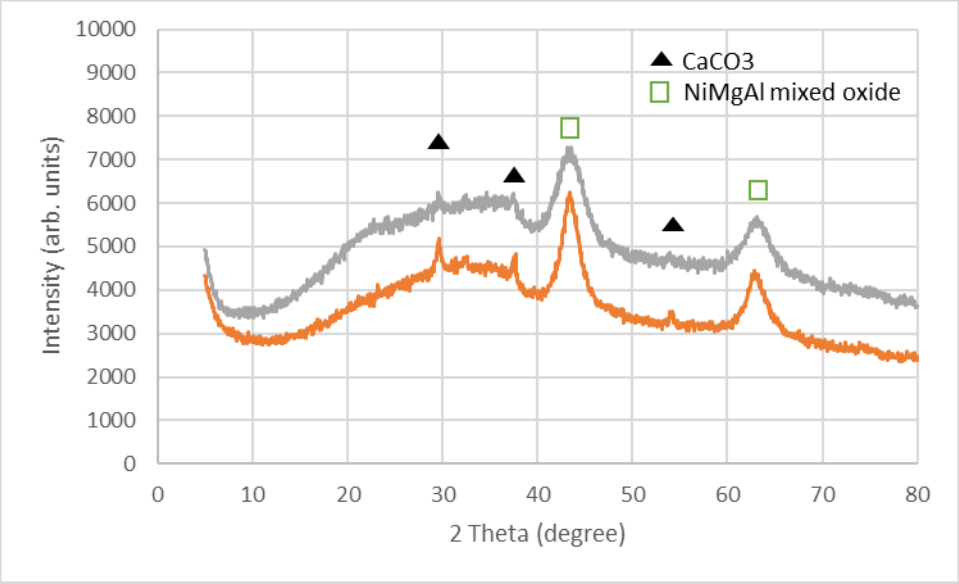

Figure 129: XRD analysis Ni10-S (grey) and Ni20-S (orange) calcined at 6500°C for 12 h with a ramp of 10°C/min.

A comparison of BET analysis conducted on the prepared samples is reported below. Table 36 shows the results obtained on the as prepared samples: Ni10-C, Ni20-C, Ni10-S and Ni20-S.

Table 36: surface area, pore volume and pore diameter of as prepared (just dried) Ni10-C, Ni20-C, Ni10-S and Ni20-S.

As prepared	Surface Area (m^2/g)	Pore vol. (cm^3/g)	Pore diam (nm)
Ni10-C	73	0.27	8
Ni20-C	48	0.16	9
Ni10-S	243	0.74	7
Ni20-S	255	0.54	8

Comparing the properties of the carbonate containing and silicate containing samples it can be observed that much higher surface areas are obtained thanks to the insertion of

silicates inside the structure of the LDH. Moreover, higher pore volume is observed in this case, although all the samples show similar average pore diameter. A slight change in the surface area and a decrease in pore volume is observed when the Ni amount is changed. On the opposite, surface area increases at higher Ni loadings for the Si-containing sample.

A deeper understanding of the pore structure is evidenced by the isothermal linear plot (Figure 130). In fact, carbonate containing samples provide type IV isotherms typical for mesoporous materials, with an hysteresis of H2 type [178,179]. This is characteristics of solids that possess interconnected pores of different shapes and sizes with not-defined structure. However, hydrotalcites are usually reported to be macroporous materials [176]. Thus, the observed mesopores may be related to the aggregation of hexagonal particles that create inter-particle porosity.

Silicate containing samples isotherm resembles a type IV isotherm, characteristics of mesoporous materials but with a very narrow hysteresis. As a high surface area and pore volume is observed in this case, it can be supposed that these results indicate the presence of very small particles. Hence the pore volume measured is related to inter-particle porosity and the high surface area is related to the small dimension of the particles themselves. The absence of a pronounced hysteresis is consistent with the interparticle porosity of of small particles. However, Type IV isotherms with H2 hysteresis have been reported for both carbonate and silicate containing hydrotalcites [176].

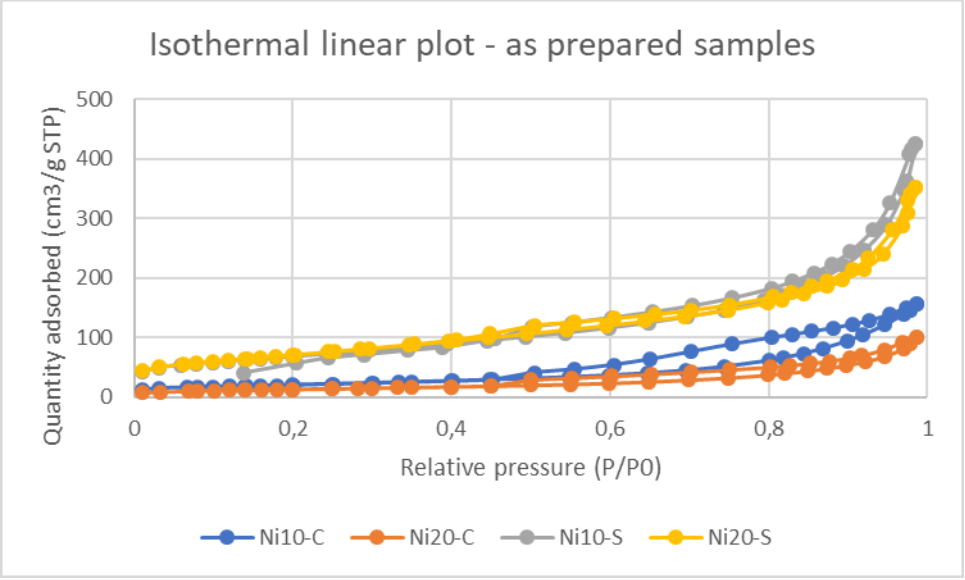

Figure 130: Isothermal linear plot of as prepared Ni10-C, Ni20-C, Ni10-S and Ni20-S,

The as-prepared samples were calcined at 500°C for 1 h or at 650°C for 12 h. An increase in surface area and pore volume is observed for the carbonate containing samples (Table 37). This is caused by the collapse of the hydrotalcite layered structure following the decomposition of carbonates to carbon dioxide. A "cratering" mechanism of the formed CO2 leads to the formation of pores, increasing the surface area[180]. The mesoporous nature is kept, together with an increase of surface area (figure 131). A slight increase in surface area is shown by Ni10-S, which may be due to a small contribution cratering effect provided by carbonates that contaminated the LDH structure. On the opposite, a slight decrease in surface area is observed on Ni20-S samples, due to particle sintering. However, the morphology of the material is maintained, as shown by adsorption-desorption isotherms which again showed no hysteresis.

Table 37: surface area, pore volume and pore diameter of Ni10-C, Ni20-C, Ni10-S and Ni20-S, calcined at 500°C.

Calcined 500°C	**Surface Area (m^2/g)**	**Pore vol. (cm^3/g)**	**Pore diam (nm)**
Ni10-C	135	0.41	11
Ni20-C	123	0.31	8
Ni10-S	266	0.63	9
Ni20-S	226	0.66	16

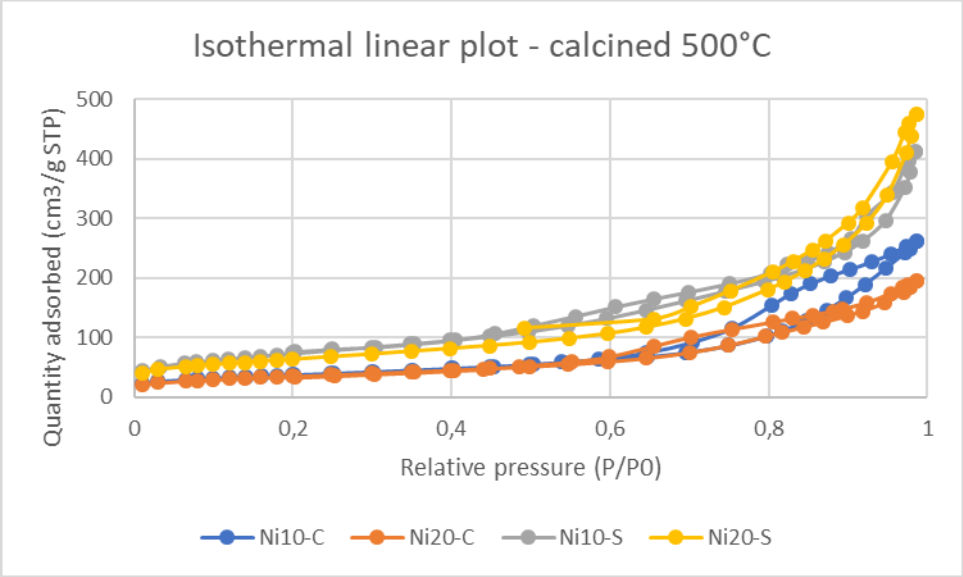

Figure 131: Isothermal linear plot of Ni10-C, Ni20-C, Ni10-S and Ni20-S calcined at 500°C for 1 h,

Calcination at 650°C for long time (12 h) leads to a decrease in surface for all the samples, compared to the calcination at 500°C for 1 h, due to sintering of the materials (Table 38). However, low sintering degree is observed in Ni20-S, which shows the highest surface area among these samples.

Table 38: surface area, pore volume and pore diameter of Ni10-C, Ni20-C, Ni10-S and Ni20-S, calcined at 650°C.

Calcined 650°C	**Surface Area (m^2/g)**	**Pore vol. (cm^3/g)**	**Pore diam (nm)**
Ni10-C	105	0.48	14
Ni20-C	107	0.34	12
Ni10-S	189	0.62	11
Ni20-S	217	0.55	9

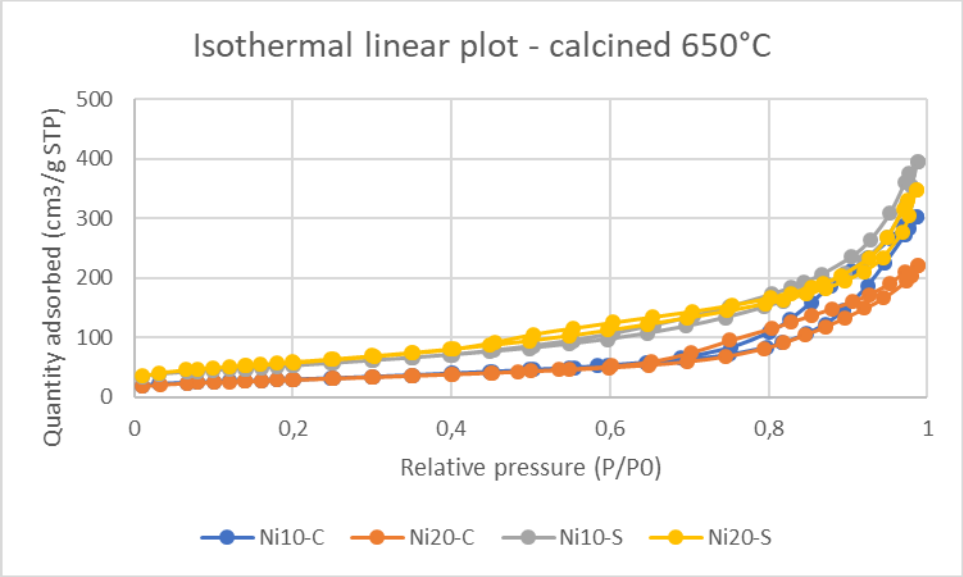

Figure 132: Isothermal linear plot of Ni10-C, Ni20-C, Ni10-S and Ni20-S calcined at 650°C for 12 h,

SEM-EDX analysis have been carried out to further understand the morphology of the samples calcined at 500°C (figure 133).

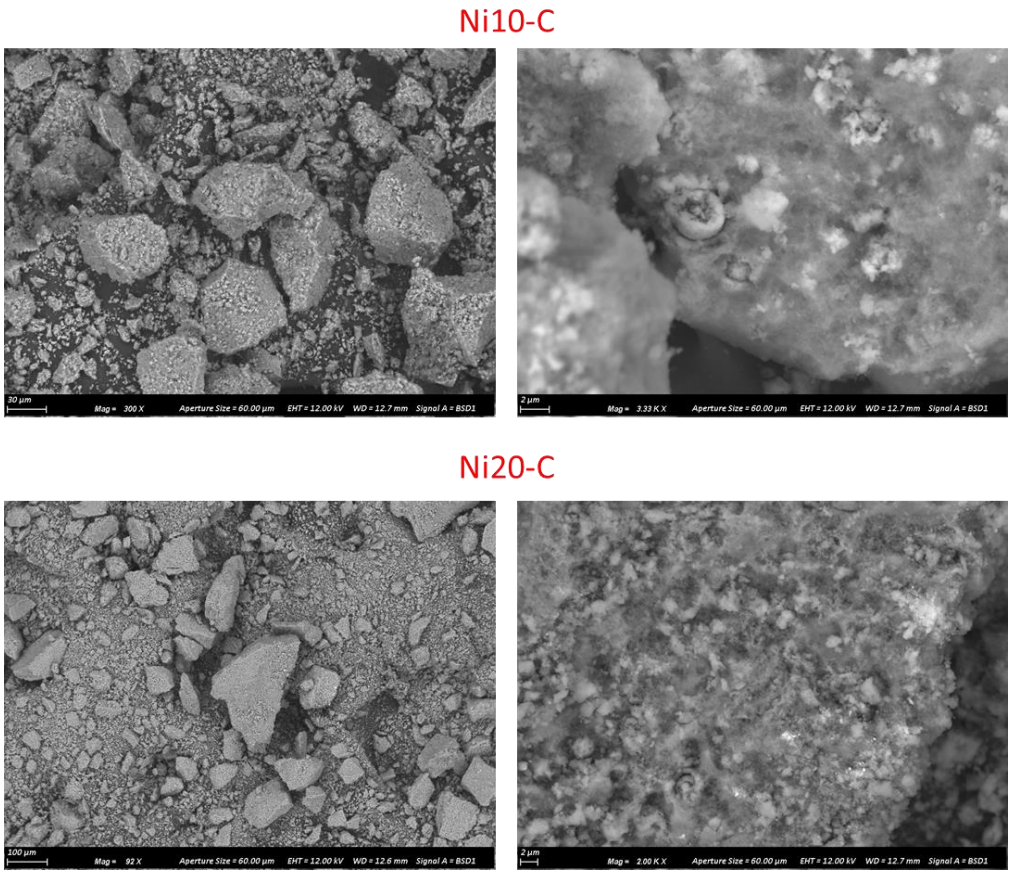

Figure 133: SEM image plot of Ni10-C, Ni20-C calcined at 500°C for 1 h.

The images of Ni10-C sample outline the formation of particles and aggregates with dimensions close to 30 microns, together with smaller crystals. A further zoom on the crystal surface showed the presence of different solids, which were distinguished thanks to their morphology and colour. Both grey and white areas were investigated by EDS and showed to contain Ca, Mg, Al and Ni. However, an enrichment in Ca content was observed in the white areas while low Ca content was found in the grey one. However, both were supposed to be mixed oxides. Surprisingly, no segregated calcium carbonate species (detected by XRD), were observed. Therefore, it was hypothesized that CaCO3, is present inside the mixed oxide porosity and thus not observable on the surface.

A similar discussion can be done for the Ni20-C sample. However, a more homogenous distribution of the grey and white areas was observed. Moreover, the grey areas were more Ca rich in this case compared to the white ones.

A different morphology is shown by the samples containing Si, as shown in figure 134.

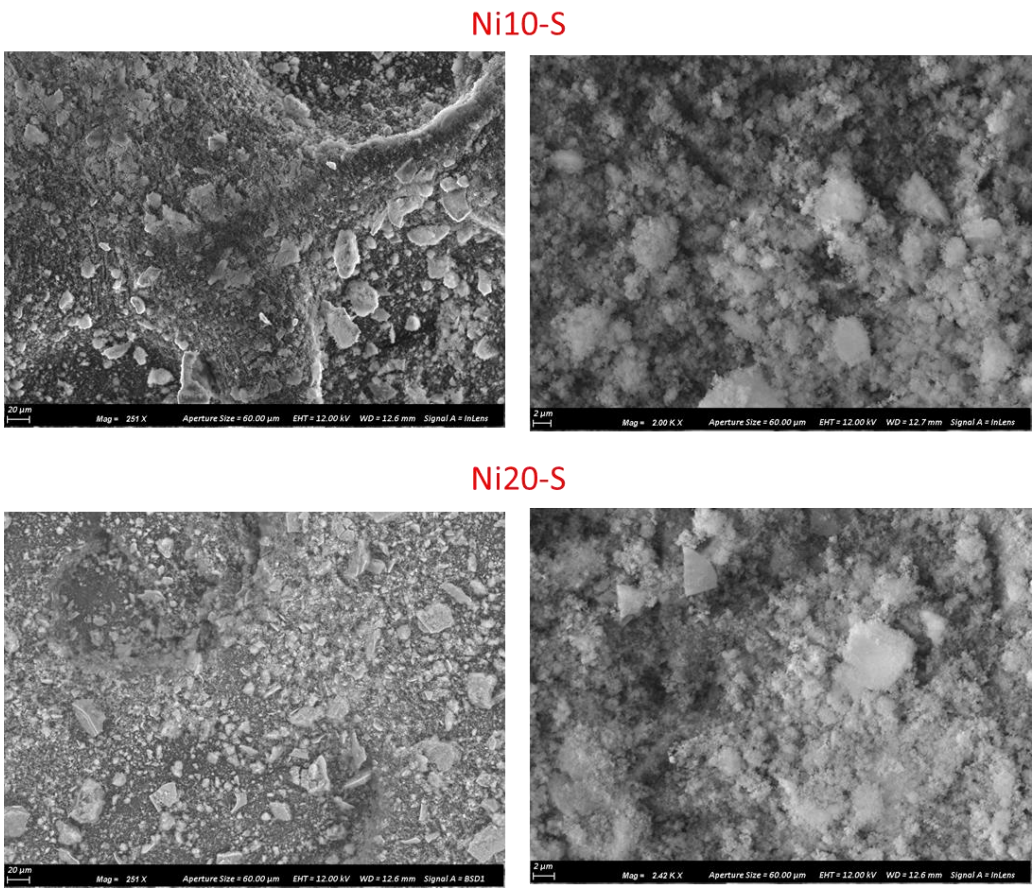

Figure 134: SEM image plot of Ni10-S, Ni20-S calcined at 500°C for 1 h.

Smaller particles are observed in this case. At further zoom, the material seems to be composed by aggregates of small and round particles. EDS analysis showed the presence of Si, Ni, Mg, Al and Ca in the particles. This suggests the formation of a mixed oxide. Again, no segregated Ca carbonate was observed which could be present inside the pores. This, together with the small particle dimension could explain the high surface area and low porosity shown by nitrogen physisorption.

The carbon dioxide adsorption capacity at 600°C was calculated by saturating the sample with CO2 at 600°C, then measuring the desorbed carbon dioxide when the sample was purged with He and heated to 800°C. A pretreatment in He heating to 800°C was done to degas the CO2 already present in the sample. Table 39 shows the results of the CO2 capture tests.

Table 39: results of the CO2 capture tests in terms of g CO_2 captured per 100g of material and sorbent conversion. Sorbent conversion is expressed as g of captured CO_2 per g of CO_2 that can be theoretically adsorbed by conversion of CaO to $CaCO_3$ and of the mixed oxide to hydrotalcite (1 mol of CO_2 for each mol of Al).

	g CO2 captured /100g	**Sorbent conversion (Ca and Al)(%)**
Ni10-C C500	18.9	119
Ni20-C C500	17.2	143
Ni10-C C650	13.5	85
Ni20-C C650	11.3	94
Ni10-S C500	1.5	51
Ni20-S C500	5.7	79

Ni10-C showed a carbon dioxide sorption capacity of 18.9 g CO2/100g sample. It was supposed that the sequestration occurred as both formation of CaCO3 from CaO and reformation of the LDH structure with intercalation of CO2 in the form of carbonate inside the layer of the hydroxide structure. A conversion of the oxide material to hydrotalcite and CaCO3 of 119% was estimated. If only CaO is supposed to sequestrate carbon dioxide a

conversion to carbonate of 180% was obtained, indicating that CO2 is adsorbed also in another form, probably in the interlayer of the re-formed LDH, balancing the charge excess provided by Al3+ presence in the structure. If CaO and MgO were assumed to be the adsorbing agents, a conversion of 49% was obtained. However, MgO-MgCO3 equilibrium curve shows that magnesium carbonate decomposition is favoured over 450°C, at atmospheric pressure [181,182]. As the operative temperature of this adsorption experiment is 600°C, it can be assumed that MgO does not participate to carbon dioxide adsorption. Thus, it seems that the adsorption occurs over CaO and in the re-formed LDH interlayer and that all the sites have been occupied.

Ni20-C displayed similar properties with a CO2 capture of 17.2 g CO2/100g sample. It is noteworthy that a lower amount of calcium has been used in this case to keep constant the M2+/M3+ ratio in Ni10-C and Ni20-C; while doubling the Ni content. Thus, an even higher conversion of 143% is obtained if Ca and Al are considered as sorbents. Ni20-C seems a promising catalyst for sorption enhanced steam reforming. In fact, it displays good sorption properties, similar to that of a sample with higher Ca loading, a high conversion of the sorbent elements and a high Ni loading. The latter should increase methane conversion in steam reforming.

Increasing the calcination temperature and time to 650°C and 12 h, the sorption properties decreased for both samples. Ni10-C captured 13.4 g CO2/100g sample, with a conversion of 85%, and Ni20-C 11.3 CO2/100g sample, with a conversion of 94%. The decrease is probably related to the fall in surface area due to the harsher calcination that resulted in a lower availability of Ca and Al on the surface. This could also be related to a change in particle size. However, Scherrer calculations on the mixed oxide peaks, showed only a slight change in particle dimension after calcination at 650°C. Unfortunately, the calculation of particle dimension of the calcium carbonate phase could not be performed due to the presence of an amorphous phase.

Silicon based samples showed lower sorption capacity and conversion due to the occupation of the Al sites of the hydrotalcites by Si.

Thus, the application of this material to enhanced steam reforming seems less promising although Si presence may favour the stability of the material in the reaction conditions.

Ni10-C calcined at 500°C was characterized after saturation with carbon dioxide to provide a better understanding of the phases involved in the sorption. The XRD analysis result is shown in figure 135.

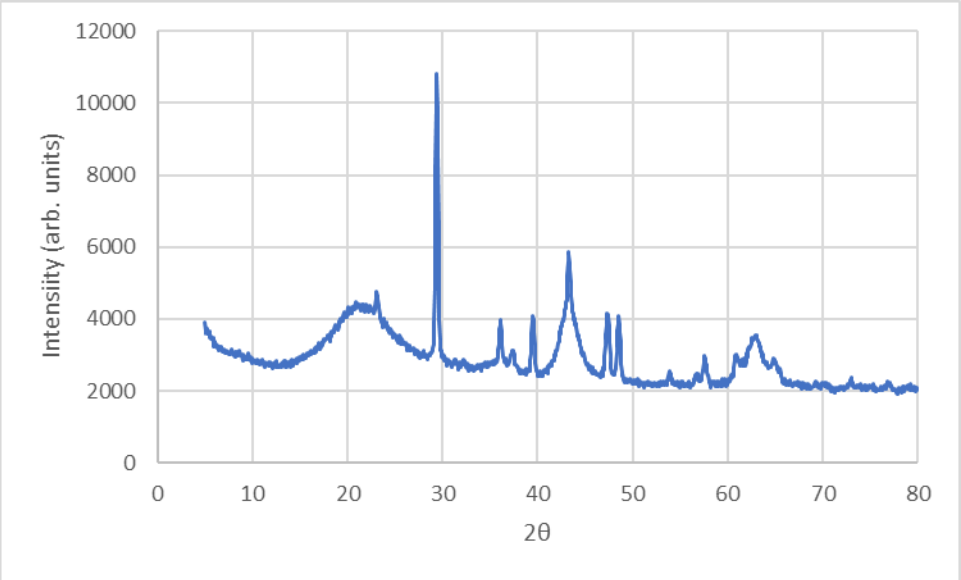

Figure 135: XRD analysis of Ni10-C sample calcined at 500°C and then saturated with CO2 at 600°C.

The pattern resembles the one obtained for the as calcined sample. This indicates that CaO is the main actor of the sorption process. However, the formation of hydrotalcite my be limited to the surface of the sample and not detected by XRD due to the presence of small, non-continuous domains.

Magnesium carbonate contribution was excluded as the MgO phase is favoured in this temperature range, as treated above.

10.3. Conclusions

Different hydrotalcite derived compounds were synthetized using Ca, Mg, Al, Ni as cations and carbonate or silicate as anion. The presence of calcium did not allow the obtainment of a pure hydrotalcite, as segregated calcium carbonate was formed. The addition of silicates allowed to obtain a material with high surface area and small particle dimension. However, when tested in the carbon dioxide capture it displayed low adsorption, due to the

sequestration of Al by Si. In fact, the active materials for adsorption were supposed to be both CaO and the mixed oxide, which could form a carbonate containing hydrotalcite. In fact, mixed oxides derived from carbonate containing hydrotalcites allowed to obtain high carbon dioxide sequestration.

11. CHAPTER 11 – CARBON DIOXIDE METHANATION ON Ni-CeZrPr CATALYSTS

The study treated in this chapter was carried out at ICPEES -Strasbourg (FR) under the supervision of Prof. Anne Cécile Roger.

11.1. Introduction

In chapter 4 it was treated the synthesis and characterization of CeZr and Zr oxides obtained by microemulsion synthesis. In the frame of a project carried out at ICPEES – CNRS of Strasbourg (FR), this synthetic technique was used to prepare a $Ce_{0,33}Zr_{0,63}Pr_{0,04}O_2$ support to be used in the carbon dioxide methanation reaction. This reaction was previously studied at ICPEES on similar supports using Ni as active phase [118,134,183–185]. The carbon dioxide methanation reaction can be seen as a promising way to convert CO_2 into fuels. In fact, methane is produced, which could be directly used in the existing energy supply chain after purification. However, hydrogen, which is usually produced from fossil fuels, is required as a reagent. Nevertheless, electricity excess provided by intermittent renewable processes such as solar panels or wind, could be used to perform water electrolysis to provide hydrogen. On the opposite, carbon dioxide is seen as a waste in many existing processes and could be used as a cheap raw material, when efficient carbon dioxide sequestration technologies will be available. Ni is the most used active phase in the methanation reaction [186–189]. The use of Ce containing supports has proved to increase

the the methane selectivity, because of the properties of Ce of activating CO_2 and its participation in the reaction mechanism [54,98,190]. This property is increased if other elements, such as Zr, are added [98]. Moreover, high Ni dispersion can be obtained on these supports [98]. This property can also help to remove eventually deposited carbon, increasing the catalyst life [54]. Nevertheless, the support synthetic technique can highly affect the catalytic activity due to different synergy provided between the support and the active phase [54,134,191]. However, it is not straightforward to select a universal synthetic method as the provided activity can vary depending on the reactions and conditions. For this reason, a $Ce_{0,33}Zr_{0,63}Pr_{0,04}O_2$ support was synthetized by microemulsion and compared with another support obtained by surfactant assisted coprecipitation [118]. Pr was inserted together with Ce and Zr as its presene was reported to increase the oxygen storage capacity of the Ce/Zr oxide [192,193]. After calcination at 500°C, the supports were impregnated with Ni nitrate, calcined again at 500°C to give NiO, and then reduced at 400°C before the tests to provide the metallic active phase. The catalysts were characterized by means of different techniques and tested in the methanation reaction under different conditions.

11.2. Characterization of the catalysts

The CeZrPr catalysts were synthetized by two different techniques: (i) microemulsion synthesis (CZPm); (ii) coprecipitation using CTAB as surfactants and NaOH as base (CZPNa). The supports were calcined under air at 500°C for 6 h, with a ramp of 2°C/min and then characterized by means of XRD, nitrogen physisorption, TPR and hydrogen chemisorption/desorption. The results of the XRD analysis are shown in Figure 136.

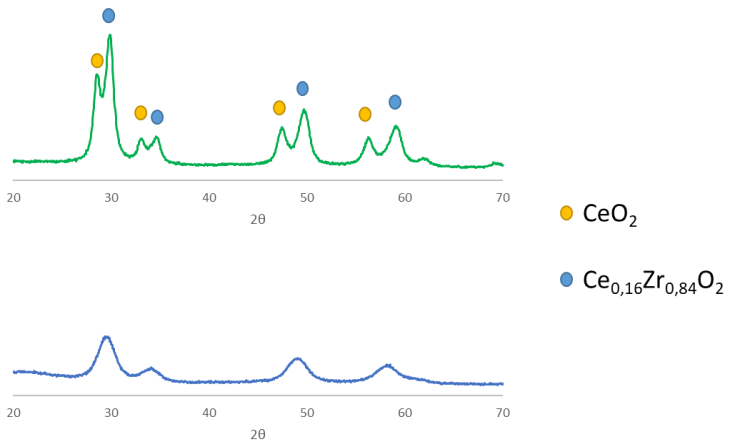

Figure 136: XRD analyses of the CeZrPr samples, CZPNa (green), CZPm (blue).

The diffractogram of the samples showed the presence of different patterns for the coprecipitated and the microemulsion samples. In fact, the former presented two different phase that could be ascribed to the presence of CeO_2 and $Ce_{0.16}Zr_{0.84}O_2$. The presence of a praseodymia phase was not detected due to its low amount and its dispersion in the Ce or CeZr phases. In the case of microemulsion synthesis a mixed oxide was obtained. In fact, only four peaks were observed, which could be associated to the formation of a CeZrPr mixed oxide. Thus, a first difference in the obtained supports regards the presence of a mixed oxide in the case of the microemulsion synthesis and of segregated oxides in the case of the coprecipitation one. This may affect the distribution of the active phase and the redox properties of the catalytic system. Scherrer equation was used to calculate the crystallite dimensions considering the reflect at 2teta = 49.0°. The crystallite average dimension was found to be 4,8 nm for the $Ce_{0.16}Zr_{0.84}O_2$ phases of the coprecipitated sample. Slightly smaller crystallites of 4,0 nm were given by the microemulsion technique, probably due to the employment of micelles which helped to contain particle grow. However, it must be noted that peak overlay of the Ce and CeZr phases is observed for the coprecipitated samples which did not allow the calculation of crystallite dimension for other reflect and of the CeO_2 phase. This could also lead to a slight underestimation of the crystallites size for these samples.

Table 40 reports surface area, pore volume and diameter of the synthetized supports. The addition of surfactant allowed to obtain high surface area in all cases. However, greater surface area is obtained for the microemulsion sample. As a similar pore volume is found in

the three samples, this can be related to the smaller particle dimensions obtained in this case. This was given by the use of micelles which allowed to slow down particle growth. Moreover, smaller pore diameter is obtained in this case, to a value similar to that of the crystallites as calculated by XRD. This suggests that the pores of the microemulsion sample are of interparticle nature.

Table 40: surface area, pore volume and average diameter for the synthetized supports after calcination at 500°C.

Sample	Surface area (m^2/g)	Pore volume (cm^3/g)	Pore diameter (nm)
CZPNa	84	0,18	8
CZPm	141	0,17	4

The catalyst morphology was investigated even after impregnation of the Ni precursor, followed by calcination at 500°C for 6 h. A decrease in surface area was observed in all cases together with lower pore volume. This can be related to pore collapse and sintering of the support that occurred due to the further treatment at high temperature. Nevertheless, the highest surface area was still shown by the microemulsion sample.

Table 41: surface area, pore volume and diameter for the synthetized catalysts.

Sample	Surface area (m^2/g)	Pore volume (cm^3/g)	Pore diameter (nm)
Ni-CZPNa	62	0,15	9
Ni-CZPm	98	0,14	4

The redox properties of both bare and impregnated supports were investigated by means of TPR using a flow of H_2 (10% in He) and a heating ramp of 15°C/min (Figures 137 and 138). The CeZrPr supports all showed one reduction peak, related to a homogeneous reduction of both surface and bulk Ce. This is favoured by the presence of other elements in the structure and can indicate high oxygen mobility between the bulk and the surface [98]. The reduction started around 400° and was centred at 600°C: a slight shift to higher temperature was observed by CZPNa, which indicates a lower support reducibility. The

hydrogen uptake was calculated and reported in table 43. The highest value was observed for CZPm. It can be due to the higher surface area of this sample which favours surface Ce availability.

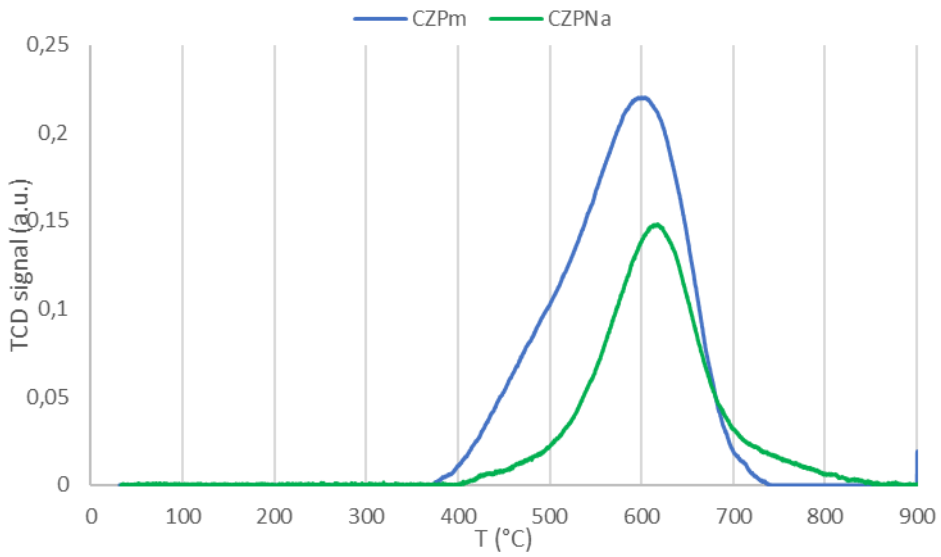

Figure 137: TPR of the bare supports, CZPNa (green), CZPm (blue).

The addition of Ni decreased the reduction temperature of the catalysts thanks to the hydrogen spillover effect. Two peaks were observed. The one at lower temperature was assigned to Ni and surface Ce reduction, while the other one to the bulk Ce reduction. The first reduction peak was observed at lower temperature in the case of the coprecipitated samples, which contrasts with the results of the bare supports. On the opposite, the Ni and Ce reduction peak for the microemulsion catalyst mainly occurs at 420°C. However, a shoulder is observed sample at lower temperatures, from 200 to 380°C. Thus, a different promotion of Ni phase is observed for the different synthetic methods, which seemed to favour the coprecipitated catalyst. In fact, a strong metal support interaction is supposed to occur on Ni-CZPm. This may provide a better interaction between the metal and support under reaction conditions, but also contributes to a decrease of redox properties of the material and lower metallic surface area (table 42). However, a higher hydrogen consumption is observed for NiCZPm.

Table 42: Ni surface area calculated by hydrogen temperature programmed desorption (TPD).

Sample	Ni surface area (m^2/g)
CZPNa	6,2
CZPm	4,0

Nevertheless, a higher % of Ce is reduced in the case of the microemulsion sample (table 43), which could be related to a a higher metal support interaction. In fact, the other supports do not show an increase in Ce reducibility upon Ni addition. Thus, the Ni deposited on the coprecipitated samples seem to be more reducible than the microemulsion one, but hydrogen spillover on the support is favoured for the latter.

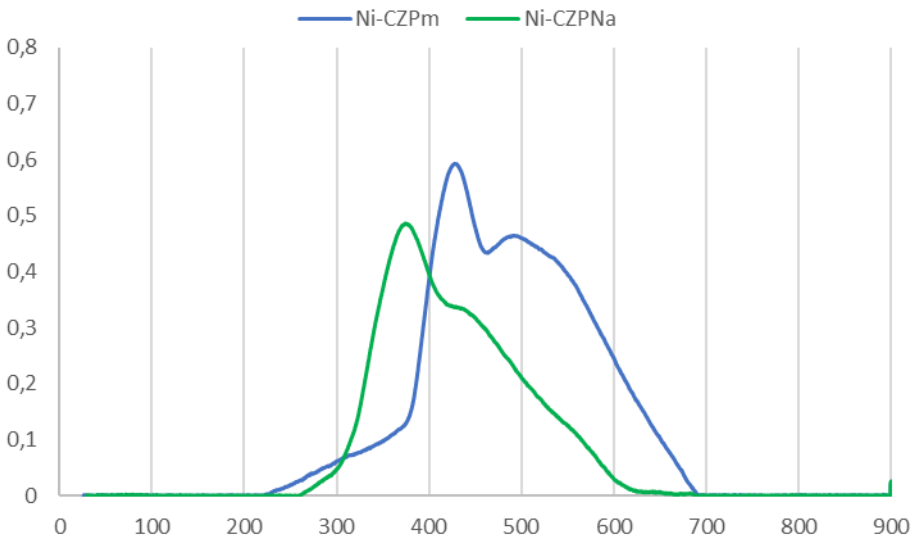

Figure 138: TPR of the impregnated catalysts, CZPNa (green), CZPm (blue).

Table 43: hydrogen uptake and metal reducibility of the supports and catalysts. A total Ni reduction and a loading of 10% wt of Ni is supposed.

Sample	Support		Catalyst	
	H_2 uptake (mmol/g)	***% Ce reduced***	***H_2 uptake (mmol/g)***	***% Ce reduced***
CZPNa	*0,60*	*30%*	*1,71*	*25%*
CZPm	*0,73*	*36%*	*2,10*	*50%*

11.3. Catalytic tests

The catalysts were tested in the methanation reaction at different temperatures and fixed GHSV (180 000 h^{-1}) and stoichiometric H_2/CO_2 ratio of 4.0. The first test was conducted at 280°C for 24h to evaluate catalytic stability. The methane yield over time is reported in Figure 139. For the Ni-CZPm catalyst an initial methane yield of 18% is obtained. However, it fast decreases to 16%, and then shows a more stable trend. In fact, less than 1% conversion is lost after 20 h. Thus, a stable catalyst is obtained by impregnating Ni over the CZPm support. This stability is probably related to a good support-metal interaction that helps to stabilize Ni particles and to the oxygen mobility of the Ce based support which helps the removal of eventually formed carbon. Similar stability is observed on Ni- CZPNa, which again highlights the positive effect of the CeZrPr based support on the Ni phase stability. However, this catalyst provided a conversion 10%, lower than that obtained with the microemulsion synthetized catalyst. Unfortunately, the first five hours of reaction were not analysed due to a technical issue. This behaviour can be related to the higher Ce reducibility obtained after Ni insertion which indicates a high interaction between Ni and Ce. In fact, even though Ni was named as active phase, Ce also participates to the reaction mechanism, helping the adsorption of CO_2 [185]. A good interaction between these two elements can thus lead to an increased methane yield. In fact, higher Ni surface area was observed for Ni-CZPNa, regardless the lower methane yield displayed. This suggests that the interaction between support and the metal has a higher impact on the methanation activity than the Ni

surface area itself. Thus, the reaction may take place at the Ni edges in contact with Ce, more than on Ni surface. However, TEM analysis has to be carry out to understand the particle morphology to estimate the extent of the particle-support edges.

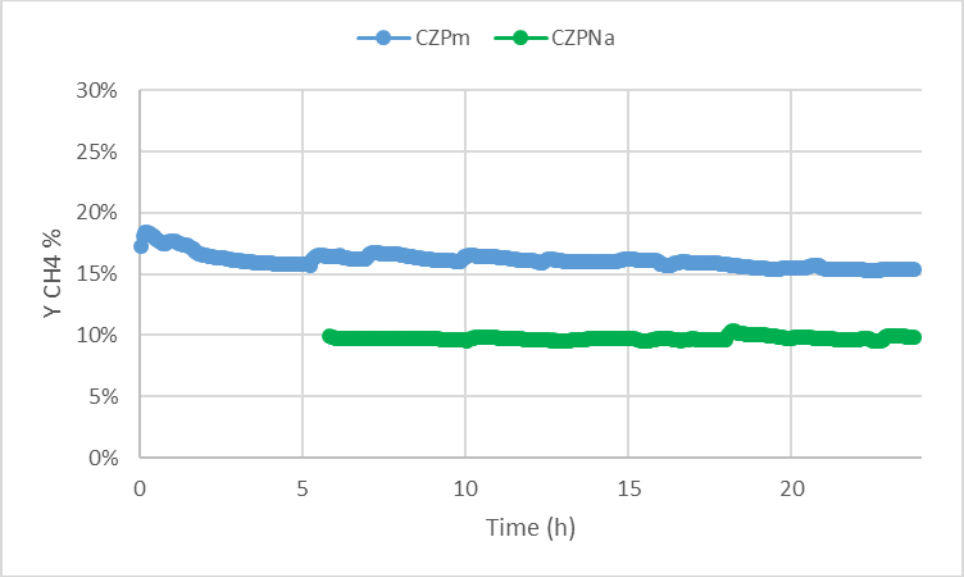

Figure 139: methane conversion over time at 280°C, 180 000 h^{-1}, 1 atm and H_2/CO_2 ratio of 4.0.

Figure 140 reports the methane yield and selectivity as a function of temperature. The equilibrium methane yield decreases with the temperature increase. Carbon dioxide methanation is in fact an exothermic reaction that occurs with a decrease in the number of gaseous moles and is thus favoured at low temperature and high pressure. The experimental methane yield of Ni-CZPm as function of temperature show a curve that starts at low conversion (16% at 280°C), increases slowly up to 300° and then has a sharper increase from 300°C to 350° and then reaches a plateau at 360°C. A further increase in temperature to 450°C provides a slight decrease in conversion, while a further increase of temperature allows to reach the equilibrium but gives lower yields. This trend can be explained by a low activity at low temperature, due to a low intrinsic kinetics in these conditions. At higher temperatures the kinetics of the catalysts are improved and lead to higher temperatures. Finally, over 400°C the yield decreases due to the thermodynamic limits given by the nature of the reaction that is favoured at low temperature. Methane selectivity over 98% is obtained in all conditions. In general, the high selectivity suggests that direct carbon dioxide methanation occurs on the catalyst without a CO desorption step. A similar yield trend was observed for Ni-CZPNa. However, lower yields were obtained in the

same conditions up to 400°C. At higher temperatures the conversion equalized suggesting that the reaction is under thermodynamic regime. Indeed the equilibrium is reached over 500°C. Again, the increased reactivity of CZPm may be linked to a higher interaction between Ce and Ni.

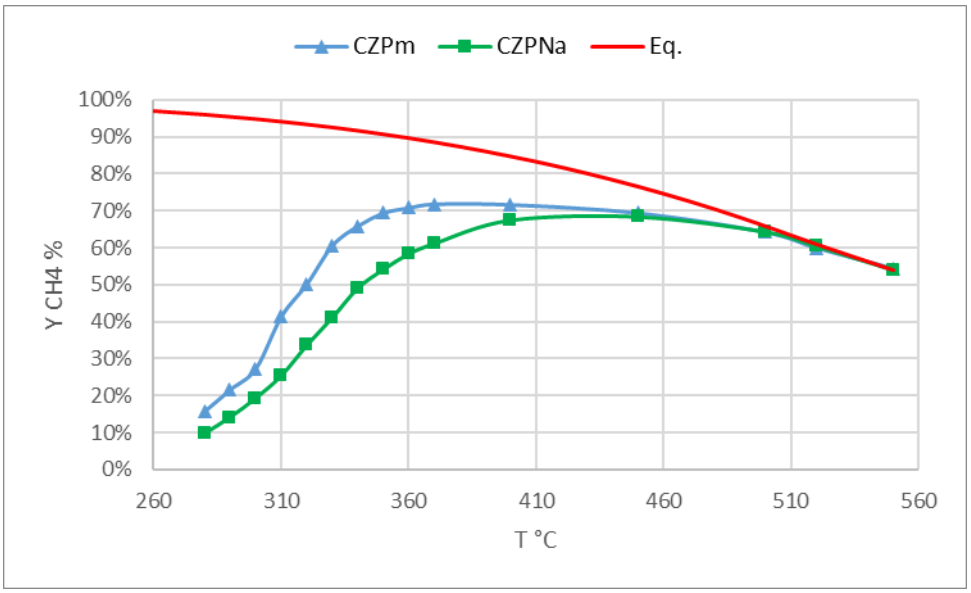

Figure 140: Experimental and equilibrium methane yields obtained at 180 000 h^{-1}, H_2/CO_2 of 4, 1 atm and different temperatures.

To further highlights the differences between the two catalysts, activation energy was calculated from Arrhenius plot, expressing the rate of methanation with the formula reported by Waldvogel, who worked previously on similar catalyst in the ICPEES laboratories [118]. The formula ia also reported here:

$$r_{metCO2} = (k * b_{CO2} * P_{CO2} * b_{H2} * P_{H2}) / ((1 + b_{CO2} * P_{CO2} + b_{H2O} * P_{H2O}) * (1 + b_{CO} * P_{CO} + b_{H2} * P_{H2})) \quad \text{(Eq. 14)}$$

where r_{metCO2} is the rate of methanation, expressed as consumed CO_2 over the grams of catalyst, k is the kinetic constant, P_i is the partial pressure of the species i, and b_i is the adsorption constant. b_i was calculated as $b_i = b_0 * e^{-Qads/RT,}$ where Qads is the heat of adsorption of the species i and b_0 is a pre-exponential factor, reported by Waldvogel [118].

From Eq. 14, k was calculated for the tests carried out at 280, 290 and 300°C. These tests were selected as a conversion lower than 30% was observed which indicated kinetic conditions and allowed to suppose the absence of the reverse water gas shift reaction [118]. Lnk was then plotted over 1/T (figure 141) and activation energy (Ea) and the pre-

exponential factor A were obtained from Arrhenius equation ($k=A*e^{-Ea/RT}$). Table 44: reports the obtained values.

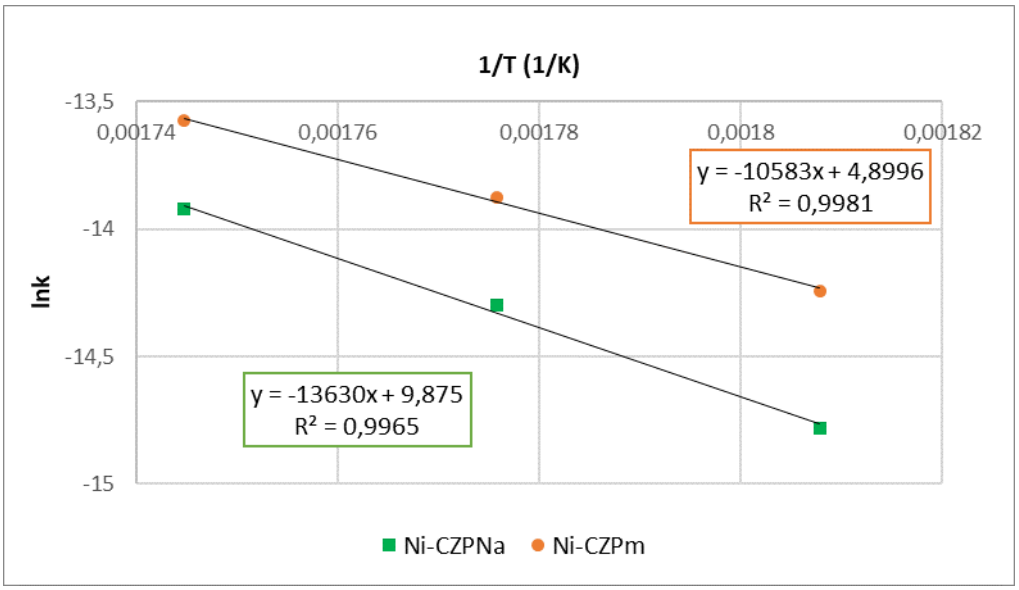

Figure 141: Arrhenius plot for the Ni-CZPm (orange) and Ni-CZPNa catalysts (green).

Table 44: Activation energy and pre-exponential factors for the Ni-CZPm and N-CZPNa catalysts and parameters used to calculate them.

	Activation Energy ***E_a (kJ/mol)***	***Pre-exponential factor*** ***A (mol/g/s)***	***Heat of Adsorption*** ***Q_{ads} (kJ/mol)***	***Pre-exponential factor*** ***b_0 (bar^{-1})***
Ni-CZPNa	**113**	**19438,3**	-	-
Ni-CZPm	**88**	**134,2**	-	-
CO_2	-	-	-99,3	$3,86.10^{-7}$
$H_{2\ préri}$	-	-	-115	$2,07.10^{-10}$
H_2	-	-	-106	$4,33.10^{-10}$
CO	-	-	-121	$2,89.10^{-9}$
H_2O	-	-	-31,4	$5,24.10^{-2}$

Ni-CZPm showed a lower activation energy for carbon dioxide methanation (88 kJ/mol) compared to Ni-CZPNa (113 kJ/mol), indicating a higher activity due to the formation of an reaction intermediate with lower energy in the rate determining step. These values were

similar to those obtained by Waldvogel on the Ni-CZPNa catalyst in the methanation of a CO_2/CO feed (120 kJ/mol) [118]. The obtained values were compared with those of literature (table 45).

Table 45: Activation energies (Ea) reported in literature for CO2 methanation.

	Herwijnen et al.	***Weatherbee et Bartholomew***	***Lee et al.***	***Aziz et al.***	***Xu et Froment***
Ea (kJ/mol)	*106*	*94*	*88*	*84*	*244*
Catalyst	*Ni/Al_2O_3*	*Ni/SiO_2*	*Ni Raney*	*Ni/SiO_2*	*$Ni/MgAl_2O_4$*
Ref.	[194]	[186]	[195]	[196]	[197]

The Ni-CZPm catalyst displays a lower or similar activation energy than those reported by other authors, which indicates it as a competitive catalyst for carbon dioxide methanation.

11.4. Conclusions

Two CeZrPr oxide supports were synthetized with two different methodology, namely the microemulsion synthesis and a surfactant assisted coprecipitation. The employment of micelles in the microemulsion synthesis allowed to get higher surface area and better support reducibility, together with the formation of a mixed oxide. Two phases were indeed observed at XRD for the coprecipitated sample, i.e. CeO_2 and $Ce_{0,16}Zr_{0,84}O_2$. After impregnation with 10%wt Ni, the coprecipitated sample showed a better Ni surface area and reducibility, which occurred at lower temperatures in the TPR experiment. However, a higher degree of Ce reduction was observed for the microemulsion sample, thanks to a better metal support interaction. This property seemed to affect the catalytic behaviour as higher yields were observed for the microemulsion-synthetized sample.

12. CONCLUSIONS

This thesis work aims to produce pure hydrogen from methane by employing a membrane reactor in which both reforming and water gas shift are carried out. The selected catalysts were based on noble metals impregnated over CeZr (CZO) or Zr (ZO) oxides synthesized by microemulsion technique. These oxides were characterized by means of different techniques which showed that peculiar properties could be obtained with this synthetic method. In particular, the use of micelles as microreactors, allowed to synthetize the desired $Ce_{0,5}Zr_{0,5}O_2$ or tetragonal ZrO_2. Moreover, small particles and a mesoporous morphology was observed, possessing a homogeneous reduction behaviour.

The synthetic parameters were modified in order to understand their influence on the oxide properties. In particular, particle dimension and surface area were moulded using aging time. A sharp rise was obtained from 1 to 5 h of aging time while a slighter one was observed when the mixture was aged for 24 h. Regarding base concentration, 1.56 M was found to be the optimal value. In fact, surface area decreased if base concentration was reduced or increased, Moreover, when concentration was too high, conditions similar to classical coprecipitation were obtained that lead to the formation of $Ce_{0,6}Zr_{0,4}O_2$ over the desired $Ce_{0,5}Zr_{0,5}O_2$. This phenomenon was also observed while increasing the Rw value, namely the amount of water in the micelles. When bigger micelles were created, a $Ce_{0,6}Zr_{0,4}O_2$ due to an environment similar to the coprecipitation synthesis.

These oxides were impregnated with different active phases and tested in different reactions, namely oxy-reforming at 750°C, water gas shift, oxy-reforming at 500°C, steam reforming at 500°C in order to find the best catalyst and conditions for the membrane reactor operation.

After impregnation with Pt or Rh, the CZO support was tested in the oxy-reforming reaction at 750°C under different operative conditions. A slight influence on the experimental conversion was observed by the steam to carbon ratio, suggesting that methane decomposition over the active phase was the limiting step in these conditions. An increase in GHSV provided a decrease in methane conversion because of the lower contact time between the reagents and the catalyst. Higher pressures provided lower equilibrium

and experimental conversions as suggested by thermodynamics. However, the experimental and equilibrium values were closer at these conditions. Rh-CZO outperformed Pt-CZO in oxy-reforming at 750°C, due to a higher selectivity toward reforming and catalytic partial oxidation. Moreover, Rh-CZO was more stable, given an improved synergy between the metal and the support, that allowed the removal of eventually deposited carbon. Thus, Rh was selected as reference catalyst for the high temperature oxy-reforming and it was employed to produce a reformate stream that was then submitted to the water gas shift reaction under different conditions. This reaction was carried out on reformate outlet using different catalysts (Pt, Rh, and PtRh mixtures on CZO). Pt-CZO gave the best results. High S/C at the reforming inlet were needed to favour the water gas shift reaction over methanation. In fact, hydrogen was consumed to give methane over the Pt catalyst at S/C 1. Moreover, increasing the contact time favoured methanation over water gas shift. This suggested that water gas shift is the fastest reaction and that methanation occurs on the CO_2 produced by it, without a CO desorption step in this reaction. In the case of Rh containing catalysts, methanation was favoured under all conditions and hydrogen was consumed rather than produced. Methanation was favoured in all conditions on the Rh containing catalysts.

These active phases (Pt, Rh, and PtRh mixtures) impregnated on the CZO support were tested in oxy-reforming at 500°C. Pt was found to be active in these conditions, though was not able to reach the equilibrium conversion. Moreover, Rh2.7-CZO showed a higher activity. It reached the conversion equilibrium in most conditions. Rh based catalysts outperformed platinum also when the Rh loading was lowered to 1%, to provide a similar metallic molar content to the Pt catalyst. An interesting trend was observed on the Rh-CZO catalysts (Rh2.7 and Rh1). An endothermic catalytic bed profile was developed on Rh2.7 while an exothermic one was shown decreasing the Rh amount. This affected the catalytic bed temperature and thus the equilibrium conversions. This was probably related to a predominance of CPO reaction when low number of Rh atoms were present on the catalyst surface. On the opposite, steam reforming takes place to a greater extent at higher Rh loadings, using the heat developed by CPO. Thus, an optimal catalytic bed temperature may be obtained by tuning the Rh loading, reducing both the exothermic and endothermic profiles. Bimetallic catalyst (PtRh) were also employed and showed synergy between the

two metals at 750°C, where the equilibrium conversion was reached. This was ascribed to the link between the oxidation properties of Pt and the reforming activity of Rh. However, this was not the case at lower temperature (500°C) were Pt was not able to provide oxidation ability and the Rh character was predominant. Finally, Ru based catalysts were selected to reduce the cost of the active phase. Ru provided similar conversion than Rh, especially when the S/C was high. In fact, S/C seemed to influence catalytic activity of Ru-CZO suggesting that steam participated to the kinetic equation. This was not the case for Rh, where methane decomposition was the rate determining step. However, Rh outperformed Ru in all the conditions thanks to its higher activity in reforming reactions. Moreover, stability due to sintering was an issue for the Ru catalyst. Thus, a Ru-CZO catalyst was produced by inserting Ru precursor in the support synthetic step. This allowed for an increased interaction between the metal and support after the reduction of the active phase. It provided lower conversion compared to impregnated Ru but increased stability, reducing sintering of the active phase.

In addition, catalytic tests were also conducted in low temperature steam reforming. Rh-based catalysts were obtained by using the $Rh_4(CO)_{12}$ neutral cluster as the active-phase precursor. In particular, the preparation method allowed the reactive deposition of the cluster on the surface of $Ce_{0.5}Zr_{0.5}O_2$ and ZrO_2 supports, which were synthetized by w/o microemulsion technique. The catalysts were found to be active in the low-temperature steam reforming process for syngas production. At high Rh loadings (0.6%) the CZOm-supported catalyst was active even at 350°C and was able to reach the equilibrium conversion, especially at low S/C ratio or at high pressures at 450 and 500°C. At lower concentrations (0.05%) and high temperature, the CZOm-supported cluster sample showed better results with respect to the analogous ZOm-supported one and to a classical Rh-impregnated CeZr catalyst. At low temperature, a deactivation effect was observed for the CZOm-supported catalyst, which could be overcome by employing a ZOm support. A detailed analysis provided evidences that the oxidation of the Rh promoted by Ce and high oxygen mobility was responsible for the fast deactivation. In these conditions, it was also observed that the cluster-based catalyst which had not been treated with hydrogen at 500°C was more active than the treated one, due to the sintering of the Rh particles. Finally,

the unreduced 0.05% Rh cluster deposited on the ZrO2 support showed significant activity at 500°C.

The low temperature steam reforming was also investigated on CeZr and Zr impregnated catalysts using Rh as active phase. Rh on zirconium oxide provided higher conversion and stability than the CeZr one. This was related to a decrease of the redox properties of Rh over CZO due to strong metal-support interaction given by the presence of Ce. For this reason, zirconium oxide (ZO) was selected as support to be used in the membrane reactor. The turnover frequency of Rh-ZO was calculated using low Rh amounts, after assessing the absence of mass transfer phenomena with a fluid dynamic study. The turnover frequency was used to calculate the optimum amount of Rh to be employed in the membrane reactor under steam reforming conditions, which resulted to be 0.75% wt/wt.

Finally, the steam reforming reaction was carried out at low temperature (400-450°C) inside a Pd-based membrane reactor. The membrane was characterized before the reactivity tests and showed high permeability. In the catalytic tests, hydrogen was readily separated by the Pd membrane. The permeation was allowed by a difference in hydrogen partial pressure between the inner and outer part of the membrane. This was provided by hydrogen generation on the catalyst and the use of sweep gas at the permeate side. Different conditions were investigated, and high methane conversions and hydrogen recoveries were obtained thanks to the high permeability of the membrane reactor which allowed to shift the equilibrium due to the Le Chatelier principle. Noteworthy, the methane conversion was higher than the equilibrium conversion of a fixed bed reactor operated in the same conditions. However, a decrease in methane conversion was observed over time. No decrease in membrane permeability was observed. Thus, the catalyst was discharged and characterized. During this operation it was observed that part of the catalyst moved from the membrane reactor to the tubes placed before and after it. This was caused by the change in pressure during operation. The characterization showed the absence of deactivation phenomena such as sintering and carbon formation. The used catalyst was tested in a fixed bed reactor ad its performances were compared with that of a fresh one. Thus, catalyst deactivation was excluded, and the reduction of methane conversion was associated to the movement of the catalyst out of the membrane reactor. This reduced the

synergy between catalyst and membrane. A new configuration will be employed in future studies to avoid this movement. However, this work demonstrated the possibility of performing the steam reforming reaction inside a Pd based membrane reactor. This allowed to sharply increase methane conversion compared to a fixed bed reactor and to separate a high flux of hydrogen from the reaction mixture with high hydrogen recoveries.

With the aim of synthetizing interesting materials for sorption enhanced steam reforming, hydrotalcite derived compounds were produced using Ca, Mg, Al, Ni as cations and carbonate or silicate as anions. A pure hydrotalcite was not obtained due to the presence of Ca, as segregated calcium carbonate was formed. High surface area and small particle dimension were obtained using silicates as anions. However, when tested in the carbon dioxide capture, they displayed low adsorption, due to the sequestration of Al by Si. The active species for adsorption were supposed to be both CaO and the mixed oxide, which could form a carbonate-containing hydrotalcite. High carbon dioxide sequestration was observed on mixed oxides derived from carbonate containing hydrotalcites.

Finally, the microemulsion synthesis was employed to synthetize a $Ce_{0.33}Zr_{0,63}Pr_{0,04}O_2$ support. It was compared with an analogous oxide synthetized by surfactant assisted coprecipitation. The employment of micelles in the microemulsion synthesis allowed to get higher surface area and better support reducibility, together with the formation of a mixed oxide. Two phases were indeed observed at XRD for the coprecipitated sample, i.e. CeO_2 and $Ce_{0,16}Zr_{0,84}O_2$. After impregnation with 10%wt Ni, the coprecipitated sample showed a better Ni surface area and reducibility, which occurred at lower temperatures in the TPR experiment. However, a higher degree of Ce reduction was observed for the microemulsion sample, thanks to a better metal support interaction. This property seemed to affect the catalytic behaviour as higher yields were observed for the microemulsion-synthetized sample.

References

1. Tuck, C.O.; Pérez, E.; Horváth, I.T.; Sheldon, R.A.; Poliakoff, M. Valorization of Biomass: Deriving More Value from Waste. *Science* **2012**, *337*, 695–699.
2. Fornasiero, P.; Graziani, M.; Graziani, M.; Graziani, M.; Graziani, M.; Graziani, M.; Graziani, M. *Renewable Resources and Renewable Energy : A Global Challenge, Second Edition*; CRC Press, 2011; ISBN 978-0-429-10645-3.
3. Hadjipaschalis, I.; Poullikkas, A.; Efthimiou, V. Overview of current and future energy storage technologies for electric power applications. *Renew. Sustain. Energy Rev.* **2009**, *13*, 1513–1522.
4. Dell, R.M.; Rand, D.A.J. Energy storage — a key technology for global energy sustainability. *J. Power Sources* **2001**, *100*, 2–17.
5. Hydrogen Council – A global CEO-level initiative with a united vision for hydrogen Available online: http://hydrogencouncil.com/ (accessed on Jun 19, 2019).
6. Korean government announces deployment of 310 hydrogen stations by 2022 Available online: https://energies.airliquide.com/korean-government-announces-deployment-310-hydrogen-stations-2022 (accessed on Jun 19, 2019).
7. Germany launches world's first hydrogen-powered train | Environment | The Guardian Available online: https://www.theguardian.com/environment/2018/sep/17/germany-launches-worlds-first-hydrogen-powered-train (accessed on Jun 19, 2019).
8. Mercedes GLC F-Cell, sono iniziate le consegne del Suv ibrido a idrogeno - La Stampa Available online: https://www.lastampa.it/2018/11/17/motori/mercedes-glc-fcell-sono-iniziate-le-consegne-del-suv-ibrido-a-idrogeno-x0jHQGMrwwEIcN95EYoMTM/pagina.html (accessed on Jun 19, 2019).
9. Hydrogen Available online: https://www.iea.org/tcep/energyintegration/hydrogen/ (accessed on Jun 19, 2019).
10. Abbasi, T.; Abbasi, S.A. 'Renewable' hydrogen: Prospects and challenges. *Renew. Sustain. Energy Rev.* **2011**, *15*, 3034–3040.
11. Armor, J.N. Catalysis and the hydrogen economy. *Catal. Lett.* **2005**, *101*, 131–135.
12. Yellow light for a green fuel. - Abstract - Europe PMC Available online: https://europepmc.org/abstract/med/14712786 (accessed on Jun 19, 2019).
13. Ferreira-Aparicio, D.P.; Benito, M.J.; Sanz, J.L. New Trends in Reforming Technologies: from Hydrogen Industrial Plants to Multifuel Microreformers. *Catal. Rev.* **2005**, *47*, 491–588.
14. Nikolaidis, P.; Poullikkas, A. A comparative overview of hydrogen production processes. *Renew. Sustain. Energy Rev.* **2017**, *67*, 597–611.
15. Roddy, D.J. A syngas network for reducing industrial carbon footprint and energy use. *Appl. Therm. Eng.* **2013**, *53*, 299–304.
16. Christensen, T.S. Adiabatic prereforming of hydrocarbons — an important step in syngas production. *Appl. Catal. Gen.* **1996**, *138*, 285–309.
17. Ahmed, S.; Krumpelt, M. Hydrogen from hydrocarbon fuels for fuel cells. *Int. J. Hydrog. Energy* **2001**, *26*, 291–301.
18. Sehested, J. Sintering of nickel steam-reforming catalysts. *J. Catal.* **2003**, *217*, 417–426.
19. Sehested, J.; Carlsson, A.; Janssens, T.V.W.; Hansen, P.L.; Datye, A.K. Sintering of Nickel Steam-Reforming Catalysts on MgAl2O4 Spinel Supports. *J. Catal.* **2001**, *197*, 200–209.
20. Smith, M.W.; Shekhawat, D. Chapter 5 - Catalytic Partial Oxidation. In *Fuel Cells: Technologies for Fuel Processing*; Shekhawat, D., Spivey, J.J., Berry, D.A., Eds.; Elsevier: Amsterdam, 2011; pp. 73–128 ISBN 978-0-444-53563-4.
21. York, A.P.E.; Xiao, T.; Green, M.L.H.; Claridge, J.B. Methane Oxyforming for Synthesis Gas Production. *Catal. Rev.* **2007**, *49*, 511–560.

22. Basile, F.; Fornasari, G.; Trifirò, F.; Vaccari, A. Partial oxidation of methane: Effect of reaction parameters and catalyst composition on the thermal profile and heat distribution. *Catal. Today* **2001**, *64*, 21–30.
23. Iaquaniello, G.; Antonetti, E.; Cucchiella, B.; Palo, E.; Salladini, A.; Guarinoni, A.; Lainati, A.; Basini, L. Natural Gas Catalytic Partial Oxidation: A Way to Syngas and Bulk Chemicals Production. *Nat. Gas - Extr. End Use* **2012**.
24. Christensen, T.S.; Primdahl, I.I. (Haldor T. Improve syngas production using autothermal reforming. *Hydrocarb. Process. U. S.* **1994**, *73:3*.
25. Aasberg-Petersen, K.; Bak Hansen, J.-H.; Christensen, T.S.; Dybkjaer, I.; Christensen, P.S.; Stub Nielsen, C.; Winter Madsen, S.E.L.; Rostrup-Nielsen, J.R. Technologies for large-scale gas conversion. *Appl. Catal. Gen.* **2001**, *221*, 379–387.
26. Rostrup-Nielsen, J.R. New aspects of syngas production and use. *Catal. Today* **2000**, *63*, 159–164.
27. Twigg, M.V. *Catalyst Handbook*; Routledge, 2018; ISBN 978-1-351-46232-7.
28. Mann, M.; Spath, P. *Life Cycle Assessment of Renewable Hydrogen Production via Wind/Electrolysis: Milestone Completion Report*; National Renewable Energy Lab., Golden, CO. (US), 2004;
29. Pen˜a, M.A.; Gómez, J.P.; Fierro, J.L.G. New catalytic routes for syngas and hydrogen production. *Appl. Catal. Gen.* **1996**, *144*, 7–57.
30. SIRCAR, S.; GOLDEN, T.C. Purification of Hydrogen by Pressure Swing Adsorption. *Sep. Sci. Technol.* **2000**, *35*, 667–687.
31. Basile, F.; Fasolini, A.; Lombardi, E. CHAPTER 7 Membrane Processes for Pure Hydrogen Production from Biomass. In *Membrane Engineering for the Treatment of Gases: Volume 2: Gas-separation Issues Combined with Membrane Reactors (2)*; The Royal Society of Chemistry, 2018; Vol. 2, pp. 212–246 ISBN 978-1-78262-875-0.
32. Saracco, G.; Specchia, V. Catalytic Inorganic-Membrane Reactors: Present Experience and Future Opportunities. *Catal. Rev.* **1994**, *36*, 305–384.
33. Lu, G.Q.; Diniz da Costa, J.C.; Duke, M.; Giessler, S.; Socolow, R.; Williams, R.H.; Kreutz, T. Inorganic membranes for hydrogen production and purification: A critical review and perspective. *J. Colloid Interface Sci.* **2007**, *314*, 589–603.
34. Kikuchi, E. Membrane reactor application to hydrogen production. *Catal. Today* **2000**, *56*, 97–101.
35. Dittmeyer, R.; Höllein, V.; Daub, K. Membrane reactors for hydrogenation and dehydrogenation processes based on supported palladium. *J. Mol. Catal. Chem.* **2001**, *173*, 135–184.
36. Tong, J.; Shirai, R.; Kashima, Y.; Matsumura, Y. Preparation of a pinhole-free Pd–Ag membrane on a porous metal support for pure hydrogen separation. *J. Membr. Sci.* **2005**, *260*, 84–89.
37. Wang, D.; Tong, J.; Xu, H.; Matsumura, Y. Preparation of palladium membrane over porous stainless steel tube modified with zirconium oxide. *Catal. Today* **2004**, *93–95*, 689–693.
38. Uemiya, S.; Matsuda, T.; Kikuchi, E. Hydrogen permeable palladium-silver alloy membrane supported on porous ceramics. *J. Membr. Sci.* **1991**, *56*, 315–325.
39. Lynch, S. Hydrogen embrittlement phenomena and mechanisms. *Corros. Rev.* **2012**, *30*, 105–123.
40. Hou, K.; Hughes, R. Preparation of thin and highly stable Pd/Ag composite membranes and simulative analysis of transfer resistance for hydrogen separation. *J. Membr. Sci.* **2003**, *214*, 43–55.
41. Amandusson, H.; Ekedahl, L.-G.; Dannetun, H. The effect of CO and O2 on hydrogen permeation through a palladium membrane. *Appl. Surf. Sci.* **2000**, *153*, 259–267.

42. Cheng, Y.S.; Yeung, K.L. Palladium–silver composite membranes by electroless plating technique. *J. Membr. Sci.* **1999**, *158*, 127–141.
43. Bryden, K.J.; Ying, J.Y. Nanostructured palladium–iron membranes for hydrogen separation and membrane hydrogenation reactions. *J. Membr. Sci.* **2002**, *203*, 29–42.
44. Jun, C.-S.; Lee, K.-H. Palladium and palladium alloy composite membranes prepared by metal-organic chemical vapor deposition method (cold-wall). *J. Membr. Sci.* **2000**, *176*, 121–130.
45. Fort, D.; Farr, J.P.G.; Harris, I.R. A comparison of palladium-silver and palladium-yttrium alloys as hydrogen separation membranes. *J. Common Met.* **1975**, *39*, 293–308.
46. Yun, S.; Ted Oyama, S. Correlations in palladium membranes for hydrogen separation: A review. *J. Membr. Sci.* **2011**, *375*, 28–45.
47. Roa, F.; Way, J.D.; McCormick, R.L.; Paglieri, S.N. Preparation and characterization of Pd–Cu composite membranes for hydrogen separation. *Chem. Eng. J.* **2003**, *93*, 11–22.
48. Fang, S.; Bi, L.; Wu, X.; Gao, H.; Chen, C.; Liu, W. Chemical stability and hydrogen permeation performance of Ni–BaZr0. 1Ce0. 7Y0. 2O3− δ in an H2S-containing atmosphere. *J. Power Sources* **2008**, *183*, 126–132.
49. Li, J.; Luo, J.-L.; Chuang, K.T.; Sanger, A.R. Chemical stability of Y-doped Ba(Ce,Zr)O3 perovskites in H2S-containing H2. *Electrochimica Acta* **2008**, *53*, 3701–3707.
50. Lin, Y.S. Inorganic Membranes for Process Intensification: Challenges and Perspective. *Ind. Eng. Chem. Res.* **2019**, *58*, 5787–5796.
51. Cardoso, S.P.; Azenha, I.S.; Lin, Z.; Portugal, I.; Rodrigues, A.E.; Silva, C.M. Inorganic Membranes for Hydrogen Separation. *Sep. Purif. Rev.* **2018**, *47*, 229–266.
52. Rosensteel, W.A.; Ricote, S.; Sullivan, N.P. Hydrogen permeation through dense BaCe0.8Y0.2O3−δ – Ce0.8Y0.2O2−δ composite-ceramic hydrogen separation membranes. *Int. J. Hydrog. Energy* **2016**, *41*, 2598–2606.
53. Fasolini, A.; Abate, S.; Barbera, D.; Centi, G.; Basile, F. Pure H2 production by methane oxy-reforming over Rh-Mg-Al hydrotalcite-derived catalysts coupled with a Pd membrane. *Appl. Catal. Gen.* **2019**, *581*, 91–102.
54. Basile, F.; Mafessanti, R.; Fasolini, A.; Fornasari, G.; Lombardi, E.; Vaccari, A. Effect of synthetic method on CeZr support and catalytic activity of related Rh catalyst in the oxidative reforming reaction. *J. Eur. Ceram. Soc.* **2019**, *39*, 41–52.
55. Bartholomew, C.H. Carbon Deposition in Steam Reforming and Methanation. *Catal. Rev.* **1982**, *24*, 67–112.
56. Yang, K.L.; Yang, R.T. The accelerating and retarding effects of hydrogen on carbon deposition on metal surfaces. *Carbon* **1986**, *24*, 687–693.
57. Rostrup-Nielsen, J.; Trimm, D.L. Mechanisms of carbon formation on nickel-containing catalysts. *J. Catal.* **1977**, *48*, 155–165.
58. Rostrup-Nielsen, J.R. Coking on nickel catalysts for steam reforming of hydrocarbons. *J. Catal.* **1974**, *33*, 184–201.
59. De Deken, J.; Menon, P.G.; Froment, G.F.; Haemers, G. On the nature of carbon in Niα-Al2O3 catalyst deactivated by the methane-steam reforming reaction. *J. Catal.* **1981**, *70*, 225–229.
60. Liu, Z.-W.; Jun, K.-W.; Roh, H.-S.; Park, S.-E. Hydrogen production for fuel cells through methane reforming at low temperatures. *J. Power Sources* **2002**, *111*, 283–287.
61. Bottino, A.; Comite, A.; Capannelli, G.; Di Felice, R.; Pinacci, P. Steam reforming of methane in equilibrium membrane reactors for integration in power cycles. *Catal. Today* **2006**, *118*, 214–222.
62. Barbieri, G.; Marigliano, G.; Perri, G.; Drioli, E. Conversion−Temperature Diagram for a Palladium Membrane Reactor. Analysis of an Endothermic Reaction: Methane Steam Reforming. *Ind. Eng. Chem. Res.* **2001**, *40*, 2017–2026.

63. Kyriakides, A.-S.; Rodríguez-García, L.; Voutetakis, S.; Ipsakis, D.; Seferlis, P.; Papadopoulou, S. Enhancement of pure hydrogen production through the use of a membrane reactor. *Int. J. Hydrog. Energy* **2014**, *39*, 4749–4760.
64. Patrascu, M.; Sheintuch, M. On-site pure hydrogen production by methane steam reforming in high flux membrane reactor: Experimental validation, model predictions and membrane inhibition. *Chem. Eng. J.* **2015**, *262*, 862–874.
65. Iulianelli, A.; Liguori, S.; Wilcox, J.; Basile, A. Advances on methane steam reforming to produce hydrogen through membrane reactors technology: A review. *Catal. Rev.* **2016**, *58*, 1–35.
66. Iulianelli, A.; Manzolini, G.; De Falco, M.; Campanari, S.; Longo, T.; Liguori, S.; Basile, A. H2 production by low pressure methane steam reforming in a Pd–Ag membrane reactor over a Ni-based catalyst: Experimental and modeling. *Int. J. Hydrog. Energy* **2010**, *35*, 11514–11524.
67. Basile, A.; Campanari, S.; Manzolini, G.; Iulianelli, A.; Longo, T.; Liguori, S.; De Falco, M.; Piemonte, V. Methane steam reforming in a Pd–Ag membrane reformer: An experimental study on reaction pressure influence at middle temperature. *Int. J. Hydrog. Energy* **2011**, *36*, 1531–1539.
68. Lin, Y.-M.; Liu, S.-L.; Chuang, C.-H.; Chu, Y.-T. Effect of incipient removal of hydrogen through palladium membrane on the conversion of methane steam reforming: Experimental and modeling. *Catal. Today* **2003**, *82*, 127–139.
69. Abu El Hawa, H.W.; Paglieri, S.N.; Morris, C.C.; Harale, A.; Douglas Way, J. Application of a Pd–Ru composite membrane to hydrogen production in a high temperature membrane reactor. *Sep. Purif. Technol.* **2015**, *147*, 388–397.
70. Shu, J.; Grandjean, B.P.A.; Neste, A.V.; Kaliaguine1, S. Catalytic palladium-based membrane reactors: A review. *Can. J. Chem. Eng.* **1991**, *69*, 1036–1060.
71. Sarić, M.; van Delft, Y.C.; Sumbharaju, R.; Meyer, D.F.; de Groot, A. Steam reforming of methane in a bench-scale membrane reactor at realistic working conditions. *Catal. Today* **2012**, *193*, 74–80.
72. Matsuka, M.; Higashi, M.; Ishihara, T. Hydrogen production from methane using vanadium-based catalytic membrane reactors. *Int. J. Hydrog. Energy* **2013**, *38*, 6673–6680.
73. Rostrup-Nielsen, J.R.; Sehested, J.; Nørskov, J.K. Hydrogen and synthesis gas by steam- and C02 reforming. In *Advances in Catalysis*; Academic Press, 2002; Vol. 47, pp. 65–139.
74. Rostrupnielsen, J.R.; Hansen, J.H.B. CO2-Reforming of Methane over Transition Metals. *J. Catal.* **1993**, *144*, 38–49.
75. Wei, J.; Iglesia, E. Reaction Pathways and Site Requirements for the Activation and Chemical Conversion of Methane on Ru−Based Catalysts. *J. Phys. Chem. B* **2004**, *108*, 7253–7262.
76. Wei, J.; Iglesia, E. Structural requirements and reaction pathways in methane activation and chemical conversion catalyzed by rhodium. *J. Catal.* **2004**, *225*, 116–127.
77. Wei, J.; Iglesia, E. Mechanism and Site Requirements for Activation and Chemical Conversion of Methane on Supported Pt Clusters and Turnover Rate Comparisons among Noble Metals. *J. Phys. Chem. B* **2004**, *108*, 4094–4103.
78. Wei, J.; Iglesia, E. Structural and Mechanistic Requirements for Methane Activation and Chemical Conversion on Supported Iridium Clusters. *Angew. Chem. Int. Ed.* **2004**, *43*, 3685–3688.
79. Wei, J.; Iglesia, E. Isotopic and kinetic assessment of the mechanism of methane reforming and decomposition reactions on supported iridium catalysts. *Phys. Chem. Chem. Phys.* **2004**, *6*, 3754–3759.
80. Rostrup-Nielsen, J.R. Activity of nickel catalysts for steam reforming of hydrocarbons. *J. Catal.* **1973**, *31*, 173–199.

81. Kikuchi, E.; Tanaka, S.; Yamazaki, Y.; Morita, Y. Steam Reforming of Hydrocarbons on Noble Metal Catalysts (Part 1). *Bull. Jpn. Pet. Inst.* **1974**, *16*, 95–98.
82. Qin, D.; Lapszewicz, J. Study of mixed steam and CO2 reforming of CH4 to syngas on MgO-supported metals. *Catal. Today* **1994**, *21*, 551–560.
83. Armor, J.N.; Martenak, D.J. Studying carbon formation at elevated pressure. *Appl. Catal. Gen.* **2001**, *206*, 231–236.
84. Bartholomew, C.H. Mechanisms of catalyst deactivation. *Appl. Catal. Gen.* **2001**, *212*, 17–60.
85. Trimm, D.L. The Formation and Removal of Coke from Nickel Catalyst. *Catal. Rev.* **1977**, *16*, 155–189.
86. Trimm, D.L. Coke formation and minimisation during steam reforming reactions. *Catal. Today* **1997**, *37*, 233–238.
87. McCarty, J.G.; Wise, H. Hydrogenation of surface carbon on alumina-supported nickel. *J. Catal.* **1979**, *57*, 406–416.
88. Bengaard, H.S.; Nørskov, J.K.; Sehested, J.; Clausen, B.S.; Nielsen, L.P.; Molenbroek, A.M.; Rostrup-Nielsen, J.R. Steam Reforming and Graphite Formation on Ni Catalysts. *J. Catal.* **2002**, *209*, 365–384.
89. Chen, D.; Christensen, K.O.; Ochoa-Fernández, E.; Yu, Z.; Tøtdal, B.; Latorre, N.; Monzón, A.; Holmen, A. Synthesis of carbon nanofibers: effects of Ni crystal size during methane decomposition. *J. Catal.* **2005**, *229*, 82–96.
90. Dibbern, H.C.; Olesen, P.; Rostrup-Nielsen, J.R.; Tottrup, P.B.; Udengaard, N.R. Make low H/sub 2//CO syngas using sulfur passivated reforming. *Hydrocarb. Process U. S.* **1986**, *65:1*.
91. Kiskinova, M.; Goodman, D.W. Modification of chemisorption properties by electronegative adatoms: H2 and CO on chlorided, sulfided, and phosphided Ni(100). *Surf. Sci.* **1981**, *108*, 64–76.
92. Christensen, K.O.; Chen, D.; Lødeng, R.; Holmen, A. Effect of supports and Ni crystal size on carbon formation and sintering during steam methane reforming. *Appl. Catal. Gen.* **2006**, *314*, 9–22.
93. Bartholomew, C.H. Sintering kinetics of supported metals: new perspectives from a unifying GPLE treatment. *Appl. Catal. Gen.* **1993**, *107*, 1–57.
94. Richardson, J.T.; Crump, J.G. Crystallite size distributions of sintered nickel catalysts. *J. Catal.* **1979**, *57*, 417–425.
95. Young, D.J.; Udaja, P.; Trimm, D.L. Deactivation Due to Metal-Catalysed Phase Transformations in Λ-Al2O3 Supports. In *Studies in Surface Science and Catalysis*; Delmon, B., Froment, G.F., Eds.; Catalyst Deactivation; Elsevier, 1980; Vol. 6, pp. 331–340.
96. Effect of alkali and alkaline-earth metals on the resistivity to coke formation and sintering of nickel-alumina catalysts | Industrial & Engineering Chemistry Research Available online: https://pubs.acs.org/doi/pdf/10.1021/ie00100a006 (accessed on Jun 19, 2019).
97. Wanke, S.E.; Flynn, P.C. The Sintering of Supported Metal Catalysts. *Catal. Rev.* **1975**, *12*, 93–135.
98. Trovarelli, A.; Fornasiero, P. *Catalysis by Ceria and Related Materials*; World Scientific, 2013; ISBN 978-1-84816-964-7.
99. Montoya, J.A.; Romero-Pascual, E.; Gimon, C.; Del Angel, P.; Monzón, A. Methane reforming with CO2 over Ni/ZrO2–CeO2 catalysts prepared by sol–gel. *Catal. Today* **2000**, *63*, 71–85.
100. Wang, H.Y.; Ruckenstein, E. Carbon dioxide reforming of methane to synthesis gas over supported rhodium catalysts: the effect of support. *Appl. Catal. Gen.* **2000**, *204*, 143–152.
101. Wang, S.; (Max) Lu, G.Q. Role of CeO2 in Ni/CeO2–Al2O3 catalysts for carbon dioxide reforming of methane. *Appl. Catal. B Environ.* **1998**, *19*, 267–277.

102. Ascención Montoya, J.; Romero, E.; Monzón, A.; Guimon, C. Methane reforming with CO2 over Ni/ZrO2-CeO2 and Ni/ZrO2-MgO catalysts synthesized by sol-gel method. In *Studies in Surface Science and Catalysis*; Corma, A., Melo, F.V., Mendioroz, S., Fierro, J.L.G., Eds.; 12th International Congress on Catalysis; Elsevier, 2000; Vol. 130, pp. 3669–3674.
103. Roh, H.-S.; Jun, K.-W.; Dong, W.-S.; Park, S.-E.; Baek, Y.-S. Highly stable Ni catalyst supported on Ce–ZrO2 for oxy-steam reforming of methane. *Catal. Lett.* **2001**, *74*, 31–36.
104. Noronha, F.B.; Fendley, E.C.; Soares, R.R.; Alvarez, W.E.; Resasco, D.E. Correlation between catalytic activity and support reducibility in the CO2 reforming of methane over Pt/CexZr1−xO2 catalysts. *Chem. Eng. J.* **2001**, *82*, 21–31.
105. Menad, S.; Ferreira-Aparicio, P.; Cherifi, O.; Guerrero-Ruiz, A.; Rodríguez-Ramos, I. Designing New High Oxygen Mobility Supports to Improve the Stability of RU Catalysts Under Dry Reforming of Methane. *Catal. Lett.* **2003**, *89*, 63–67.
106. Ivanova, A.S. Physicochemical and catalytic properties of systems based on CeO2. *Kinet. Catal.* **2009**, *50*, 797–815.
107. Duwez, P.; Odell, F.; Brown, F.H. Stabilization of Zirconia with Calcia and Magnesia Available online: https://ceramics.onlinelibrary.wiley.com/doi/abs/10.1111/j.1151-2916.1952.tb13081.x (accessed on Jun 24, 2019).
108. Yashima, M.; Arashi, H.; Kakihana, M.; Yoshimura, M. Raman Scattering Study of Cubic–Tetragonal Phase Transition in Zr1−xCexO2 Solid Solution. *J. Am. Ceram. Soc.* **1994**, *77*, 1067–1071.
109. Turko, G.A.; Ivanova, A.S.; Plyasova, L.M.; Litvak, G.S.; Rogov, V.A. Synthesis and Characterization of Fluorite-Like Ce-Zr-Y-La-O Systems. *Kinet. Catal.* **2005**, *46*, 884–890.
110. Boutonnet, M.; Lögdberg, S.; Elm Svensson, E. Recent developments in the application of nanoparticles prepared from w/o microemulsions in heterogeneous catalysis. *Curr. Opin. Colloid Interface Sci.* **2008**, *13*, 270–286.
111. Eriksson, S.; Nylén, U.; Rojas, S.; Boutonnet, M. Preparation of catalysts from microemulsions and their applications in heterogeneous catalysis. *Appl. Catal. Gen.* **2004**, *265*, 207–219.
112. Martínez-Arias, A.; Fernández-García, M.; Ballesteros, V.; Salamanca, L.N.; Conesa, J.C.; Otero, C.; Soria, J. Characterization of High Surface Area Zr−Ce (1:1) Mixed Oxide Prepared by a Microemulsion Method. *Langmuir* **1999**, *15*, 4796–4802.
113. Capek, I. Preparation of metal nanoparticles in water-in-oil (w/o) microemulsions. *Adv. Colloid Interface Sci.* **2004**, *110*, 49–74.
114. Moulik, S.P.; Paul, B.K. Structure, dynamics and transport properties of microemulsions. *Adv. Colloid Interface Sci.* **1998**, *78*, 99–195.
115. Schulman, J.H.; Friend, J.A. Light scattering investigation of the structure of transparent oil-water disperse systems. II. *J. Colloid Sci.* **1949**, *4*, 497–509.
116. Chemistry, I.U. of P. and A. IUPAC Gold Book - amphipathic Available online: http://goldbook.iupac.org/html/A/A00302.html (accessed on Sep 4, 2018).
117. Malik, M.A.; Wani, M.Y.; Hashim, M.A. Microemulsion method: A novel route to synthesize organic and inorganic nanomaterials. *Arab. J. Chem.* **2012**, *5*, 397–417.
118. Waldvogel, A. Mise au point d'un catalyseur performant pour la chaîne de procédé Power-to-Methane et étude cinétique, University o Strasbourg, 2017.
119. Albertazzi, S.; Basile, F.; Benito, P.; Del Gallo, P.; Fornasari, G.; Gary, D.; Rosetti, V.; Vaccari, A. Effect of silicates on the structure of Ni-containing catalysts obtained from hydrotalcite-type precursors. *Catal. Today* **2007**, *128*, 258–263.
120. Mafessanti, R. Catalysts and processes for next-generation H2 production. Tesi di dottorato, alma, 2014.
121. Barbera, D. Innovative Processes for Hydrogen Production. tesi dottorato, University of Bologna, 2013.

122. Giovanardi, S. Sviluppo di un sistema integrato innovativo per la contemporanea produzione e separazione di H2 ultrapuro, attraverso oxy-reforming, water-gas shift e membrane al Pd. Tesi di laurea, 2016.
123. Tabanelli, T.; Paone, E.; Blair Vásquez, P.; Pietropaolo, R.; Cavani, F.; Mauriello, F. Transfer Hydrogenation of Methyl and Ethyl Levulinate Promoted by a ZrO2 Catalyst: Comparison of Batch vs Continuous Gas-Flow Conditions. *ACS Sustain. Chem. Eng.* **2019**, *7*, 9937–9947.
124. Chuah, G.K. An investigation into the preparation of high surface area zirconia. *Catal. Today* **1999**, *49*, 131–139.
125. Chuah, G.K.; Jaenicke, S.; Cheong, S.A.; Chan, K.S. The influence of preparation conditions on the surface area of zirconia. *Appl. Catal. Gen.* **1996**, *145*, 267–284.
126. Srinivasan, R.; Harris, M.B.; Simpson, S.F.; Angelis, R.J.D.; Davis, B.H. Zirconium oxide crystal phase: The role of the pH and time to attain the final pH for precipitation of the hydrous oxide. *J. Mater. Res.* **1988**, *3*, 787–797.
127. Zhang, F.; Chen, C.-H.; Hanson, J.C.; Robinson, R.D.; Herman, I.P.; Chan, S.-W. Phases in Ceria–Zirconia Binary Oxide (1−x)CeO2–xZrO2 Nanoparticles: The Effect of Particle Size. *J. Am. Ceram. Soc.* **2006**, *89*, 1028–1036.
128. Reporting physisorption data for gas/solid systems with special reference to the determination of surface area and porosity (Recommendations 1984) : Pure and Applied Chemistry Available online: https://www.degruyter.com/view/j/pac.1985.57.issue-4/pac198557040603/pac198557040603.xml (accessed on Oct 5, 2019).
129. Boaro, M.; Vicario, M.; de Leitenburg, C.; Dolcetti, G.; Trovarelli, A. The use of temperature-programmed and dynamic/transient methods in catalysis: characterization of ceria-based, model three-way catalysts. *Catal. Today* **2003**, *77*, 407–417.
130. Fornasiero, P.; Kašpar, J.; Graziani, M. On the rate determining step in the reduction of CeO2–ZrO2 mixed oxides. *Appl. Catal. B Environ.* **1999**, *22*, L11–L14.
131. Fornasiero, P.; Balducci, G.; Di Monte, R.; Kašpar, J.; Sergo, V.; Gubitosa, G.; Ferrero, A.; Graziani, M. Modification of the Redox Behaviour of CeO2Induced by Structural Doping with ZrO2. *J. Catal.* **1996**, *164*, 173–183.
132. Djinović, P.; Osojnik Črnivec, I.G.; Erjavec, B.; Pintar, A. Influence of active metal loading and oxygen mobility on coke-free dry reforming of Ni–Co bimetallic catalysts. *Appl. Catal. B Environ.* **2012**, *125*, 259–270.
133. Wang, Q.; Yue, M.; Zhong, Q.; Cui, M.; Huang, X.; Hou, Y.; Wang, L.; Yang, Y.; Long, Z.; Feng, Z. Structure and properties of cerium zirconium mixed oxide prepared under different precipitate aging processes. *J. Rare Earths* **2016**, *34*, 695–703.
134. Ocampo, F.; Louis, B.; Kiwi-Minsker, L.; Roger, A.-C. Effect of Ce/Zr composition and noble metal promotion on nickel based CexZr1−xO2 catalysts for carbon dioxide methanation. *Appl. Catal. Gen.* **2011**, *392*, 36–44.
135. Shido, T.; Iwasawa, Y. Reactant-Promoted Reaction Mechanism for Water-Gas Shift Reaction on Rh-Doped CeO2. *J. Catal.* **1993**, *141*, 71–81.
136. Donazzi, A.; Beretta, A.; Groppi, G.; Forzatti, P. Catalytic partial oxidation of methane over a 4% Rh/α-Al2O3 catalyst: Part I: Kinetic study in annular reactor. *J. Catal.* **2008**, *255*, 241–258.
137. Khajenoori, M.; Rezaei, M.; Nematollahi, B. Preparation of noble metal nanocatalysts and their applications in catalytic partial oxidation of methane. *J. Ind. Eng. Chem.* **2013**, *19*, 981–986.
138. Au, C.-T.; Ng, C.-F.; Liao, M.-S. Methane Dissociation and Syngas Formation on Ru, Os, Rh, Ir, Pd, Pt, Cu, Ag, and Au: A Theoretical Study. *J. Catal.* **1999**, *185*, 12–22.
139. Panagiotopoulou, P.; Kondarides, D.I.; Verykios, X.E. Selective methanation of CO over supported noble metal catalysts: Effects of the nature of the metallic phase on catalytic performance. *Appl. Catal. Gen.* **2008**, *344*, 45–54.

140. Solymosi, F.; Erdöhelyi, A.; Bánsági, T. Methanation of CO2 on supported rhodium catalyst. *J. Catal.* **1981**, *68*, 371–382.
141. Falbo, L.; Visconti, C.G.; Lietti, L.; Szanyi, J. The effect of CO on CO2 methanation over Ru/Al2O3 catalysts: a combined steady-state reactivity and transient DRIFT spectroscopy study. *Appl. Catal. B Environ.* **2019**, *256*, 117791.
142. Meiri, N.; Dinburg, Y.; Amoyal, M.; Koukouliev, V.; Nehemya, R.V.; Landau, M.V.; Herskowitz, M. Novel process and catalytic materials for converting CO2 and H2 containing mixtures to liquid fuels and chemicals. *Faraday Discuss.* **2015**, *183*, 197–215.
143. Kaila, R.K.; Gutiérrez, A.; Slioor, R.; Kemell, M.; Leskelä, M.; Krause, A.O.I. Zirconia-supported bimetallic RhPt catalysts: Characterization and testing in autothermal reforming of simulated gasoline. *Appl. Catal. B Environ.* **2008**, *84*, 223–232.
144. Cronauer, D.C.; Krause, T.; Salinas, J.; Wagner, A.L.; Wagner, J.P. Comparison of Rh, Pt and Rh-Pt supported on an oxide-ion conducting substrate as catalysts for autothermal reforming methane.; 2006; Vol. 231.
145. Fasolini, A.; Ruggieri, S.; Femoni, C.; Basile, F. Highly Active Catalysts Based on the Rh4 (CO) 12 Cluster Supported on Ce0. 5Zr0. 5 and Zr Oxides for Low-Temperature Methane Steam Reforming. *Catalysts* **2019**, *9*, 800.
146. Grunwaldt, J.-D.; Basini, L.; Clausen, B.S. In Situ EXAFS Study of Rh/Al2O3 Catalysts for Catalytic Partial Oxidation of Methane. *J. Catal.* **2001**, *200*, 321–329.
147. Basini, L.; Marchionna, M.; Aragno, A. Drift and mass spectroscopic studies on the reactivity of rhodium clusters at the surface of polycrystalline oxides. *J. Phys. Chem.* **1992**, *96*, 9431–9441.
148. Carrero, A.; Calles, J.; Vizcaíno, A. Effect of Mg and Ca addition on coke deposition over Cu–Ni/SiO2 catalysts for ethanol steam reforming. *Chem. Eng. J.* **2010**, *163*, 395–402.
149. Velasquez, M.; Batiot-Dupeyrat, C.; Gallego, J.; Santamaria, A. Chemical and morphological characterization of multi-walled-carbon nanotubes synthesized by carbon deposition from an ethanol–glycerol blend. *Diam. Relat. Mater.* **2014**, *50*, 38–48.
150. Charisiou, N.D.; Tzounis, L.; Sebastian, V.; Hinder, S.J.; Baker, M.A.; Polychronopoulou, K.; Goula, M.A. Investigating the correlation between deactivation and the carbon deposited on the surface of Ni/Al2O3 and Ni/La2O3-Al2O3 catalysts during the biogas reforming reaction. *Appl. Surf. Sci.* **2019**, *474*, 42–56.
151. Galetti, A.E.; Gomez, M.F.; Arrúa, L.A.; Abello, M.C. Hydrogen production by ethanol reforming over NiZnAl catalysts: influence of Ce addition on carbon deposition. *Appl. Catal. Gen.* **2008**, *348*, 94–102.
152. Fornasiero, P.; Kašpar, J.; Sergo, V.; Graziani, M. Redox Behavior of High-Surface-Area Rh-, Pt-, and Pd-Loaded Ce0.5Zr0.5O2Mixed Oxide. *J. Catal.* **1999**, *182*, 56–69.
153. Mamontov, E.; Brezny, R.; Koranne, M.; Egami, T. Nanoscale Heterogeneities and Oxygen Storage Capacity of Ce0.5Zr0.5O2. *J. Phys. Chem. B* **2003**, *107*, 13007–13014.
154. Lemaux, S.; Bensaddik, A.; van der Eerden, A.M.J.; Bitter, J.H.; Koningsberger, D.C. Understanding of Enhanced Oxygen Storage Capacity in Ce0.5Zr0.5O2: The Presence of an Anharmonic Pair Distribution Function in the Zr−O2 Subshell as Analyzed by XAFS Spectroscopy. *J. Phys. Chem. B* **2001**, *105*, 4810–4815.
155. Luo, M.-F.; Zheng, X.-M. Redox behaviour and catalytic properties of Ce0.5Zr0.5O2-supported palladium catalysts. *Appl. Catal. Gen.* **1999**, *189*, 15–21.
156. Song, W.; Popa, C.; Jansen, A.P.J.; Hensen, E.J.M. Formation of a Rhodium Surface Oxide Film in Rhn/CeO2(111) Relevant for Catalytic CO Oxidation: A Computational Study. *J. Phys. Chem. C* **2012**, *116*, 22904–22915.
157. Koros, W.J.; Fleming, G. Membrane-based gas separation. *J. Membr. Sci.* **1993**, *83*, 1–80.
158. Basile, A. Hydrogen production using Pd-based membrane reactors for fuel cells. *Top. Catal.* **2008**, *51*, 107.

159. Dolan, M.; Dave, N.; Ilyushechkin, A.; Morpeth, L.; McLennan, K. Composition and operation of hydrogen-selective amorphous alloy membranes. *J. Membr. Sci.* **2006**, *285*, 30–55.
160. Reynolds, S.P.; Ebner, A.D.; Ritter, J.A. Stripping PSA cycles for CO2 recovery from flue gas at high temperature using a hydrotalcite-like adsorbent. *Ind. Eng. Chem. Res.* **2006**, *45*, 4278–4294.
161. Ramírez-Moreno, M.J.; Romero-Ibarra, I.C.; Hernández-Pérez, M.; Pfeiffer, H. CO2 adsorption at elevated pressure and temperature on Mg–Al layered double hydroxide. *Ind. Eng. Chem. Res.* **2014**, *53*, 8087–8094.
162. Yong, Z.; Mata, V.; Rodrigues, A.E. Adsorption of carbon dioxide at high temperature—a review. *Sep. Purif. Technol.* **2002**, *26*, 195–205.
163. Yong, Z.; Rodrigues, A.E. Hydrotalcite-like compounds as adsorbents for carbon dioxide. *Energy Convers. Manag.* **2002**, *43*, 1865–1876.
164. Wang, Q.; Tang, S.V.Y.; Lester, E.; O'Hare, D. Synthesis of ultrafine layered double hydroxide (LDHs) nanoplates using a continuous-flow hydrothermal reactor. *Nanoscale* **2013**, *5*, 114–117.
165. Soares, J.L.; Moreira, R.F.; José, H.J.; Grande, C.A.; Rodrigues, A.E. Hydrotalcite materials for carbon dioxide adsorption at high temperatures: characterization and diffusivity measurements. *Sep. Sci. Technol.* **2005**, *39*, 1989–2010.
166. Cavani, F.; Trifiro, F.; Vaccari, A. Hydrotalcite-type anionic clays: Preparation, properties and applications. *Catal. Today* **1991**, *11*, 173–301.
167. Wijitwongwan, R. (Ploy); Intasa-ard, S. (Grace); Ogawa, M. Preparation of Layered Double Hydroxides toward Precisely Designed Hierarchical Organization. *ChemEngineering* **2019**, *3*, 68.
168. Wang, Q.; Wu, Z.; Tay, H.H.; Chen, L.; Liu, Y.; Chang, J.; Zhong, Z.; Luo, J.; Borgna, A. High temperature adsorption of CO2 on Mg–Al hydrotalcite: effect of the charge compensating anions and the synthesis pH. *Catal. Today* **2011**, *164*, 198–203.
169. Yong, Z.; Mata, V.; Rodrigues, A.E. Adsorption of carbon dioxide onto hydrotalcite-like compounds (HTlcs) at high temperatures. *Ind. Eng. Chem. Res.* **2001**, *40*, 204–209.
170. Wang, Q.; Tay, H.H.; Ng, D.J.W.; Chen, L.; Liu, Y.; Chang, J.; Zhong, Z.; Luo, J.; Borgna, A. The Effect of Trivalent Cations on the Performance of Mg-M-CO3 Layered Double Hydroxides for High-Temperature CO2 Capture. *ChemSusChem* **2010**, *3*, 965–973.
171. Hutson, N.D.; Attwood, B.C. High temperature adsorption of CO 2 on various hydrotalcite-like compounds. *Adsorption* **2008**, *14*, 781–789.
172. Wang, X.P.; Yu, J.J.; Cheng, J.; Hao, Z.P.; Xu, Z.P. High-temperature adsorption of carbon dioxide on mixed oxides derived from hydrotalcite-like compounds. *Environ. Sci. Technol.* **2007**, *42*, 614–618.
173. Gupta, H.; Fan, L.-S. Carbonation−Calcination Cycle Using High Reactivity Calcium Oxide for Carbon Dioxide Separation from Flue Gas. *Ind. Eng. Chem. Res.* **2002**, *41*, 4035–4042.
174. Lysikov, A.I.; Salanov, A.N.; Okunev, A.G. Change of CO2 Carrying Capacity of CaO in Isothermal Recarbonation−Decomposition Cycles. *Ind. Eng. Chem. Res.* **2007**, *46*, 4633–4638.
175. Arpentinier, P.; Basile, F.; Gallo, P.D.; Fornasari, G.; Gary, D.; Rosetti, V.; Vaccari, A. Role of the hydrotalcite-type precursor on the properties of CPO catalysts. *Catal. Today* **2005**, *99*, 99–104.
176. Albertazzi, S.; Basile, F.; Benito, P.; Del Gallo, P.; Fornasari, G.; Gary, D.; Rosetti, V.; Vaccari, A. Effect of silicates on the structure of Ni-containing catalysts obtained from hydrotalcite-type precursors. *Catal. Today* **2007**, *128*, 258–263.
177. Basile, F.; Benito, P.; Fornasari, G.; Gazzoli, D.; Pettiti, I.; Rosetti, V.; Vaccari, A. Ni-catalysts obtained from silicate intercalated HTlcs active in the catalytic partial oxidation of methane: Influence of the silicate content. *Catal. Today* **2009**, *142*, 78–84.

178. Groen, J.C.; Pérez-Ramírez, J. Critical appraisal of mesopore characterization by adsorption analysis. *Appl. Catal. Gen.* **2004**, *268*, 121–125.
179. Rouquerol, J.; Rouquerol, F.; Llewellyn, P.; Maurin, G.; Sing, K.S. *Adsorption by powders and porous solids: principles, methodology and applications*; Academic press, 2013; ISBN 0-08-097036-2.
180. Reichle, W.T. Synthesis of anionic clay minerals (mixed metal hydroxides, hydrotalcite). *Solid State Ion.* **1986**, *22*, 135–141.
181. Zarghami, S.; Hassanzadeh, A.; Arastoopour, H.; Abbasian, J. Effect of Steam on the Reactivity of MgO-Based Sorbents in Precombustion CO2 Capture Processes. *Ind. Eng. Chem. Res.* **2015**, *54*, 8860–8866.
182. Wang, Q.; Sun, L.; Courson, C.; Pfeiffer, H.; Shi, Y.; Bruce, D.W.; O'Hare, D.; Walton, R.I. *Pre-combustion Carbon Dioxide Capture Materials*; Royal Society of Chemistry, 2018; ISBN 1-78801-492-8.
183. Ocampo, F.; Louis, B.; Roger, A.-C. Methanation of carbon dioxide over nickel-based Ce0. 72Zr0. 28O2 mixed oxide catalysts prepared by sol–gel method. *Appl. Catal. Gen.* **2009**, *369*, 90–96.
184. Ocampo, F.; Louis, B.; Kiennemann, A.; Roger, A. CO2 methanation over Ni-Ceria-Zirconia catalysts: effect of preparation and operating conditions.; IOP Publishing, 2011; Vol. 19, p. 012007.
185. Aldana, P.U.; Ocampo, F.; Kobl, K.; Louis, B.; Thibault-Starzyk, F.; Daturi, M.; Bazin, P.; Thomas, S.; Roger, A. Catalytic CO2 valorization into CH4 on Ni-based ceria-zirconia. Reaction mechanism by operando IR spectroscopy. *Catal. Today* **2013**, *215*, 201–207.
186. Weatherbee, G.D.; Bartholomew, C.H. Hydrogenation of CO2 on group VIII metals: I. Specific activity of NiSiO2. *J. Catal.* **1981**, *68*, 67–76.
187. Yamasaki, M.; Habazaki, H.; Asami, K.; Izumiya, K.; Hashimoto, K. Effect of tetragonal ZrO2 on the catalytic activity of Ni/ZrO2 catalyst prepared from amorphous Ni–Zr alloys. *Catal. Commun.* **2006**, *7*, 24–28.
188. Yamasaki, M.; Komori, M.; Akiyama, E.; Habazaki, H.; Kawashima, A.; Asami, K.; Hashimoto, K. CO2 methanation catalysts prepared from amorphous Ni–Zr–Sm and Ni–Zr–misch metal alloy precursors. *Mater. Sci. Eng. A* **1999**, *267*, 220–226.
189. Aksoylu, A.E.; Mısırlı, Z.; Önsan, Z.İ. Interaction between nickel and molybdenum in Ni–Mo/Al2O3 catalysts: I: CO2 methanation and SEM-TEM studies. *Appl. Catal. Gen.* **1998**, *168*, 385–397.
190. Laosiripojana, N.; Assabumrungrat, S. Methane steam reforming over Ni/Ce–ZrO2 catalyst: Influences of Ce–ZrO2 support on reactivity, resistance toward carbon formation, and intrinsic reaction kinetics. *Appl. Catal. Gen.* **2005**, *290*, 200–211.
191. Azancot, L.; Bobadilla, L.F.; Santos, J.L.; Córdoba, J.M.; Centeno, M.A.; Odriozola, J.A. Influence of the preparation method in the metal-support interaction and reducibility of Ni-Mg-Al based catalysts for methane steam reforming. *Int. J. Hydrog. Energy* **2019**, *44*, 19827–19840.
192. Wu, X.; Wu, X.; Liang, Q.; Fan, J.; Weng, D.; Xie, Z.; Wei, S. Structure and oxygen storage capacity of Pr/Nd doped CeO2–ZrO2 mixed oxides. *Solid State Sci.* **2007**, *9*, 636–643.
193. Wang, Q.; Zhao, B.; Li, G.; Zhou, R. Application of Rare Earth Modified Zr-based Ceria-Zirconia Solid Solution in Three-Way Catalyst for Automotive Emission Control. *Environ. Sci. Technol.* **2010**, *44*, 3870–3875.
194. Van Herwijnen, T.; Van Doesburg, H.; De Jong, W. Kinetics of the methanation of CO and CO2 on a nickel catalyst. *J. Catal.* **1973**, *28*, 391–402.
195. Lee, G.D.; Moon, M.J.; Park, J.H.; Park, S.S.; Hong, S.S. Raney Ni catalysts derived from different alloy precursors Part II. CO and CO 2 methanation activity. *Korean J. Chem. Eng.* **2005**, *22*, 541–546.

196. Aziz, M.; Jalil, A.; Triwahyono, S.; Mukti, R.; Taufiq-Yap, Y.; Sazegar, M. Highly active Ni-promoted mesostructured silica nanoparticles for CO2 methanation. *Appl. Catal. B Environ.* **2014**, *147*, 359–368.
197. Xu, J.; Froment, G.F. Methane steam reforming, methanation and water-gas shift: I. Intrinsic kinetics. *AIChE J.* **1989**, *35*, 88–96.